Modeling of the mechanical behavior of fibrous soft tissues : influence of fibre-fibre bonds, and of corrugation and fibre orientation

Chenghe Piao

THÈSE POUR OBTENIR LE GRADE DE DOCTEUR DE L'UNIVERSITÉ DE MONTPELLIER

En Mécanique, Génie Civil et Architecture

École doctorale : Information, Structures et Systèmes

Unité de recherche : Laboratoire de Mécanique et Génie Civil (LMGC)

Modeling of the mechanical behavior of fibrous soft tissues: influence of fibre-fibre bonds, and of corrugation and fibre orientation

---

Modélisation du comportement mécanique de tissus mous fibreux : influence des liens fibre-fibre, de l'ondulation et de l'orientation des fibres

Présentée par Chenghe PIAO
le 16 décembre 2022

Sous la direction de Pascale ROYER et Christiane WAGNER-KOCHER

Devant le jury composé de

Yann MONERIE, Professeur, LMGC/Université de Montpellier	Président du jury
Martine PITHIOUX, Directrice de Recherche, ISM/CNRS	Examinatrice
Jean-Marc ALLAIN, Professeur, M3DISIM/Ecole Polytechnique	Rapporteur
Cédric LAURENT, Maître de conférences HDR, LEM3/ENSEM/Université de Lorraine	Rapporteur
Pascale ROYER, Directrice de Recherche, LMGC/CNRS	Co-directrice de thèse
Christiane WAGNER-KOCHER, Maîtresse de conférences, LMGC/Université de Montpellier	Co-directrice de thèse
Simon LE FLOC'H, Maître de conférences, LMGC/Université de Montpellier	Invité, Encadrant
Patrick CAÑADAS, Maître de conférences, LMGC/Université de Montpellier	Invité, Encadrant

UNIVERSITÉ DE MONTPELLIER

Remerciements

Je vis en France depuis 2016 lorsque j'ai débuté ma formation d'ingénieur à Polytech Montpellier. En décembre 2022, j'ai soutenu ma thèse démarrée en octobre 2019 et ai obtenu avec succès mon doctorat. Je vis donc depuis plus de 6 années en France et je tiens ici à remercier tous ceux qui m'ont aidé et soutenu depuis mon arrivée.

Tout d'abord, je remercie ma co-directrice de thèse, **Pascale Royer**, pour son soutien et son aide de tous les instants. Je me souviendrai toujours de ses efforts pour me donner une meilleure compréhension du contexte scientifique du sujet au début de ma thèse. Je lui adresse mes meilleures pensées de bon rétablissement et mes vœux de bonne santé.

Je remercie également, ma co-directrice de thèse, **Christiane Wagner-Kocher** pour m'avoir traité comme si j'étais son fils et pour m'avoir fait sentir son empathie et son soutien permanent. Bien qu'elle ait déménagé en Corée pendant ma thèse, elle a continué à suivre l'avancement de ma thèse malgré les 8 heures de décalage horaire.

Je remercie mon co-encadrant, **Simon Le Floc'h**, pour ses idées innovantes et sa rigueur scientifique. Les discussions avec lui sur de nombreux détails m'ont donné confiance dans l'avancement de mes travaux. Je me souviendrai toujours de ses efforts pour comprendre et vérifier chaque détail de ma thèse.

Je remercie mon co-encadrant, **Patrick Cañadas**. J'ai le plaisir de le connaître depuis ma formation d'ingénieur, son ouverture d'esprit et son humour m'ont toujours accompagné avec joie. Après qu'il ait relu mon manuscrit, je savais qu'il n'y avait pas d'inquiétude quant au placement des virgules.

Cette équipe avec laquelle j'ai travaillé durant ces années de thèse est une véritable chance pour moi et cela m'accompagnera durant toute ma vie. En effet,

travailler avec quatre différents spécialistes est d'une richesse exceptionnelle. Ils m'ont toujours écouté, m'ont toujours conseillé, m'ont toujours encouragé tant d'un point de vue professionnel que personnel. J'espère que nous resterons toujours en contact.

Merci à **Yann Monerie**, qui m'a guidé depuis ma formation d'ingénieur, et que je remercie également pour ses commentaires pertinents et importants sur mon modèle. Merci aussi à **Loïc Daridon**, pour nos intéressantes discussions scientifiques ainsi que pour ses conseils cruciaux sur mes travaux.

Merci à **Franck Jourdan**, qui dirige l'équipe BIOTIC, pour son soutien permanent durant ma thèse. Merci à **Stéphane Pagano**, directeur du LMGC, pour son accueil et pour m'avoir soutenu lors du concours de candidature à cette thèse. Merci à **Franck Nicoud** et **Aurélie Niel Marchal** pour leurs conseils et leur aide lors de ma candidature à cette thèse.

Merci à **André Chrysochoos**, **Bertrand Wattrisse**, **Olivier Arnould**, **Jean-Michel Muracciole** et **Hervé Louche** pour leur aide durant ma formation d'ingénieur. Merci à **Nathalie Rubiano**, **Pascale Tournan** et **Sandra Durand** pour leur aide administrative pendant ma formation d'ingénieur à Polytech.

Merci à **Yvan Duhamel**, **Jonathan Barés**, **Rémy Mozul**, **Fréderic Dubois**, **Gille Camp**, **Stephan Devic**, **Vincent Huon**, **Norbert Deleutre** et **Thierry Vigo** pour leur aide et soutien technique.

Merci à **Annarella Remerciaro**, **Laure Di Meilla**, **Cyril Videau**, **Caroline Dat**, **François Gibier**, **Roxane Cremer**, **Isabelle Redon**et **Sonia Benaissa** pour leur soutien administratif au LMGC.

Merci à **Cristina Cavinato**, **Mathieu Renouf**, **Delphine Jullien**, **Sandrine Bardet**, **Bruno Clair**, **Cédric Montero**, **Serge Mora** et **Emilien Azéma** pour toutes nos intéressantes discussions scientifiques

Merci à mes collègues hors LMGC, en particulier merci à **Jean Boisson** (ENSTA Paris), **Jiří Burša** (Brno University of Technology), **Mazza Edoardo** (ETH Zurich), **Pascal Swider** (IMFT, Toulouse), **Holzapfel Gerhard** (Graz University of Technology), **Dmytro Kuksenko**, **Pauline Assemat** (IMFT Toulouse) et **Adel Moreno** (IMFT Toulouse) pour toutes les si fructueuses discussions scientifiques.

Merci à mes collègues et amis de thèse **Théo Simonet** et **Max Sonzogni** pour l'aide qu'ils m'ont apportée depuis mon arrivée en France durant ma formation d'ingénieur, mais aussi pour m'avoir aidé à améliorer mon francais. Merci à **Jonaz Vasquez-Villegas** pour son aide lors de mon intégration dans l'équipe ainsi que pour son aide lors de la programmation sur Cast3M.

Merci à mes collègues de l'équipe BIOTIC : **Vincent Serantoni**, **Léa Boillereaux**, **Nathan Collin**, **Emilie Parpaillon**, **Noémie Petitjean**, **Jimmy Teixeira** et **Gilles Dusfour** pour leurs contributions au projet de l'équipe BIOTIC ainsi que pour

cette solidarité d'équipe que j'ai ressentie tout au long de ma thèse et au delà.

Merci à tous mes collègues doctorants, et en particulier à **Sneha Hegde**, **Samuel Kurtz**, **Thomas Boursat**, **Agathe Bignon**, **Willliam Le Goff**, **Hui Lian**, **Tai-Yun Hsieh**, **Hsien-Tsung Hu**, **Manuel Cardenas**, **Oscar Polania**, **Félix Laboup**, **Thierry Ndzana Satoh**, **Clément Tosi**, **Xavier Maetz**, **Camelia Ayed**, **Alaa Al Fay** et **Keovathana Run** pour toutes les pauses café et les soirées, grâce à vous j'ai bien pu profiter de ma vie de doctorant.

Merci à **Zhuo Peng**, **Weiyi Wang**, **Siyuan Niu**, **Junyi Chen**, **Serge Deguez**, **Byunghee** et **Yuna Shi** pour ces soutiens spirituels pendant ma these.

Enfin, j'aimerais aussi remercier mes parents, **Feng Piao** et **Lanxiang Xu** pour leur amour et leur soutien constant.

Depuis mon arrivée en France en 2016, en tant qu'étranger ne parlant pas francais, j'ai souvent rencontré des difficultés dans la vie. Je me sens vraiment très chanceux d'avoir rencontré des amis et des collègues aussi chaleureux et gentils. Au cours de ces années de vie en France, j'ai été touché milles fois par tous ces amis. Je suis sincèrement reconnaissant à toutes les personnes qui m'ont aidé, sans leur aide je n'aurais pas pu réussir à ma thèse. Le diplôme de doctorat marque la fin de ma vie d'étudiant et cela signifie aussi un nouveau chapitre de ma vie. J'aimerais de tout cœur rester en contact avec tous ces amis car ils sont pour moi une incroyable richesse dans ma vie.

Contents

Resumé

Les tissus conjonctifs sont des tissus biologiques qui permettent de maintenir la forme du corps et de ses organes ; ils assurent leur cohésion ainsi que leur soutien interne. La plupart des tissus conjonctifs mous sont fibreux, comme par exemple les artères, l'annulus fibrosus, les tendons et ligaments, etc. L'étude des coefficients de Poisson de tissus mous fibreux a depuis peu retenu l'attention de nombreux auteurs de travaux dans le domaine de la modélisation mécanique, car des valeurs élevées et/ou négatives ont été mesurées expérimentalement. Ce travail de thèse se concentre principalement sur les évolutions des coefficients de Poisson dans les tissus mous fibreux en fonction de l'arrangement des fibres, et plus spécifiquement, de leurs ondulations et de leur organisation spatiale.

Le manuscrit est organisé en quatre chapitres.

Le premier a un pour objectifs de décrire la microstructure et de présenter un état de l'art sur la mesure expérimentale et la prédiction par modèles des coefficients les Poisson de tissus mous conjonctifs fibreux (artère, annulus fibrosus, tendon et ligament).

Dans un premier temps, la microstructure et les composants des tissus de l'artère, de l'annulus fibrosus, des tendons et des ligaments sont présentés.

Dans ces tissus, la structure des fibres de collagène est ondulée ainsi que le montre l'exemple de l'annulus fibrosus, illustré sur la Figure 1.

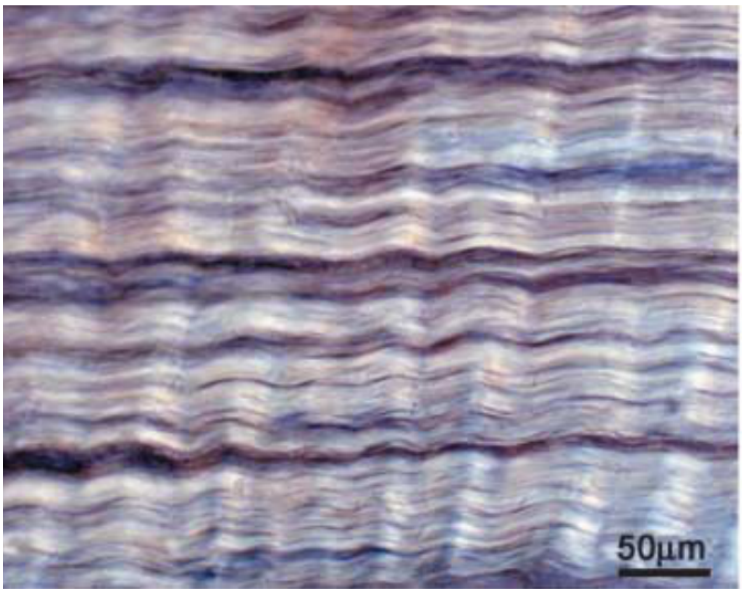

Figure 1: Structure des fibres de collagène dans l'annulus fibrosus. Reproduit de *Pezowicz et al.* [2005].

Puis, une revue bibliographique sur la mesure expérimentale de coefficients de Poisson de tissus mous fibreux est proposée, suivie d'une synthèse des modèles mécaniques permettant de prédire ces coefficients de Poisson.

Par la suite, on considèrera les tissus mous fibreux comme un matériau composite avec des fibres ondulées. On résume ici des modèles composite mécaniques présentant ce type de structure.

On y justifie ainsi l'intérêt et les motivations des travaux présentés dans les chapitres suivants. Un modèle micromécanique analytique de l'annulus fibrosus est proposé dans le deuxième chapitre, basé sur des observations issues de la littérature. Ce tissu est constitué de plusieurs lamelles où les fibres de collagène sont disposées en parallèle dans chaque lamelle. L'orientation des fibres diffère d'une lamelle à l'autre comme montré dans la Figure 2a. Dans ce modèle, la fibre a une microstructure ondulée

et sa forme est considérée comme étant sinusoïdale. L'ondulation des fibres et de la structure lamellaire est montrée sur la Figure 2b. L'effet de la structure des fibres ondulées sur le coefficient de Poisson est alors étudié. Nous modélisons la structure lamellaire du tissu annulus fibrosus comme un composite stratifié renforcé par des fibres parallèles ondulées. Ce modèle prend en compte la dispersion des fibres dans les différentes couches. Afin de comprendre transformation de la matrice de rigidité effective orientée, nous présentons dans un premier temps la méthode de transformation de la matrice de rigidité. Ensuite, nous introduisons en détail la transformation de la matrice de rigidité effective du composite renforcé par des fibres à ondulations sinusoïdales qui est proposée et vérifiée par *Xiao et al.* [2020]. Puis, une solution analytique, qui prend en compte les multiples couches et leur orientation pour trouver la matrice de rigidité élastique effective, est présentée. Enfin, en tenant compte du domaine physiologique étendu du tissu de l'annulus fibrosus, une étude paramétrique du modèle micromécanique est menée pour analyser l'influence de chaque paramètre sur les propriétés mécaniques globales ainsi que l'effet des fibres ondulées sur le coefficient de Poisson du composite.

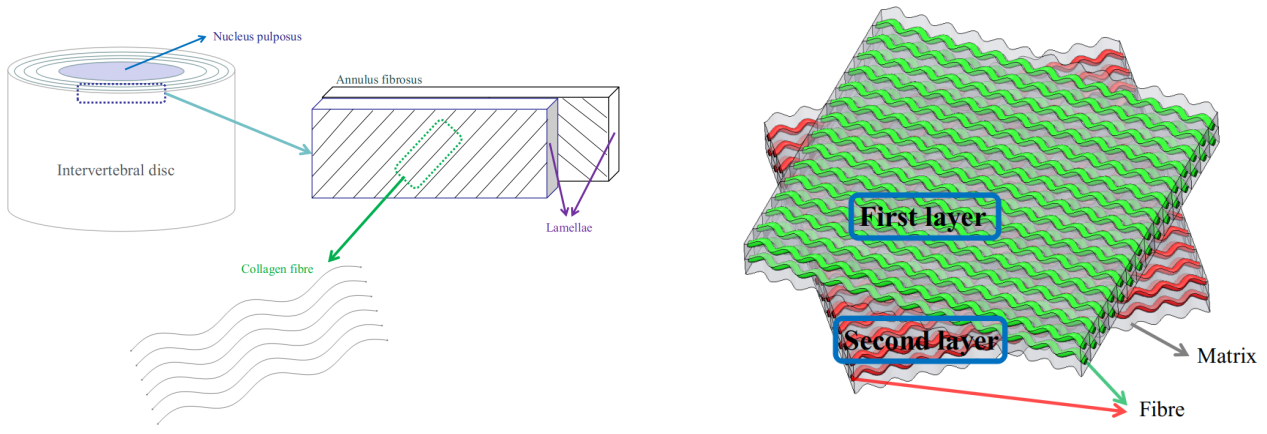

(a) (b)

Figure 2: (a) Schéma des composants et de la microstructure du disque intervertébral. (b) Structure composite lamellaire.

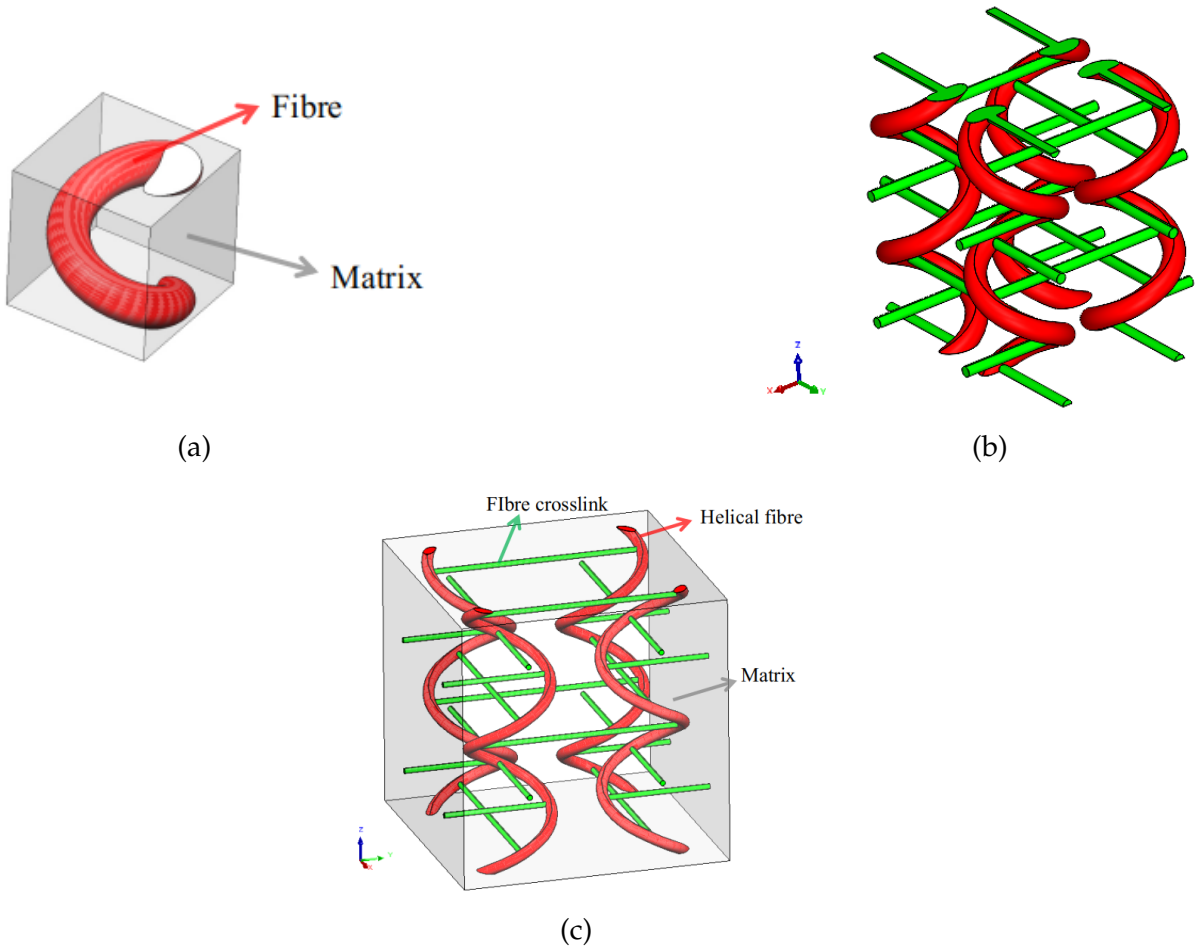

Figure 3: (a) Volume élémentaire représentatif (VER) du composite renforcé par un arrangement périodique de fibres hélicoïdales non connectées. (b) VER des fibres hélicoïdales reliées entre elles par des liens mais sans matrice. (c) VER du composite fibres/matrice renforcé par des fibres hélicoïdales avec liens.

Suite à des observations issues de la littérature, nous nous intéressons ensuite aux tissus fibreux mous tels que les artères et les tendons qui possèdent une microstructure de fibres de collagène en hélices interconnectées. Trois microstructures sont proposées et étudiées : un composite renforcé par un arrangement périodique de fibres hélicoïdales non connectées, des fibres hélicoïdales reliées entre elles par des liens mais sans matrice et un composite fibres/matrice renforcé par des fibres hélicoïdales avec liens. Les volumes élémentaires représentatifs (VER) des trois matériaux sont représentés sur la Figure 3. Dans un premier temps, la théorie de l'homogénéisation

asymptotique et son implémentation numérique avec validation sont présentées. Une étude paramétrique est ensuite menée afin de comprendre l'influence des connexions entre fibres sur les propriétés mécaniques globales des matériaux modèles proposés. Cette étude paramétrique montre les effets de la fraction volumique de fibres, de l'angle d'hélice et de la position des liens sur les propriétés mécaniques macroscopiques. De plus, le rôle de la matrice sur le comportement mécanique global est également étudié. Enfin, les effets de la matrice et des fibres hélocoïdales avec liens sur le coefficient de Poisson global sont montrés.

Suite aux deux études précédentes concernant des composites renforcés par des fibres ondulées, où les fibres et la matrice supposent des conditions d'interface parfaites et ont une grande différence de rigidité, nous nous interessons à leur étude expérimentale, ce type de travaux sont actuellement encore très rares dans la litterature. Le dernier chapitre de ce manuscrit présente donc un travail exploratoire sur un procédé de fabrication de matériaux modèles composés de silicone et de fibres hélicoïdales, permettant d'explorer leurs comportements mécaniques. Une méthode de fabrication de matériau modèle composite renforcé par des fibres hélicoïdales est développée. Une analyse par éléments finis est également présentée pour prédire le comporte-ment mécanique du composite à fibre helicoïdale.

Finalement, d'après ce travail de thèse , on conclut que la microstructure des fibres ondulées influence sensiblement les coefficients de Poisson globaux du tissu mou fibreux. L'amplitude d'ondulation des fibres 2D réduit la réponse auxétique dans la structure stratifiée ; la position des liens entre les fibres change du tout au tout les coefficients de Poisson effectifs (de négatifs < 0 à positifs > 0.5) ; et la matrice réduit l'effet auxétique.

List of Figures

List of Tables

Introduction

The tissues and cell biomechanics (BIOTIC) team of the mechanical and civil engineering laboratory (LMGC) in Montpellier, France, has been studying the intervertebral disc for more than 10 years. Over this time, the auxetic behavior of annulus fibrosus tissue has been described several times (*Baldit et al.* [2014]; *Dusfour et al.* [2020]). As the auxetic response is nonintuitive and its mechanics are unknown in annulus fibrosus tissue, we tried to find the mechanical explanation for the auxetic behavior. In addition, the auxetic bahavior has been reported in artery and tendon tissue. Therefore, the subject of this thesis was proposed in order to find an explanation for the counterintuitive volume changes of soft tissue during their mechanical solicitation. A study of the Poisson's ratio values in annulus fibrosus and their mechanical explanation could be of importance in the domain of biomechanical modeling of soft fibrous tissues, as most of the corresponding models developed until now have been based on the assumption of a quasi-incompressible behavior of these living materials (i.e., a value of Poisson's ratio ≈ 0.5 for isotropic material). Here, we aim to uncover information useful for further modeling developments in the study of the mechanical behaviour of soft living tissues. This thesis mainly focuses on the role of fibre microstructure arrangement in the behavior of the Poisson's ratio in soft tissue. Here, particular attention is given to the feature of fibre corrugation. We apply the linear elastic model because the determination of Poisson's ratios is clearer in the framework of a linear model than in a nonlinear model.

Chapter 1 mainly provides a literature review on the Poisson's ratio of fibrous, soft connective tissue and outlines our motivation for the work in the following chapters. First, we present the most up-to-date understanding of the microstructure and components of fibrous soft tissue. We then provide a summary of the literature on the Poisson's ratio of fibrous soft tissues and the predictions of mechanical models. Finally, we present composite

models involving crimped structures and their applications.

In Chapter 2, we present an analytical micromechanical model for studying the lamellar composite structure of annulus fibrosus tissue. Annulus fibrosus tissue is made up of several lamellae (hereafter also referred to as layers). The collagen fibres are arranged in parallel in each lamella and the fibre orientation differs from one lamella to its neighbors. The parallel fibres in each lamella have been observed to have a crimped microstructure. The proposed model takes into account the fibre dispersion in different layers and considers fibre waviness as a sinusoidal shape. First, we outline and demonstrate the stiffness matrix transformation method. We then provide details of how we deduce an effective stiffness matrix of composite reinforced by fibres characterised by a sinusoidal waviness. Subsequently, we propose an analytical solution that takes into account the multiple layers and the orientation of the parallel fibres of each layer in order to find the effective elastic stiffness matrix. Finally, we study various parameters of the model over the extended physiological range of annulus fibrosus tissue in order to analyze the influence of each parameter on the global mechanical properties of the proposed micromechanical model.

In chapter 3, we study the soft fibrous tissues by considering them as helical-fibre-reinforced composite, and study the effects of cross-linking between fibres and the presence of a matrix thereof. The assumption of the helical fibre structure is based on observations in the literature of tissue from tendon and the arterial wall. First, we present asymptotic homogenization theory and a numerical implementation method. We then validate this method. Finally, we study the properties of helical-fibre-reinforced composite and helical fibres with cross-links separately, before amalgamating the two to study composite reinforced with cross-linked helical fibres.

In chapter 4, we show how we developed a method for manufacturing helical-fibre-reinforced-composite model material. We also present a finite element analysis that we use to predict the mechanical behavior of the fabricated composite. In the last section, we summarize the main results of the thesis and propose perspectives for further work.

CHAPTER 1

Scientific context

The connective tissues are a group of tissues that maintain the form of the body and its organs, and provide cohesion and internal support. Of the many types of connective tissue of the human body, fibrous connective soft tissue contains many fibres, and is found for example in the arterial wall, annulus fibrosus, tendons, and ligaments. Classically, most models developed so far to describe the mechanical behavior of such soft tissues have been based on the assumption of quasi-incompressibility of the material: a Poisson's ratio $\approx$ 0.49. This assumption was probably mainly related to the predominance of the liquid phase within biological tissues, which is known to be quasi-incompressible. However, recently, the Poisson's ratio of fibrous soft tissue has received increasing attention in the field of mechanical modeling because values of greater than 0.5 as well as negative values have both been measured experimentally. Such a large range of Poisson's ratios reported in the literature could be due to experimental conditions or tissue microstructure. The present thesis mainly focuses on changes in the Poisson's ratio of fibrous soft tissue attributable to characteristics of their fibre structure, and more specifically, to the effects of corrugation.

This chapter mainly provides a review of the literature on Poisson's ratios of fibrous soft connective tissue in order to explain the motivations of the work presented in the following chapters. To this end, first the micro-structure and components of artery, annulus fibrosus, tendon, and ligament tissues are presented in section 1.1, in which the structure of corrugated collagen fibre is emphasized. A summary of the literature on the Poisson's ratio of fibrous soft tissues is then provided in section 1.2 together with a review of the predictions provided by mechanical models. Subsequently, as we consider the fibrous soft tissue as composite material containing crimped fibres, in section 1.3 we describe some of

the various mechanical composite models involving crimped fibre structures. Finally, the motivation behind this work and the aims of this thesis are outlined in section 1.4.

1.1 Fibrous soft tissues: micro-structure and components

1.1.1 Artery tissue

The artery is a kind of vessel, transporting blood from the heart to the other tissues or organs of the body. The healthy artery wall is composed of three layers: intima, media, and adventitia. Figure 1.1 shows a diagrammatic model of the major components of arterial tissue.

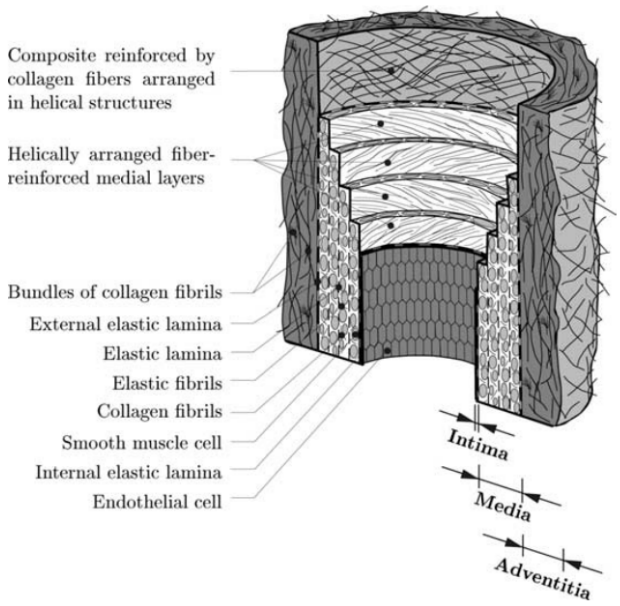

Figure 1.1: Diagrammatic model of the major components of arterial tissue. The tissue consists of three layers: intima, media, and adventitia. Diagram reproduced from *Holzapfel et al.* [2000].

1.1.1.1 Intima

The intima is the inner layer of the artery and consists of a single layer of endothelial cells and an internal elastic lamina. It is the interface between blood vessel walls and the flowing blood itself. The internal elastic lamina provides structural cohesion and support for axial pretension (*Farand et al.* [2007], *Timmins et al.* [2010]), and is mainly composed of dispersed, oriented collagen fibres (*Canham et al.* [1989]; *Finlay et al.* [1995]) and elastin fibres, which are made of a rubber-like protein arranged in a three-dimensional network.

1.1.1.2 Media

The media is the middle layer of the artery and consists of collagen, elastin, and smooth muscle cells (*Holzapfel et al.* [2000]). Collagen in media is made up of 30% type I and 70% type III (*von der Mark* [1981]; *Shekhonin et al.* [1985]). The media has a varying number of medial lamellar units, each of which is about 10 μm thick (*Bohr et al.* [1980]). From a morphological point of view, the media has a periodical concentric separation between the lamellar units (*Morin et al.* [2019]). The elastin, bundles of collagen fibres, and smooth muscle cells together constitute a continuous fibrous helix (*Staubesand* [1959]). The wavy form of collagen fibres (*Morin et al.* [2019]; *Niestrawska et al.* [2022]), as shown in Figure 1.2, is oriented cricumferentially (*O'Connell et al.* [2008]; *Timmins et al.* [2010]; *Hill et al.* [2012]) and is closely associated with the lamellae (*Dingemans et al.* [2000]). Upon loading, the collagen fibres relax, or "decrimp", and stretch to prevent over distension of the vessel (*Morin et al.* [2019]). Moreover, there are cross-links between collagen fibres and the morphology of the elastic lamellae presents a fibrous texture suggestive of a crisscrossed scaffold (*Ushiki* [2002]).

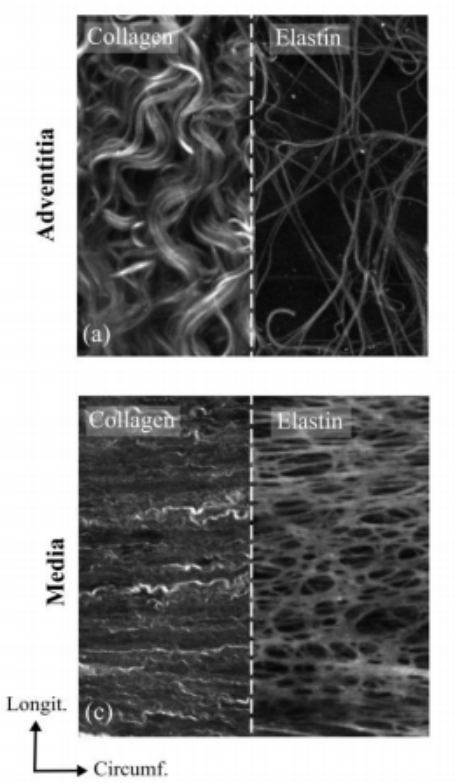

Figure 1.2: Collagen and elastin fibre microstrucutre in media and adventitia layers. Image reproduced from *Morin et al.* [2019].

1.1.1.3 Adeventita

The adventitia is the outer layer of the artery and consists of fibroblasts, fibrocytes, histological ground substance, elastin, and collagen fibres. The collagen fibres of the adventitia are primarily Type II (*von der Mark* [1981]) and pack into thick bundles (*Morin et al.* [2019]) of helical form (*Roy et al.* [2010]; *Rezakhaniha et al.* [2012]; *Schrauwen et al.* [2012]; *Morin et al.* [2019]), as shown in Figure 1.2. The elastin of the adventitia takes the form of a low-density meshwork made of variously oriented fibres. Due to the corrugation or crimped nature of the collagen in the adventitia, the collagen network is capable of undergoing important morphological rearrangements under mechanical loading (*Billiar and Sacks* [1997]; *Billiar and Sacks* [1997]).

1.1.2 Annulus fibrosus tissue

Before describing the annulus fibrosus tissue, let us begin by describing the vertebral column to better understand its location and function. The vertebral column, also known as the spine, is part of the axial skeleton. The human spine consists of 33 bony vertebrae with 23 cartilaginous intervertebral discs – 6 in the cervical region (neck), 12 in the thoracic region (middle back), and 5 in the lumbar region (lower back) as shown in Figure 1.3.

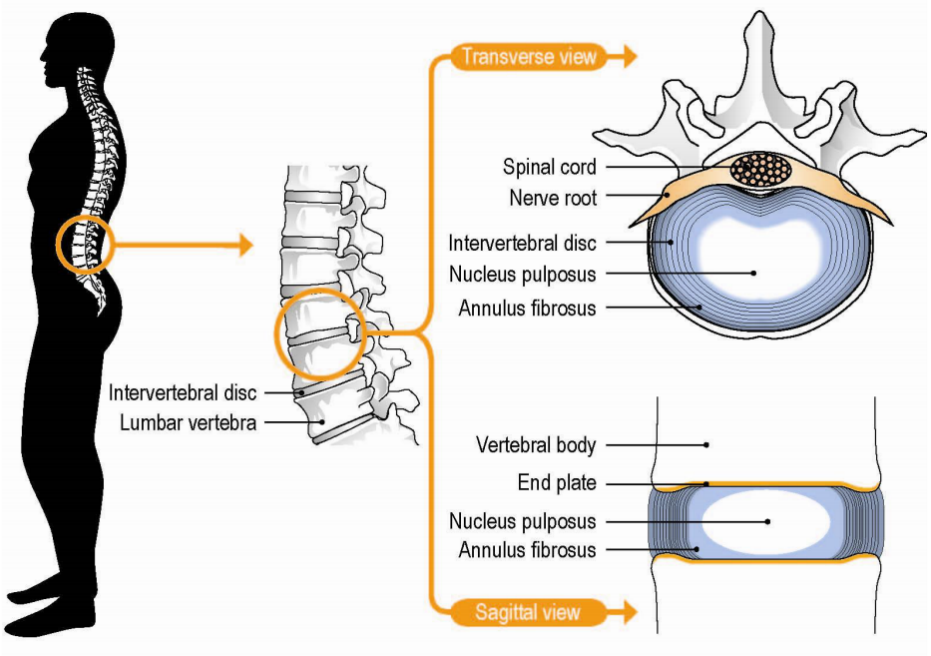

Figure 1.3: Anatomical diagram with a description of the location and components of the intervertebral disc. Image reproduced from *Barreto Henriksson* [2010].

There are 7 cervical vertebrae, 12 thoracic, 5 lumbar, 5 sacral, and 4 caudal, of with those of the lumbar being the largest. The vertebrae bear the load applied to the spine, and support and protect the spinal cord. The vertebrae consist of a vertebral body and laminae that extend from this latter and enclose the spinal cord.

The intervertebral discs are flattened and cylindrical. Together, these elements support the movements of the spine, as well as the transmission and damping of mechanical effort. The intervertebral disc is composed of outer annulus fibrosus (AF) and inner nucleus pulposus (NP), and the endplates – one at the superior end of the disc and one at the inferior end – serve as interfaces with the two adjacent vertebrae (see Figure 1.3).

The central nucleus pulposus is composed of $80\% - 90\%$ water, with the remainder made up of extra cellular matrix and cellular elements that have a distribution of $4 * 10^3 / mm^3$. The collagen of the extra cellular matrix is mainly type II, with small amounts of types VI and XI (*Barreto Henriksson* [2010]).

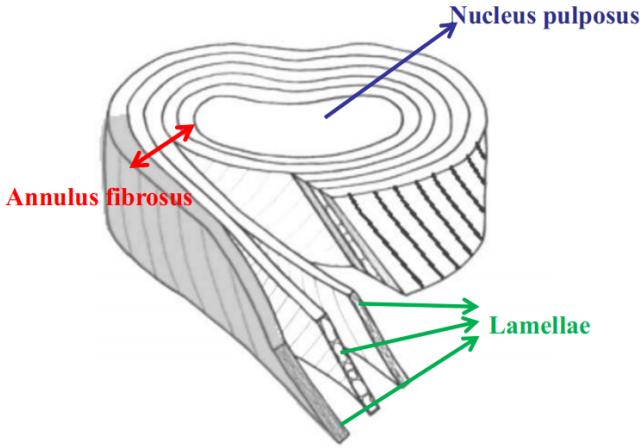

Figure 1.4: Diagram of the annulus fibrosus lamellae. Image reproduced from *Pezowicz* [2010]

The annulus fibrosus (AF) is a fibrosus soft tissue containing $60\% - 85\%$ water, with the remainder made up of cellular elements, collagen fibres, microfibrilles, and proteoglycans. The AF consists of several concentric lamellae, with the collagen fibres of each individual lamina being arranged in parallel. As shown in Figure 1.4, the parallel collagen fibres within each lamella are of an opposing orientation from one lamella to the next. The outer annulus fibrosus, which is made up of Type I and Type II collagen, dominates the inner AF [*Bhattacharya and Dubey*, 2021]. The parallel fibres in each lamella are observed to have a crimped microstructure, as shown in Figure 1.5a, and cross-links are found between crimped fibres at a smaller scale, as shown in Figure 1.5b.

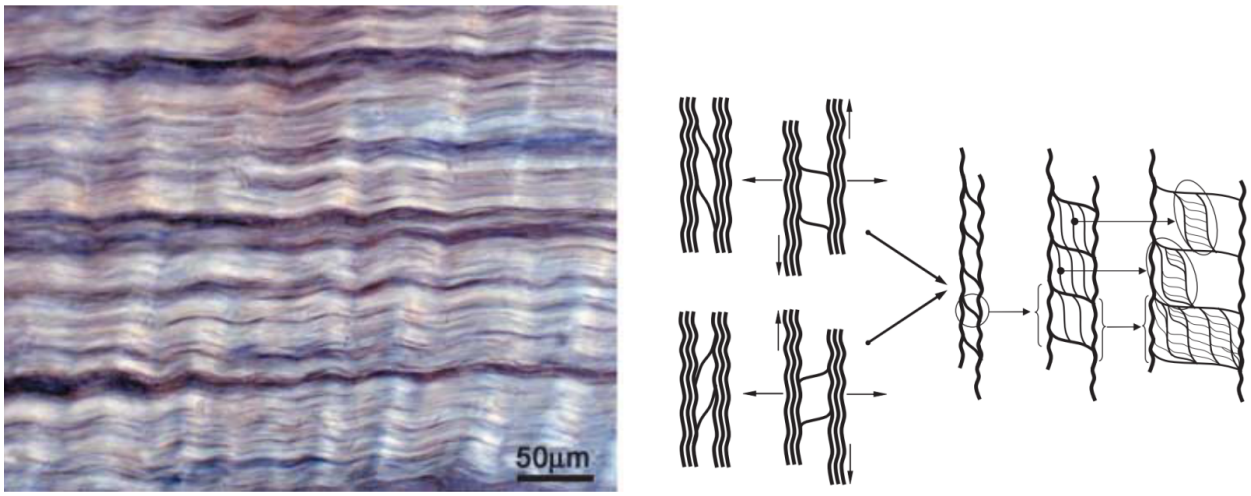

(a) (b)

Figure 1.5: (a) Collagen fibre structure in the annulus fibrosus. (b) Schematic diagram of interconnectivity involving mono-cross-over of collagen in the annulus fibrosus. Diagram reproduced from *Pezowicz et al.* [2005].

1.1.3 Tendons and ligaments

Tendons are tough bands of dense fibrous connective tissue connecting muscle to bone, as shown in Figure 1.6a, while ligaments are structures that connect bone to bone, as shown in Figure 1.6b, but their histological properties are similar. Tendon transmits the mechanical forces of muscle contraction to the skeletal system, allowing mobility in and of the body, and maintains joint stability (*Jozsa et al.* [1991]), whereas ligaments limit the mobility of articulations and prevent certain movements.

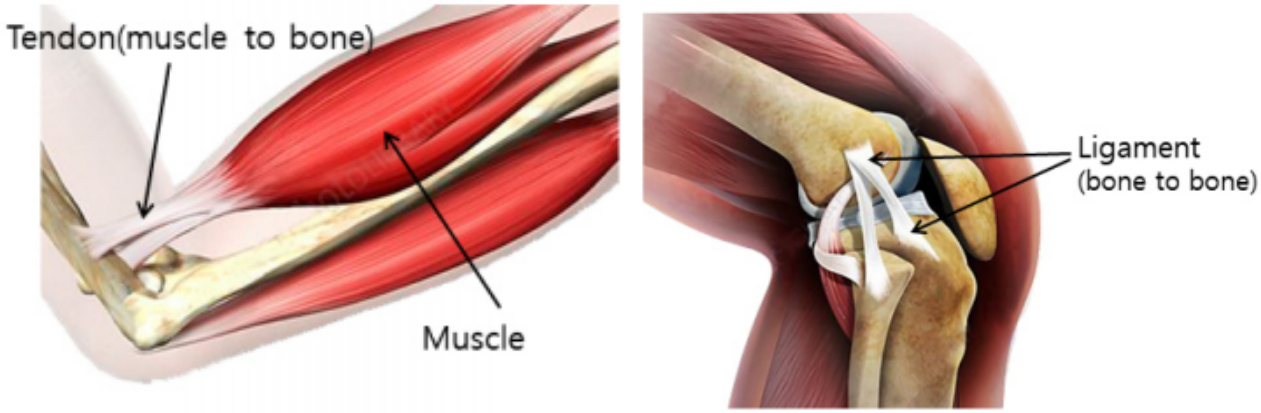

(a) (b)

Figure 1.6: Anatomy and function of (a) tendons and (b) ligaments. Image reproduced from *Im and Kim* [2020].

The human tendons and ligaments normally consist of both collagen and elastin embedded in a proteoglycan–water matrix with fibroblasts and fibrocytes between the collagen fibres *Kannus* [2000]. Ligament has a similar hierarchical structure to tendon, but with different fibre volume fractions and proteoglycan matrix percentages.

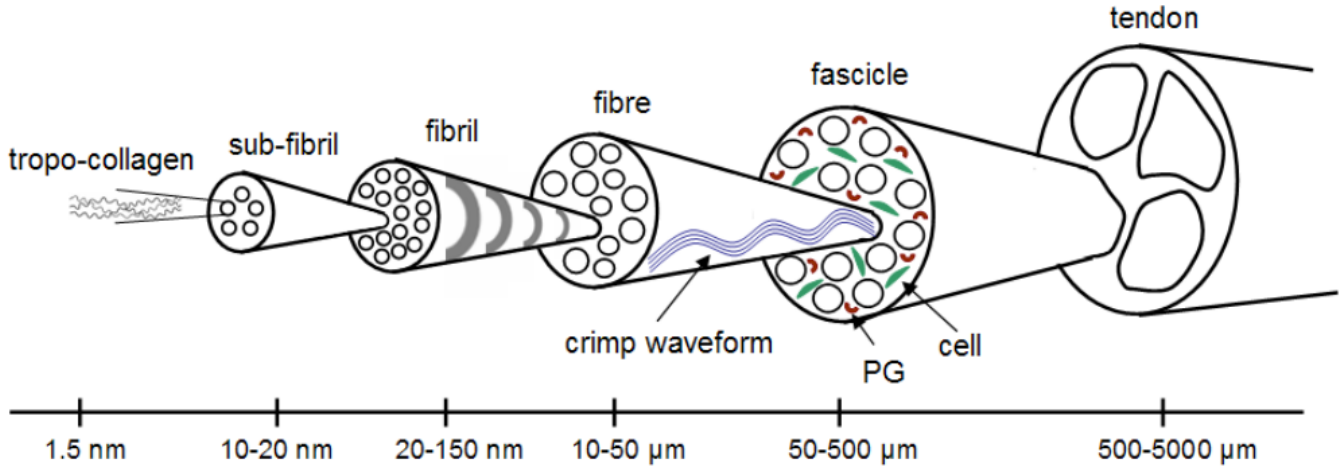

Figure 1.7: Schematic diagram of the organization of the structure of tendon, from the collagen fibrils to the entire tendon. The crimp waveform is shown at the fibril and fibre level. Image reproduced from *Schlecht* [2012].

Tendon and ligament are hierarchically organized in several distinct levels, as shown for tendon in Figure 1.7. The first unit of the mature tendon is formed from collagen I molecules, which organized as triple-helix polypeptide chains (*Asahara et al.* [2017]). The stacking of microfibrils leads to the assembly of fibrils, which are arrayed in a parallel mode to form collagen fibres. The collagen fibres are then packed into larger units called fascicles, and these bundles are wrapped to form the complete tendon. Moreover, the collagen fibres and fibrils of tendons and ligaments both show a wavy configuration. This corrugation feature of collagen fibres and fibrils is widely reported in the literature, in which both 2D crimp (*Yahia and Drouin* [1989]; *Diamant et al.* [1972]; *Liao and Vesely* [2003]; *Kastelic et al.* [1978]), as shown in Figure 1.8a, and helix-like structure (*Verzár* [1964]; *Evans and Barbenel* [1975]; *Liao* [2003]; *de Campos Vidal and Mello* [2009]) are observed, as shown in Figure 1.8b.

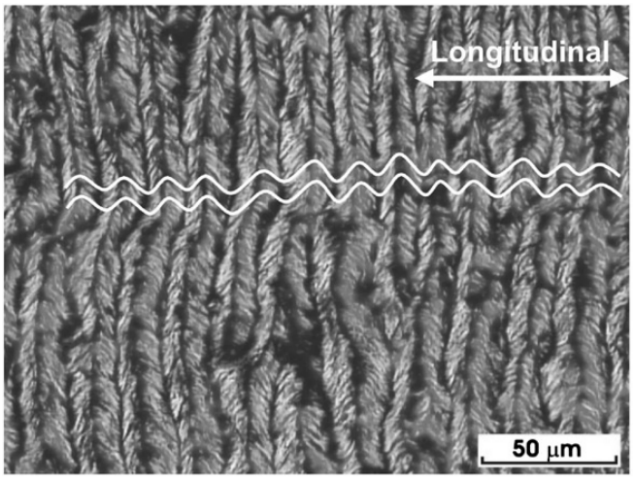

(a)

(b)

Figure 1.8: (a) Polarized light image of mitral valve chordae tendineae (tendons of the heart). Image reproduced from *Liao and Vesely* [2003]. (b) Scanning electron micrograph of human tendon. Image reproduced from *Evans and Barbenel* [1975].

1.2 Poisson's ratio of fibrous soft tissues and its predictions by mechanical models

In the sciences of materials and solid mechanics, the Poisson's ratio is used to describe the relation between the deformation of a material in one direction and its deformation in a perpendicular direction, and is the ratio of the relative contraction strain (normal to an applied load) to the relative extension strain (the direction of the applied load). The Poisson's ratio term ν_{ij} characterizes the strain in the j direction produced by the loading in the i direction *Boresi et al.* [1985], and can be expressed as:

$$\nu_{ij} = -\frac{\varepsilon_j}{\varepsilon_i} \tag{1.1}$$

where ε_i and ε_j are the strains along mutually perpendicular axes i and j, respectively. The positive strain indicates extension and the negative strain indicates contraction.

Figure 1.9 shows the behavior of a conventional material under tension and compression loading. Generally, when a material is expanded (respectively, compressed) along the direction i, it contracts (respectively, expands) in the perpendicular direction j.

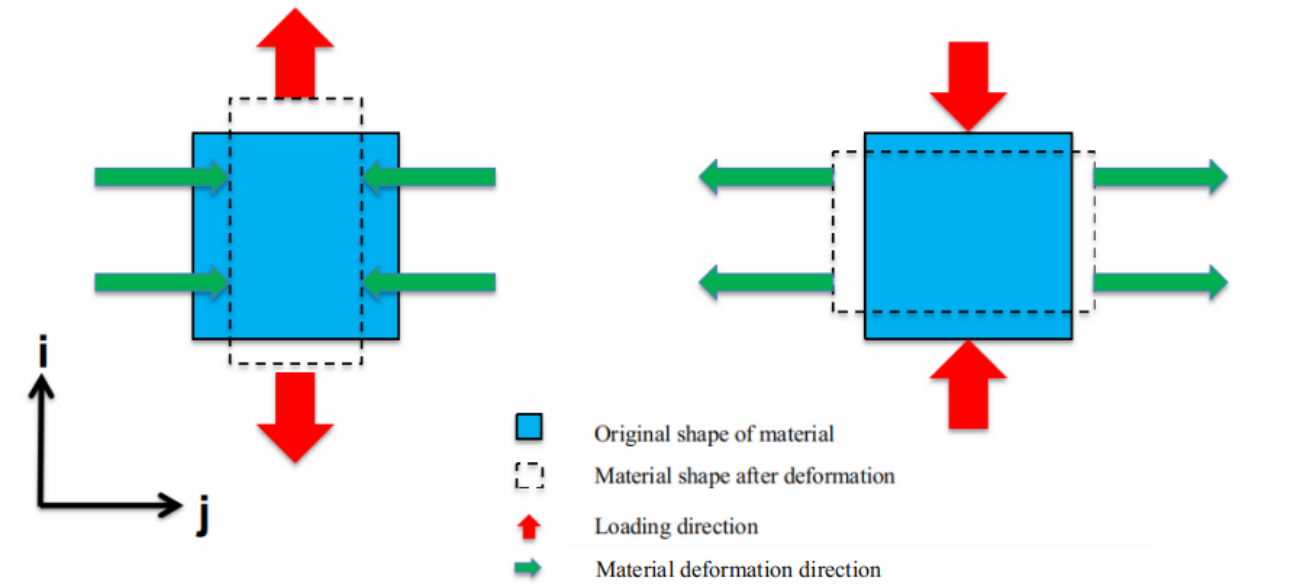

Figure 1.9: Behavior of conventional material under tension (left) and compression (right) loading

For a linear isotropic material in a three-dimensional (3D) coordinate system (x, y, z), the Poisson's ratios ν_{ij} $(i, j = x, y, z)$ are the same in all directions. Most isotropic materials have Poisson's ratio values ranging from 0 to 0.5; for example, most steels and rigid polymers exhibit Poisson's ratio values of about 0.3, and rubber has a Poisson ratio of nearly 0.5.

For an orthotropic material with three mutually perpendicular planes of symmetry, the Poisson's ratios ν_{ij} $(i, j = x, y, z)$ are specific for each direction. Therefore, when characterizing the strain in the j $(j = x, y, z)$ direction produced by the loading in the i (x, y, z) direction, six Poisson 's ratios can be defined: ν_{xy}, ν_{yx}, ν_{xz}, ν_{zx}, ν_{yz}, and ν_{zy} . However, with the symmetry of the stress–strain relations, the Poisson's ratios follow the relationships (*Boresi et al.* [1985]):

$$\frac{\nu_{xy}}{E_x} = \frac{\nu_{yx}}{E_y} \qquad \frac{\nu_{xz}}{E_x} = \frac{\nu_{zx}}{E_z} \qquad \frac{\nu_{yz}}{E_y} = \frac{\nu_{zy}}{E_z} \tag{1.2}$$

where E_x, E_y, and E_z denote the orthotropic elastic moduli in the coordinate system (x, y, z).

Some materials or structures exhibit negative Poisson's ratios, and are therefore described as having an auxetic property, showing unusual and counterintuitive mechanical behavior. As shown in Figure 1.10, when stretched (respectively, compressed), an auxetic material becomes thicker (respectively, thinner) in the direction perpendicular to that of the load.

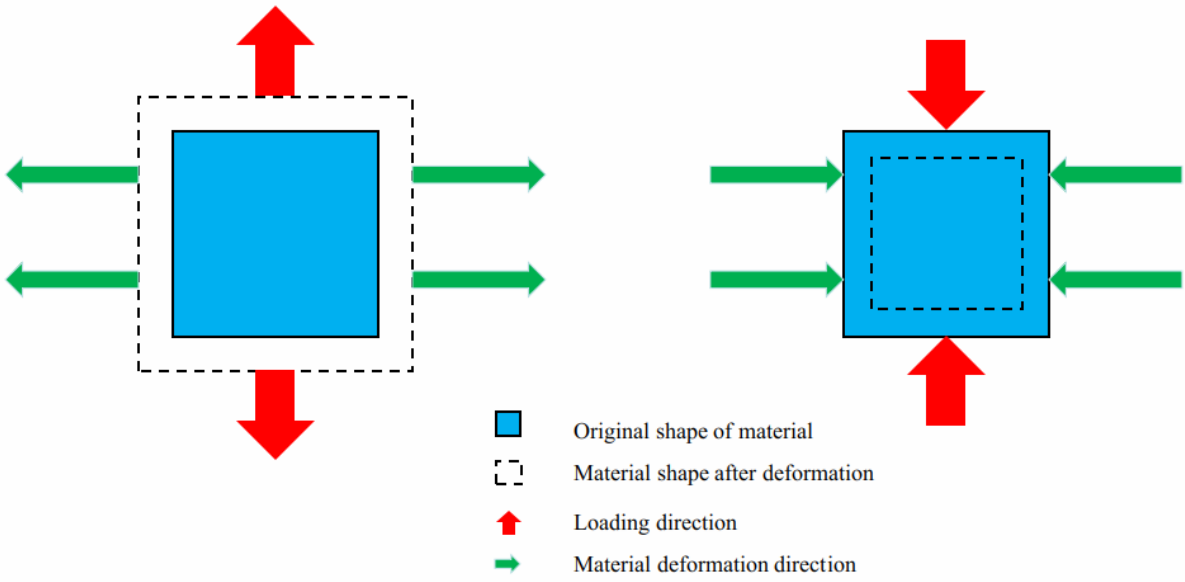

Figure 1.10: Behavior of auxetic material under tension (left) and when compressed (right).

1.2.1 Artery tissue

Artery tissue is usually considered an orthotropic material. The Poisson's ratio of the arterial wall has motivated studies of its internal microstructure, and more specifically of the collagen fibre structure and arrangement. Several studies have reported measurements of the Poisson's ratio of arteries, with the first such study performed in 1969 (*Patel et al.* [1969]). The published experimental results are summarized in Table 1.1 in the framework of a unifying coordinate system; the cylindrical coordinate system setting used to define the Poisson's ratios of this tissue is shown in Figure 1.11. In most studies, arteries are stretched in an in vitro environment, except for those of *Patel et al.* [1969] and *Hasegawa et al.* [1997], who evaluated the Poisson's ratio of dog and human arteries, respectively, in vivo. However, the Poisson's ratios of arteries reported so far are inconsistent (see Table 1.1), and both positive ($\nu > 1.0$) and negative ($\nu < 0.0$) values have been measured (*Liu et al.* [2011]), while arteries have been widely observed to be orthotropic along the longitudinal, circumferential, and radial directions. The causes for this large difference in experimental results could be due to many factors, such as the different types of artery tissue studied (*Hasegawa et al.* [1997]) or the different layers (media or intact vessel) studied, or differences in extension conditions, strain measurement techniques, test specimen conditions (fresh, or frozen and thawed), and so on. As the arterial tissue can be divided into three main parts (intima, media, and adventitia), rather than studying the intact arterial wall, more recently the media and adventitia layers were isolated and studied separately (*Timmins et al.* [2010]; *Liu et al.*

[2011]; *Skacel and Bursa* [2016]; *Santamaría et al.* [2020]; *Skacel and Bursa* [2022]). Comparing the experimental extension conditions in the literature, the strain velocity, loading pressure, and the maximum stretch strain might also affect the measured values (*Patel et al.* [1969]; *Nahon et al.* [1986]; *Cox* [1975]; *Karimi et al.* [2016]; *Santamaría et al.* [2020]). Both *Santamaría et al.* [2020] and *Skacel and Bursa* [2022] noted that frozen and thawed artery specimens show different experimental results compared to when using fresh tissue. Indeed, *Santamaría et al.* [2020] note that frozen and thawed tissues may have nonphysiological hydraulic permeability properties, and that freezing and thawing may cause the destruction of cell membranes. Moreover, several individual negative out-of-plane Poisson's ratios ($\nu_{\theta r}$, ν_{zr}) were measured with frozen and thawed test specimens among the 12 specimens used in experiments (*Skacel and Bursa* [2016]; *Skacel and Bursa* [2022]), but no negative Poisson's ratio was found in tests with fresh specimens (*Skacel and Bursa* [2022]).

Recently, the auxetic behavior of soft tissue has received increased attention (*Piao et al.* [2021]). Negative Poisson's ratios were measured by *Timmins et al.* [2010], *Lillie et al.* [2010], *Skacel and Bursa* [2016], and *Santamaría et al.* [2020] in arterial tissues, and *Skacel and Bursa* [2022] reject their previous experimental observations. *Timmins et al.* [2010] proposed that the auxetic response could be due to the variable and inhomogeneous alignment of elastin and collagen fibres in the arterial wall. Such lateral expansion was predicted by a nonlinear hyperelastic anisotropic model of arterial wall with two families of perfectly aligned collagen fibres (*Holzapfel et al.* [2000], known as the HGO model), as presented by *Gasser et al.* [2006], who further proposed a GOH model with dispersed fibre orientations. *Skacel and Bursa* [2016] reported a negative Poisson's ratio exhibited by a GOH model and provided a comprehensive analysis of the auxetic response with distributed fibre orientations. *Nolan et al.* [2014] also identified auxetic behavior with a compressible form of the HGO model, called HGO-C , analyzing the predicted lateral stresses induced during uniaxial stretching, and proposed a modified anisotropic model (MA model) to avoid them. Similarly, *Latorre et al.* [2016] noticed an unrealistic transversal deformation response predicted by the HGO and GOH models, and proposed their What-You-Prescribe-Is-What-You-Get (WYPIWYG) model as a solution. *Volokh* [2017] applied the HGO model to study auxetic behavior based on the angular integration (AI) approach. *Fereidoonnezhad et al.* [2020] consider that auxetic behavior is primarily influenced by the ratio of fibre-to-matrix stiffness and is accentuated by strain-stiffening fibres in a constant stiffness matrix. These authors propose a bilinear strain-stiffening fibre and matrix model (BLFM), which allows close control of the fibre–matrix stiffness ratio to eliminate auxetic behavior.

Author	Type of artery tissue	Test environment	Poisson's ratio range
Patel et al. [1969]	Dog thoracic aorta	In vivo	Average range of 3 groups test with different extension conditions $\nu_{r\theta} : 0.71 - 0.80$, $\nu_{\theta r} : 0.52 - 0.59$, $\nu_{\theta z} : 0.26 - 0.29$ $\nu_{z\theta} : 0.20 - 0.29$, $\nu_{rz} : 0.71 - 0.74$, $\nu_{zr} : 0.41 - 0.48$
Cox [1975]	Canine carotid artery	In vitro	Parameters vary with different load conditions $\nu_{r\theta} : 0.518 - 762$, $\nu_{\theta r} : 0.417 - 0.565$, $\nu_{\theta z} : 0.290 - 0.325$
Weizsäcker et al. [1983]	Rat carotid artery	In vitro	Parameters ranging nearly from 0 to 1 Physiological values: $\nu_{\theta z} \approx 0.35$, $\nu_{z\theta} \approx 0.45$, $\nu_{\theta r} \approx 0.45$
Nahon et al. [1986]	Canine lilac artery	In vitro	Parameters vary with different pressure loading $\nu_{\theta z} : 0.49 - 0.57$, $\nu_{z\theta} : 0.54 - 0.63$
Hasegawa et al. [1997]	Human carotid artery Human abdominal aorta	In vivo	Average $\nu_{\theta r} \approx 0.12$ (Human carotid artery) Average $\nu_{\theta r} \approx 0.46$ (Human abdominal aorta)
Zhang et al. [2002]	Bovine aorta	In vitro	$\nu_{z\theta} = 0.17 \pm 0.02$
Lillie et al. [2010]	Porcine thoracic aorta	In vitro	$\nu_{\theta z} \approx 0.2$, $\nu_{z\theta} : 0.2 - 0.4$
Timmins et al. [2010]	Bovine common carotid artery (media)	In vitro	10 % strain in the circumferential direction led to a tendency towards thickening to the radial direction (Auxetic behavior)
Liu et al. [2011]	Porcine left anterior descending artery	In vitro	Intact vessel $\nu_{\theta z} : (-0.26) - (-0.13)$, $\nu_{\theta r} : 1.13 - 1.26$, $\nu_{zr} : 1.26 - 1.68$ Media $\nu_{\theta z} : (-0.20) - (-0.06)$, $\nu_{\theta r} : 1.06 - 1.20$, $\nu_{zr} : 1.05 - 1.25$
Karimi et al. [2016]	Human coronary artery	In vitro	Strain rate: 5 mm/min $\nu_{z\theta} \approx 0.49098$ (Healthy arterial walls) $\nu_{z\theta} \approx 0.49330$ (atherosclerotic arterial walls) Strain rate: 20 mm/min $\nu_{z\theta} \approx 0.49156$ (Healthy arterial walls) $\nu_{z\theta} \approx 0.49702$ (atherosclerotic arterial walls)
Skacel and Bursa [2016]	Porcine aortic wall (media)	In vitro	In-plane value ($\nu_{\theta z}$, $\nu_{z\theta}$): 0.2 - 0.5 Out-of-plane value ($\nu_{\theta r}$, ν_{zr}): Mostly positive mean values not exceeding 0.5 with individual negative value
Santamaría et al. [2020]	Porcine thoracic aorta	In vitro	With tensile strain along circumferential direction about 13 % Strain along the radial direction for intima: 4.58 % Strain along the radial direction for adventitia: 3.80 % Swelling effect (auxetic behavior) on the radial direction for media
Skacel and Bursa [2022]	Porcine arterial wall (media)	In vitro	For the fresh specimens In-plane value ($\nu_{\theta z}$, $\nu_{z\theta}$): 0.3 - 0.4 Out-of-plane value ($\nu_{\theta r}$, ν_{zr}): 0.5 - 0.7 No negative Poisson's ratio observed with fresh test specimens Individual negative ν_{zr} measured with frozen & thawed test specimens

Table 1.1: Experimental results of Poisson's ratio reported in the literature on arteries.

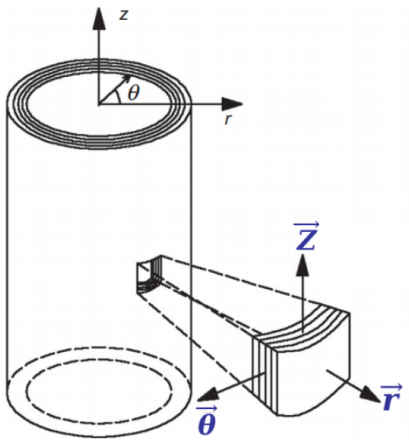

Figure 1.11: Segment of the artery showing the cylindrical coordinate system $(\vec{\theta}, \vec{z}, \vec{r})$ used to study its mechanics. Image reproduced from *Bai and Bai* [2014].

Furthermore, the subject of Poisson's ratio of arterial wall study is closely related to its compressibility feature. In mechanical modeling, the tissue of the artery wall is commonly considered as incompressible; although this assumption is still under investigation because of inconsistencies in experimental results (*Carew et al.* [1968]; *Chuong and Fung* [1984]; *Volokh* [2006]; *Di Puccio et al.* [2012]; *Yosibash et al.* [2014]).

1.2.2 Annulus fibrosus tissue

The annulus fibrosus (AF) tissue consists of several lamellae, with the collagen fibres arranged in parallel within each one. The parallel fibres have been observed to have a crimped microstructure (*Pezowicz et al.* [2005]). Similarly to the arteries, the tissue of AF also exhibits an orthotropic behavior.

Most of the tensile experiments reported in the literature for AF are uniaxial tests (*Elliott and Setton* [2001]; *Guerin and Elliott* [2006]; *Guerin and Elliott* [2006]; *Lewis et al.* [2008]; *O'Connell et al.* [2009]; *Cherblanc et al.* [2011]; *Baldit et al.* [2014]; *Dusfour et al.* [2020]), although biaxial tensile tests have also been performed (*Bass et al.* [2004]; *O'Connell et al.* [2012]). The Poisson's ratio measurements obtained so far for AF are summarized in Table 1.2 within a unified coordinate system; see Figure 1.11 for the cylindrical coordinate system used to study the Poisson's ratio in AF. These latter measurements of the Poisson's ratio for AF show a large range, from -0.57 ($\nu_{\theta r}$, *Derrouiche et al.* [2019a]) to 2.32 ($\nu_{\theta z}$, *Wagner and Lotz* [2004]). The difference in experimental results could be due to many factors, such as differences in: the types of AF tissue analyzed, the subsections of AF tissue analyzed (inner or outer AF; *Elliott and Setton* [2001]), extension conditions, test specimen status (degenerated or non-degenerated AF), strain measurement techniques, specimen-storage-

Author	Type of annulus fibrosus tissue	Poisson's ratio range
Elliott and Setton [2001]	Human AF	Inner AF: $\nu_{\theta z} = 1.86 \pm 2.06$, $\nu_{\theta r} = 0.88 \pm 0.71$, $\nu_{z\theta} = 1.58 \pm 0.67$ Outer AF: $\nu_{\theta z} = 1.77 \pm 0.65$, $\nu_{\theta r} = 0.33 \pm 0.68$, $\nu_{z\theta} = 0.66 \pm 0.22$ $\nu_{zr} = 0.14 \pm 0.10$, $\nu_{r\theta} = 0.51 \pm 0.20$
Wagner and Lotz [2004]	Human AF	In tension: $\nu_{\theta r} = 0.40 \pm 0.15$, $\nu_{\theta z} = 2.32 \pm 0.87$ In compression: $\nu_{\theta r} = 0.73 \pm 0.21$, $\nu_{\theta z} = 0.87 \pm 0.49$
Guerin and Elliott [2006]	Outer human AF	Non-degenerated: $\nu_{\theta z} = 4.64 \pm 4.12$ Degenerated: $\nu_{\theta z} = 2.08 \pm 0.88$
Lewis et al. [2008]	Outer rabbit AF	Ratio of transverse to axial indentation a semblance of the Poisson's ratios $\nu_{z\theta}$: 0.33 - 0.47
O'Connell et al. [2009]	Human AF	Nondegenerate AF: $\nu_{r\theta} = 0.79 \pm 0.42$, $\nu_{z\theta} = 0.61 \pm 0.35$, $\nu_{\theta z} = 2.27 \pm 0.87$ Degenerate AF: $\nu_{r\theta} = 0.46 \pm 0.31$, $\nu_{z\theta} = 0.61 \pm 0.28$, $\nu_{\theta z} = 1.88 \pm 1.01$
Cherblanc et al. [2011]	Pig AF	$\nu_{\theta z} = 0.9 \pm 0.25$
Baldit et al. [2014]	Pig AF	$\nu_{\theta z} : 0.8 - 1.1$ $\nu_{\theta r}$ not given but wide range are observed even negative $\nu_{\theta r}$ (auxetic behavior)
Derrouiche et al. [2019a]	Bovine AF	Details see Table 1.3
Dusfour et al. [2020]	pig AF	Poisson's ratio not given, with dilatation along the circumferential direction auxetic behaviors observed in both axial and radial directions

Table 1.2: Experimental results of Poisson's ratio reported in the literature on annulus fibrosus tissue.

solution osmolarity, and so on. Both *Guerin and Elliott* [2006] and *O'Connell et al.* [2009] found that AF degeneration influences Poisson's ratio measurement results. Moreover, *Wagner and Lotz* [2004] showed that the loading type, that is, tension or compression, has an effect on Poisson's ratio results. Furthermore, *Derrouiche et al.* [2019a] presented results showing that the different saline concentrations and strain rates used in extension tests also affect such measurements (see details in Table 1.3). As the strain rate decreases, both $\nu_{\theta z}$ and $\nu_{\theta r}$ decrease, and as specimen storage NaCl concentration increases, both $\nu_{\theta z}$ and $\nu_{\theta r}$ increase.

NaCl concentration (g/L)	strain rate (s^{-1})	Poisson's ratio $\nu_{\theta z}$	Poisson's ratio $\nu_{\theta r}$
0	$2 * 10^{-3}$	0.887 ± 0.19	-0.468 ± 0.1
	$2 * 10^{-4}$	0.74 ± 0.16	-0.574 ± 0.12
9	$2 * 10^{-3}$	0.92 ± 0.2	$-0.2 \pm 0.0.04$
	$2 * 10^{-4}$	0.74 ± 0.16	-0.387 ± 0.08
18	$2 * 10^{-3}$	0.963 ± 0.21	-0.146 ± 0.03
	$2 * 10^{-4}$	0.811 ± 0.17	-0.29 ± 0.06

Table 1.3: Experimental Poisson's ratio for different saline concentrations and strain rates. Table reproduced from *Derrouiche et al.* [2019a].

Although the range of reported Poisson's ratio results is considerable, the orthotropic features of AF along the longitudinal, circumferential, and radial directions are consistently observed. Comparing all the experimental results in the literature, values of $\nu_{\theta r}$ are usually much lower than those of $\nu_{\theta z}$ (*Elliott and Setton* [2001]; *Wagner and Lotz* [2004]; *Baldit et al.* [2014]; *Derrouiche et al.* [2019a]), and even negative $\nu_{\theta r}$ values (auxetic behavior) were recently reported by *Baldit et al.* [2014], *Derrouiche et al.* [2019a], and *Dusfour et al.* [2020]. In other words, with extension along the circumferential direction, AF is rarely seen to shrink in the radial direction but is observed to expand in some cases. Interpretations of such observations were proposed by *Derrouiche et al.* [2019b] and *Derrouiche et al.* [2020], who invoke mechanical-based and chemical-based fluid flow interactions until chemo-mechanical equilibrium. We note that *Derrouiche et al.* [2019a] reported an auxetic behavior in the plane of the lamellae only, but *Dusfour et al.* [2020] found such a behavior in both the radial and longitudinal directions.

In order to predict AF Poisson's ratios using mechanical modeling, *Elliott and Setton* [2001] implemented a linear anisotropic material model of the AF to determine a complete set of model properties and to predict the behaviors of AF tissue under idealized kinematic states. According to the model predictions presented by these latter authors, interactions between fibre populations in the multilamella AF contribute significantly to the mechanical behavior of the material, suggesting that a model for AF made up of physically isolated

concentric lamellae may not be appropriate. *Derrouiche et al.* [2019a] presented a chemo-mechanical approach to studying the intrinsic osmo-inelastic response of the annulus fibrosus in relation to the microstructure of the layered, reinforced soft tissue, the biochemical environment, and the mechanical loading conditions, which successfully captures the variations in osmolarity, strain rate, and auxeticity. *Kandil et al.* [2019] proposed a chemo-viscoelastic model as part of a microstructure-based approach in order to predict the regional dependency of the annulus response, in which the auxetic behavior is identified in the plane of the lamellae. Comparing their measurements with predictions of the HGO model (*Holzapfel et al.* [2000]), *Dusfour et al.* [2020] found an auxetic response, but poor agreement between model and experimental results. Furthermorethe AF is widely modeled by applying a fibre-induced anisotropic hyperelastic material (*Wu and Yao* [1976]; *Eberlein et al.* [2001]; *Peng et al.* [2006]; *O'Connell et al.* [2009]). These models describe the fibres and the matrix using the principle invariants of the Green deformation tensor and structural tensors representing the collagen fibre populations (*O'Connell et al.* [2012]).

1.2.3 Tendon

Several studies have investigated the Poisson's ratio of tendons experimentally. Most of these studies were conducted in vitro (*Lynch et al.* [2002]; *Lynch et al.* [2003]; *Cheng and Screen* [2007]; *Vergari et al.* [2011]; *Chernak and Thelen* [2012]; *Thorpe et al.* [2013]; *Thorpe et al.* [2014]; *Vella Wood et al.* [2019]), but several measurements of tendon deformation have been made in vivo (*Maganaris et al.* [2001]; *Iwanuma et al.* [2011]; *Obst et al.* [2014]), and *Gatt et al.* [2015] estimated human Achilles tendon deformations by performing both in vitro and in vivo tests. Some values from Poisson's ratio measurements for tendon are summarized in Table 1.4 in the framework of a unified coordinate system, and the coordinate system used to study Poisson's ratios of the Achilles tendon is shown in Figure 1.12. The reported Poisson's ratios for tendon show a similarly large spread to the ratios for artery and AF. The difference in experimental results could again be due to many factors, such as differences in the: types of tendon tissue analyzed (*Thorpe et al.* [2013]; *Gatt et al.* [2015]), loading conditions (*Thorpe et al.* [2014]), strain measurement techniques, and so on.

Although the published Poisson's ratios cover a significant range, the orthotropic feature of tendon is demonstrated by *Lynch et al.* [2002] and *Lynch et al.* [2003], and the fibre-aligned Poisson's ratio is found to be larger than the transverse Poisson's ratio from their tests on rabbit patellar tendon and sheep flexor tendon, respectively. Comparing all the reported Poisson's ratio measurements in the literature, both large positive ($\nu_{yx} > 2$, *Lynch et al.* [2003]) and negative values are observed, even descending to -9.86 (*Gatt et al.* [2015]). The negative Poisson's ratio is unexpected for tendon, but such auxetic behavior was recently

Author	Type of tendon or ligament	Poisson's ratio range
Lynch et al. [2002]	Rabbit patellar tendon	$\nu_{xy} = 0.11 \pm 0.106$, $\nu_{yx} = 0.80 \pm 0.179$
Lynch et al. [2003]	Sheep flexor tendon	$\nu_{yx} = 2.98 \pm 2.59$ $\nu_{xy} = 0.488 \pm 0.653$
Cheng and Screen [2007]	Rat tail tendon	$\nu_{yx} \approx 0.8$, with some data exceeding 1
Vergari et al. [2011]	Horse equine superficial digital flexor tendon	$nu_{yx} = 0.55 \pm 0.12$
Iwanuma et al. [2011]	Human Achilles tendon	Extramuscular free tendinous component $\nu_{yx} \approx 0.6$
Chernak and Thelen [2012]	Porcine flexor tendon	ν_{yx}: 0.82 – 1.64
Thorpe et al. [2013]	Horse equine superficial digital flexor (SDFT) Horse common digital extensor (CDET)	SDFT: $\nu_{yx} \approx 1.36$ CDET: 2< $\nu_{yx} < 4.0$ (from results figure)
Reese and Weiss [2013]	Rat tail tendon	ν_{yx}: 2.0 - 2.4
Thorpe et al. [2014]	Horse superficial digital flexor tendon	Control sample: $\nu_{yx} = 0.91 \pm 0.45$ (4% strain), $\nu_{yx} = 1.58 \pm 0.32$(8% strain) Fatigue loaded sample: $\nu_{yx} = -0.08 \pm 0.38$ (4%), $\nu_{yx} = -0.1 \pm 0.41$ (8%) After preconditioned sample: $\nu_{yx} = 0.46 \pm 0.53$ (4%), $\nu_{yx} = 0.10 \pm 0.24$ (8%)
Gatt et al. [2015]	Human achilles tendon Human peroneus brevis Sheep deep flexor tendon Pig deep flexor tendon	ν_{yx}: (-1.44) - (-0.39) ν_{yx}: (-3.81) - (-0.166) ν_{yx}: (-9.86) - (-0.37), ν_{yz}: 1.217 - 3.035 ν_{yx}: (-3.11) - (-0.34)
Vella Wood et al. [2019]	Pig flexor tendon	Not given directly, negative Poisson's ratio (auxetic behavior) are confirmed

Table 1.4: Poisson's ratio values measured for tendon and reported in the literature.

reported by *Thorpe et al.* [2014], *Gatt et al.* [2015], and *Vella Wood et al.* [2019] in several tests among all the measurements. *Gatt et al.* [2015] speculate that the crimped microstructure of the fibres of tendons is likely to play a role in the generation of their anomalous, auxetic behavior.

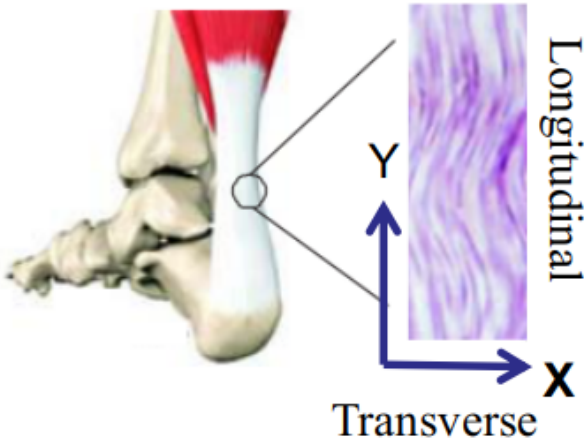

Figure 1.12: Segment of tendon showing the X-Y coordinate system used in studies of the Poisson's ratio. Image reproduced from *Marino and Vairo* [2013].

In an attempt to predict the Poisson's ratios of tendon, *Yin and Elliott* [2004] used a transversely isotropic biphasic mixture model and simultaneously studied the viscoelastic mechanical behavior of tendon under uniaxial tensile loading. *Reese et al.* [2010] constructed a micromechanical finite element model to represent crimped fibres with a super-helical organization. The model was composed of fibrils embedded within a matrix material, and a homogenization procedure was performed to determine both the effective Poisson's ratio and the Poisson function. *Xiao et al.* [2020] studied the Poisson's ratios of tendons and ligaments using an analytical microstructure model, in which the form of the collagen fibres is sinusoidal.

1.3 Mechanical models of composite with crimp fibre structure

Crimped structures commonly exist in biological materials, from nanoscale to macroscale. For example, at the nanoscale, deoxyribonucleic acid (DNA) has a double helix structure; at the microscale, collagen fibrils are in the form of triple helix polypeptide chains; and at the macroscale, ventricular myocardial bands and the human umbilical cord have a helical structure *Carpi et al.* [2010]. In addition, the helical structure on the fibre scale is observed both in connective tissues and wood (*Freed and Doehring* [2005]; *Zorzetto and Ruffoni* [2019]).

The reason for the preference for helical structures in biological materials is not yet clear, although *Snir and Kamien* [2005] found that the helix structure allows the entropy of an object to be maximized. Moreover, *Moulton et al.* [2020] presented various examples of curvature and torsion generation and demonstrated the impact of residual stress on the generation of curvature.

As presented in the previous sections, collagen fibre corrugation, or crimping, is widely reported in fibrous soft tissues such as artery, annulus fibrosus, tendon, and ligament. In mechanical models proposed so far in the literature, fibrous soft tissues are usually considered as composite materials reinforced by fibres. In the present work, we focus in particular on the crimped fibre structure. Below, we summarize the composite models that have been presented so far in the literature – with specific attention to reinforced composites and those including crimped structures–, and their applications.

In 1973, *Mori and Tanaka* [1973] first proposed a method to calculate the average internal stress in the matrix of a material containing inclusions with transformation strain, which is widely used to estimate the constitutive relationships of composites. *Hashin* [1983] reviewed the analytical solutions regarding the effective modulus of composites reinforced with straight fibres. *Hsiao and Daniel* [1996] proposed an analytical model for determining elastic properties and compressive strength as a function of fibre waviness. *Garnich and Karami* [2004] studied the stiffness and strength of composites reinforced with wavy fibres using a finite element micromechanics approach. *Karami and Garnich* [2005a] and *Karami and Garnich* [2005b] studied effective moduli and the thermoelastic behavior of composites reinforced with fibres with periodic waviness using a finite element micromechanical model. *Kashtalyan* [2005] presented an analytical approach to determining the stresses in laminated composites with ply waviness subjected to compressive or flexural loading. *Drago and Pindera* [2007] calculated the macroscopic effective moduli of the statistically homogeneous and periodically heterogeneous materials in unidirectional composites with large fibre/matrix property. *Gattu et al.* [2008] proposed a finite-volume direct averaging micromechanics (FVDAM) theory for periodically heterogeneous materials, and *Khatam and Pindera* [2009] applied this theory to investigate the effective moduli and thermal expansion coefficients of lamellar composites with wavy architectures. *Abdin et al.* [2016] described a method for extending mean-field theory to discontinuous composites reinforced with wavy fibres. *Xiao et al.* [2020] presented an analytical solution for describing the effects of embedded microstructures on the macroscopic elastic properties of tendons and ligaments, which are considered as planar composites reinforced with crimped fibres. *Reese et al.* [2010] used homogenization methods and finite element micromechanical models to study a helical fibril organization and to find the large Poisson's ratios in biological tissues. *Khani et al.* [2016] studied the mechanical elastic properties of composites reinforced by helical fibres,

and finally, *Karami et al.* [2009] and *Kuksenko et al.* [2018] studied the large deformation homogenized mechanical response of composites reinforced by wavy fibres.

1.4 Conclusion and discussion

In this chapter, we present a summary of the literature on Poisson's ratios for artery, annulus fibrosus, and tendon tissues, emphasizing that both large positive and negative Poisson's ratios have been found experimentally. The negative Poisson's ratio, also known as the auxetic behavior, appears counterintuitive, and has also been reported for skin tissue (*Veronda and Westmann* [1970]; *Lees et al.* [1991]), tibia bone (*Williams and Lewis* [1982]), axoloti embryonic epithelia (*Wiebe and Brodland* [2005]), and for the bovine cornea (*Patten and Wess* [2013]). *Lees et al.* [1991] proposed that the highly corrugated microstructure of the material in skin tissue might be the cause of the auxetic behavior of this latter. *Gatt et al.* [2015] speculated that the crimped fibre structure might be the cause of the auxetic behavior in tendons. *Timmins et al.* [2010] described that the variable and inhomogeneous alignment of elastin and collagen fibres in arterial wall might be causing the observed auxeticity in that tissue.

Although it has been suggested that the crimped fibre structure may be the key driver of the negative Possion's ratios observed in soft tissues, there is currently little evidence of the link between the two. On the contrary, *Reese et al.* [2010] show that helical fibres may contribute to larger Poisson's ratios. The chemo-mechanical approach proposed by *Derrouiche et al.* [2019a] can be used to estimate the auxetic behavior linked to local changes in osmolarity in annulus fibrosus tissue. The negative Poisson's ratio of arterial walls is also predicted by the HGO and HGO-like models (*Holzapfel et al.* [2000]), and was found by these authors to be linked to the levels of fibre–matrix material stiffness and fibre dispersion. However, as the auxetic behavior is not always found in arterial tissue, *Nolan et al.* [2014], *Latorre et al.* [2016], *Volokh* [2017], and *Fereidoonnezhad et al.* [2020] proposed their HGO-based model to avoid the auxetic response.

So far, there have been relatively few studies on the nature of auxetic behavior in soft tissue. Nevertheless, synthetic structures known to show an auxetic behavior are increasingly being applied in tissue engineering scaffolds (*Jin et al.* [2021]; *Mardling et al.* [2020]; *Kim et al.* [2021]; *Jiang et al.* [2023]). The purpose of this thesis is to study changes in the Poisson's ratio of fibrous soft tissue as a function of the microstructure of this latter, and specifically of the level of corrugation of the crimped fibres. This work is designed to help us to better understand the role of microstructure in soft tissues and to serve as a reference for further tissue engineering and scaffold development.

CHAPTER 2

Micromechanical model of lamellar structure in the annulus fibrosus tissue

2.1 Introduction

The intervertebral disc consists of the nucleus pulposus and the annulus fibrosus (AF) with an endplate at both the top and bottom end, serving as the interface between vertebra and the intervertebral discs. The nucleus pulposus is the inner gel-like part, which is surrounded by the annulus fibrosus as shown in Figure 2.1. The AF consists of several lamellae, where the collagen fibres are arranged in parallel in each lamella and the fibre orientation differs from one lamella to its neighbors. The outer AF is made up of Type I collagen and Type II collagen dominates the inner AF ([*Bhattacharya and Dubey*, 2021]). The parallel fibres in each lamella have been found to have a crimped microstructure (*Pezowicz et al.* [2005]), as shown in Figure 2.1.

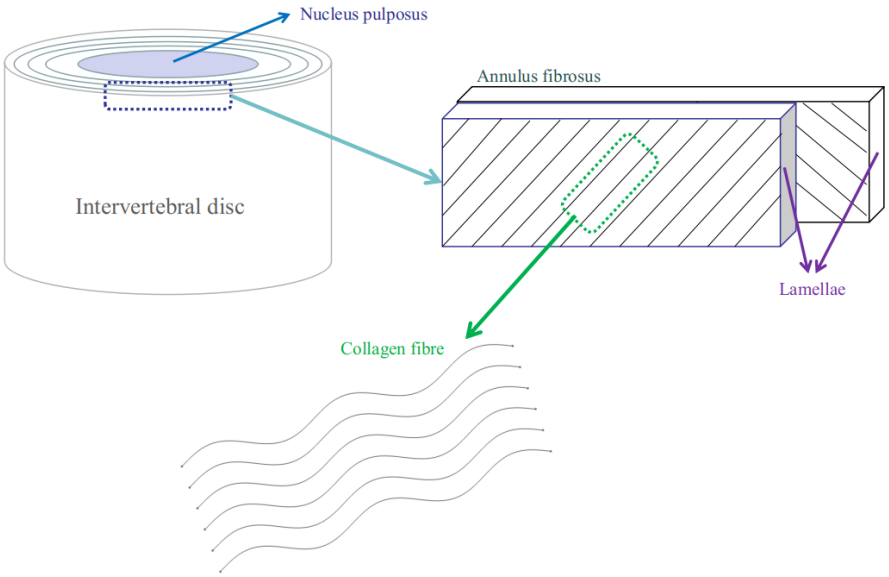

Figure 2.1: Scheme of intervertebral disc components and microstructure.

Consequently, we propose to model the lamellar structure in AF tissue as a fibre-reinforced composite whose fibres have a crimped microstructure as shown in Figure 2.2. In particular, we consider an analytical micromechanical model to study the effective elastic parameters of lamellar structure in AF tissue. This model takes into account the dispersion of the fibres in different layers and considers fibre waviness as a sinusoidal shape.

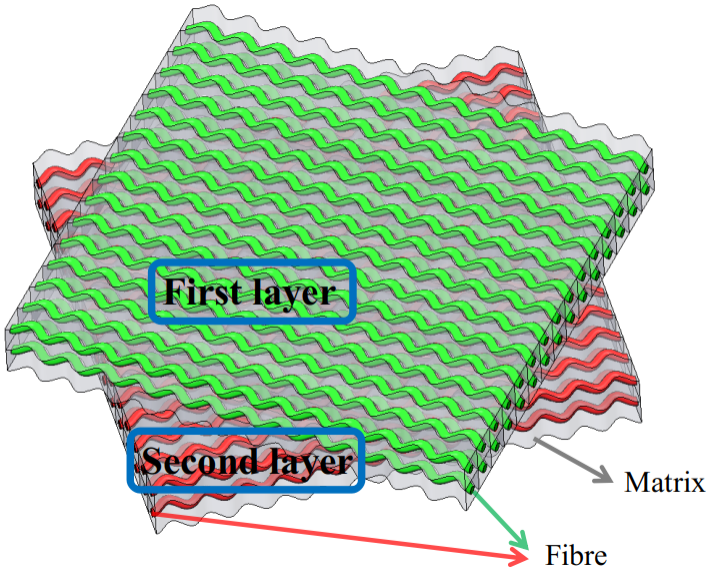

Figure 2.2: Lamellar composite structure under consideration.

2.2 Stiffness matrix transformation

In order to better understand the development of the oriented effective stiffness matrix, which is presented in more detail in sections 2.3 and 2.4, we introduce the stiffness matrix transformation method in this section. First, we outline the general transformation matrix in section 2.2.1; details can also be found in the reviews by *Daniel et al.* [2006] and *Sinha* [2006]. We then present our transformation of the stiffness matrix in section 2.2.2.

2.2.1 Transformation relation

2.2.1.1 Transformation of coordinates

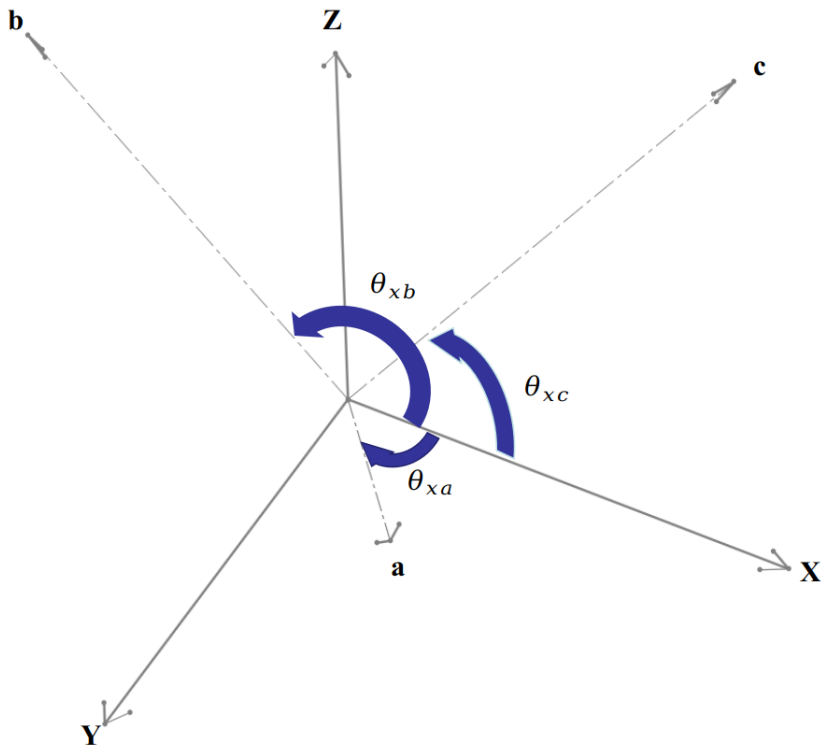

Figure 2.3: Two mutually perpendicular systems, x, y, z and a, b, c.

The rules associated with transformation of vectors are followed to find the transformation of coordinates. Let us consider two perpendicular coordinate systems x, y, z and a, b, c, as shown in Figure 2.3. A geometrical point respects the following relationship in these systems:

$$\begin{Bmatrix} a \\ b \\ c \end{Bmatrix} = \left[T_{coor}\right] \begin{Bmatrix} x \\ y \\ z \end{Bmatrix}, \tag{2.1}$$

where $\left[T_{coor}\right]$ represents the coordinate transformation matrix and is defined as:

$$\left[T_{coor}\right] = \begin{bmatrix} m_1 & n_1 & p_1 \\ m_2 & n_2 & p_2 \\ m_3 & n_3 & p_3 \end{bmatrix}, \tag{2.2}$$

where m_i, n_i ,and p_i are the direction cosines of axis i, that is,

$$\begin{aligned} m_1 &= cos\theta_{xa} \qquad n_1 = cos\theta_{ya} \qquad p_1 = cos\theta_{za} \\ m_2 &= cos\theta_{xb} \qquad n_2 = cos\theta_{yb} \qquad p_2 = cos\theta_{zb} \\ m_3 &= cos\theta_{xc} \qquad n_3 = cos\theta_{yc} \qquad p_3 = cos\theta_{zc}. \end{aligned} \tag{2.3}$$

The angles θ_{ij} are measured from axis i to axis j as shown in Figure 2.3.

2.2.1.2 Transformation of strains

We consider that u_x, u_y, and u_z are displacement components of a given geometrical domain with respect to the coordinate system x, y, z, and u_a, u_b, u_c are the displacement components corresponding to the a, b, c system. Similarly to the transformation of coordinates, we have

$$\begin{Bmatrix} u_a \\ u_b \\ u_c \end{Bmatrix} = \left[T_{coor}\right] \begin{Bmatrix} u_x \\ u_y \\ u_z \end{Bmatrix}. \tag{2.4}$$

Thus, the corresponding strain components ε_{xyz} in the x, y, z coordinates and ε_{abc} in the a, b, c system satisfy the following relations:

$$\varepsilon_a = \frac{\partial u_a}{\partial a} \qquad \varepsilon_x = \frac{\partial u_x}{\partial x}, \tag{2.5}$$

$$\frac{\partial u_a}{\partial a} = m_1 \frac{\partial u_x}{\partial a} + n_1 \frac{\partial u_y}{\partial a} + p_1 \frac{\partial u_z}{\partial a}. \tag{2.6}$$

Following the chain rule, we have

$$\frac{\partial u_x}{\partial a} = \frac{\partial u_x}{\partial x}\frac{\partial x}{\partial a} + \frac{\partial u_x}{\partial y}\frac{\partial y}{\partial a} + \frac{\partial u_x}{\partial z}\frac{\partial z}{\partial a} = m_1 \frac{\partial u_x}{\partial x} + n_1 \frac{\partial u_x}{\partial y} + p_1 \frac{\partial u_x}{\partial z}, \tag{2.7}$$

with $\frac{\partial x}{\partial a} = m_1$, $\frac{\partial y}{\partial a} = n_1$, and $\frac{\partial z}{\partial a} = p_1$.

In a similar way, we have

$$\frac{\partial u_y}{\partial a} = m_1 \frac{\partial u_y}{\partial x} + n_1 \frac{\partial u_y}{\partial y} + p_1 \frac{\partial u_y}{\partial z}, \tag{2.8}$$

$$\frac{\partial u_z}{\partial a} = m_1 \frac{\partial u_z}{\partial x} + n_1 \frac{\partial u_z}{\partial y} + p_1 \frac{\partial u_z}{\partial z}. \tag{2.9}$$

By substituting Equations 2.6, 2.7, 2.8, and 2.9 into Equation 2.5, we obtain

$$\frac{\partial u_a}{\partial a} = m_1^2 \frac{\partial u_x}{\partial x} + n_1^2 \frac{\partial u_y}{\partial y} + p_1^2 \frac{\partial u_z}{\partial z} + n_1 p_1 (\frac{\partial u_y}{\partial z} + \frac{\partial u_z}{\partial y}) + p_1 m_1 (\frac{\partial u_x}{\partial z} + \frac{\partial u_z}{\partial x}) + m_1 n_1 (\frac{\partial u_x}{\partial y} + \frac{\partial u_y}{\partial_x}) \tag{2.10}$$

or

$$\varepsilon_a = m_1^2 \varepsilon_x + n_1^2 \varepsilon_y + p_1^2 \varepsilon_z + n_1 p_1 \gamma_{yz} + p_1 m_1 \gamma_{xz} + m_1 n_1 \gamma_{xy}. \tag{2.11}$$

We set $\varepsilon_{xyz} = \{\varepsilon_x \ \varepsilon_y \ \varepsilon_z \ \gamma_{yz} \ \gamma_{xz} \ \gamma_{xy}\}^T$, which are the strain components in x, y, z coordinates and $\varepsilon_{abc} = \{\varepsilon_a \ \varepsilon_b \ \varepsilon_c \ \gamma_{bc} \ \gamma_{ac} \ \gamma_{ab}\}^T$, which are the strain components in a, b, c coordinates. Proceeding with the same calculation, we have

$$\begin{Bmatrix} \varepsilon_a \\ \varepsilon_b \\ \varepsilon_c \\ \gamma_{bc} \\ \gamma_{ac} \\ \gamma_{ab} \end{Bmatrix} = \left[T_\varepsilon\right] \begin{Bmatrix} \varepsilon_x \\ \varepsilon_y \\ \varepsilon_z \\ \gamma_{yz} \\ \gamma_{xz} \\ \gamma_{xy} \end{Bmatrix}, \tag{2.12}$$

where the strain transformation matrix $\left[T_\varepsilon\right]$ is given by

$$\left[T_\varepsilon\right] = \begin{bmatrix} m_1^2 & n_1^2 & p_1^2 & n_1p_1 & p_1m_1 & m_1n_1 \\ m_2^2 & n_2^2 & p_2^2 & n_2p_2 & n_2m_2 & m_2n_2 \\ m_3^2 & n_3^2 & p_3^2 & n_3p_3 & p_3m_3 & m_3n_3 \\ 2m_2m_3 & 2n_2n_3 & 2p_2p_3 & n_2p_3+n_3p_2 & p_2m_3+p_3m_2 & m_2n_3+m_3n_2 \\ 2m_3m_1 & 2n_3n_1 & 2p_3p_1 & n_3p_1+n_1p_3 & p_3m_1+p_1m_3 & m_3n_1+m_1n_3 \\ 2m_1m_2 & 2n_1n_2 & 2p_1p_2 & n_1p_2+n_2p_1 & p_1m_2+p_2m_1 & m_1n_2+m_2n_1 \end{bmatrix}. \tag{2.13}$$

2.2.1.3 Transformation of Stresses

We set $\sigma_{xyz} = \{\sigma_x\ \sigma_y\ \sigma_z\ \tau_{yz}\ \tau_{xz}\ \tau_{xy}\}^T$ as the stress components in x, y, and z coordinates and $\sigma_{abc} = \{\sigma_a\ \sigma_b\ \sigma_c\ \tau_{bc}\ \tau_{ac}\ \tau_{ab}\}^T$ as the stress components in a, b, and c coordinates. Let $\delta\varepsilon_{abc}$ and $\delta\varepsilon_{xyz}$ be the virtual strains in the coordinates a, b, and c and x, y, and z, respectively. The work done by stress in the two coordinate systems is the same, and therefore

$$\delta\varepsilon_{abc}^T\sigma_{abc} = \delta\varepsilon_{xyz}^T\sigma_{xyz}, \tag{2.14}$$

$$\delta\varepsilon_{abc}^T = (T_\varepsilon\delta\varepsilon_{xyz})^T = \delta\varepsilon_{xyz}^T T_\varepsilon^T. \tag{2.15}$$

Substituting Equation 2.15 into Equation 2.14, we have

$$\sigma_{abc} = T_\varepsilon^{-T}\sigma_{xyz}. \tag{2.16}$$

We note the stress transformation matrix $T_\sigma = T_\varepsilon^{-T}$, with

$$\left[T_\sigma\right] = \begin{bmatrix} m_1^2 & n_1^2 & p_1^2 & 2n_1p_1 & 2p_1m_1 & 2m_1n_1 \\ m_2^2 & n_2^2 & p_2^2 & 2n_2p_2 & 2n_2m_2 & 2m_2n_2 \\ m_3^2 & n_3^2 & p_3^2 & 2n_3p_3 & 2p_3m_3 & 2m_3n_3 \\ m_2m_3 & n_2n_3 & p_2p_3 & n_2p_3+n_3p_2 & p_2m_3+p_3m_2 & m_2n_3+m_3n_2 \\ m_3m_1 & n_3n_1 & p_3p_1 & n_3p_1+n_1p_3 & p_3m_1+p_1m_3 & m_3n_1+m_1n_3 \\ m_1m_2 & n_1n_2 & p_1p_2 & n_1p_2+n_2p_1 & p_1m_2+p_2m_1 & m_1n_2+m_2n_1 \end{bmatrix}. \tag{2.17}$$

We take T_σ as the general transformation matrix and denote it as T_{ij}, which satisfies

$$\begin{Bmatrix} \sigma_a \\ \sigma_b \\ \sigma_c \\ \tau_{bc} \\ \tau_{ac} \\ \tau_{ab} \end{Bmatrix} = \left[T_{ij}\right] \begin{Bmatrix} \sigma_x \\ \sigma_y \\ \sigma_z \\ \tau_{yz} \\ \tau_{xz} \\ \tau_{xy} \end{Bmatrix}, \tag{2.18}$$

and

$$\left[T_\varepsilon\right] = \left[R_{ij}\right] \left[T_{ij}\right] \left[R_{ij}^{-1}\right], \tag{2.19}$$

where R_{ij} can be expressed as

$$\left[R_{ij}\right] = \begin{bmatrix} 1 & 0 & 0 & 0 & 0 & 0 \\ 0 & 1 & 0 & 0 & 0 & 0 \\ 0 & 0 & 1 & 0 & 0 & 0 \\ 0 & 0 & 0 & 2 & 0 & 0 \\ 0 & 0 & 0 & 0 & 2 & 0 \\ 0 & 0 & 0 & 0 & 0 & 2 \end{bmatrix}. \tag{2.20}$$

Therefore, we can use T_{ij} as

$$\begin{Bmatrix} \varepsilon_a \\ \varepsilon_b \\ \varepsilon_c \\ \frac{1}{2}\gamma_{bc} \\ \frac{1}{2}\gamma_{ac} \\ \frac{1}{2}\gamma_{ab} \end{Bmatrix} = \left[T_{ij}\right] \begin{Bmatrix} \varepsilon_x \\ \varepsilon_y \\ \varepsilon_z \\ \frac{1}{2}\gamma_{yz} \\ \frac{1}{2}\gamma_{xz} \\ \frac{1}{2}\gamma_{xy} \end{Bmatrix}, \tag{2.21}$$

or as

$$\begin{Bmatrix} \varepsilon_a \\ \varepsilon_b \\ \varepsilon_c \\ \gamma_{bc} \\ \gamma_{ac} \\ \gamma_{ab} \end{Bmatrix} = \left[R_{ij}\right] \left[T_{ij}\right] \left[R_{ij}^{-1}\right] \begin{Bmatrix} \varepsilon_x \\ \varepsilon_y \\ \varepsilon_z \\ \gamma_{yz} \\ \gamma_{xz} \\ \gamma_{xy} \end{Bmatrix}, \tag{2.22}$$

with

$$\left[T_{ij}\right] = \begin{bmatrix} m_1^2 & n_1^2 & p_1^2 & 2n_1p_1 & 2p_1m_1 & 2m_1n_1 \\ m_2^2 & n_2^2 & p_2^2 & 2n_2p_2 & 2n_2m_2 & 2m_2n_2 \\ m_3^2 & n_3^2 & p_3^2 & 2n_3p_3 & 2p_3m_3 & 2m_3n_3 \\ m_2m_3 & n_2n_3 & p_2p_3 & n_2p_3+n_3p_2 & p_2m_3+p_3m_2 & m_2n_3+m_3n_2 \\ m_3m_1 & n_3n_1 & p_3p_1 & n_3p_1+n_1p_3 & p_3m_1+p_1m_3 & m_3n_1+m_1n_3 \\ m_1m_2 & n_1n_2 & p_1p_2 & n_1p_2+n_2p_1 & p_1m_2+p_2m_1 & m_1n_2+m_2n_1 \end{bmatrix}. \tag{2.23}$$

2.2.2 Transformation of stiffness matrix

The stress-strain relations in the x, y, z coordinate system are

$$\begin{Bmatrix} \varepsilon_a \\ \varepsilon_b \\ \varepsilon_b \\ \gamma_{bc} \\ \gamma_{ac} \\ \gamma_{ab} \end{Bmatrix} = \left[S_{ij}\right] \begin{Bmatrix} \sigma_a \\ \sigma_b \\ \sigma_c \\ \tau_{bc} \\ \tau_{ac} \\ \tau_{ab} \end{Bmatrix} \tag{2.24}$$

and

$$\begin{Bmatrix} \sigma_a \\ \sigma_b \\ \sigma_c \\ \tau_{bc} \\ \tau_{ac} \\ \tau_{ab} \end{Bmatrix} = \left[C_{ij}\right] \begin{Bmatrix} \varepsilon_a \\ \varepsilon_b \\ \varepsilon_c \\ \gamma_{bc} \\ \gamma_{ac} \\ \gamma_{ab} \end{Bmatrix}, \tag{2.25}$$

where S_{ij} is the compliance matrix, which is the inverse of the stiffness matrix C_{ij}.

It is noted that the strain tensor used is written in a contracted notation as

$$\gamma_{bc} = 2\varepsilon_{bc}, \qquad \gamma_{ac} = 2\varepsilon_{ac}, \qquad \gamma_{ab} = 2\varepsilon_{ab}, \tag{2.26}$$

where

$$\varepsilon_{bc} = \frac{1}{2}\left(\frac{\partial u_b}{\partial c} + \frac{\partial u_c}{\partial_b}\right), \qquad \varepsilon_{ac} = \frac{1}{2}\left(\frac{\partial u_a}{\partial c} + \frac{\partial u_c}{\partial_a}\right), \qquad \varepsilon_{ab} = \frac{1}{2}\left(\frac{\partial u_a}{\partial b} + \frac{\partial u_b}{\partial_a}\right), \tag{2.27}$$

as we have

$$\begin{Bmatrix} \sigma_a \\ \sigma_b \\ \sigma_c \\ \tau_{bc} \\ \tau_{ac} \\ \tau_{ab} \end{Bmatrix} = \left[T_{ij}\right] \begin{Bmatrix} \sigma_x \\ \sigma_y \\ \sigma_z \\ \tau_{yz} \\ \tau_{zx} \\ \tau_{xy} \end{Bmatrix} \tag{2.28}$$

and

$$\begin{Bmatrix} \varepsilon_a \\ \varepsilon_b \\ \varepsilon_c \\ \gamma_{bc} \\ \gamma_{ac} \\ \gamma_{ab} \end{Bmatrix} = \left[R_{ij}\right] \left[T_{ij}\right] \left[R_{ij}^{-1}\right] \begin{Bmatrix} \varepsilon_x \\ \varepsilon_y \\ \varepsilon_z \\ \gamma_{yz} \\ \gamma_{xz} \\ \gamma_{xy} \end{Bmatrix}. \tag{2.29}$$

Applying the stress-strain relations to the transformation relations in the x, y, z coordinate system, we have

$$\begin{Bmatrix} \varepsilon_x \\ \varepsilon_y \\ \varepsilon_z \\ \gamma_{yz} \\ \gamma_{xz} \\ \gamma_{xy} \end{Bmatrix} = \left[R_{ij}\right] \left[T_{ij}^{-1}\right] \left[R_{ij}^{-1}\right] \left[S_{ij}\right] \left[T_{ij}\right] \begin{Bmatrix} \sigma_x \\ \sigma_y \\ \sigma_z \\ \tau_{yz} \\ \tau_{xz} \\ \tau_{xy} \end{Bmatrix}. \tag{2.30}$$

We set the transformed compliance matrix as

$$\left[\hat{S}_{ij}\right] = \left[R_{ij}\right] \left[T_{ij}^{-1}\right] \left[R_{ij}^{-1}\right] \left[S_{ij}\right] \left[T_{ij}\right], \tag{2.31}$$

and the transformed stiffness matrix is

$$\left[\hat{C}_{ij}\right] = \left[\hat{S}_{ij}\right]^{-1}. \tag{2.32}$$

2.3 Effective mechanical behavior of composite reinforced by corrugated fibres

In this section, we provide a detailed introduction to the development of an effective stiffness matrix of composite reinforced by fibres of a particular sinusoidal waviness as shown in Figure 2.8a, which was first proposed and verified by *Xiao et al.* [2020]. To this end, in section 2.3.1 we first present an analytical solution based on the *Mori and Tanaka* [1973] Eshelby equivalent inclusion method for a stiffness matrix of composite reinforced by straight fibres as shown in Figure 2.4. A transformation matrix of straight and corrugated fibre arrangements is then presented in section 2.3.2. Finally, an effective stiffness matrix of composite reinforced by fibres of sinusoidal waviness is deduced in section 2.3.3.

2.3.1 Effective stiffness matrix of composite reinforced by straight fibres

Here, we present an analytical solution based on the Eshelby equivalent inclusion method for the effective stiffness matrix of composite reinforced by straight fibres, as shown in Figure 2.4.

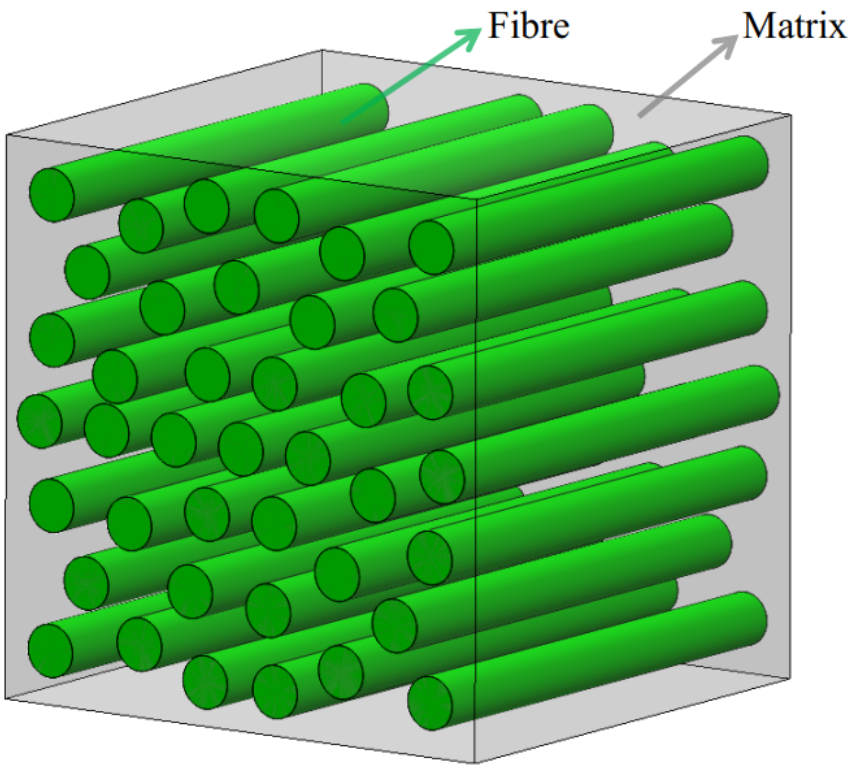

Figure 2.4: Composite reinforced by straight fibres.

The effective elastic constitutive relation of composite material is written as follows:

$$\bar{\sigma} = \bar{C} : \bar{\varepsilon} \qquad \bar{\varepsilon} = \bar{S} : \bar{\sigma}, \tag{2.33}$$

where $\bar{C}$ is the stiffness matrix of the composite reinforced by the straight fibres and $\bar{S}$ is the inverse matrix of $\bar{C}$. Also, $\bar{\sigma}$ and $\bar{\varepsilon}$ represent the average stress and strain tensors respectively in the composite.

We set

$$\bar{\sigma} = V_m \hat{\sigma}_m + V_f \hat{\sigma}_f \qquad \bar{\varepsilon} = V_m \hat{\varepsilon}_m + V_f \hat{\varepsilon}_f, \tag{2.34}$$

where $\hat{\sigma}_f$ and $\hat{\varepsilon}_f$ are the average stress and strain tensors in the fibres, and $\hat{\sigma}_m$ and $\hat{\varepsilon}_m$ are the average stress and strain tensors in the matrix. Moreover, V_f and V_m are the volume fractions of the fibres and the matrix, respectively.

The mechanical strain interaction of fibres and matrix based on the Eshelby equivalent inclusion method can be expressed as

$$\hat{\varepsilon}_f = B : \hat{\varepsilon}_m, \tag{2.35}$$

where B is the concentration tensor whose details can be found in *Parnell* [2016], which can be expressed as

$$B = [I + P : (C^f - C^m)]^{-1}, \tag{2.36}$$

where I is the identity tensor, C^f and C^m are the elastic stiffness tensor of isotropic fibre and matrix media, respectively, and P is the polarization tensor. We refer to *Hill* [1965] for a thorough explanation of this latter, but note here that it has the following relation:

$$P = S^E : S^m, \tag{2.37}$$

where S^m is the elastic compliance of the isotropic matrix media ($S^m = [C^m]^{-1}$), which can be expressed as

$$\left[S^m\right] = \begin{bmatrix} S^m_{11} & S^m_{12} & S^m_{13} & 0 & 0 & 0 \\ S^m_{12} & S^m_{22} & S^m_{23} & 0 & 0 & 0 \\ S^m_{13} & S^m_{23} & S^m_{33} & 0 & 0 & 0 \\ 0 & 0 & 0 & S^m_{44} & 0 & 0 \\ 0 & 0 & 0 & 0 & S^m_{55} & 0 \\ 0 & 0 & 0 & 0 & 0 & S^m_{66} \end{bmatrix}, \tag{2.38}$$

and S^E is the Eshelby tensor, which can be expressed as

$$\left[S^E\right] = \begin{bmatrix} S^E_{1111} & S^E_{1122} & S^E_{1133} & 0 & 0 & 0 \\ S^E_{2211} & S^E_{2222} & S^E_{2233} & 0 & 0 & 0 \\ S^E_{3311} & S^E_{3322} & S^E_{3333} & 0 & 0 & 0 \\ 0 & 0 & 0 & S^E_{2323} & 0 & 0 \\ 0 & 0 & 0 & 0 & S^E_{1313} & 0 \\ 0 & 0 & 0 & 0 & 0 & S^E_{1212} \end{bmatrix}. \tag{2.39}$$

The average stress $\hat{\sigma}_f$ is

$$\hat{\sigma}_f = C^f : \hat{\varepsilon}_f = C^f : B : \hat{\varepsilon}_m. \tag{2.40}$$

The average stress and strain tensors in the composite can be written in terms of $\hat{\sigma}_m$ as

$$\bar{\sigma} = V_m\hat{\sigma}_m + V_f\hat{\sigma}_f = V_m\hat{\sigma}_m + V_fC^f : B : \hat{\varepsilon}_m = V_m\hat{\sigma}_m + V_fC^f : B : (S^m : \hat{\sigma}_m) \tag{2.41}$$

$$\bar{\varepsilon} = V_m\hat{\varepsilon}_m + V_f\hat{\varepsilon}_f = V_m(S^m : \hat{\sigma}_m) + V_fB : (S^m : \hat{\sigma}_m). \tag{2.42}$$

From Equations 2.41 and 2.42, the compliance matrix $\bar{S}$ of the composite can be obtained as

$$\bar{S} = (V_mI + V_fB) : (V_mC^m + V_fC^f : B)^{-1}. \tag{2.43}$$

The Eshelby tensor S^E for an ellipsoidal inclusion —as shown in Figure 2.5a, where a_1, a_2, and a_3 are half the ellipsoidal length along the x, y, and z axis, respectively— in a homogeneous matrix is constant and depends solely on the form of the inclusion and the matrix material.

The Eshelby tensor for the elliptic cylinder inclusion (which means $a_1 = \infty$) is given by *Mura* [2013] as

$$S^E_{1111} = S^E_{1122} = S^E_{1133} = 0, \tag{2.44}$$

$$S^E_{2222} = \frac{1}{2(1-\nu_m)}\left[\frac{a_3^2 + 2a_3a_2}{(a_3+a_2)^2} + (1-2\nu_m)\frac{a_3}{a_3+a_2}\right], \tag{2.45}$$

$$S^E_{3333} = \frac{1}{2(1-\nu_m)}\left[\frac{a_2^2 + 2a_3a_2}{(a_3+a_2)^2} + (1-2\nu_m)\frac{a_2}{a_3+a_2}\right], \tag{2.46}$$

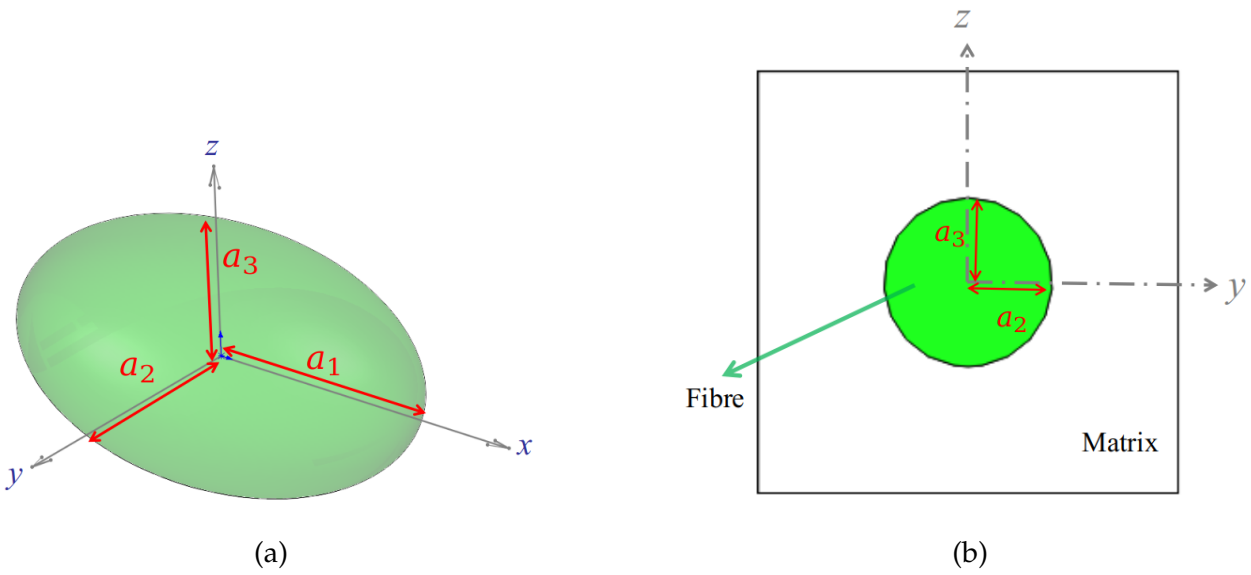

(a) (b)

Figure 2.5: (a) Ellipsoidal inclusion with coordinates. (b) Straight-fibre-reinforced composite plane y-z section.

$$S^E_{2233} = \frac{1}{2(1-\nu_m)}\left[\frac{a_3^2}{(a_3+a_2)^2} - (1-2\nu_m)\frac{a_3}{a_3+a_2}\right], \tag{2.47}$$

$$S^E_{3322} = \frac{1}{2(1-\nu_m)}\left[\frac{a_2^2}{(a_3+a_2)^2} - (1-2\nu_m)\frac{a_2}{a_3+a_2}\right], \tag{2.48}$$

$$S^E_{2211} = \frac{1}{2(1-\nu_m)}\frac{2\nu_m a_3}{a_3+a_2}, \tag{2.49}$$

$$S^E_{3311} = \frac{1}{2(1-\nu_m)}\frac{2\nu_m a_2}{a_3+a_2}, \tag{2.50}$$

$$S^E_{2323} = \frac{1}{2(1-\nu_m)}\left[\frac{a_3^2+a_2^2}{2(a_3+a_2)^2} + \frac{1-2\nu_m}{2}\right], \tag{2.51}$$

$$S^E_{1212} = \frac{a_3}{2(a_2+a_3)}, \tag{2.52}$$

$$S^E_{1313} = \frac{a_2}{2(a_2+a_3)}, \tag{2.53}$$

where ν_m is the Poisson's ratio of a matrix.

The fibres in the matrix are considered to have a circular cross-section, which means $a_3 = a_2$, and therefore the Eshelby tensor can be derived as

$$S^E_{2222} = S^E_{3333} = \frac{1}{2(1-\nu_m)}(\frac{5}{4} - \nu_m), \tag{2.54}$$

$$S^E_{2233} = S^E_{3322} = \frac{1}{2(1-\nu_m)}(\nu_m - \frac{1}{4}), \tag{2.55}$$

$$S^E_{2211} = S^E_{3311} = \frac{\nu_m}{2(1-\nu_m)}, \tag{2.56}$$

$$S^E_{2323} = \frac{1}{2(1-\nu_m)}(\frac{3}{4} - \nu_m), \tag{2.57}$$

$$S^E_{1212} = S^E_{1313} = \frac{1}{4}. \tag{2.58}$$

We assume the composite to be transversally isotropic material in the y-z plane with an elastic compliance $\bar{S}$ that can be expressed as

$$\left[\bar{S}\right] = \begin{bmatrix} \bar{S}_{11} & \bar{S}_{12} & \bar{S}_{12} & 0 & 0 & 0 \\ \bar{S}_{12} & \bar{S}_{22} & \bar{S}_{23} & 0 & 0 & 0 \\ \bar{S}_{12} & \bar{S}_{23} & \bar{S}_{22} & 0 & 0 & 0 \\ 0 & 0 & 0 & \bar{S}_{44} = 2(\bar{S}_{22} - \bar{S}_{23}) & 0 & 0 \\ 0 & 0 & 0 & 0 & \bar{S}_{66} & 0 \\ 0 & 0 & 0 & 0 & 0 & \bar{S}_{66} \end{bmatrix}. \tag{2.59}$$

Inserting Equations 2.36, 2.54, 2.55, 2.56, 2.57, and 2.58 into Equation 2.43, we get the following equivalent compliance matrix element:

$$\bar{S}_{11} = \frac{E_f(1+\nu_m)\left[-2 + 2\nu_m + V_m(1-2\nu_m)\right] - V_m E_m(1+\nu_f)(1-2\nu_f)}{b_1}, \tag{2.60}$$

$$\bar{S}_{12} = \frac{V_m\nu_m E_m(1+\nu_f)(1-2\nu_f) + E_f(1+\nu_m)[2\nu_f(1-\nu_m) + V_m(\nu_m - 2\nu_f + 2\nu_m\nu_f)]}{b_1}, \tag{2.61}$$

$$\bar{S}_{22} = \frac{b_2}{b_3} + \frac{b_4}{4}, \tag{2.62}$$

$$\bar{S}_{23} = \frac{b_2}{b_3} - \frac{b_4}{4}, \tag{2.63}$$

$$\bar{S}_{66} = \frac{2(1+\nu_m)\left[V_m E_f(1+\nu_m) + E_m(1+\nu_f)(2-V_m)\right]}{E_m\left[V_m E_m(1+\nu_f) + E_f(1+\nu_m)(2-V_m)\right]}, \tag{2.64}$$

where E_f and E_m represent the Young's modulus of fibre and matrix, respectively; ν_f is the Poisson's ratio of the fibre; b_1, b_2, b_3, and b_4 are expressed as

$$\begin{aligned} b_1 = &- V_m^2 E_m^2(1+\nu_f)(1-2v_f) + E_f^2(1+\nu_m)(1-V_m)\left[-2+2\nu_m + V_m(1-2\nu_m)\right] + \\ &V_m E_m E_f\left[-3+\nu_f+4\nu_m\nu_f + V_m(2-\nu_m-\nu_f-4\nu_m\nu_f)\right], \end{aligned} \tag{2.65}$$

$$\begin{aligned} b_2 = &E_m E_f(1+\nu_m)\{-2+2\nu_f+2\nu_m-2\nu_m\nu_f + \\ &V_m[3-2\nu_m-3\nu_f-2\nu_m\nu_f + V_m(-2+\nu_m+\nu_f+4\nu_m\nu_f)]\} - \\ &V_m E_f^2(1+\nu_m)^2(1-V_m)(1-2\nu_m) + V_m E_m^2(1+\nu_f)(1-2\nu_f)(-2+V_m+V_m\nu_m), \end{aligned} \tag{2.66}$$

$$\begin{aligned} b_3 = &2E_m\{-V_m^2E_m^2(1+v_f)(1-2v_f) + E_f^2(1+v_m)(1-V_m)[-2+2\nu_m+V_m(1-2\nu_m)] + \\ &V_m E_m E_f[-3+\nu_f(1+4\nu_m) + V_m(2-\nu_m-\nu_f-4\nu_m\nu_f)]\}, \end{aligned} \tag{2.67}$$

$$b_4 = \frac{2(1+\nu_m)[V_m E_f(1+\nu_m)(3-4\nu_m) + E_m(1+\nu_f)(4-3V_m-4\nu_m+4V_m\nu_m)]}{E_m[V_m E_m(1+\nu_f) + E_f(1+\nu_m)(4-V_m-4\nu_m)]}. \tag{2.68}$$

2.3.2 Transformation matrix of fibre arrangement

2.3.2.1 Straight fibre transformation

The fibres are set to be straight and arranged in parallel, and θ represents the angle between the fibre orientation and the x-axis of the Cartesian coordinates as shown in Figure 2.6.

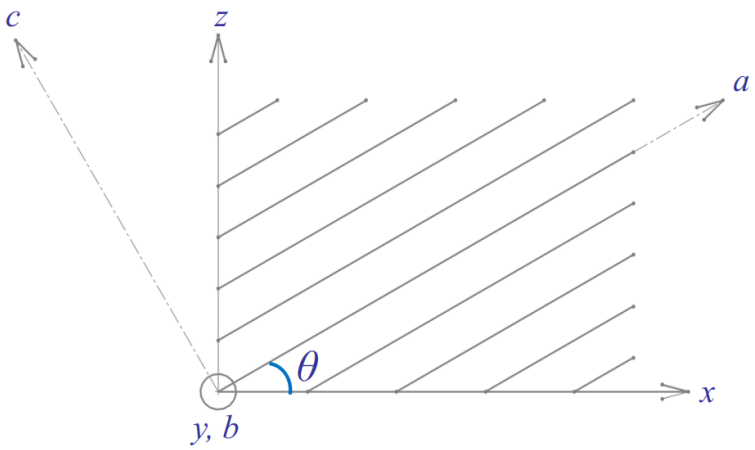

Figure 2.6: Straight fibre orientation and Cartesian coordinates.

The principle fibre orientation is along axis a and the fibre orientation coordinates are defined as

$$\begin{cases} a = cos(\theta)x + sin(\theta)z \\ b = y \\ c = -sin(\theta)x + cos(\theta)z. \end{cases} \tag{2.69}$$

The transformation component of fibre orientation and Cartesian coordinates can be obtained as:

$$m_1 = cos\theta_{xa} = \frac{1 * (cos(\theta))}{\sqrt{1^2} \cdot \sqrt{cos^2(\theta) + sin^2(\theta)}} = cos(\theta). \tag{2.70}$$

The other components are obtained in the same manner.

$$\begin{array}{llll} m_2 = cos\theta_{xb} = 0 & m_3 & = cos\theta_{xc} = sin(\theta) & \\ n_1 = cos\theta_{ya} = 0 & n_2 & = cos\theta_{yb} = 1 & n_3 = cos\theta_{yc} = 0 \\ p_1 = cos\theta_{za} = 0 & p_2 & = cos\theta_{zb} = 0 & p_3 = cos\theta_{zc} = cos(\theta). \end{array} \tag{2.71}$$

Thus, the general transformation matrix T_{ij}^{st} for the parallel straight fibres is

$$\left[T_{ij}^{st}\right] = \begin{bmatrix} cos^2(\theta) & 0 & sin^2(\theta) & 0 & 2cos(\theta)sin(\theta) & 0 \\ 0 & 1 & 0 & 0 & 0 & 0 \\ sin^2(\theta) & 0 & cos^2(\theta) & 0 & -2cos(\theta)sin(\theta) & 0 \\ 0 & 0 & 0 & cos(\theta) & 0 & -sin(\theta) \\ -sin(\theta)cos(\theta) & 0 & sin(\theta)cos(\theta) & 0 & cos^2(\theta) - sin^2(\theta) & 0 \\ 0 & 0 & 0 & sin(\theta) & 0 & cos(\theta) \end{bmatrix}. \quad (2.72)$$

The inverse transformation matrix $T_{ij}^{st\,-1}$ is:

$$\left[T_{ij}^{st\,-1}\right] = \begin{bmatrix} cos^2(\theta) & 0 & sin^2(\theta) & 0 & -2cos(\theta)sin(\theta) & 0 \\ 0 & 1 & 0 & 0 & 0 & 0 \\ sin^2(\theta) & 0 & cos^2(\theta) & 0 & 2cos(\theta)sin(\theta) & 0 \\ 0 & 0 & 0 & cos(\theta) & 0 & sin(\theta) \\ sin(\theta)cos(\theta) & 0 & -sin(\theta)cos(\theta) & 0 & cos^2(\theta) - sin^2(\theta) & 0 \\ 0 & 0 & 0 & -sin(\theta) & 0 & cos(\theta) \end{bmatrix}. \quad (2.73)$$

2.3.2.2 Corrugated fibre transformation

The fibre corrugation is assumed to be planar sinusoidal in the x-z plane. Here, β represents the angle between the principle fibre direction and the x-axis of the Cartesian coordinates as shown in Figure 2.7.

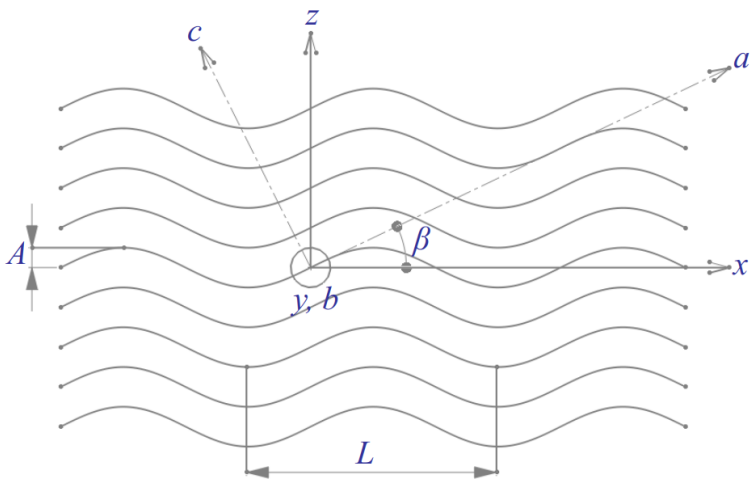

Figure 2.7: Corrugated fibre and Cartesian coordinates.

The crimped fibre shape is defined as

$$z = Asin(\frac{2\pi}{L}x), \tag{2.74}$$

where A is the amplitude and L represents the wavelength of the wavy fibre as shown in Figure 2.7.

From Equation 2.74, we have

$$tan\beta = \frac{dz}{dx} = \frac{2\pi A}{L}cos(\frac{2\pi}{L}x) \qquad \beta = arctan(\frac{2\pi A}{L}cos(\frac{2\pi}{L}x)). \tag{2.75}$$

Therefore,

$$cos\beta = [1 + (\frac{2\pi A}{L}cos(\frac{2\pi}{L}x))^2]^{-\frac{1}{2}}, \tag{2.76}$$

$$sin\beta = \frac{2\pi A}{L}cos(\frac{2\pi}{L}x)[1 + (\frac{2\pi A}{L}cos(\frac{2\pi}{L}x))^2]^{-\frac{1}{2}}. \tag{2.77}$$

The general transformation matrix T_{ij}^{sin} for the corrugated fibres can be derived with the same calculation as before.

$$\left[T_{ij}^{sin}\right] = \begin{bmatrix} cos^2(\beta(x)) & 0 & sin^2(\beta(x)) & 0 & 2cos(\beta(x))sin(\beta(x)) & 0 \\ 0 & 1 & 0 & 0 & 0 & 0 \\ sin^2(\beta(x)) & 0 & cos^2(\beta(x)) & 0 & -2cos(\beta(x))sin(\beta(x)) & 0 \\ 0 & 0 & 0 & cos(\beta(x)) & 0 & -sin(\beta(x)) \\ -sin(\beta(x))cos(\beta(x)) & 0 & sin(\beta(x))cos(\beta(x)) & 0 & cos^2(\beta(x)) - sin^2(\beta(x)) & 0 \\ 0 & 0 & 0 & sin(\beta(x)) & 0 & cos(\beta(x)) \end{bmatrix}. \tag{2.78}$$

2.3.3 Effective stiffness of composite reinforced by fibres of sinusoidal waviness

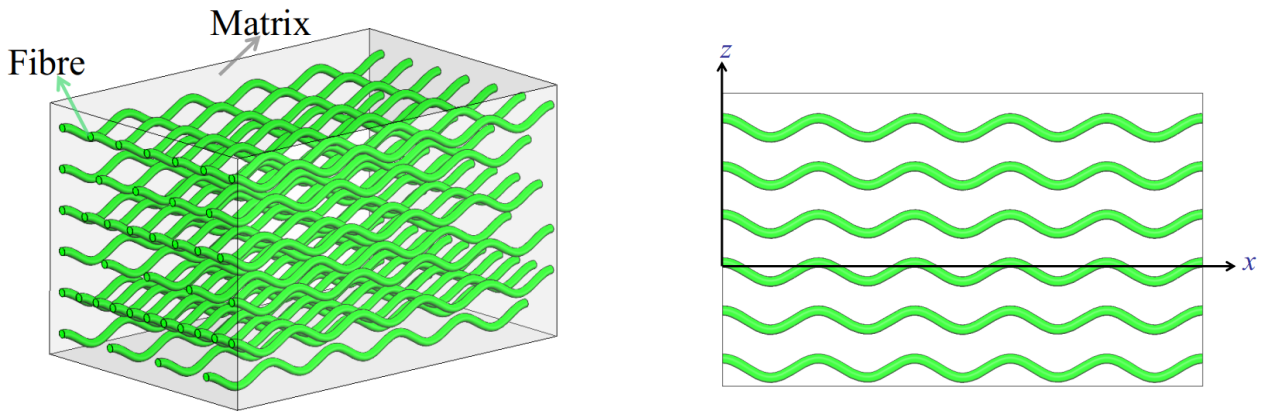

(a) (b)

Figure 2.8: (a) Composite reinforced by fibres of uniform sinusoidal waviness. (b) Composite x-z plane section and axis.

We present the analytical solution to find the effective stiffness matrix $\hat{C}_{ij}^{sin}$ $(i,j = 1,2,3,4,5,6)$ of composite reinforced by fibres of uniform sinusoidal waviness as shown in Figure 2.8. The average transformed inverse compliance matrix $\hat{S}_{ij}^{sin}$ is obtained by integrating the compliance matrix $\bar{S}$ along one wavelength of the sinusoidal shape in the x-direction as

$$\hat{S}_{ij}^{sin}(\beta(A,L)) = \int_0^L \hat{S}_{ij}(\beta(A,L))dx, \tag{2.79}$$

where

$$\left[\hat{S}_{ij}\right] = \left[R_{ij}\right]\left[T_{ij}^{sin}\right]^{-1}\left[R_{ij}\right]^{-1}\left[\bar{S}_{ij}\right]\left[T_{ij}^{sin}\right], \tag{2.80}$$

and $\beta = arctan(\frac{2\pi A}{L}cos(\frac{2\pi}{L}x))$ and $x \in [0,L]$.

We then have

$$\left[\hat{C}_{ij}^{sin}\right] = \left[\hat{S}_{ij}^{sin}\right]^{-1}. \tag{2.81}$$

We set

$$g = \frac{1}{L}\int_0^L cos^4\beta dx = \frac{1}{L}\int_0^L [[1+(\frac{2\pi A}{L}cos(\frac{2\pi}{L}x))^2]^{-\frac{1}{2}}]^4 dx = \frac{2A^2L\pi^2 + L^3}{\sqrt{4A^2\pi^2+L^2}(L^2+4A^2\pi^2)}, \tag{2.82}$$

$$h = \frac{1}{L}\int_0^L sin^4\beta dx = \frac{(L^2+4A^2\pi^2)\sqrt{4A^2\pi^2+L^2} - 6A^2L\pi^2 - L^3}{\sqrt{4A^2\pi^2+L^2}(L^2+4A^2\pi^2)}, \tag{2.83}$$

$$m = \frac{1}{L}\int_0^L sin^2\beta cos^2\beta dx = \frac{2A^2L\pi^2}{(L^2+4A^2\pi^2)\sqrt{4A^2\pi^2+L^2}}, \tag{2.84}$$

$$n = \frac{1}{L}\int_0^L cos^2\beta dx = \frac{L}{\sqrt{4A^2\pi^2+L^2}}, \tag{2.85}$$

$$p = \frac{1}{L}\int_0^L sin^2\beta dx = \frac{\sqrt{4A^2\pi^2+L^2}-L}{\sqrt{4A^2\pi^2+L^2}}, \tag{2.86}$$

$$q = \frac{1}{L}\int_0^L (cos^2(\beta) - sin^2(\beta))^2 dx = g - 2m + h. \tag{2.87}$$

We note that, before integration, terms $\hat{S}_{15}$, $\hat{S}_{25}$, $\hat{S}_{35}$, and $\hat{S}_{46}$ are not zero, but these terms become zero during integration over the period.

The non-zero element of matrix $\hat{S}_{ij}^{sin}$ can be expressed as

$$\left[\hat{S}_{ij}^{sin}\right] = \begin{bmatrix} \hat{S}_{11}^{sin} & \hat{S}_{12}^{sin} & \hat{S}_{13}^{sin} & 0 & 0 & 0 \\ \hat{S}_{12}^{sin} & \hat{S}_{22}^{sin} & \hat{S}_{23}^{sin} & 0 & 0 & 0 \\ \hat{S}_{13}^{sin} & \hat{S}_{23}^{sin} & \hat{S}_{33}^{sin} & 0 & 0 & 0 \\ 0 & 0 & 0 & \hat{S}_{44}^{sin} & 0 & 0 \\ 0 & 0 & 0 & 0 & \hat{S}_{55}^{sin} & 0 \\ 0 & 0 & 0 & 0 & 0 & \hat{S}_{66}^{sin} \end{bmatrix}, \tag{2.88}$$

where

$$\hat{S}_{11}^{sin} = g\bar{S}_{11} + m(2\bar{S}_{12} + \bar{S}_{66}) + h\bar{S}_{22}, \tag{2.89}$$

$$\hat{S}_{12}^{sin} = n\bar{S}_{12} + p\bar{S}_{23}, \tag{2.90}$$

$$\hat{S}_{13}^{sin} = m(\bar{S}_{11} + \bar{S}_{22} - \bar{S}_{66}) + (h+g)\bar{S}_{12}, \tag{2.91}$$

$$\hat{S}_{22}^{sin} = \bar{S}_{22}, \tag{2.92}$$

$$\hat{S}_{23}^{sin} = p\bar{S}_{12} + n\bar{S}_{23}, \tag{2.93}$$

$$\hat{S}_{33}^{sin} = m(2\bar{S}_{12} + \bar{S}_{66}) + h\bar{S}_{11} + g\bar{S}_{22}, \tag{2.94}$$

$$\hat{S}_{44}^{sin} = 2n(\bar{S}_{22} - \bar{S}_{23}) + p\bar{S}_{66}, \tag{2.95}$$

$$\hat{S}_{55}^{sin} = 4m(\bar{S}_{11} + \bar{S}_{22} - 2\bar{S}_{12}) + q\bar{S}_{66}, \tag{2.96}$$

$$\hat{S}_{66}^{sin} = 2p(\bar{S}_{22} - \bar{S}_{23}) + n\bar{S}_{66}. \tag{2.97}$$

2.4 Effective mechanical behavior of lamellar composite reinforced by corrugated fibres with alternatively oriented layers

In this section, we propose an analytical solution that takes into account the multiple layers and the orientation of each layer to find the effective elastic stiffness matrix. The single-lamella and multiple-lamellae solutions are presented in sections 2.4.1 and 2.4.2, respectively.

2.4.1 Single layer

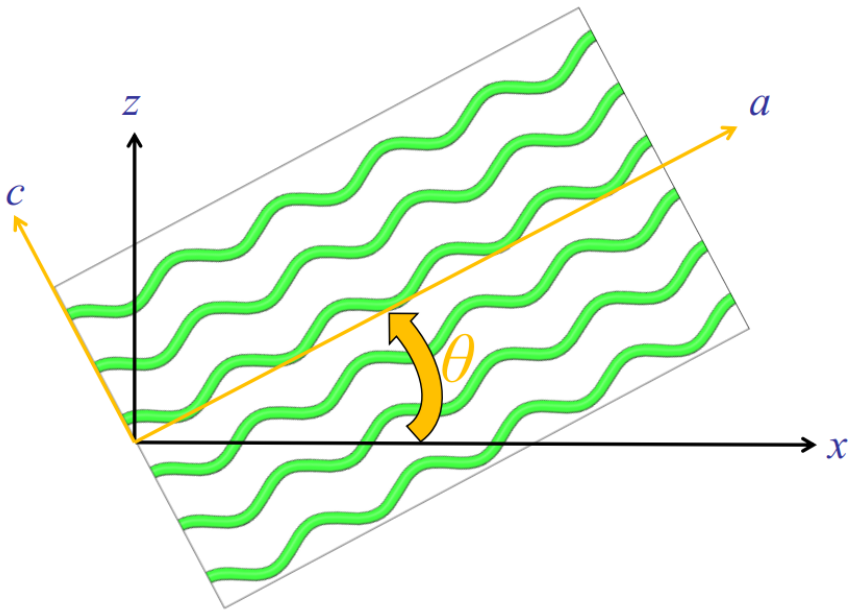

Figure 2.9: Composite orientation in the Cartesian coordinate system.

One layer (or lamella) of the composite reinforced by fibres of uniform sinusoidal waviness is rotated by an angle of θ around the Y-axis as shown in Figure 2.9. The effective stiffness matrix of this layer $\tilde{C}_{ij}^{layer1}$ and its inverse compliance $\tilde{S}_{ij}^{layer1}$ can be deduced as

$$\left[\tilde{S}_{ij}^{layer1}\right] = \left[R_{ij}\right]\left[T_{ij}^{st}\right]^{-1}\left[R_{ij}\right]^{-1}\left[\hat{S}_{ij}^{sin}\right]\left[T_{ij}^{st}\right] \qquad \left[\tilde{C}_{ij}^{layer1}\right] = \left[\tilde{S}_{ij}^{layer1}\right]^{-1}. \tag{2.98}$$

The nonzero element of matrix $\tilde{S}_{ij}^{layer1}$ can be expressed as

$$\left[\tilde{S}_{ij}^{layer1}\right] = \begin{bmatrix} \tilde{S}_{11}^{layer1} & \tilde{S}_{12}^{layer1} & \tilde{S}_{13}^{layer1} & 0 & \tilde{S}_{15}^{layer1} & 0 \\ \tilde{S}_{12}^{layer1} & \tilde{S}_{22}^{layer1} & \tilde{S}_{23}^{layer1} & 0 & \tilde{S}_{25}^{layer1} & 0 \\ \tilde{S}_{13}^{layer1} & \tilde{S}_{23}^{layer1} & \tilde{S}_{33}^{layer1} & 0 & \tilde{S}_{35}^{layer1} & 0 \\ 0 & 0 & 0 & \tilde{S}_{44}^{layer1} & 0 & \tilde{S}_{46}^{layer1} \\ \tilde{S}_{15}^{layer1} & \tilde{S}_{25}^{layer1} & \tilde{S}_{35}^{layer1} & 0 & \tilde{S}_{55}^{layer1} & 0 \\ 0 & 0 & 0 & \tilde{S}_{46}^{layer1} & 0 & \tilde{S}_{66}^{layer1} \end{bmatrix}, \tag{2.99}$$

where

$$\tilde{S}_{11}^{layer1} = \hat{S}_{11}^{sin} cos^4\theta + \hat{S}_{33}^{sin} sin^4\theta + (2\hat{S}_{13}^{sin} + \hat{S}_{55}^{sin}) cos^2\theta sin^2\theta, \tag{2.100}$$

$$\tilde{S}_{12}^{layer1} = \hat{S}_{12}^{sin} cos^2\theta + \hat{S}_{23}^{sin} sin^2\theta, \tag{2.101}$$

$$\tilde{S}_{13}^{layer1} = \hat{S}_{13}^{sin} (sin^4\theta + cos^4\theta) + (\hat{S}_{11}^{sin} + \hat{S}_{33}^{sin} - \hat{S}_{55}^{sin}) cos^2\theta sin^2\theta, \tag{2.102}$$

$$\tilde{S}_{15}^{layer1} = (2\hat{S}_{11}^{sin} - 2\hat{S}_{13}^{sin} - \hat{S}_{55}^{sin}) sin\theta cos^3\theta + (2\hat{S}_{13}^{sin} - 2\hat{S}_{33}^{sin} + \hat{S}_{55}^{sin}) sin^3\theta cos\theta, \tag{2.103}$$

$$\tilde{S}_{22}^{layer1} = \hat{S}_{22}^{sin}, \tag{2.104}$$

$$\tilde{S}_{23}^{layer1} = \hat{S}_{12}^{sin} sin^2\theta + \hat{S}_{23}^{sin} cos^2\theta, \tag{2.105}$$

$$\tilde{S}_{25}^{layer1} = 2(\hat{S}_{12}^{sin} - \hat{S}_{23}^{sin}) cos\theta sin\theta, \tag{2.106}$$

$$\tilde{S}_{33}^{layer1} = \hat{S}_{11}^{sin} sin^4\theta + \hat{S}_{33}^{sin} cos^4\theta + (2\hat{S}_{13}^{sin} + \hat{S}_{55}^{sin}) cos^2\theta sin^2\theta, \tag{2.107}$$

$$\tilde{S}_{35}^{layer1} = (2\hat{S}_{13}^{sin} - 2\hat{S}_{33}^{sin} + \hat{S}_{55}^{sin})sin\theta cos^3\theta + (2\hat{S}_{11}^{sin} - 2\hat{S}_{13}^{sin} - \hat{S}_{55}^{sin})sin^3\theta cos\theta, \tag{2.108}$$

$$\tilde{S}_{44}^{layer1} = \hat{S}_{66}^{sin} sin^2\theta + \hat{S}_{44}^{sin} cos^2\theta, \tag{2.109}$$

$$\tilde{S}_{46}^{layer1} = (\hat{S}_{66}^{sin} - \hat{S}_{44}^{sin})sin\theta cos\theta, \tag{2.110}$$

$$\tilde{S}_{55}^{layer1} = 4(\hat{S}_{11}^{sin} + \hat{S}_{33}^{sin} - 2\hat{S}_{13}^{sin})sin^2\theta cos^2\theta + \hat{S}_{55}^{sin}(cos^2\theta - sin^2\theta)^2, \tag{2.111}$$

$$\tilde{S}_{66}^{layer1} = \hat{S}_{44}^{sin} sin^2\theta + \hat{S}_{66}^{sin} cos^2\theta. \tag{2.112}$$

2.4.2 Multiple layers

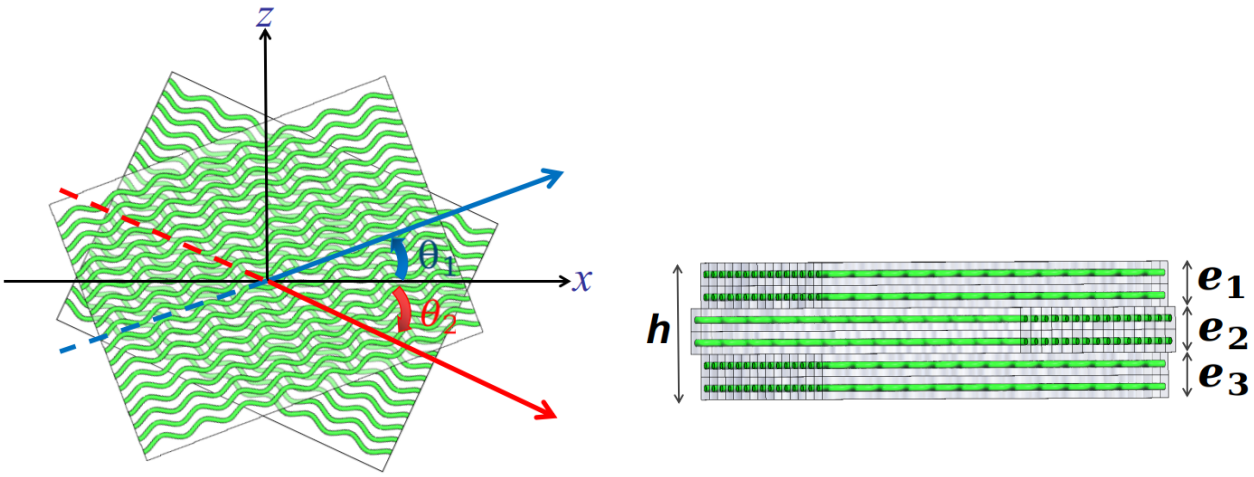

(a) (b)

Figure 2.10: Organization of the synthetic laminate (a) Multilayer laminate with coordinate system. Two lamellae are shown, the first and second layers are orientated by θ_1 and θ_2 around the y-axis with respect to the x-axis, respectively. (b) Schema of laminate layer thickness.

We introduced an analytical approach to find the effective elastic stiffness of a matrix of multiple layers by applying *Sun and Li* [1988] formulations. Each considered layer or "lamella" is a thick composite reinforced by fibres of uniform sinusoidal waviness, as shown in section 2.4.1. The coordinate system is set so that the x- and z-axes lie in the plane of

the lamella and the y-axis is perpendicular to that plane. The laminate composite contains r orthotropic fibre composite lamellae and each lamella is rotated by a corresponding angle $\theta_k, (k = 1, 2, 3 \cdots)$ around the y-axis as shown in Figure 2.10a.

The effective macro-stresses σ^{total} and macro-strains ε^{total} are defined as

$$\sigma_{ij}^{total} = \frac{1}{V} \int_V \sigma_{ij} dV, \tag{2.113}$$

and

$$\varepsilon_{ij}^{total} = \frac{1}{V} \int_V \varepsilon_{ij} dV, \tag{2.114}$$

where V is the volume that contains the total thickness of one lamella.

The in-plane dimensions are kept infinitesimal so that the stresses and strains in each layer are uniform in the planar directions. As the stresses and strains in each lamella are constant, Equations 2.113 and 2.114 can be integrated as

$$\sigma_{ij}^{total} = \sum_{k=1}^{r} V_k (\sigma_{ij})_k, \tag{2.115}$$

and

$$\varepsilon_{ij}^{total} = \sum_{k=1}^{r} V_k (\varepsilon_{ij})_k, \tag{2.116}$$

where $(\sigma_{ij})_k$ and $(\varepsilon_{ij})_k$ are the stresses and strains in the kth $(k = 1, 2, 3 \cdots)$ layer, and

$$V_k = \frac{e_k}{h}, \tag{2.117}$$

where e_k is the thickness of the kth lamella, and h is the total thickness of the laminate as shown in Figure 2.10b.

We assume the following in terms of the stress and displacement conditions at the interfaces of the layers:

$$\begin{cases} (\varepsilon_{xx})_k = \varepsilon_{xx}^{total} \\ (\varepsilon_{zz})_k = \varepsilon_{zz}^{total} \\ (\gamma_{xz})_k = \gamma_{xz}^{total} \\ (\sigma_{yy})_k = \sigma_{yy}^{total} \\ (\sigma_{xy})_k = \sigma_{xy}^{total} \\ (\sigma_{yz})_k = \sigma_{yz}^{total} \end{cases}. \tag{2.118}$$

The effective elastic stiffness matrix of the multilayer laminate $\tilde{C}_{ij}^{total}$ can be expressed as

$$\left[\tilde{C}_{ij}^{total}\right] = \begin{bmatrix} \tilde{C}_{11}^{total} & \tilde{C}_{12}^{total} & \tilde{C}_{13}^{total} & 0 & \tilde{C}_{15}^{total} & 0 \\ \tilde{C}_{12}^{total} & \tilde{C}_{22}^{total} & \tilde{C}_{23}^{total} & 0 & \tilde{C}_{25}^{total} & 0 \\ \tilde{C}_{13}^{total} & \tilde{C}_{23}^{total} & \tilde{C}_{33}^{total} & 0 & \tilde{C}_{35}^{total} & 0 \\ 0 & 0 & 0 & \tilde{C}_{44}^{total} & 0 & \tilde{C}_{46}^{total} \\ \tilde{C}_{15}^{total} & \tilde{C}_{25}^{total} & \tilde{C}_{35}^{total} & 0 & \tilde{C}_{55}^{total} & 0 \\ 0 & 0 & 0 & \tilde{C}_{46}^{total} & 0 & \tilde{C}_{66}^{total} \end{bmatrix}. \tag{2.119}$$

The nonzero element of $\tilde{C}_{ij}^{total}$ can be obtained from Equations 2.115, 2.116, and 2.118 as (*Sun and Li* [1988]):

$$\tilde{C}_{11}^{total} = \sum_{k=1}^{r} V_k(\tilde{C}_{11}^{layer1})_k + \sum_{k=2}^{r}((\tilde{C}_{12}^{layer1})_k - \lambda_{12})V_k((\tilde{C}_{12}^{layer1})_1 - (\tilde{C}_{12}^{layer1})_k)/(\tilde{C}_{22}^{layer1})_k \tag{2.120}$$

$$\tilde{C}_{12}^{total} = \sum_{k=1}^{r} V_k(\tilde{C}_{12}^{layer1})_k + \sum_{k=2}^{r}((\tilde{C}_{22}^{layer1})_k - \lambda_{22})V_k((\tilde{C}_{12}^{layer1})_1 - (\tilde{C}_{12}^{layer1})_k)/(\tilde{C}_{22}^{layer1})_k \tag{2.121}$$

$$\tilde{C}_{13}^{total} = \sum_{k=1}^{r} V_k(\tilde{C}_{13}^{layer1})_k + \sum_{k=2}^{r}((\tilde{C}_{12}^{layer1})_k - \lambda_{12})V_k((\tilde{C}_{23}^{layer1})_1 - (\tilde{C}_{23}^{layer1})_k)/(\tilde{C}_{22}^{layer1})_k \tag{2.122}$$

$$\tilde{C}_{22}^{total} = 1/(\sum_{k=1}^{r} V_k/(\tilde{C}_{22}^{layer1})_k), \tag{2.123}$$

$$\tilde{C}_{23}^{total} = \sum_{k=1}^{r} V_k(\tilde{C}_{23}^{layer1})_k + \sum_{k=2}^{r}((\tilde{C}_{22}^{layer1})_k - \lambda_{22})V_k((\tilde{C}_{23}^{layer1})_1 - (\tilde{C}_{23}^{layer1})_k)/(\tilde{C}_{22}^{layer1})_k \tag{2.124}$$

$$\tilde{C}_{33}^{total} = \sum_{k=1}^{r} V_k(\tilde{C}_{33}^{layer1})_k + \sum_{k=2}^{r}((\tilde{C}_{23}^{layer1})_k - \lambda_{23})V_k((\tilde{C}_{23}^{layer1})_1 - (\tilde{C}_{23}^{layer1})_k)/(\tilde{C}_{22}^{layer1})_k \tag{2.125}$$

$$\tilde{C}_{15}^{total} = \sum_{k=1}^{r} V_k(\tilde{C}_{15}^{layer1})_k + \sum_{k=2}^{r}((\tilde{C}_{12}^{layer1})_k - \lambda_{12})V_k((\tilde{C}_{25}^{layer1})_1 - (\tilde{C}_{25}^{layer1})_k)/(\tilde{C}_{22}^{layer1})_k \tag{2.126}$$

$$\tilde{C}_{25}^{total} = \sum_{k=1}^{r} V_k(\tilde{C}_{25}^{layer1})_k + \sum_{k=2}^{r}((\tilde{C}_{22}^{layer1})_k - \lambda_{22})V_k((\tilde{C}_{25}^{layer1})_1 - (\tilde{C}_{25}^{layer1})_k)/(\tilde{C}_{22}^{layer1})_k \quad (2.127)$$

$$\tilde{C}_{35}^{total} = \sum_{k=1}^{r} V_k(\tilde{C}_{35}^{layer1})_k + \sum_{k=2}^{r}((\tilde{C}_{23}^{layer1})_k - \lambda_{23})V_k((\tilde{C}_{25}^{layer1})_1 - (\tilde{C}_{25}^{layer1})_k)/(\tilde{C}_{22}^{layer1})_k \quad (2.128)$$

$$\tilde{C}_{55}^{total} = \sum_{k=1}^{r} V_k(\tilde{C}_{55}^{layer1})_k + \sum_{k=2}^{r}((\tilde{C}_{25}^{layer1})_k - \lambda_{25})V_k((\tilde{C}_{25}^{layer1})_1 - (\tilde{C}_{25}^{layer1})_k)/(\tilde{C}_{22}^{layer1})_k \quad (2.129)$$

$$\tilde{C}_{44}^{total} = (\sum_{k=1}^{r} V_k(\tilde{C}_{44}^{layer1})_k/\Delta_k)/\Delta \quad (2.130)$$

$$\tilde{C}_{46}^{total} = (\sum_{k=1}^{r} V_k(\tilde{C}_{46}^{layer1})_k/\Delta_k)/\Delta \quad (2.131)$$

$$\tilde{C}_{66}^{total} = (\sum_{k=1}^{r} V_k(\tilde{C}_{66}^{layer1})_k/\Delta_k)/\Delta \quad (2.132)$$

where

$$\lambda_{12} = \tilde{C}_{12}^{total}, \quad (2.133)$$

$$\lambda_{23} = \tilde{C}_{23}^{total}, \quad (2.134)$$

$$\lambda_{22} = \tilde{C}_{22}^{total}, \quad (2.135)$$

$$\lambda_{25} = \tilde{C}_{25}^{total}, \quad (2.136)$$

$$\Delta = (\sum_{k=1}^{r} V_k(\tilde{C}_{44}^{layer1})_k/\Delta_k)(\sum_{k=1}^{r} V_k(\tilde{C}_{66}^{layer1})_k/\Delta_k) - (\sum_{k=1}^{r} V_k(\tilde{C}_{46}^{layer1})_k/\Delta_k)^2, \quad (2.137)$$

$$\Delta_k = (\tilde{C}_{44}^{layer1})_k(\tilde{C}_{66}^{layer1})_k - (\tilde{C}_{46}^{layer1})_k^2. \quad (2.138)$$

The effective elastic compliance matrix of multiple layer $\tilde{S}_{ij}^{total}$ is

$$[\tilde{S}_{ij}^{total}] = [\tilde{C}_{ij}^{total}]^{-1}. \tag{2.139}$$

2.5 Model limit verification

We further verify the proposed model by considering a special case, $A = 0$, where the fibres contained in the laminate are straight. When $A = 0$, from Equation 2.82 - 2.87, we have

$$\begin{cases} g = 1 & h = 0 & m = 0 \\ n = 1 & p = 0 & q = 1. \end{cases} \tag{2.140}$$

Then, from Equation 2.89 - 2.97, we have

$$\begin{cases} \hat{S}_{11}^{sin} = \bar{S}_{11} & \hat{S}_{12}^{sin} = \bar{S}_{12} & \hat{S}_{13}^{sin} = \bar{S}_{12} \\ \hat{S}_{23}^{sin} = \bar{S}_{23} & \hat{S}_{33}^{sin} = \bar{S}_{22} & \hat{S}_{55}^{sin} = \bar{S}_{66} \\ \hat{S}_{66}^{sin} = \bar{S}_{66} & \hat{S}_{44}^{sin} = 2n(\bar{S}_{22} - \bar{S}_{23}), \end{cases} \tag{2.141}$$

and therefore

$$[\hat{S}_{ij}^{sin}] = [\bar{S}_{ij}]. \tag{2.142}$$

As shown from Equation 2.142, when $A = 0$, all terms in $\hat{S}_{ij}^{sin}$ are equal to the corresponding terms in $\bar{S}_{ij}$, which verifies our model for the special limit case for straight fibres.

We also verify our model by considering the special case $\theta = 0$, which represents the case where the layers are not rotated with respect to one another. When $\theta = 0$, we have

$$cos\theta = 1 \qquad sin\theta = 0. \tag{2.143}$$

The terms in $\tilde{S}_{ij}^{layer1}$ can then be deduced from Equation 2.100 - 2.112, as

$$\begin{cases} & \tilde{S}_{11}^{layer1} = \hat{S}_{11}^{sin} & \tilde{S}_{12}^{layer1} = \hat{S}_{12}^{sin} & \tilde{S}_{13}^{layer1} = \hat{S}_{13}^{sin} \\ & \tilde{S}_{22}^{layer1} = \hat{S}_{22}^{sin} & \tilde{S}_{23}^{layer1} = \hat{S}_{23}^{sin} & \tilde{S}_{33}^{layer1} = \hat{S}_{33}^{sin} \\ & \tilde{S}_{44}^{layer1} = \hat{S}_{44}^{sin} & \tilde{S}_{55}^{layer1} = \hat{S}_{55}^{sin} & \tilde{S}_{66}^{layer1} = \hat{S}_{66}^{sin}, \\ \tilde{S}_{15}^{layer1} = 0 & \tilde{S}_{25}^{layer1} = 0 & \tilde{S}_{35}^{layer1} = 0 & \tilde{S}_{46}^{layer1} = 0 \end{cases} \tag{2.144}$$

and therefore we have

$$[\tilde{S}_{ij}^{layer1}] = [\hat{S}_{ij}^{sin}]. \tag{2.145}$$

When $\theta = 0$, all the terms in $\tilde{S}_{ij}^{layer1}$ are equal to the corresponding terms in $\hat{S}_{ij}^{sin}$, which also further verifies the model for the limit case for nonrotated layers.

2.6 Parameter study

We consider the lamellar structure in annulus fibrosus tissues as corrugated-fibre-reinforced composite and study the composite mechanical behavior by applying the micromechanical model introduced in section 2.4. The aim of our parameter study is to explore whether or not it is possible to use our model, within the extended physiological range, to analyze the influence of each parameter on the global mechanical properties of the annulus fibrosus tissue. Furthermore, we want to prioritize the parameters that influence the negative Poisson's effect on tissues as reported in the literature.

Our parameter study of annulus fibrosus tissue is based on parameters reported in the literature (see Table 2.1). Collagen has the elastic modulus from the molecular to tissue scale, and the mechanical stiffness decreases as the hierarchy scale increases; in other words, $E_{monomer} > E_{fibril} > E_{fibre} > E_{tissue}$ (*Zhang et al.* [2007]). Although the collagen elastic modulus is most often reported at the lamella scale (*Skaggs et al.* [1994]; *Holzapfel et al.* [2005]), there are examples in the literature of the elastic modulus studied at the single collagen fibre scale. *Ambard and Cherblanc* [2009] showed the collagen fibre elastic modulus to range from $6.6MPa$ to $12.3MPa$ using a tensile test on lamb and pig annulus fibrosus tissues as part of their development of a rheological model. Also, the collagen Type I single-fibre elastic modulus was measured to between 100 MPa and 360 MPa in rat tail tendon using an approach combining optical tweezers, atomic force microscopy, and exploitation of Euler-Bernoulli elasticity theory. As Type I collagen fibres are the most prevalent fibres (*Sharabi et al.* [2018]) in annulus fibrosus tissue, we consider that the measured collagen fibre modulus can also be applied in annulus fibrosus tissue. The mechanical properties of the ground matrix of bovine annulus fibrosus were measured by *Cortes and Elliott* [2012] using tensile and confined compression tests, revealing an aggregate modulus of $10.18 \pm 3.32KPa$. The fibre volume fractions have been found to range from 0.05 to 0.245 based on the description that AF comprises 65% - 90% wet weight (water) and 50% - 70% dry weight (collagen) (see *Ducheyne* [2015]). The Poisson's ratio range of the fibre and matrix used in our model is based on a previous modeling study, which is summarized by *Sharabi et al.* [2018]. The layer orientation angle used in the present study, that is the angle between the fibres of

one lamella and those of its neighbors, is based on the findings of *Baldit* [2018]; namely that the fibre orientation in the circumferential direction varies between lamellae by 25° to 45°. The fibre crimp angle is assumed to vary between 20° and 45° as described by *Sharabi* [2022]; that is, the range of the fibre crimp angle is level is taken as $arctan20^\circ < \frac{4A}{L} < arctan45^\circ$ ($0.08 < \frac{A}{L} < 0.25$). Furthermore, the annulus fibrosus consists of 7 - 25 lamellae (*Daroff and Aminoff* [2014]; *Baldit* [2018]), and the layers are 0.14 - 0.52 *mm* in thickness and grow thicker in the lateral portion and inner layers of the annulus (*Daroff and Aminoff* [2014]).

The effective moduli for a laminate of one or multiple layers are obtained from $\tilde{S}_{ij}$ (here, $\tilde{S}_{ij}$ represents $\tilde{S}_{ij}^{layer1}$ or $\tilde{S}_{ij}^{total}$ according to the particular application) as:

$$\begin{cases} \tilde{E_x} = \dfrac{1}{\tilde{S}_{11}} & \tilde{E_y} = \dfrac{1}{\tilde{S}_{22}} & \tilde{E_z} = \dfrac{1}{\tilde{S}_{33}} \\ \tilde{\nu}_{xy} = -\dfrac{\tilde{S}_{21}}{\tilde{S}_{11}} & \tilde{\nu}_{xz} = -\dfrac{\tilde{S}_{31}}{\tilde{S}_{11}} & \tilde{\nu}_{yz} = -\dfrac{\tilde{S}_{32}}{\tilde{S}_{22}} \\ \tilde{\nu}_{yx} = -\dfrac{\tilde{S}_{12}}{\tilde{S}_{22}} & \tilde{\nu}_{zx} = -\dfrac{\tilde{S}_{13}}{\tilde{S}_{33}} & \tilde{\nu}_{zy} = -\dfrac{\tilde{S}_{23}}{\tilde{S}_{33}} \end{cases}, \tag{2.146}$$

where the terms $\tilde{E_x}$, $\tilde{E_y}$, and $\tilde{E_z}$ are the effective elastic modulus along the x, y, and z directions, respectively. Also, the term $\tilde{\nu}_{ij}$ is the effective Poisson's ratio, which characterizes the strain in the j direction produced by the loading in the i direction.

Parameter	Meaning	Value	References
E_f	Collagen fibre modulus	6.6 MPa - 360 MPa	*Ambard and Cherblanc* [2009]ï¼Œ*Sharabi et al.* [2018]
E_m	Extracellular matrix modulus	10.18 ± 3.32 KPa	*Cortes and Elliott* [2012]
V_f	Collagen fibre volume fraction	0.05 - 0.245	*Ducheyne* [2015]
V_m	Matrix volume fraction	0.755 - 0.95	$V_m = 1 - V_f$
ν_f	Collagen fibre Poisson's ratio	0.3 - 0.35	*Sharabi et al.* [2018]
ν_m	Extracellular matrix Poisson's ratio	0.4 - 0.48	*Sharabi et al.* [2018]
θ	Layer orientation angle	25° - 45°	*Baldit* [2018]
$\frac{A}{L}$	Collagen fibre crimp level	0.08 - 0.25	*Sharabi* [2022]
e_k	Thickness of each layers	0.14 - 0.52 *mm*	*Daroff and Aminoff* [2014]
r	Total number of layer	7 - 25	*Daroff and Aminoff* [2014], *Baldit* [2018]

Table 2.1: Mechanical parameters of annulus fibrosus tissues reported in the literature.

2.7 Results of the parametric study

In this section, the effective elastic properties of composites of single or multiple layers are quantified using a theoretical analysis. Parametric analyses of the Poisson's ratio and elastic modulus are also presented.

2.7.1 Single layer

2.7.1.1 Effects of fibre crimp level and layer orientation

In order to test the effects of fibre crimp level and layer orientation, we applied the following constraints to our model. The elastic modulus of fibres E_f is set to $100MPa$ and that of the matrix E_m is set to $10KPa$. The Poisson's ratio of fibre ν_f and matrix ν_m are set to 0.3 and 0.4, respectively. The fibre volume fraction V_f is set to 20 % in this analysis. With these parameters, the model is able to predict the axial effective elastic modulus and effective Poisson's ratio as functions of fibre crimp level ($0.01 < \frac{A}{L} < 0.3$) and layer orientation angle ($20^\circ < \theta < 70^\circ$), as shown in Figure 2.12 and 2.14. The orientation angle θ and coordinate system settings are represented in Figure 2.11.

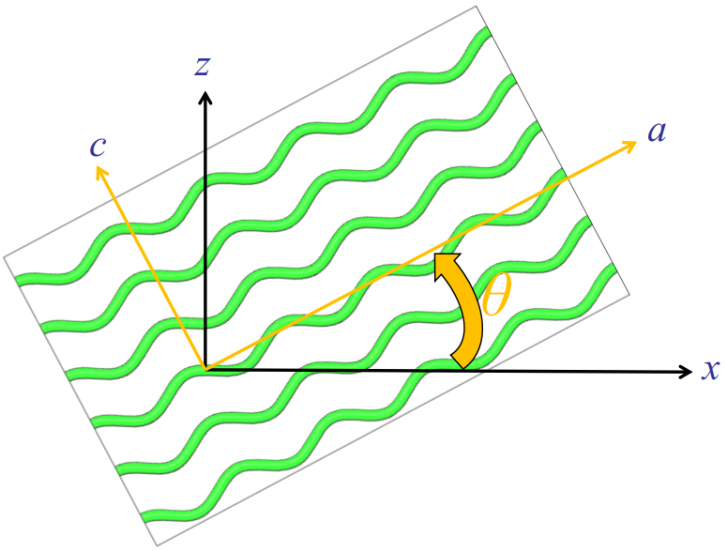

Figure 2.11: Single layer composite orientation in the given coordinate systems.

Figure 2.12 shows that the axial elastic modulus is jointly influenced by fibre crimp level $\frac{A}{L}$ and layer orientation angle θ. The effective elastic modulus E_x has a maximum value when both $\frac{A}{L}$ and θ decrease simultaneously and the effective elastic modulus E_z has a maximum value when $\frac{A}{L}$ is small and θ is large. As expected, E_x and E_z are symmetrical at each fibre crimp level on the axis of θ = 45°. This is clearly shown in Figure 2.13a for a given $\frac{A}{L} = 0.01$. From Equations 2.92, 2.104, and 2.146, we can see that for the single layer, the effective elastic modulus E_y is not affected by the fibre crimp level or layer orientation.

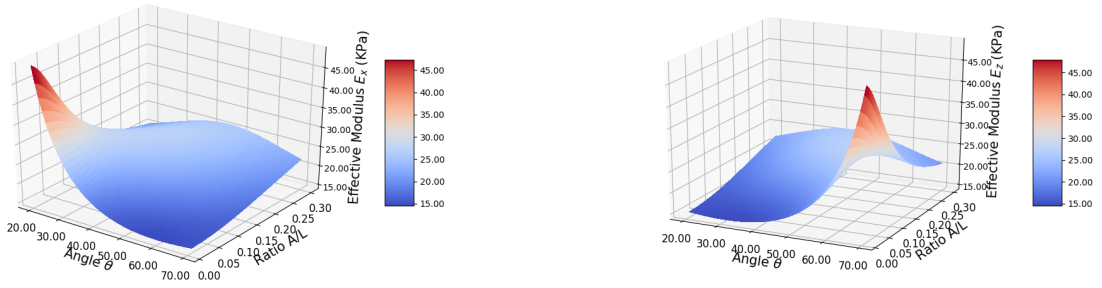

(a) (b)

Figure 2.12: Effective axial elastic modulus under load applied along (a) the x-axis and (b) the z-axis as a function of fibre crimp level and alternative layer orientation. Value settings for each parameter are $E_f = 100MPa$, $E_m = 10KPa$, $\nu_f = 0.3$, $\nu_m = 0.4$, and $V_f = 20\%$ (parameters taken in the physiological range).

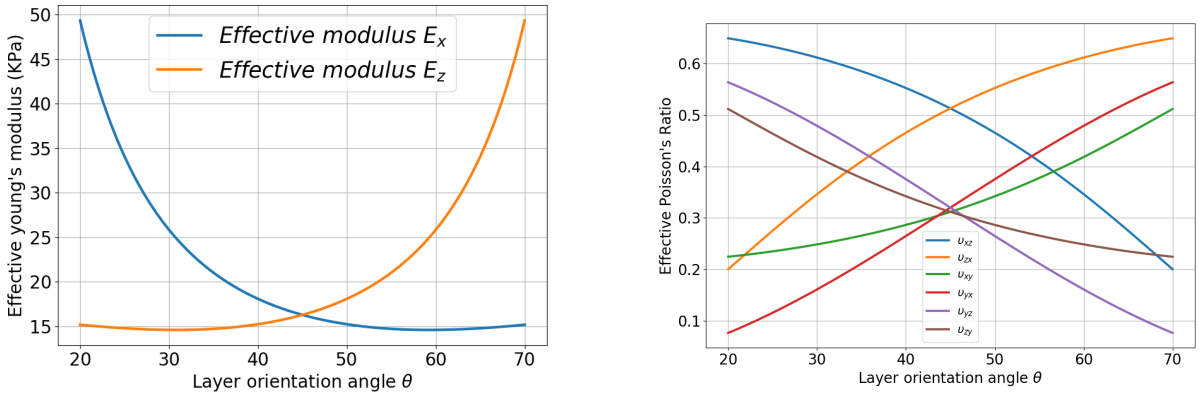

(a) (b)

Figure 2.13: Effects on axial elastic moduli when $\frac{A}{L}$ is set to 0.01. (a) Effective axial elastic moduli E_x and E_z versus layer orientation angle θ. (b) Effective Poisson's ratio ν_{ij} versus layer orientation angle θ in the physiological range of the annulus fibrosus. Value settings for each parameter are $E_f = 100MPa$, $E_m = 10KPa$, $\nu_f = 0.3$, $\nu_m = 0.4$, $\frac{A}{L} = 0.01$, and $V_f = 20\%$.

Figure 2.14 shows how the effective Poisson's ratio ν_{ij} varies with changes to fibre crimp level $\frac{A}{L}$ and layer orientation θ. We note that ν_{ij} represents the effective Poisson's ratio that characterizes the strain in the j direction produced by loading in the i direction, as mentioned above. Interestingly, due to the strongly anisotropic composites under study, all the $\nu_{ij}(i, j = x, y, z)$ appear different from each other. However, ν_{xy} and ν_{zy}, ν_{xz} and ν_{zx}, and ν_{yz} and ν_{yx} are symmetrical regardless of crimp level when $\theta = 45°$. This symmetrical feature can also

be verified in Figure 2.13b, which shows how ν_{ij} varies with changes to θ when $\frac{A}{L}$ is set to 0.01.

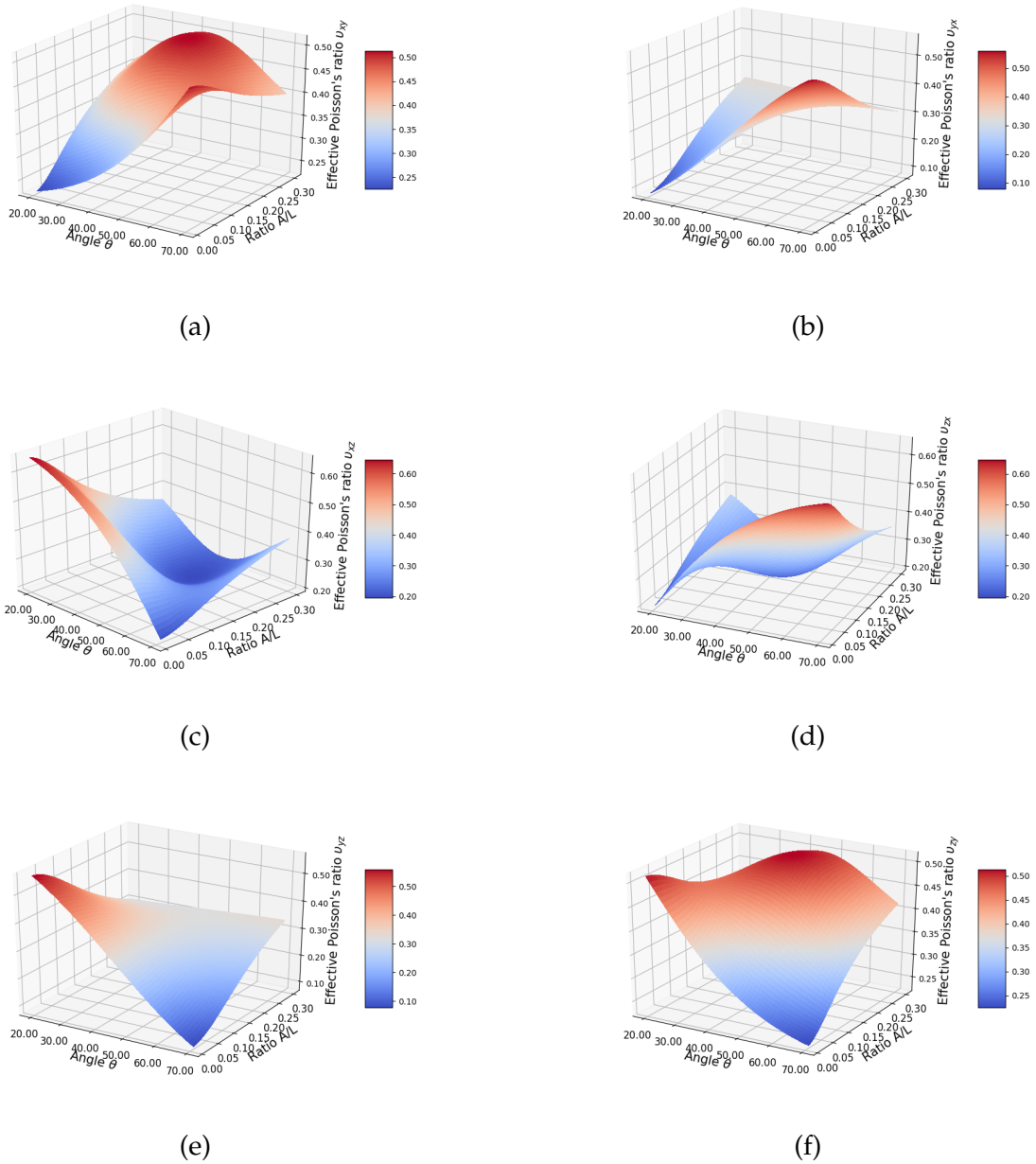

(a) (b) (c) (d) (e) (f)

Figure 2.14: Effective Poisson's ratio (a) ν_{xy}, (b) ν_{yx}, (c) ν_{xz}, (d) ν_{zx}, (e) ν_{yz} and (f) ν_{zy} with respect to different fibre crimp level and different layer orientation. Values setting of each parameter: $E_f = 100MPa$, $E_m = 10KPa$, $\nu_f = 0.3$, $\nu_m = 0.4$, $V_f = 20\%$ (Parameters in the physiological range).

2.7.1.2 Effect of fibre volume fraction and fibre crimp level

In order to test the effects of fibre volume fraction and fibre crimp level, we applied the following constraints to our model, setting the elastic modulus of fibres E_f to $100MPa$ and the elastic modulus of the matrix E_m to $10KPa$. The Poisson's ratios of fibre ν_f and matrix ν_m are set to 0.3 and 0.4, respectively. The layer orientation angle θ is set to 30°. With these parameters, the model is able to predict the axial effective elastic modulus and effective Poisson's ratio as a function of fibre crimp level in range of $0.01 < \frac{A}{L} < 0.3$ and fibre volume fraction in the range of $0.05 < V_f < 0.3$, as shown in Figures 2.15 and 2.16.

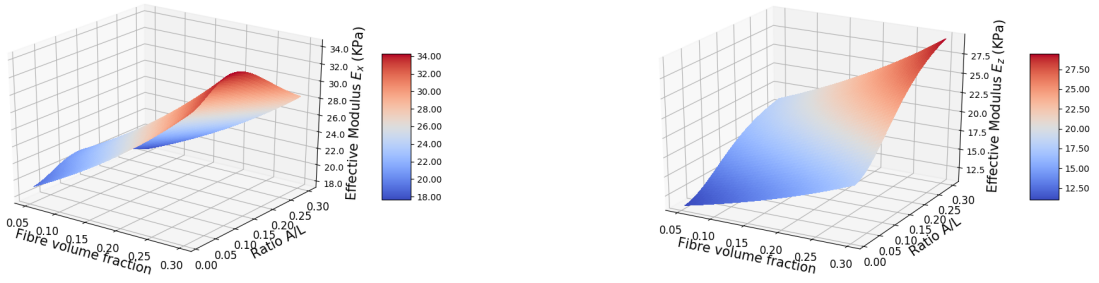

(a) (b)

Figure 2.15: Effective axial elastic modulus under load applied along (a) the x-axis, (b) the y-axis, and (c) the z-axis as a function of fibre crimp level and fibre volume fraction. The value settings for each parameter are $E_f = 100MPa$, $E_m = 10KPa$, $\nu_f = 0.3$, $\nu_m = 0.4$, and $\theta = 30^\circ$ (parameters in the physiological range).

Figure 2.15 shows how the axial elastic modulus varies with changes to fibre crimp level $\frac{A}{L}$ and fibre volume fraction V_f. Of the two, V_f has the greater impact on elastic modulus. E_x and E_z increase as V_f increases. E_y is not affected by $\frac{A}{L}$ according to Equations 2.92, 2.104, and 2.146. E_x increases at small crimp levels and then declines as $\frac{A}{L}$ increases, as shown in Figure 2.15a, and E_z gradually increases as $\frac{A}{L}$ increases from 0.01 to 0.3 as shown in Figure 2.15b when the V_f ranges from 0.05 to 0.3.

Figure 2.16 shows how the effective Poisson's ratio ν_{ij} varies with changes to $\frac{A}{L}$ and V_f. Fibre volume fraction V_f has little influence on effective Poisson's ratios ν_{ij}. When $\frac{A}{L}$ increases, ν_{xy} and ν_{yx} rise, but ν_{xz} and ν_{yz} decline. As $\frac{A}{L}$ increases, ν_{zx} first decreases and then increases, whereas ν_{zy} increases first and then decreases. It is noted that the maximum and the minimum values of each of the effective Poisson's ratios ν_{ij} are outside of the range of $0.3 - 0.4$ (range of the Poisson's ratio of the fibre and matrix). Also, the maximum value of the effective Poisson's ratio ν_{xz} is even higher than 0.5.

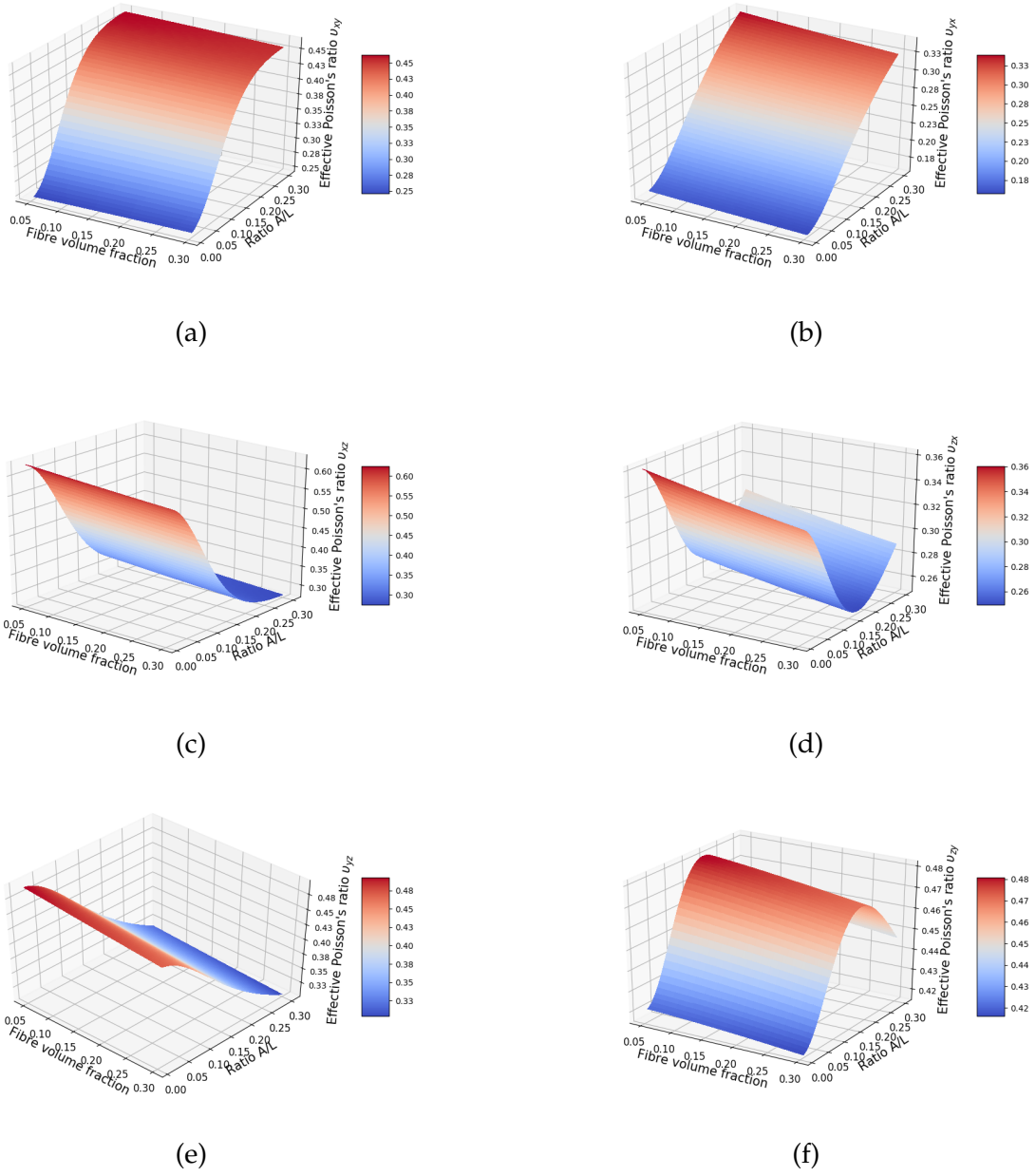

Figure 2.16: Effective Poisson's ratio (a) ν_{xy}, (b) ν_{yx}, (c) ν_{xz}, (d) ν_{zx}, (e) ν_{yz} and (f) ν_{zy} with respect to different fibre crimp level and different fibre volume fraction. Values setting of each parameter: $E_f = 100MPa$, $E_m = 10KPa$, $\nu_f = 0.3$, $\nu_m = 0.4$, $\theta = 30^\circ$ (Parameters in the physiological range).

2.7.1.3 Effect of matrix Poisson's ratio and fibre crimp level

In order to test the effects of matrix Poisson's ratio and fibre crimp level, we applied the following constraints to our model, setting the elastic modulus of fibres E_f to $100MPa$ and

the elastic modulus of the matrix E_m to $10KPa$. The Poisson's ratio of fibre ν_f is set to 0.3; the layer orientation angle θ is set to 30°; and the fibre volume fraction is set to 20%. With these parameters, the model is able to predict the axial effective elastic modulus and effective Poisson's ratio as a function of fibre crimp level ($0.01 < \frac{A}{L} < 0.3$) and matrix Poisson's ratio ($0.3 < \nu_m < 0.5$) as shown in Figures 2.17 and 2.18

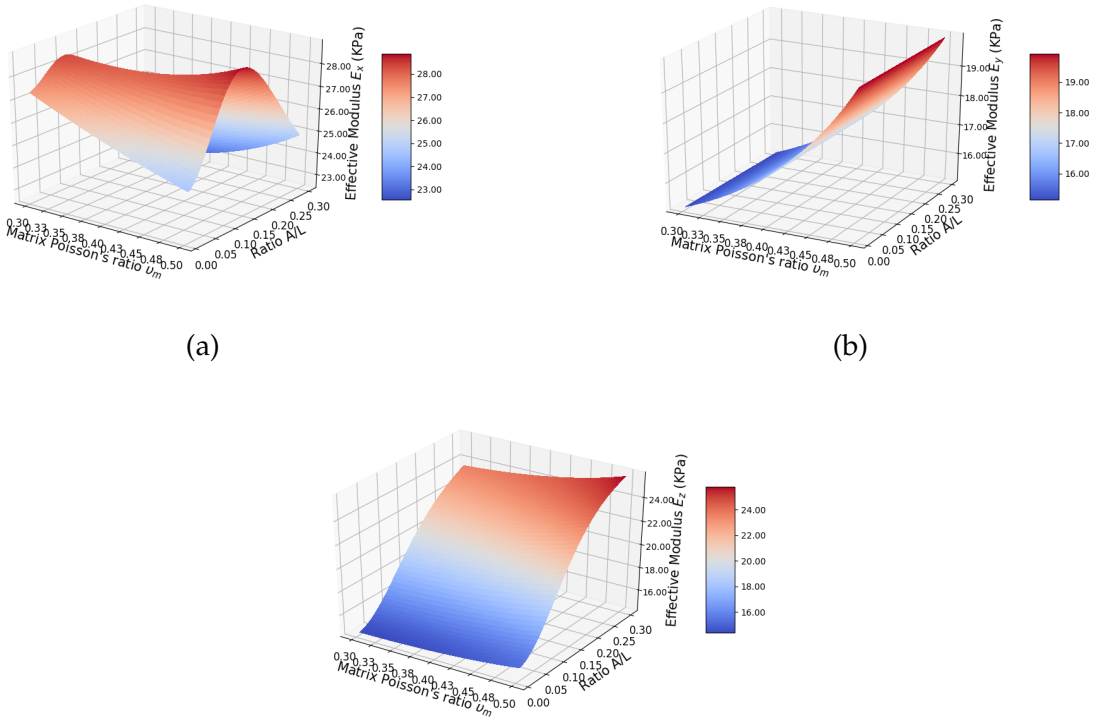

(a) (b)

(c)

Figure 2.17: Effective axial elastic modulus under load applied along (a) the x-axis, (b) the y-axis, and (c) the z-axis as a function of fibre crimp level and matrix Poisson's ratio. The value settings for each parameter are $E_f = 100MPa$, $E_m = 10KPa$, $\nu_f = 0.3$, $V_f = 20\%$, and $\theta = 30°$.

Figure 2.17 shows how axial elastic modulus varies with changes to fibre crimp level $\frac{A}{L}$ and matrix Poisson's ratio ν_m. E_y is not affected by $\frac{A}{L}$ and increases with increasing ν_m as shown in Figure 2.17b. E_z slightly increases as ν_m increases from 0.3 to 0.48, and rises gradually with increasing $\frac{A}{L}$ as shown in Figure 2.17c. E_x increases at small $\frac{A}{L}$ and then declines for large values of $\frac{A}{L}$. E_x decreases as ν_m increases for small values of $\frac{A}{L}$, but increases as ν_m increases for large values of $\frac{A}{L}$, as shown in Figure 2.17a.

Figure 2.18 shows how the effective Poisson's ratio ν_{ij} varies with changes to fibre crimp level $\frac{A}{L}$ and matrix Poisson's ratio ν_m. Each effective Poisson's ratio ν_{ij} increases with

increasing ν_m at all values of $\frac{A}{L}$ within the range tested. When $\frac{A}{L}$ increases, ν_{xy} and ν_{yx} rise, but ν_{xz} and ν_{yz} decline. As $\frac{A}{L}$ increases, ν_{zx} first decreases and then increases, whereas ν_{zy} increases first and then decreases. When $\nu_m = 0.5$, the effective Poisson's ratios ν_{xy}, ν_{xz}, ν_{yz} and ν_{zy} can be very high, with values of up to 0.75. We note that maximum values of ν_{xy} and ν_{yx} are obtained for highly crimped fibres ($\frac{A}{L} = 0.3$), whereas maximum values for ν_{xz} and ν_{yz} are obtained for only slightly corrugated fibres ($\frac{A}{L} = 0.01$). A maximum value for ν_{zy} is attained at a specific value of $\frac{A}{L} = 0.18$.

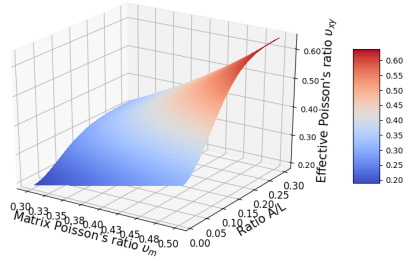

(a)

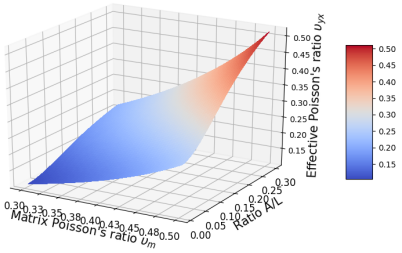

(b)

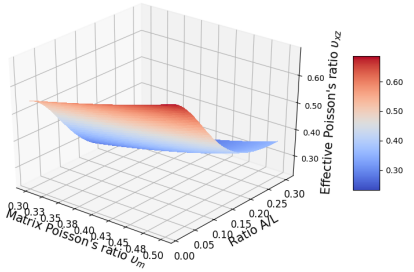

(c)

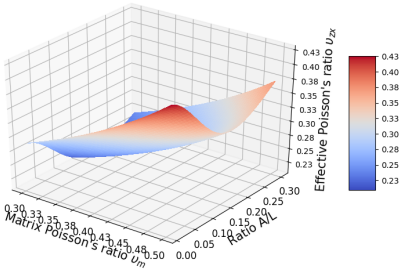

(d)

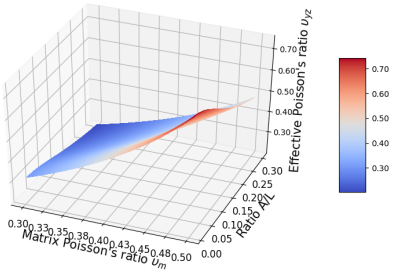

(e)

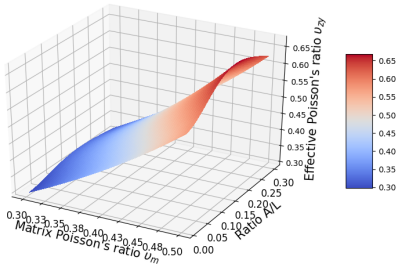

(f)

Figure 2.18: Effective Poisson's ratio (a) ν_{xy}, (b) ν_{yx}, (c) ν_{xz}, (d) ν_{zx}, (e) ν_{yz} and (f) ν_{zy} with respect to different fibre crimp level and different matrix Poisson's ratio. Values setting of each parameter: $E_f = 100MPa$, $E_m = 10KPa$, $\nu_f = 0.3$, $V_f = 20\%$, $\theta = 30°$.

2.7.1.4 Effect of fibre crimp level and elastic modulus ratio of the materials

The elastic modulus of the matrix E_m is set to $10KPa$. The Poisson's ratios of fibre ν_f and matrix ν_m are set to 0.3 and 0.4, respectively. The layer orientation angle θ is set to 30° and the fibre volume fraction is set to 20%. The parameters predict the axial effective elastic modulus and effective Poisson's ratio as a function of fibre crimp level in the range of $0.01 < \frac{A}{L} < 0.3$ and elastic modulus ratios of the fibre and matrix in the range $10^1 < \frac{E_f}{E_m} < 10^5$, as shown in Figure 2.19 and 2.20.

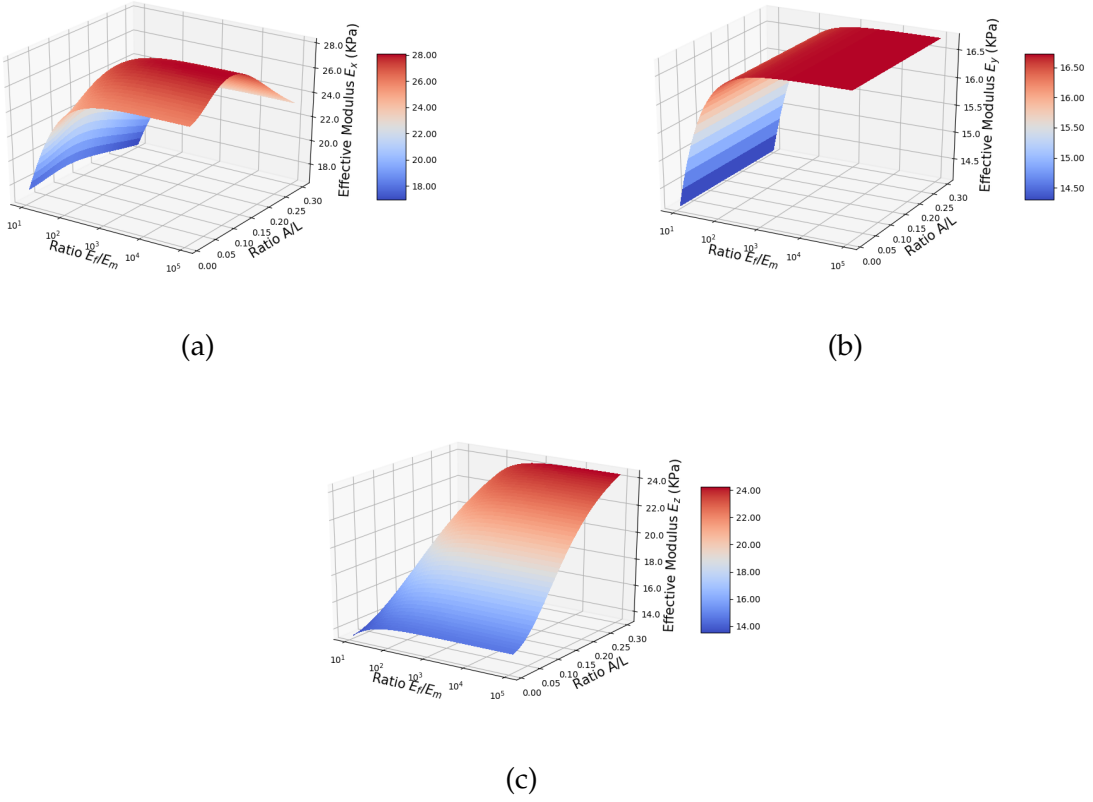

Figure 2.19: Effective axial elastic modulus under load applied along (a) the x-axis, (b) y-axis, and (c) z-axis as a function of fibre crimp level and elastic modulus ratio. The value settings for each parameter are $E_m = 10KPa$, $\nu_f = 0.3$, $\nu_m = 0.4$, $V_f = 20\%$, and $\theta = 30°$.

Figure 2.19 shows how axial elastic modulus varies with changes to fibre crimp level $\frac{A}{L}$ and elastic modulus ratio of the fibre and matrix $\frac{E_f}{E_m}$. We note that the logarithm values of $\frac{E_f}{E_m}$ were used to draw the figure. E_y is not affected by $\frac{A}{L}$. As $\frac{E_f}{E_m}$ rises, E_y increases significantly when $\frac{E_f}{E_m}$ is less than about 10^2, but the behavior of E_y changes slightly when $\frac{E_f}{E_m}$ is greater than 10^2, as shown in Figure 2.19b. E_z rises gradually with increasing $\frac{A}{L}$ and $\frac{E_f}{E_m}$, as shown in Figure 2.19c. E_x increases at small $\frac{A}{L}$ and then declines at larger $\frac{A}{L}$, and increases significantly

with increasing $\frac{E_f}{E_m}$ until about $\frac{E_f}{E_m} = 10^2$ at all levels of $\frac{A}{L}$ in the range tested as shown in Figure 2.19c.

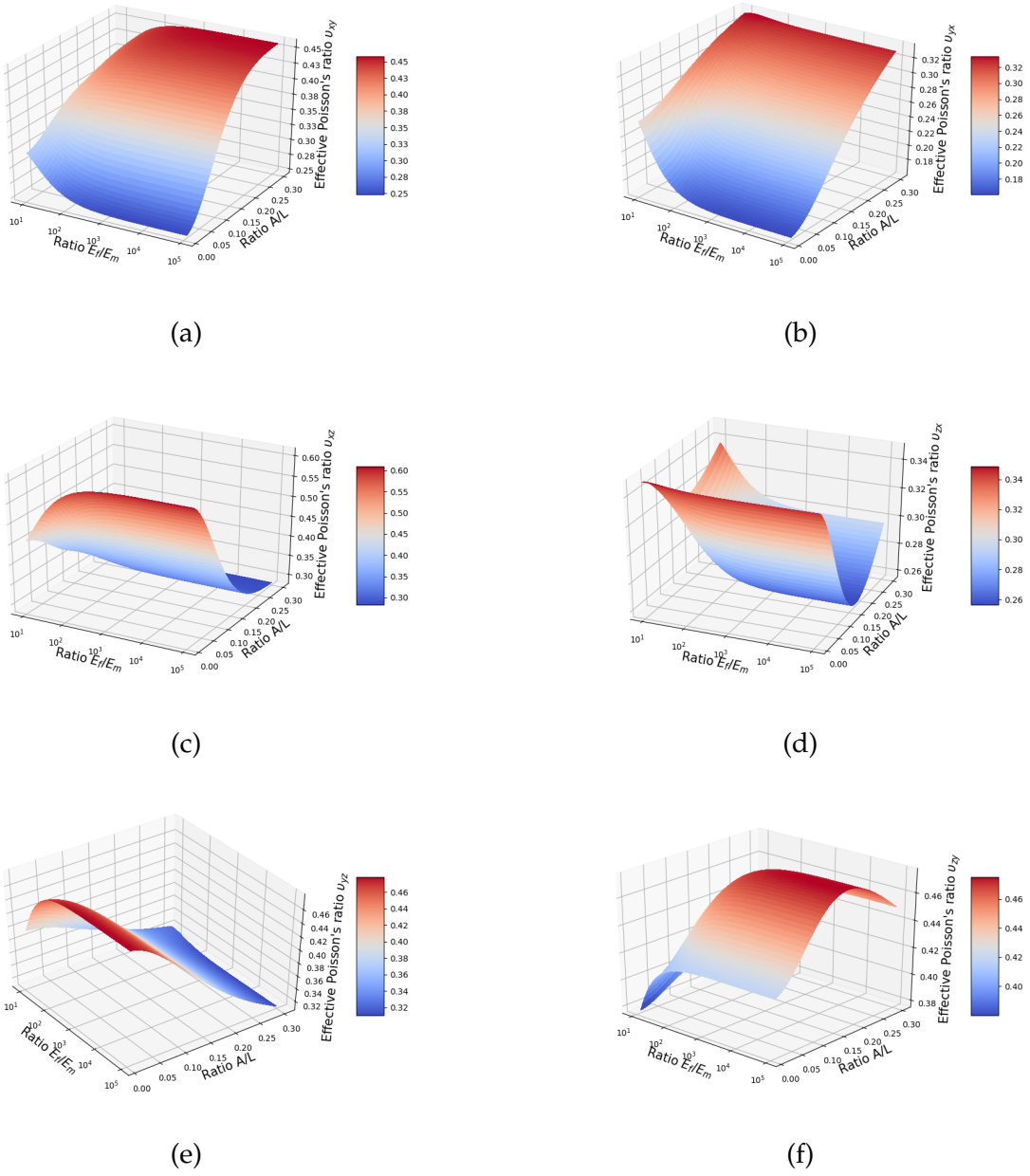

Figure 2.20: Effective Poisson's ratios (a) ν_{xy}, (b) ν_{yx}, (c) ν_{xz}, (d) ν_{zx}, (e) ν_{yz}, and (f) ν_{zy} as a function of fibre crimp level and elastic modulus ratio. The values settings for each parameter are $E_m = 10KPa$, $\nu_f = 0.3$, $\nu_m = 0.4$, $V_f = 20\%$, and $\theta = 30^\circ$.

Figure 2.20 shows how effective Poisson's ratio ν_{ij} varies with changes to fibre crimp level $\frac{A}{L}$ and elastic modulus ratio $\frac{E_f}{E_m}$. Changes in $\frac{E_f}{E_m}$ above and beyond about 10^2 have little

effect on effective Poisson's ratios ν_{ij}. However, when $\frac{E_f}{E_m} < 10^2$, as $\frac{E_f}{E_m}$ rises, ν_{xy}, ν_{yx}, and ν_{zx} decrease, and ν_{xz}, ν_{yz}, and ν_{zy} increase. As $\frac{A}{L}$ increases, $\nu_x y$ and ν_{yx} rise, and ν_{xz} and ν_{yz} decline. As $\frac{A}{L}$ increases, ν_{zx} first decreases and then increases, whereas ν_{zy} increases first and then decreases.

2.7.2 Double layers

2.7.2.1 Effect of fibre crimp level and layer orientation

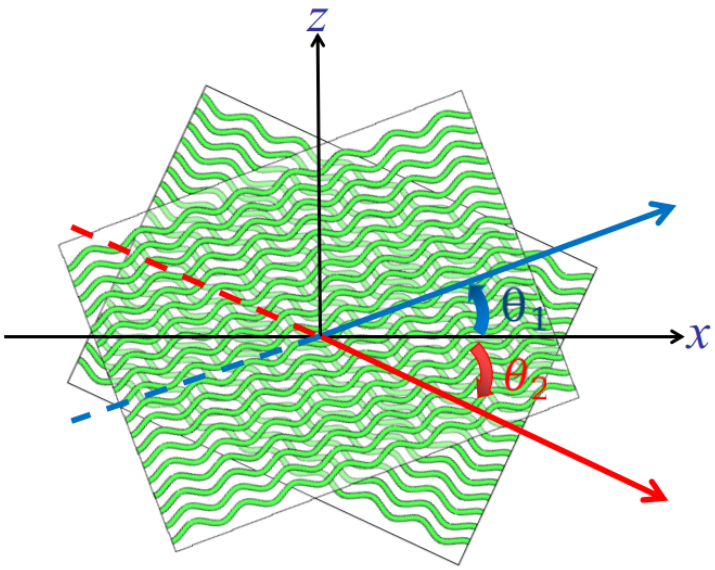

Figure 2.21: Double-layer laminate within the Cartesian coordinate system. The first and second layers are orientated by θ_1 and θ_2 around the y-axis with respect to the x-axis, respectively.

In order to test the effects of fibre crimp level and layer orientation for double layers, we applied the following constraints to our model. In this analysis, the number of layers r is set to 2, both layers have the same thickness of 0.5 mm ($e_1 = e_2$), and the orientation of the first and second layers is symmetrical either side of the x-axis, which means $\theta_1 = -\theta_2$. The elastic modulus of the fibres E_f is set to $100MPa$, the elastic modulus of the matrix E_m is set to $10KPa$, and the fibre volume fraction V_f is 20%. The Poisson's ratio of fibre ν_f and matrix ν_m are set to 0.3 and 0.4, respectively. These parameters predict the axial effective elastic modulus and effective Poisson's ratio as a function of fibre crimp level over the range $0.01 < \frac{A}{L} < 0.3$ and layer orientation angle in the range $20° < \theta_1 < 70°$ (and therefore -20° $< \theta_2 <$ -70°), as shown in Figures 2.22 and 2.23. The orientation angle of the two layers with respect to the x-axis, θ_1 and θ_2, and the reference coordinate system are represented in Figure 2.21.

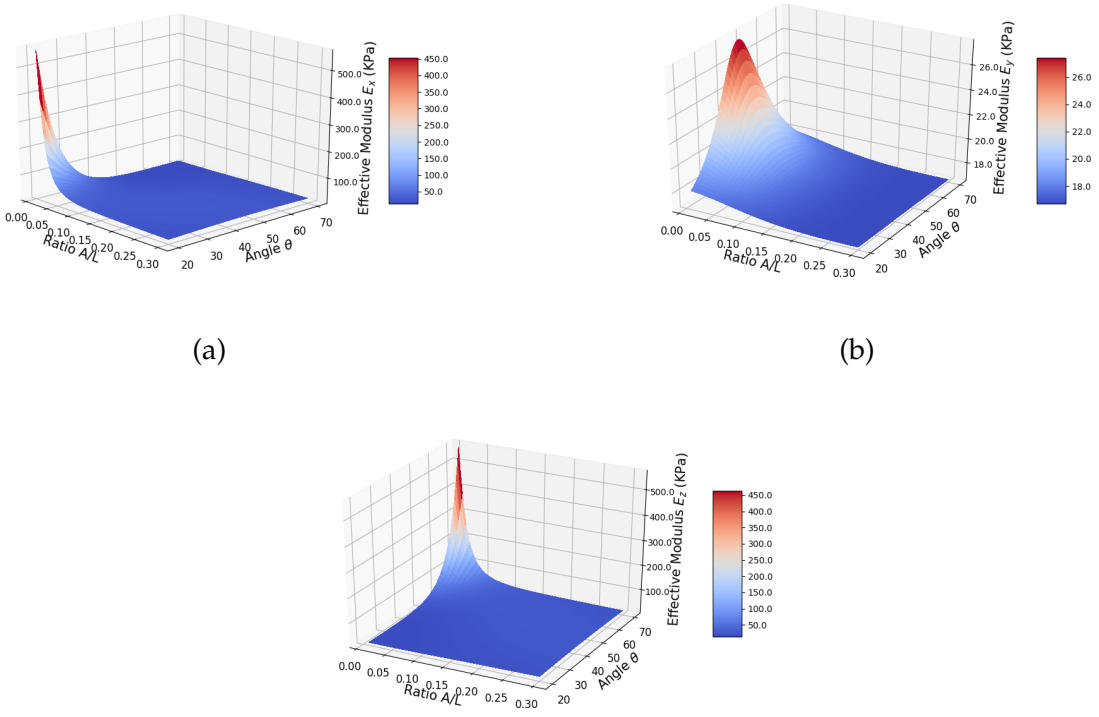

Figure 2.22: Effective axial elastic modulus under load applied along (a) the x-axis, (b) y-axis, and (c) z-axis as a function of fibre crimp level and relative orientation of the two layers. Values setting of each parameter: $r = 2$, $e_1 = e_2 = 0.5mm$, $E_f = 100Mpa$, $E_m = 10KPa$, $\nu_f = 0.3$, $\nu_m = 0.4$, $V_f = 20\%$, and $\theta_1 = -\theta_2$.

Figure 2.22 shows that, for the double layer arranged symmetrically on the x-axis, the axial elastic modulus is jointly influenced by the fibre crimp level $\frac{A}{L}$ and layer orientation angle θ. We note that the logarithm values of E_x, E_y, and E_z are used to draw the figure. Similar to the observation for the analysis of a single layer in section 2.7.1.1, the effective elastic modulus E_x has a maximum value when $\frac{A}{L}$ and θ decrease simultaneously; the effective elastic modulus E_z has a maximum value when $\frac{A}{L}$ is small and θ is large; and the effective elastic moduli E_x and E_z are symmetrical at each fibre crimp level when $\theta = 45°$. However, unlike the observations in section 2.7.1.1, the maximum values of E_x and E_z are much higher than for single-layer situation, and E_y is significantly affected by relative layer orientation when $\frac{A}{L}$ is small. Also, E_y increases as θ increases until 45° after which it declines.

Figure 2.23 shows how the effective Poisson's ratio ν_{ij} varies with changes to fibre crimp level $\frac{A}{L}$ and layer orientation θ for the two layers arranged symmetrically on the x-axis.

The change of each ν_{if} is similar to that observed in section 2.7.1.1, ν_{xy} and ν_{zy}, ν_{xz} and ν_{zx}, and ν_{yz} and ν_{yx} are symmetrical at all values of $\frac{A}{L}$ in the range tested when θ = 45°. Interestingly, when $\frac{A}{L}$ is small, ν_{xy}, ν_{yx}, ν_{yz}, and ν_{zy} have negative values. As $\frac{A}{L}$ increases, the negative Poisson's ratio gradually disappears, and over the range of $\frac{A}{L}$= 0.01 - 0.3, ν_{ij} is never negative.

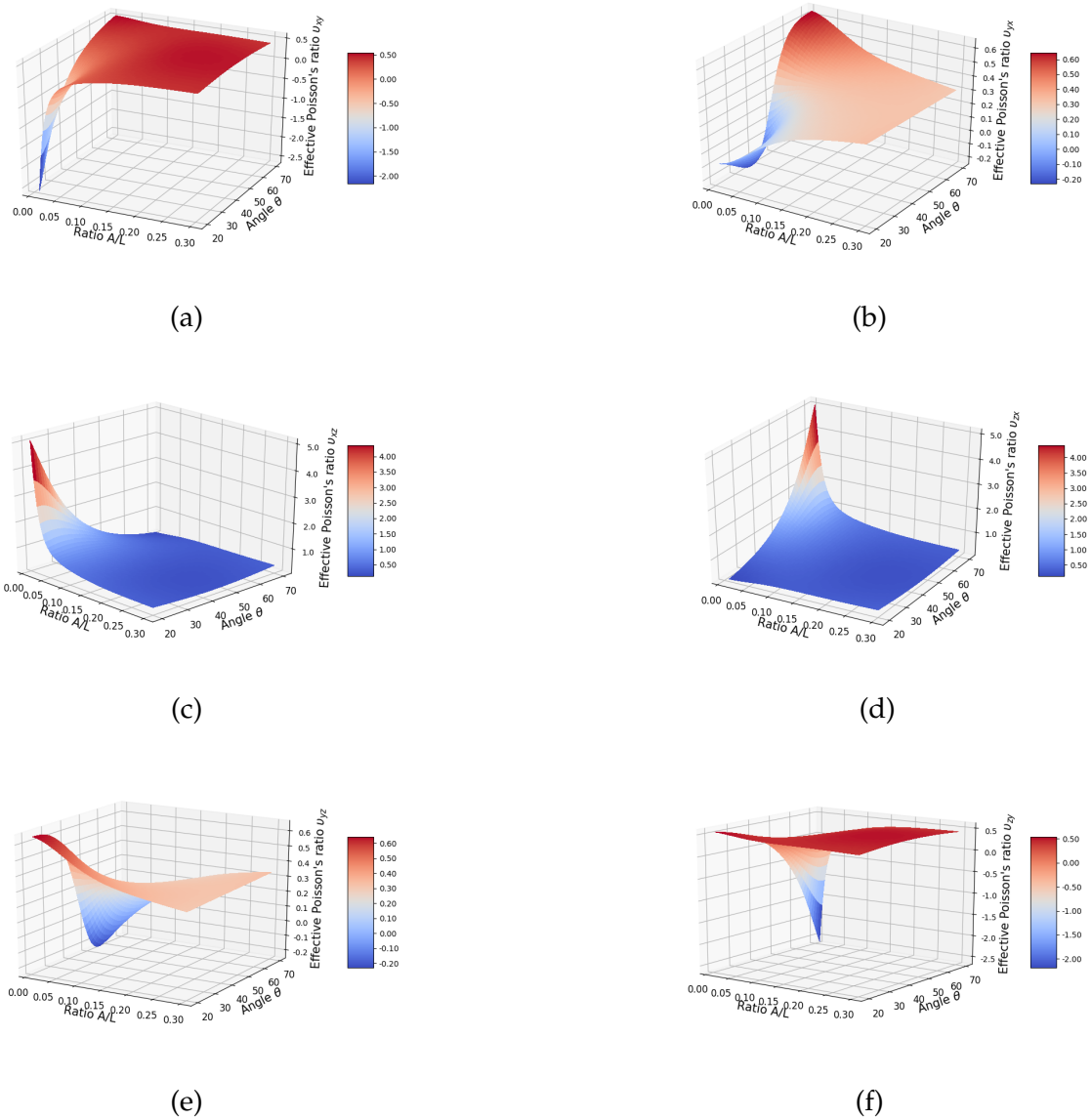

(a) (b)

(c) (d)

(e) (f)

Figure 2.23: Effective Poisson's ratio (a) ν_{xy}, (b) ν_{yx}, (c) ν_{xz}, (d) ν_{zx}, (e) ν_{yz} and (f) ν_{zy} with respect to different fibre crimp level and different layer orientation for double layers. Values setting of each parameter: $r = 2$, $e_1 = e_2 = 0.5mm$, $E_f = 100Mpa$, $E_m = 10KPa$, $\nu_f = 0.3$, $\nu_m = 0.4$, $V_f = 20\%$, $\theta_1 = -\theta_2$.

2.7.2.2 Effect of layer thickness and fibre crimp level

In order to test the effects of layer thickness and fibre crimp level, we applied the following constraints to our model. The elastic modulus of fibres E_f is set to $100MPa$, the elastic modulus of the matrix E_m is set to $10KPa$, and the fibre volume fraction V_f is 20%. The Poisson's ratio of fibre ν_f and matrix ν_m are set to 0.3 and 0.4, respectively. The number of layers r is set to 2. The thickness of the first layer is set to 0.3 mm and that of the second layer is set to range from 0.1 to 0.6 mm (parameters in the physiological range). The orientation angles of the first layer θ_1 and second layer θ_2 with respect to the x-axis are equal and opposite and are set to 30° and -30°, respectively; the two layers are alligned at an angle of 60° and have a line of symmetry in the x-axis. With these parameters, the model is able to predict the axial effective elastic modulus and effective Poisson's ratio as a function of fibre crimp level in the range $0.01 < \frac{A}{L} < 0.3$ and layer-thickness ratio over the range of $0.33 < \frac{e_2}{e_1} < 2.0$, as shown in Figures 2.24 and 2.25.

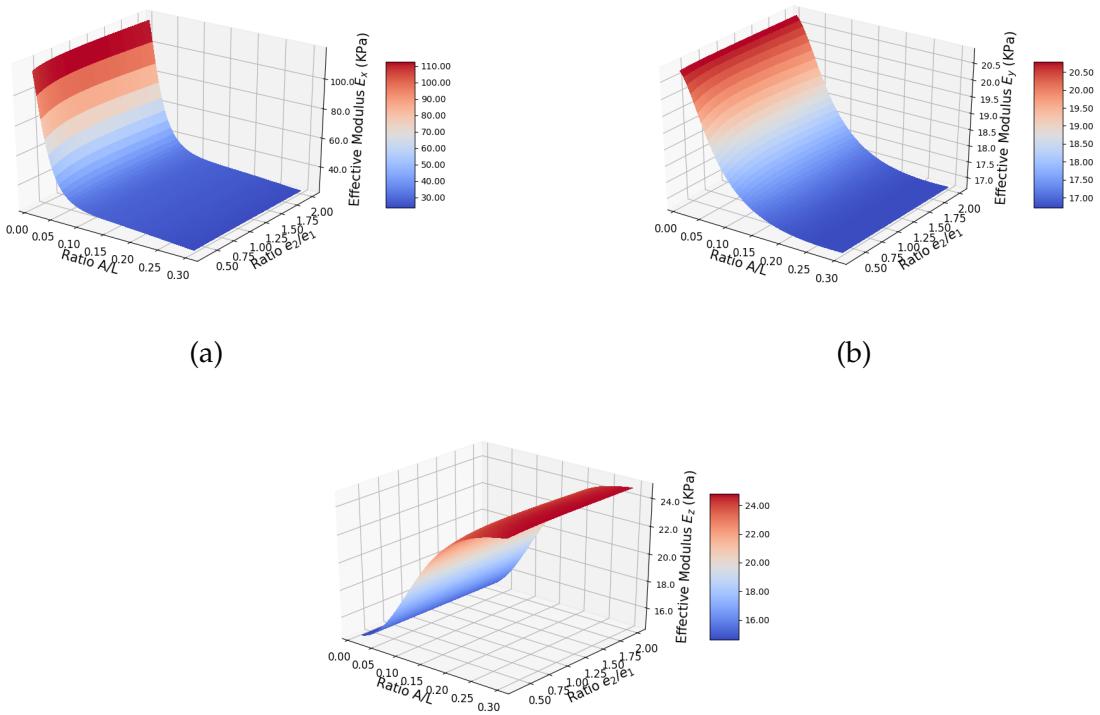

Figure 2.24: Effective axial elastic modulus under load applied along (a) the x-axis, (b) y-axis, and (z) z-axis as a function of fibre crimp level and layer-thickness ratio between two layers. The value settings for each parameter are $r = 2$, $E_f = 100Mpa$, $E_m = 10KPa$, $\nu_f = 0.3$, $\nu_m = 0.4$, $V_f = 20\%$, $e_1 = 0.3mm$, and $\theta_1 = -\theta_2 = 30°$.

Figure 2.24 shows how the axial elastic modulus varies with changes to $\frac{A}{L}$ and $\frac{e_2}{e_1}$ for the two layers alligned at an angle of 60 degrees with respect to one another. E_x, E_y, and E_z are less affected by $\frac{e_2}{e_1}$ and as $\frac{A}{L}$ increases, E_x and E_y decline but E_z increases.

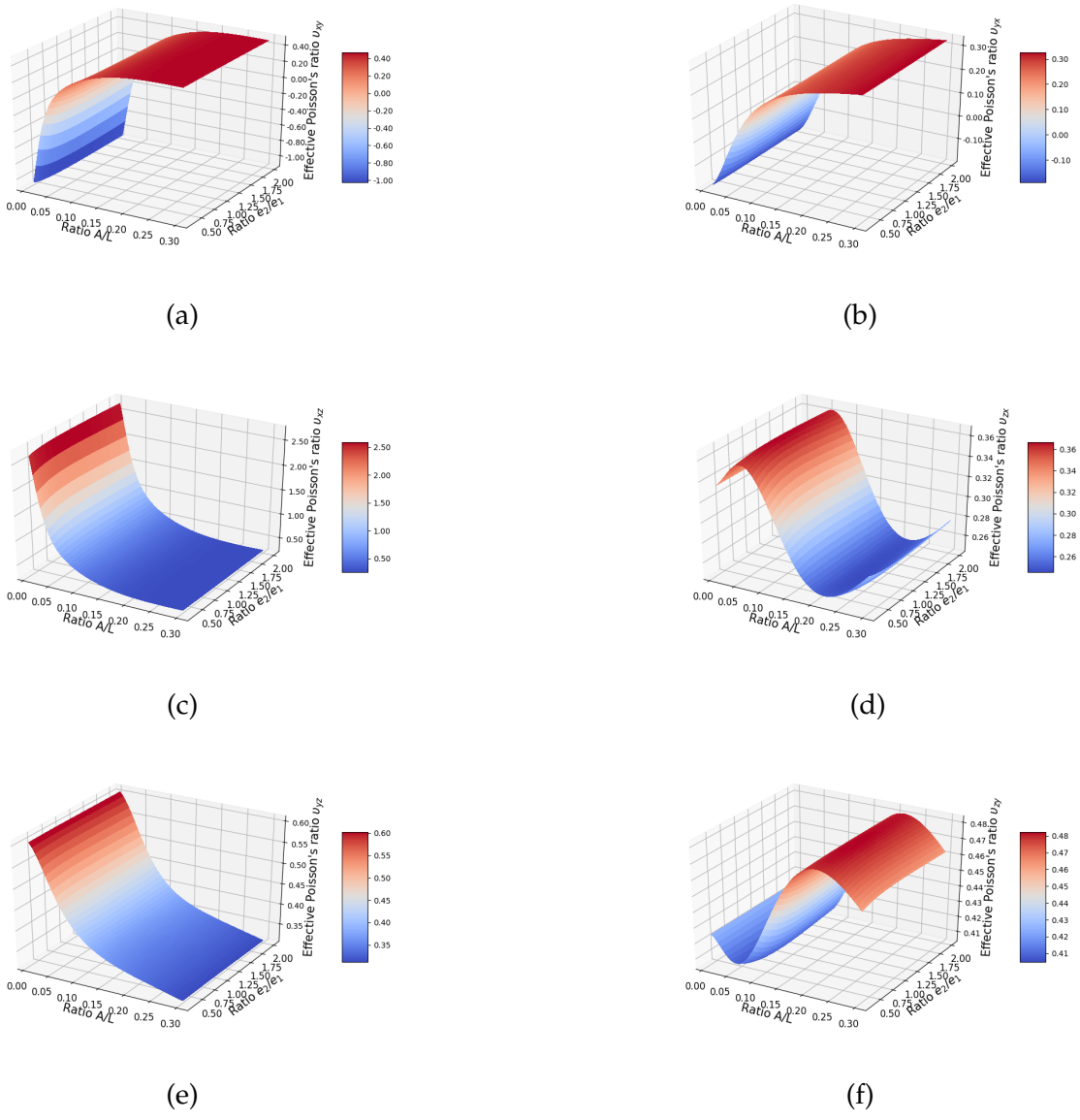

Figure 2.25: Effective Poisson's ratio (a) ν_{xy}, (b) ν_{yx}, (c) ν_{xz}, (d) ν_{zx}, (e) ν_{yz} and (f) ν_{zy} with respect to different fibre crimp level and different layer thickness ratio for double layers. Values setting of each parameter: $r = 2$, $E_f = 100Mpa$, $E_m = 10KPa$, $\nu_f = 0.3$, $\nu_m = 0.4$, $V_f = 20\%$, $e_1 = 0.3mm$, $\theta_1 = -\theta_2 = 30^\circ$.

Figure 2.25 shows how ν_{ij} varies with changes to $\frac{A}{L}$ and $\frac{e_2}{e_1}$ for the two layers arranged symmetrically on either side of the x-axis. The layer-thickness ratio $\frac{e_2}{e_1}$ has little effect on ν_{ij}.

When $\frac{A}{L}$ increases, ν_{xy} and ν_{yx} rise, but ν_{xz} and ν_{yz} decline. As $\frac{e_2}{e_1}$ increases in the range from 0.01 to 0.3, ν_{zx} first increases, then decreases, and then increases again slightly, whereas ν_{zy} first decreases, then increases, and then slightly decreases again.

2.7.2.3 Effect of fibre crimp level and elastic modulus ratio of the materials

In order to test the effects of fibre crimp level and elastic modulus ratio of the materials, we applied the following constraints to our model. The elastic modulus of the matrix E_m is set to $10KPa$, and the fibre volume fraction V_f is 20%. The Poisson's ratio of fibre ν_f and matrix ν_m are set to 0.3 and 0.4, respectively. The number of layers r is set to 2 and both layers have the same thickness of 0.5 mm ($e_1 = e_2$). The orientation angles of the first layer θ_1 and second layer θ_2 are as above, in section 2.7.2.2, and are symmetrical about the x-axis. With these parameters, the model is able to predict the axial effective elastic modulus and effective Poisson's ratio as a function of fibre crimp level ($0.01 < \frac{A}{L} < 0.3$) and elastic modulus ratio of the fibre and matrix ($10^1 < \frac{E_f}{E_m} < 10^5$), as shown in Figure 2.26 and 2.27.

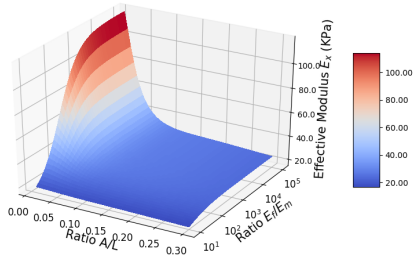

(a)

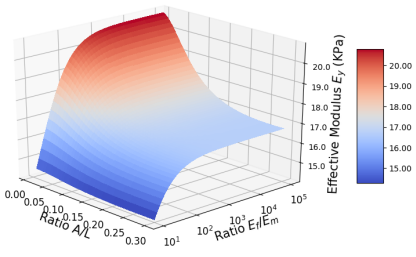

(b)

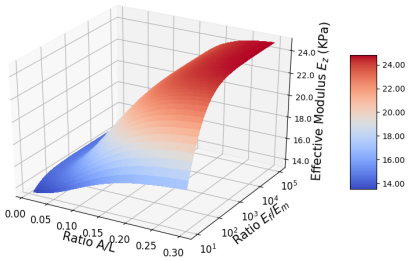

(c)

Figure 2.26: Effective axial elastic modulus under load applied along (a) the x-axis (b), y-axis, and (d) z-axis as a function of fibre crimp level and elastic modulus ratio. The value settings of each parameter are $r = 2$, $E_m = 10KPa$, $\nu_f = 0.3$, $\nu_m = 0.4$, $V_f = 20\%$, $e_1 = e_2 = 0.5mm$, and $\theta_1 = -\theta_2 = 30°$.

Figure 2.26 shows how axial elastic modulus varies with changes to fibre crimp level $\frac{A}{L}$ and elastic modulus ratio of the fibre and matrix $\frac{E_f}{E_m}$. Here, E_x, E_y, and E_z increase significantly as $\frac{E_f}{E_m}$ rises until 10^3, but their behaviour changes slightly when $\frac{E_f}{E_m}$ is greater than 10^3. As $\frac{A}{L}$ increases, E_x and E_y decline, but E_z increases.

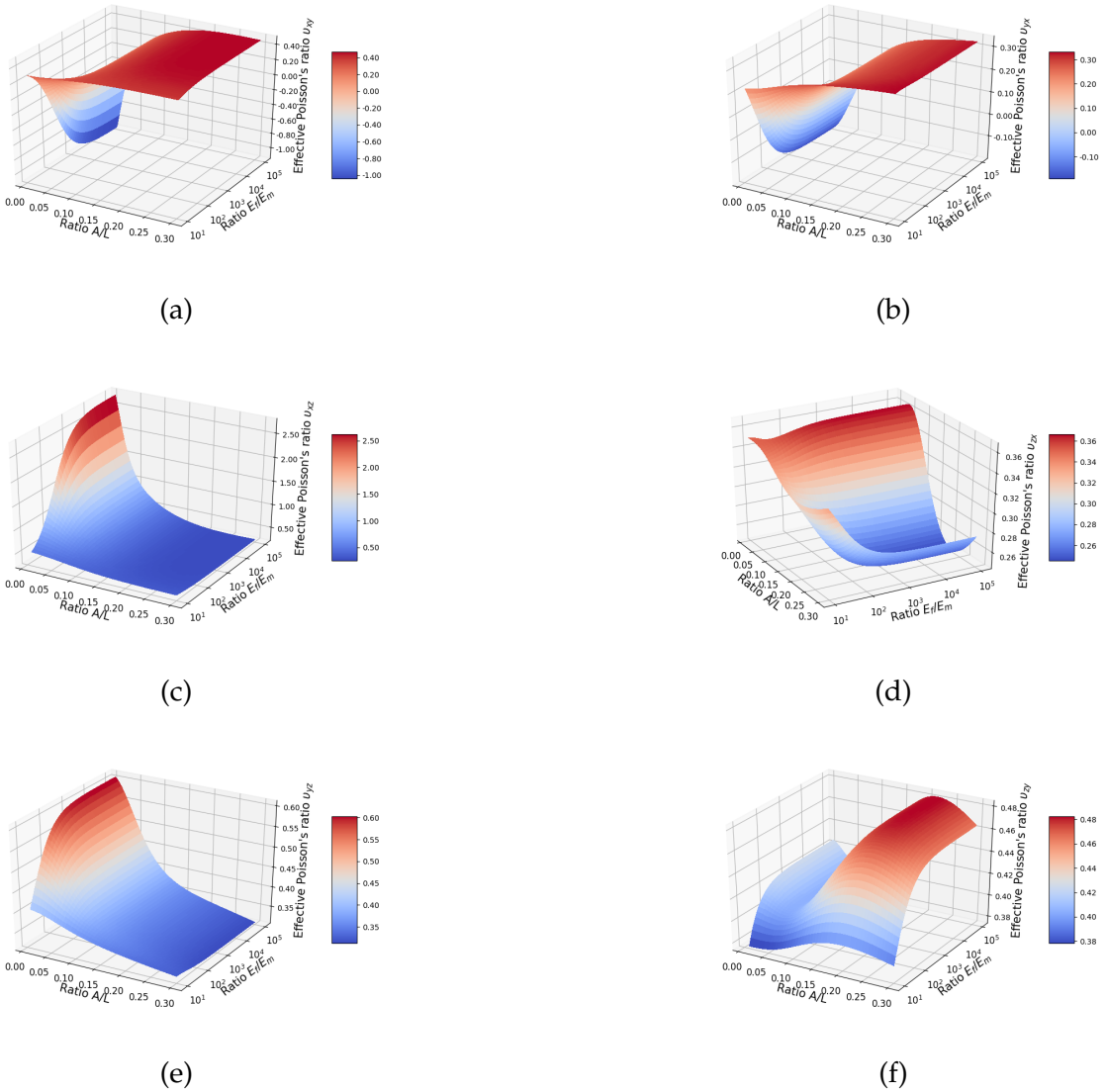

Figure 2.27: Effective Poisson's ratio (a) ν_{xy}, (b) ν_{yx}, (c) ν_{xz}, (d) ν_{zx}, (e) ν_{yz} and (f) ν_{zy} with respect to different fibre crimp level and different elastic modulus ratios. Values setting of each parameter: $r = 2$, $E_m = 10KPa$, $\nu_f = 0.3$, $\nu_m = 0.4$, $V_f = 20\%$, $e_1 = e_2 = 0.5mm$, $\theta_1 = -\theta_2 = 30°$.

Figure 2.27 shows how the effective Poisson's ratios ν_{ij} vary with changes to fibre crimp level $\frac{A}{L}$ and elastic modulus ratio $\frac{E_f}{E_m}$. When $\frac{E_f}{E_m} > 10^3$, $\frac{E_f}{E_m}$ has little impact on effective

Poisson's ratios ν_{ij}. However, when $\frac{E_f}{E_m} < 10^3$, as $\frac{E_f}{E_m}$ rises, ν_{xy}, ν_{yx} and ν_{zx} decrease, and ν_{xz}, ν_{yz}, and ν_{zy} increase. As $\frac{A}{L}$ increases, $\nu_x y$ and ν_{yx} rise, and ν_{xz} and ν_{yz} decline. As $\frac{A}{L}$ increases, ν_{zx} first decreases and then increases, whereas ν_{zy} increases first and then decreases.

2.7.2.4 Effect of layer orientation symmetry

The relative orientation of the successive layers of the AF changes from the inner layer closest to the nucleus pulposus to the outer layer, as reported by *Marcolongo et al.* [2017] and *Baldit* [2018]. Therefore, there should be asymmetrically arranged layers in the AF as a whole. In this analysis, we study the effect of layer orientation symmetry on the axial elastic modulus of our model AF by changing the respective orientation of the layers. The elastic modulus of fibres E_f is set to $100MPa$, elastic modulus of the matrix E_m is set to be $10KPa$, and the fibre volume fraction V_f is 20%. The Poisson's ratio of fibre ν_f and matrix ν_m are set to 0.3 and 0.4, respectively, and the fibre crimp level $\frac{A}{L}$ is set to 0.1. The number of layers r is set to 2, and they have the same thickness of 0.5 mm ($e_1 = e_2$). The orientation angles of the first layer θ_1 are set to -20°, -30°, -45°, -60° and -70° in separate test runs. These parameters predict the axial effective elastic modulus and effective Poisson's ratio as a function of θ_2 in the range from 20° to 70° as shown in Figures 2.28 and 2.29.

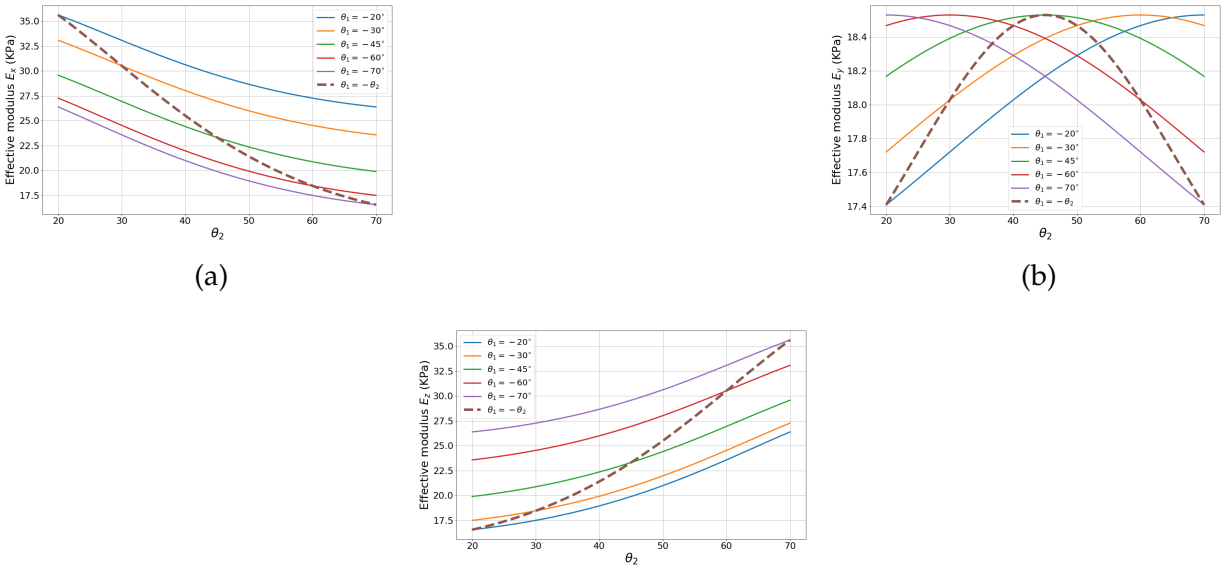

(a) (b)

(c)

Figure 2.28: Effective axial elastic modulus under load applied along (a) the x-axis, (b) y-axis, and (c) z-axis as a function of relative layer orientation in a two-layer model. The value settings for each parameter are $r = 2$, $E_f = 100MPa$, $E_m = 10KPa$, $\nu_f = 0.3$, $\nu_m = 0.4$, $V_f = 20\%$, $e_1 = e_2 = 0.5mm$, and $\frac{A}{L} = 0.1$.

Figure 2.28 shows how the axial elastic modulus varies with changes to the orientation angle of the second layer θ_2 with respect to the x-axis for different values of θ_1. The first layer angle θ_1 is set to -20°, -30°, -45°, -60°, -70° and -θ_2, providing six different cases to analyze. For each case, as $|\theta_1|$ and $|\theta_2|$ increase, E_x decreases and E_z increases, and when $|\theta_1| + |\theta_2| = 90°$, E_y reaches its maximum value.

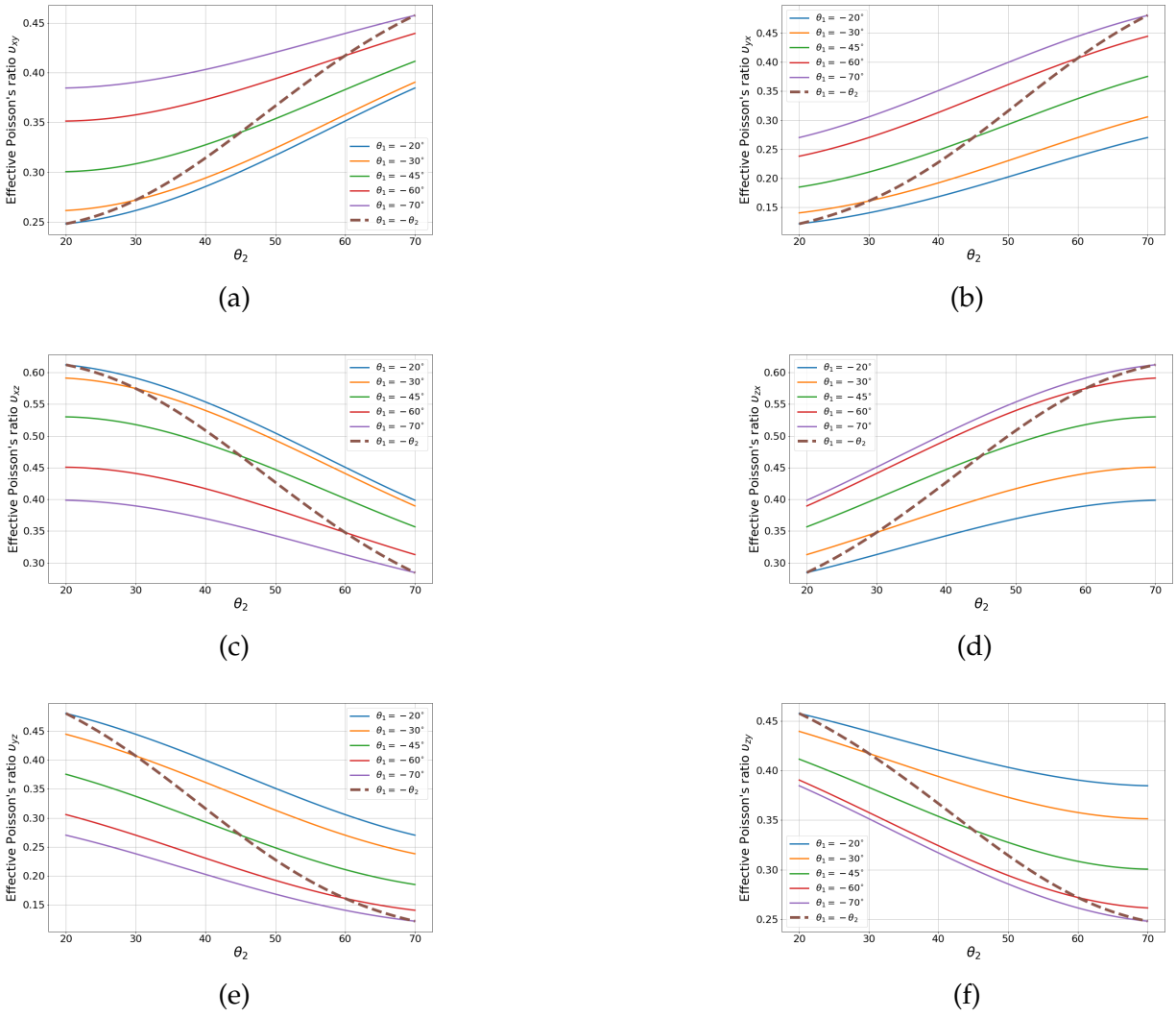

Figure 2.29: Effective Poisson's ratios (a) ν_{xy}, (b) ν_{yx}, (c) ν_{xz}, (d) ν_{zx}, (e) ν_{yz}, and (f) ν_{zy} as a function of relative layer orientation for a two-layer model. The value settings for each parameter are $r = 2$, $E_f = 100MPa$, $E_m = 10KPa$, $\nu_f = 0.3$, $\nu_m = 0.4$, $V_f = 20\%$, $e_1 = e_2 = 0.5mm$, and $\frac{A}{L} = 0.1$.

Figure 2.29 shows how the effective Poisson's ratios ν_{ij} vary with changes to the orientation angle of the second layer θ_2 with respect to the x-axis for different values of θ_1. As $|\theta_1|$ and $|\theta_2|$ increase, ν_{xy}, ν_{yx}, and ν_{zy} increase, and ν_{xz}, ν_{yz}, and ν_{zy} decrease. Compared

with the impact of layer orientation angle θ presented in section 2.7.2.1, where the two layers are always symmetrically oriented with respect to the x-axis, the asymmetry has less of an impact on the Poisson's ratios.

2.7.3 Multiple layers

In this analysis, we study the effective mechanical properties of a composite model with ten layers ($r = 10$) as a function of the relative orientation of the successive layers and fibre crimp level; a laminate schematic diagram and the coordinate system are shown in Figure 2.30 and the layer orientation angle settings are shown in Table 2.2. We note that the properties of the ten-layer symmetrically arranged laminate with the constant angle between successive layers are exactly the same as those of the two-layer laminate, and can be obtained by calculation. The different angle settings are based on the nature of AF, in which the relative orientation of successive layers varies from the inner layer closest to the nucleus to the outer layer. In cases 1 and 2, the average orientation angle of 10 layers is $|40°|$, and in case 1, a wider range of orientation angles is tested. In case 3, the orientation angle is set at a constant 40° between successive layers $|\theta_k|$ =40°, (k = 1, 2, 3 $\cdots$). The thickness of each layer is set to 0.5 mm. The elastic modulus of fibres E_f is set to $100MPa$, the elastic modulus of the matrix E_m is set to $10KPa$, and the fibre volume fraction V_f is set to 20%. The Poisson's ratio of fibre ν_f and matrix ν_m are set to 0.3 and 0.4, respectively. These parameters predict the axial effective elastic modulus and effective Poisson's ratio as a function of the relative orientation of the successive layers as well as fibre crimp level in the range $0.01 < \frac{A}{L} < 0.3$, as shown in Figures 2.31 and 2.32.

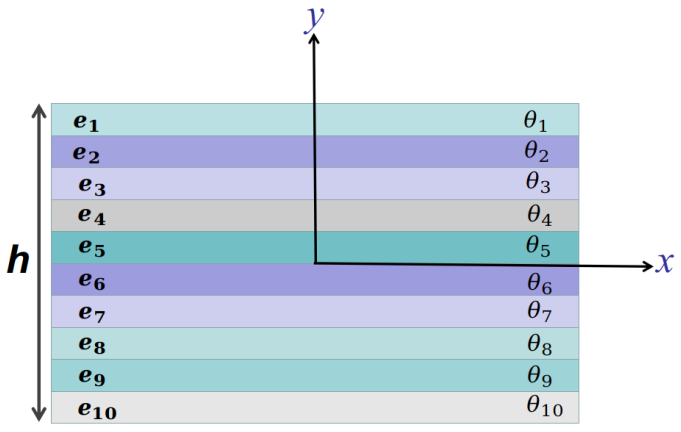

Figure 2.30: Schema of multi-layer laminate, showing the reference coordinate system. h represents the total thickness of the laminate, θ_k (k = 1,2,3 $\cdots$) is the orientated angle around the y-axis with respect to the x-axis for the kth layer and e_k is the thickness of the kth lamella.

Layer number	θ_1	θ_2	θ_3	θ_4	θ_5	θ_6	θ_7	θ_8	θ_9	θ_{10}
Case 1	20°	-20°	30°	-30°	40°	-40°	50°	-50°	60°	-60°
Case 2	30°	-30°	35°	-35°	40°	-40°	45°	-45°	50°	-50°
Case 3	40°	-40°	40°	-40°	40°	-40°	40°	-40°	40°	-40°

Table 2.2: Layer orientation angle settings for each of the ten lamellae of the model. Three cases are studied.

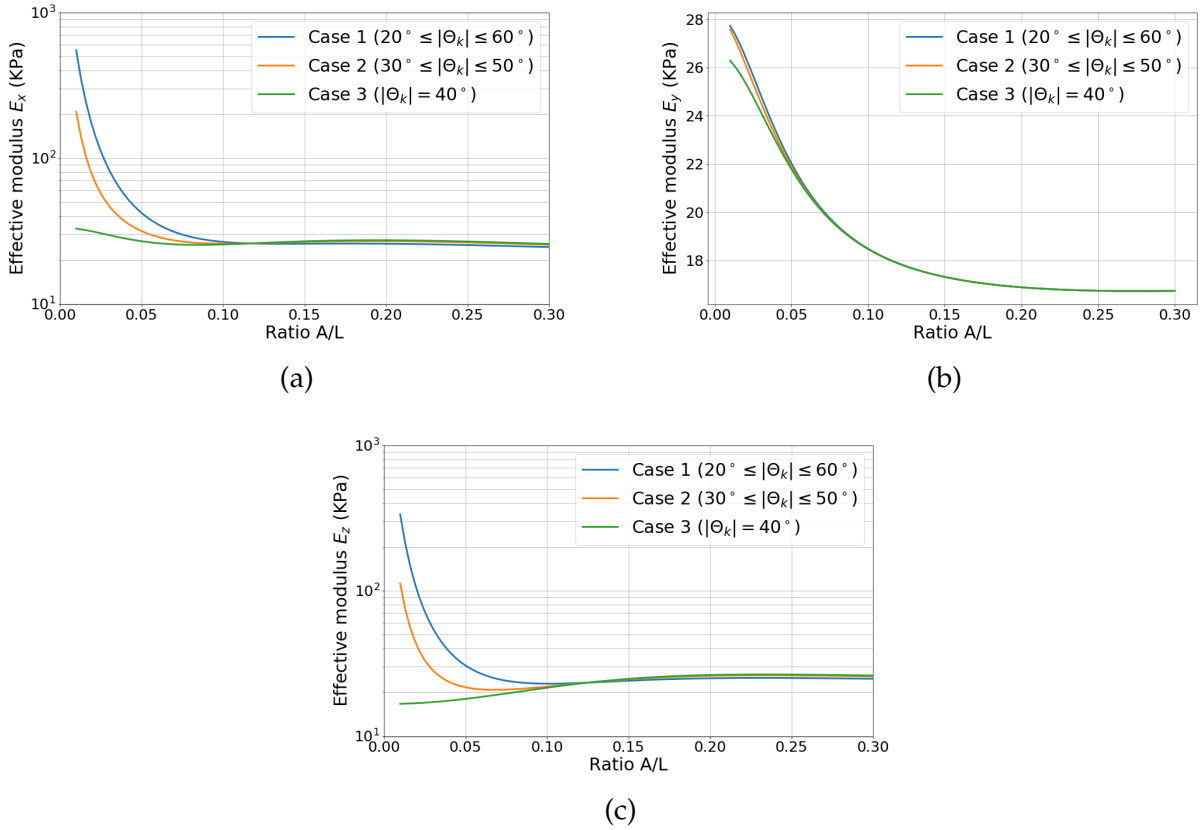

Figure 2.31: Effective axial elastic modulus of a ten-layer laminate model under load applied along (a) the x-axis, (b) the y-axis, and (c) the z-axis as a function of fibre crimp level and relative orientation of the successive layers. The value settings for the fixed parameters are $r = 10$, $E_f = 100MPa$, $E_m = 10KPa$, $\nu_f = 0.3$, $\nu_m = 0.4$, $V_f = 20\%$, and $e_k = 0.5mm$.

Figure 2.31 shows how the axial elastic modulus varies with changes to fibre crimp level $\frac{A}{L}$ throughout the laminate and orientation angle between each of its ten layers (or no change as in case 3). Each effective elastic modulus changes significantly when $\frac{A}{L} < 0.1$, and as $\frac{A}{L}$ increases, each effective elastic modulus gradually stabilizes. The values of E_x and E_z differ significantly between cases 1, 2, and 3 when $\frac{A}{L} < 0.1$, but when $\frac{A}{L} > 0.1$, E_x and E_z stabilize in all three cases at about the same value. The values of E_y and its behavior

with increasing $\frac{A}{L}$ are very similar in all three cases. Interestingly, the values of E_x, E_y and E_z for case 2 are always in between those of cases 1 and 3, which shows that even if the average orientation angle between successive layers is the same for all cases, the larger the range of layer orientation angles in the laminate, the larger the difference between the global effective modulus and the constantly oriented case (the constant oriented angle is the average oriented angle in the other cases) modulus.

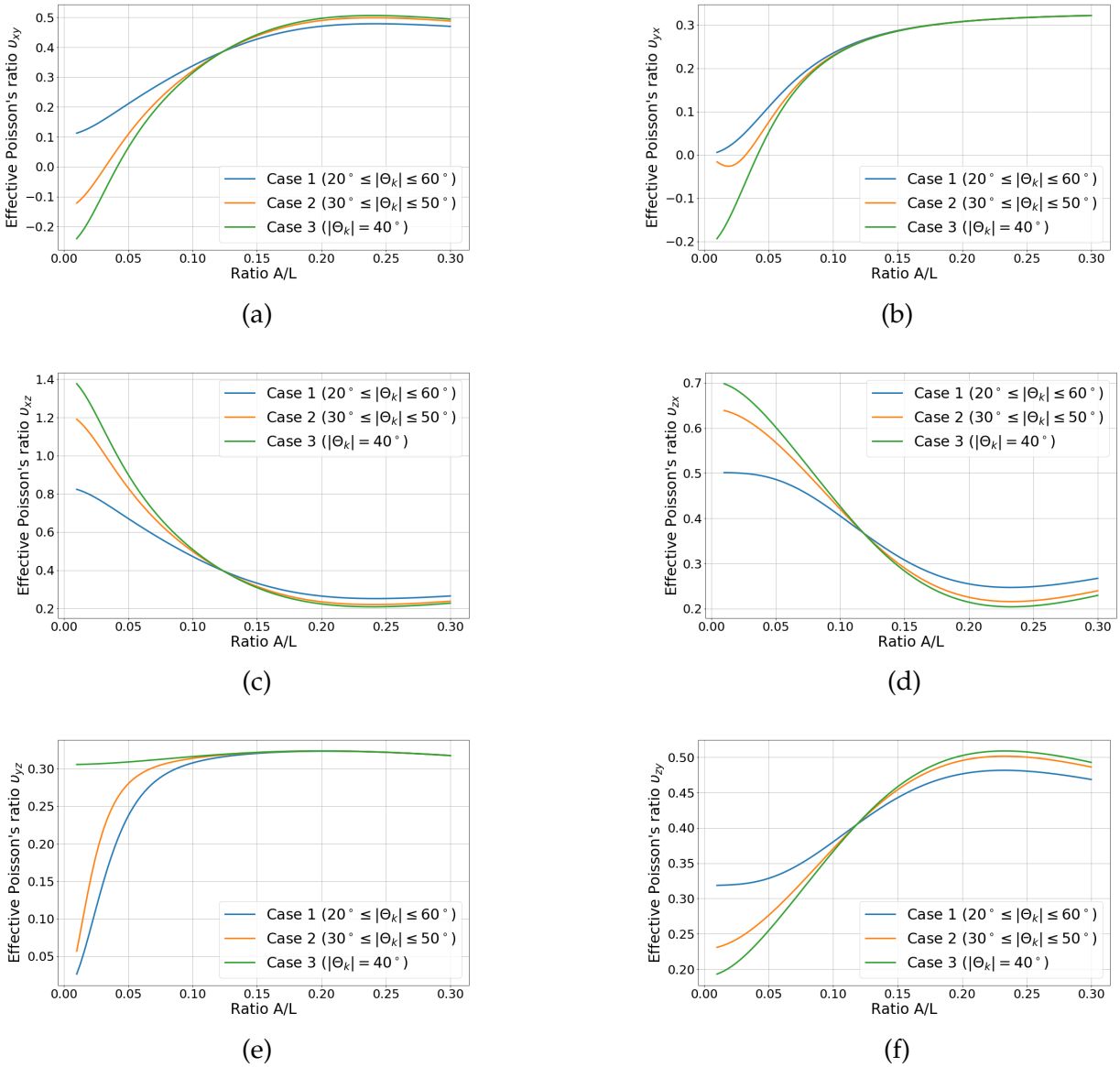

Figure 2.32: Effective Poisson's ratios (a) ν_{xy}, (b) ν_{yx}, (c) ν_{xz}, (d) ν_{zx}, (e) ν_{yz}, and (f) ν_{zy} for a ten-layer laminate model as a function of fibre crimp level and relative orientation of the successive layers of the laminate model. The value settings for the parameters are $r = 10$, $E_f = 100MPa$, $E_m = 10KPa$, $\nu_f = 0.3$, $\nu_m = 0.4$, $V_f = 20\%$, $e_k = 0.5mm$.

Figure 2.32 shows how the effective Poisson's ratios ν_{ij} of a ten-layer laminate model vary with changes to the fibre crimp level $\frac{A}{L}$ in the laminate as a whole and changes to orientation angle between each of its ten successive layers (or no change as in case 3). The behavior of the Poisson's ratios in cases 1 and 2 is the same as that of case 3 where the orientation angle between successive layers is constant. Each effective ν_{ij} value in case 2 is always between the values of cases 1 and 3 at each increment in $\frac{A}{L}$, which indicates that the trend seen for the Poisson's ratios is the same as that seen for the effective elastic modulus: the larger the range of layer orientation angles in the laminate, the larger the difference between the global effective Poisson's ratio and the average case Poisson's ratio.

2.8 Discussion

In this chapter, we use an analytical micromechanical model to study the effective mechanical properties of the lamellar composite structure of annulus fibrosus tissue, with a focus on the roles of the orientation angle between the parellel fibres of successive lamellae and the corrugation, or crimp level, of those fibres. The lamellar structure of composite has been studied by *Remund et al.* [2011] and *Zhou et al.* [2020], for example, but the collagen-fibre crimp level was not considered in those studies.

For a single-layer composite, when the value of crimp level $\frac{A}{L}$ is small ($\frac{A}{L} < 0.1$), it has a large influence on E_x and E_z but has no effect on E_y, and all of the Poisson's ratios ν_{ij} are affected by $\frac{A}{L}$. The orientation angle between successive layers θ affects E_x and E_z as well as each ν_{ij}. In addition, ν_{xy} and ν_{zy}, ν_{xz} and ν_{zx}, ν_{yz} and ν_{yx}, and E_x and E_z are symmetrical if $\theta = 45^\circ$. The fibre volume fraction V_f has little influence on ν_{ij} but does impact on the effective elastic modulus. Moreover, the Poisson's ratio of the matrix ν_m influences each ν_{ij} but has little impact on the effective elastic modulus. Interestingly, each effective elastic modulus and ν_{ij} change significantly with changing elastic modulus ratio of fibre and matrix $\frac{E_f}{E_m}$ only when $\frac{E_f}{E_m} < 10^2$.

For a two-layer laminate, as opposed to the single-layer case, θ and $\frac{A}{L}$ both influence E_y. In addition, the range of ν_{ij} is significantly expanded: the minimum value is even negative and the maximum value is close to 5. The ratio of the thickness of the first layer to that of the second, that is, the layer thickness ratio $\frac{e_2}{e_1}$, has little effect on both effective elastic modulus and ν_{ij}. The same trends are seen for the two-layer laminate as for the single-layer case: each effective elastic modulus and ν_{ij} change significantly only when $\frac{E_f}{E_m} < 10^3$. Compared with the impact of layer orientation angle θ, the asymmetry of the layer orientation either side of the x-axis, as shown in Figure 2.21, has less impact on the Poisson's ratio. Testing the effects of incrementally increasing the relative orientation angle of the successive layers of a

ten-layer laminate from one end to the other and within different ranges on both effective elastic modulus and ν_{ij}, we observe that the size of the range impacts on the global effective mechanical behavior, causing it to deviate from that of a laminate with a constant orientation angle between the fibres of one layer and those of the next. Further, the larger the range, the larger difference between the global effective mechanical properties of the laminate and those of the laminate with constant orientation angle.

It is known that, for isotropic solids, the Poisson's ratio is in general smaller than 0.5, but the Poisson's ratio in certain microstructures of the composites under study can be significantly larger than 0.5, as shown in Figures 2.14 and 2.23. This is because of the effects of corrugated fibres and alternately oriented layer. In section 2.7.2.1, negative Poisson's ratios are observed in a two-layer laminate when the fibre crimp level $\frac{A}{L}$ is small, which is not found in the single-layer laminate in section 2.7.1.1. Materials with negative Poisson's ratios, also known as auxetic materials, show unusual and counterintuitive mechanical behaviour, namely they become thicker perpendicular to the loading direction. The negative Poisson's ratios are seen in the x-y and y-z planes but not in the x-z plane. Such a situation might be caused by a specific fibre–matrix stiffness ratio and fibre dispersion. As fibres are considered slightly corrugated when $\frac{A}{L}$ is small, when the dispersed fibres are stretched, the fibre-matrix stiffness ratio causes the matrix between the fibres to be compressed, which can lead to expansion in the x-y and y-z planes. Similar observations were reported by *Herakovich* [1984] and *Sun and Li* [1988] based on analytical analysis, and by *Volokh* [2017] and *Fereidoonnezhad et al.* [2020] based on numerical simulation tests, and by *Baldit et al.* [2014], *Dusfour et al.* [2020], and *Derrouiche et al.* [2019a] based on tensile experiments on AF. Larger negative maximum Poisson's ratios are observed in Figures 2.23a and 2.23f, which is likely due to the larger fibre–matrix stiffness ratio ($\frac{E_f}{E_m} = 10^4$) compared to that reported in *Herakovich* [1984] and *Sun and Li* [1988]. As $\frac{A}{L}$ increases, the negative Poisson's ratios gradually disappear, that is to say, one of the mechanical effects of the corrugated fibres in the microstructure of the laminate model studied here is to reduce its auxetic behavior. In conclusion, because of the fibre-matrix stiffness ratio and fibre dispersion, the laminate composite shows an auxetic behavior in the planes perpendicular to the plane of the lamellae. However, this behavior is not easily constrained because of the joint influence of fibre crimp level and successive layer orientation.

The proposed micromechanical model can be used to quickly estimate the mechanical properties of alternately oriented laminates embedded with crimped fibres using theoretical calculations only, and can easily be used to analyze the influence of each of the parameters discussed above on the effective mechanical properties of the modeled material. The modulus of fibre E_f and matrix E_m, the Poisson's ratios of fibre ν_f and matrix ν_m, volume fraction of the fibres V_f and matrix V_m, fibre crimp level $\frac{A}{L}$, relative orientation angle of

successive layers θ_k, layer thickness e_k, and total number of layers r are taken into account as parameters potentially modifying the mechanical properties of the laminate studied here. The model described has been designed to mimic and therefore study the morphological aspects of AF but the approaches and techniques employed are also applicable to other fibre-reinforced biological tissues and biocomposites.

The stress-strain curve of AF tissue is usually J-shaped (*Vergari et al.* [2017]) and the collagen fibres reorient in response to load (*Cassidy et al.* [1989]; *Marchand and Ahmed* [1990]; *Ambard and Cherblanc* [2009]). However, the present study is limited to testing the effects of the weak strain of the laminate material, which is considered a linear behavior, and the effects of reorientation of the crimped fibres while the modeled tissue is stretching are not taken into account. As mentioned in section 1.1.2, cross-links are found between crimped fibres at a smaller scale, and these are also not taken into account in the proposed model. It is also noted that the *Mori and Tanaka* [1973] Eshelby equivalent inclusion method provides the best estimates when the fibre volume fractions are relatively low (below 60%) (*Kwon and Dharan* [1995]; *Ju and Yanase* [2010]; *Saadat et al.* [2015]). The fibre volume fraction of AF tissue is estimated to range from 5% to 24.5%, as shown in Table 2.1. Therefore, we consider the Eshelby method to be suitable for use in conjunction with the proposed AF model, but for other applications, the limits of fibre volume fraction should be reconsidered and an alternative method for estimation of fibre volume fraction may be needed. Furthermore, in our model, the strain experienced by each layer along the x-axis and z-axis is assumed to be equal to the global strain on the multi-layer laminate along the x-axis and z-axis, respectively, and the stress on each layer along the y-axis is assumed to be the same as the global stress acting along the y-axis, as shown in Equation 2.118, but no accepted methods exist at present to verify these assumptions for AF tissue. Moreover, the fibres and matrix are assumed to have perfect interface conditions, but the true nature of these conditions has not yet been determined for AF tissue.

CHAPTER 3

Study of soft tissues with helical fibre structure

3.1 Introduction

As introduced in chapter 1, many soft tissues, such as aortic wall [*Niestrawska et al.*, 2016], [*Morin et al.*, 2019] and tendon [*Verzár*, 1964], [*Evans and Barbenel*, 1975], [*Liao*, 2003], [*Harvey et al.*, 2010], are found to incorporate a microstructure of helical collagen fibres, as shown in Figure 3.1. Cross-links are also widely observed between the collagen fibres ([*Giudici et al.*, 2020] [*Pezowicz et al.*, 2005]) and the impact of these features on the mechanical performance of a bottom-up spring-node model of collagen *Chen et al.* [2017] has been explored.

Considering that helical structures exist in soft tissue, here we present a numerical study of their effects on the mechanical properties of a soft-tissue model using a double-scale asymptotic homogenization method. We model soft tissue here as a composite material of a matrix reinforced with helical fibres. We assume a perfect bind between the matrix and the embedded fibres. We consider a periodic arrangement of helical fibres, with or without cross-links and with or without matrix, with the aim being to investigate their specific implication on the overall mechanical properties of the composite tissue. To this end, we first present the asymptotic homogenization theory and numerical implementation method in section 3.2, which can also be found in *Vasquez-villegas* [2022]. We then present our study of the properties of composite reinforced with helical fibres, helical fibres with cross-links alone, and composite reinforced with helical fibres with cross-links in sections 3.3, 3.4, and 3.5, respectively. Finally, we discuss our results in section 3.6.

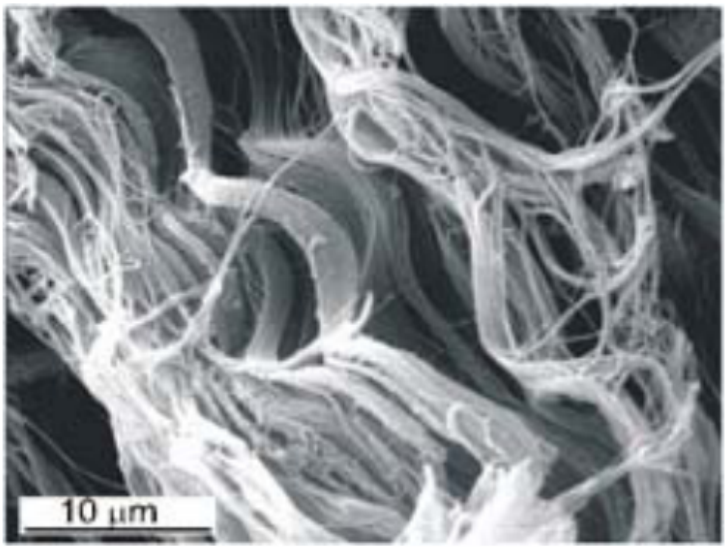

Figure 3.1: Crimped collagen fibrils in chordæ tendineæ. (Reproduced from *Liao* [2003])

3.2 Calculation of the effective elastic tensor for the periodic microstructure

As a first approximation of soft tissue reinforced with helical fibres, we assume a composite model with a periodic structure. We use the double-scale asymptotic homogenization method to derive the effective behavior and elastic stiffness tensor. In this section, first we present the homogenization theory of linear elastic behavior over a periodic material in section 3.2.1, and then we discuss the numerical solution of the homogenization equation in section 3.2.2. Finally, we validate the finite element analysis method by comparing both analytical and numerical results in the section 3.2.3.

3.2.1 Homogenization theory of linear elastic behavior for a periodic material

The homogenization method is used to determine the effective mechanical properties of heterogeneous periodic media from the properties of the constitutive materials and their microstructure. For the case of a linear elastic model, these effective properties can be determined by the asymptotic expansion homogenization method at multiple scales. The method accounts for the scale separation by introducing a separation parameter ε, which represents the ratio of the period of the structure to a typical length in the region. The method, which is based on asymptotic expansions in powers of the small parameter ε, was specifically developed for periodically distributed medium (*Bensoussan et al.* [1978]; *Sánchez-Palencia* [1980]). In this section, we present the steps we take to derive a macroscopic

description of the effective four-order elastic tensor for the case of a two-phase periodic cell material (*Caillerie* [1987]).

3.2.1.1 Description of the medium under consideration

We consider a periodic two-phase medium that has a macroscopic characteristic size L. We then define a periodic cell Ω, noted as a representative elementary volume (REV) with a characteristic size l, as shown in Figure 3.2. Ω_1 and Ω_2 represent the two phases in the periodic cell and Γ represents the common interface between them. The periodic interfaces (S_1 and S_2) are associated with the phases Ω_1 and Ω_2, respectively, as shown in Figure 3.2.

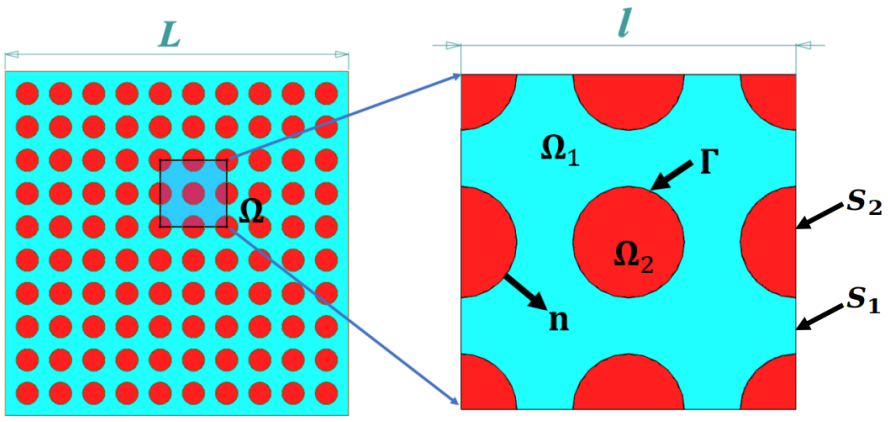

Figure 3.2: Diagram of the periodic medium, showing the REV cell with period Ω, and the periodic phases Ω_1 and Ω_2 and interfaces S_1 and S_2.

We use $\vec{X}$ as the physical spatial variable, and $\vec{y}$, $\vec{x}$ as dimensionless space variables that respectively describe variations on the microscopic and macroscopic scales; we introduce relations for these in Equation 3.1. We define ε to formulate the separation condition of different scales, with the REV for the medium being small compared to the macroscopic volume. See the relation between these in Equation 3.2.

$$\vec{y} = \frac{\vec{X}}{l} \qquad \vec{x} = \frac{\vec{X}}{L}. \tag{3.1}$$

$$\varepsilon = \frac{l}{L} << 1. \tag{3.2}$$

Due to the two spatial variables with respect to $\vec{X}$, the gradient operator can be written as

$$\frac{\partial}{\partial X_i} = \frac{\partial}{\partial y_i}\frac{\partial y_i}{\partial X_i} + \frac{\partial}{\partial x_i}\frac{\partial x_i}{\partial X_i}, \tag{3.3}$$

$$\vec{\nabla}_X = \frac{1}{l}\vec{\nabla}_y + \frac{1}{L}\vec{\nabla}_x. \tag{3.4}$$

We take the macroscopic viewpoint and reintroduce Equation 3.4 by inserting the dimensionless number as:

$$\vec{\nabla} = L\vec{\nabla}_X = \varepsilon^{-1}\vec{\nabla}_y + \vec{\nabla}_x. \tag{3.5}$$

Due to the separation of scales, the quantity $\Phi = \Phi(\vec{x}, \vec{y})$ appears as a function of two dimensionless variables, and Φ is looked for in the form of an asymptotic expansion in power of ε as:

$$\Phi = \Phi^0(\vec{x}, \vec{y}) + \varepsilon\Phi^1(\vec{x}, \vec{y}) + \varepsilon^2\Phi^2(\vec{x}, \vec{y}) + ... \tag{3.6}$$

The method we follow to look for Φ is described here. We assume the local description to be given and we look for the equivalent macroscopic description. First of all, we choose the macroscopic or microscopic viewpoint. The expansions are made in the form of Eq.3.6 with $y = \frac{x}{\varepsilon}$ or $x = \varepsilon y$. We then proceed to the nondimensionless local description. The dimensionless numbers are evaluated as functions of powers of ε, where the physical problem is taken into account. Finally, the asymptotic expansions are substituted as in Eq.3.6 into the normalized description.

3.2.1.2 Dimensionless local description

For the two-phase medium under consideration, the period Ω is composed of two elastic materials occupying the domains Ω_1 and Ω_2. The elastic tensors associated with these domains are A_1 and A_2, respectively. The microscopic description on the periodic cell Ω, is given by:

$$\vec{\nabla} \cdot \sigma_\alpha = 0 \qquad within \quad \Omega_\alpha, \quad (\alpha = 1, 2), \tag{3.7}$$

$$\sigma_\alpha = A_\alpha : e(\vec{u}_\alpha) \qquad within \quad \Omega_\alpha, \quad (\alpha = 1, 2), \tag{3.8}$$

$$\sigma_1 \cdot \vec{n}_1 + \sigma_2 \cdot \vec{n}_2 = 0 \qquad over \quad \Gamma, \tag{3.9}$$

$$\vec{u}_1 = \vec{u}_2 \qquad over \quad \Gamma, \tag{3.10}$$

where σ_α represents the stress tensor, $\vec{u}_\alpha$ is the displacement, $\vec{n}_1$ and $\vec{n}_2$ are the unit normal vectors and satisfy $\vec{n}_1 = -\vec{n}_2$ *over* Γ , and e is the strain tensor defined by:

$$e(\vec{u}_\alpha) = \frac{1}{2}(\vec{\nabla}\vec{u}_\alpha + \vec{\nabla}^T\vec{u}_\alpha). \tag{3.11}$$

The elastic tensor A_α is a fourth-order tensor and satisfies the symmetries:

$$(A_{ijkh})_\alpha = (A_{khij})_\alpha = (A_{jikh})_\alpha = (A_{ijhk})_\alpha. \tag{3.12}$$

Our description of the modeled material assumes perfect adhesion between the two domains and their respective elastic properties are of the same order of magnitude.

3.2.1.3 Asymptotic expansion

To proceed in the homogenization of the microscopic description, we look for σ_α and u_α in the form of asymptotic expansions. The expansion of $\vec{u}_\alpha$ is written as:

$$\vec{u}_\alpha(\vec{x},\vec{y}) = \vec{u}^0_\alpha(\vec{x},\vec{y}) + \varepsilon\vec{u}^1_\alpha(\vec{x},\vec{y}) + \varepsilon^2\vec{u}^2_\alpha(\vec{x},\vec{y}) + ..., \tag{3.13}$$

where the function u^i_α is periodic with respect to the local variable $\vec{y} = \frac{\vec{X}}{l}$ of period 1.
The strain tensor 3.11 can be deduced by applying the derivation rule 3.5 as follows.

$$e(\vec{u}_\alpha) = \varepsilon^{-1}e_y(\vec{u}_\alpha) + e_x(\vec{u}_\alpha). \tag{3.14}$$

Therefore, Equation 3.8 indicates that the asymptotic expansion of σ_α starts in ε^{-1} as:

$$\sigma_\alpha(\vec{x},\vec{y}) = \varepsilon^{-1}\sigma^{-1}_\alpha(\vec{x},\vec{y}) + \varepsilon^0\sigma^0_\alpha(\vec{x},\vec{y}) + \varepsilon^1\sigma^1_\alpha(\vec{x},\vec{y}) + ..., \tag{3.15}$$

where the function σ^i_α is Ω-periodic in $\vec{y}$.

3.2.1.4 Perturbation equation

Introducing the asymptotic expansions 3.13 and 3.15, the gradient expression 3.5, and the strain tensor 3.14 into the Equations 3.7, 3.8, 3.9, and 3.10, we obtain the following cascade of developments in power of ε:

- For Equation 3.7:

$$(\varepsilon^{-1}\vec{\nabla}_y + \vec{\nabla}_x)\cdot(\varepsilon^{-1}\sigma^{-1}_\alpha + \varepsilon^0\sigma^0_\alpha + \varepsilon^1\sigma^1_\alpha + \cdots) = 0, \tag{3.16}$$

$$\mathcal{O}(\varepsilon^{-2}) \qquad \vec{\nabla}_y \cdot \sigma_s^{-1} = 0, \tag{3.17}$$

$$\mathcal{O}(\varepsilon^{-1}) \qquad \vec{\nabla}_y \cdot \sigma_\alpha^0 + \vec{\nabla}_x \cdot \sigma_\alpha^{-1} = 0, \tag{3.18}$$

$$\mathcal{O}(\varepsilon^{0}) \qquad \vec{\nabla}_y \cdot \sigma_\alpha^1 + \vec{\nabla}_x \cdot \sigma_\alpha^0 = 0, \tag{3.19}$$

$$\dots$$

- For Equation 3.8:

$$\varepsilon^{-1}\sigma_\alpha^{-1} + \varepsilon^0\sigma_\alpha^0 + \varepsilon^1\sigma_\alpha^1 + \cdots = A_\alpha : (\varepsilon^{-1}e_y + e_x)(\vec{u}_\alpha^0 + \varepsilon\vec{u}_\alpha^1 + \varepsilon^2\vec{u}_\alpha^2 + ...), \tag{3.20}$$

$$\mathcal{O}(\varepsilon^{-1}) \qquad \sigma_\alpha^{-1} = A_\alpha : e_y(\vec{u}_\alpha^0), \tag{3.21}$$

$$\mathcal{O}(\varepsilon^{0}) \qquad \sigma_\alpha^0 = A_\alpha : [e_y(\vec{u}_\alpha^1) + e_x(\vec{u}_\alpha^0)], \tag{3.22}$$

$$\mathcal{O}(\varepsilon^{1}) \qquad \sigma_\alpha^1 = A_\alpha : [e_y(\vec{u}_\alpha^2) + e_x(\vec{u}_\alpha^1)], \tag{3.23}$$

$$\dots$$

- For Equation 3.9:

$$(\varepsilon^{-1}\sigma_1^{-1} + \varepsilon^0\sigma_1^0 + \varepsilon^1\sigma_1^1 + \cdots) \cdot \vec{n}_1 + (\varepsilon^{-1}\sigma_2^{-1} + \varepsilon^0\sigma_2^0 + \varepsilon^1\sigma_2^1 + \cdots) \cdot \vec{n}_2 = 0, \tag{3.24}$$

$$\mathcal{O}(\varepsilon^{-1}) \qquad \sigma_1^{-1} \cdot \vec{n}_1 + \sigma_2^{-1} \cdot \vec{n}_2 = 0, \tag{3.25}$$

$$\mathcal{O}(\varepsilon^{0}) \qquad \sigma_1^0 \cdot \vec{n}_1 + \sigma_2^0 \cdot \vec{n}_2 = 0, \tag{3.26}$$

$$\mathcal{O}(\varepsilon^{1}) \qquad \sigma_1^1 \cdot \vec{n}_1 + \sigma_2^1 \cdot \vec{n}_2 = 0, \tag{3.27}$$

$$\dots$$

- For Equation 3.10:

$$\vec{u}_1^0 + \varepsilon\vec{u}_1^1 + \varepsilon^2\vec{u}_1^2 + \cdots = \vec{u}_2^0 + \varepsilon\vec{u}_2^1 + \varepsilon^2\vec{u}_2^2 + \cdots, \tag{3.28}$$

$$\vec{u}_1^0 = \vec{u}_2^0 \tag{3.29}$$

$$\vec{u}_1^1 = \vec{u}_2^1 \tag{3.30}$$

$$\vec{u}_1^2 = \vec{u}_2^2 \tag{3.31}$$

$$\cdots$$

where $\mathcal{O}$ is the term of relative order ε. From the developments above, we can determine the following boundary value problem.

3.2.1.5 Homogenization

Determination of σ_α^{-1} and $\vec{u}_\alpha^0$

From Equations 3.17, 3.21, 3.25, and 3.29, the boundary first-order value problem reads as follows:

$$\begin{cases} \vec{\nabla}_y \cdot (A_\alpha : e_y(\vec{u}_\alpha^0)) = 0 & \text{within} \quad \Omega_\alpha, \quad (\alpha = 1, 2), \quad (3.32) \\ (A_1 : e_y(\vec{u}_1^0)) \cdot \vec{n}_1 + (A_2 : e_y(\vec{u}_2^0)) \cdot \vec{n}_2 = 0 & \text{over} \quad \Gamma, \quad (3.33) \\ \vec{u}_1^0 = \vec{u}_2^0 & \text{over} \quad \Gamma, \quad (3.34) \end{cases}$$

where $\vec{u}_1$ and $\vec{u}_2$ are Ω-periodic in $\vec{y}$. Therefore, the displacement is constant over the period Ω, which means that it only depends on the macroscopic variable $\vec{x}$:

$$\vec{u}_\alpha^0 = \vec{u}_{\vec{x}}^0. \tag{3.35}$$

Consequently, we can deduce from Equation 3.21 that

$$\sigma_\alpha^{-1} = 0. \tag{3.36}$$

Determination of σ_α^0 and $\vec{u}_\alpha^1$

For the following order value problem, from Equations 3.18, 3.22, 3.26, 3.30, and 3.36, we have:

$$\begin{cases} \vec{\nabla}_y \cdot (A_\alpha : [e_y(\vec{u}_\alpha^1) + e_x(\vec{u}_\alpha^0)]) = 0 & \text{within } \Omega_\alpha, \ (\alpha = 1,2), \quad (3.37) \\ (A_1 : [e_y(\vec{u}_1^1) + e_x(\vec{u}_1^0)]) \cdot \vec{n}_1 + (A_2 : [e_y(\vec{u}_2^1) + e_x(\vec{u}_2^0)]) \cdot \vec{n}_2 = 0 & \text{over } \Gamma, \quad (3.38) \\ \vec{u}_1^1 = \vec{u}_2^1 & \text{over } \Gamma. \quad (3.39) \end{cases}$$

The unknown problem is determined to be u_α^1. The elastic tensor A_α ensures the existence of the unique solution, which is a linear function of $e_x(\vec{u}^0)$:

$$u_{\alpha_i}^1 = \xi_{\alpha_i}^{lm}(\vec{y}) e_{x_{lm}}(\vec{u}^0) + \tilde{u}_{\alpha_i}^1(\vec{x}), \quad (3.40)$$

where $\tilde{u}_{\alpha_i}^1(\vec{x})$, $(\alpha = 1,2)$, are additive functions and the functions $\xi_{\alpha_i}^{lm}$, $(\alpha = 1,2)$ represent the third-order tensor components. $\xi_{\alpha_i}^{lm}$ is the particular solution of $u_{\alpha_i}^1 = \xi_{\alpha_i}^{lm}$ for the boundary value problem 3.32, 3.33, and 3.34 when $e_{xij}(\vec{u}_\alpha^0) = \delta_{il}\delta_{jm}$, where l and m are fixed. The functions $\xi_{\alpha_i}^{lm}$ satisfy:

$$\begin{cases} \dfrac{\partial}{\partial_{y_j}}(A_{\alpha_{ijkh}} e_{y_{kh}}(\vec{\xi}_\alpha^{lm}) + A_{\alpha_{ijlm}}) = 0 & \text{within} \quad \Omega_\alpha, (\alpha = 1,2). \ (3.41) \\ (A_{1_{ijkh}} e_{y_{kh}}(\vec{\xi}_1^{lm}) + A_{1_{ijlm}}) \cdot n_{1_j} + (A_{2_{ijkh}} e_{y_{kh}}(\vec{\xi}_2^{lm}) + A_{2_{ijlm}}) \cdot n_{2_j} = 0 & \text{over} \quad \Gamma, \quad (3.42) \\ \vec{\xi}_1^{kh} = \vec{\xi}_2^{kh} & \text{over} \quad \Gamma, \quad (3.43) \end{cases}$$

where $\vec{\xi}_\alpha^{kh}$, $(\alpha = 1,2)$ are Ω-periodic in $\vec{y}$. The unique solution requires that $\xi_{\alpha_i}^{lm}$ has a zero mean over the periodic cell Ω:

$$< \xi_\alpha^{kh} >_\Omega = 0, \quad (3.44)$$

where $< \bullet >$ is the cell volume average described as:

$$< \bullet >_{\Omega_\alpha} = \frac{1}{|\Omega|} \int_{\Omega_\alpha} \bullet \, d\Omega \qquad (\alpha = 1,2). \quad (3.45)$$

We therefore have:

$$\sigma_\alpha^0 = (A_{\alpha_{ijlm}} e_{y_{lm}}(\vec{\xi}^{lm}) + A_{ijkh}) e_{x_{kh}}(\vec{u}_\alpha^0). \quad (3.46)$$

First-order compatibility condition

Let us consider the next order boundary value problem from 3.19 and 3.27:

$$\begin{cases} \vec{\nabla}_y \cdot \sigma_\alpha^1 + \vec{\nabla}_x \cdot \sigma_\alpha^0 = 0 & \text{within} \quad \Omega_\alpha, (\alpha = 1,2), \quad (3.47) \\ \sigma_1^1 \cdot \vec{n}_1 + \sigma_2^1 \cdot \vec{n}_2 = 0 & \text{over} \quad \Gamma. \quad (3.48) \end{cases}$$

Integrating the Equation 3.47 over the period Ω leads to a necessary and sufficient condition for the solution of $\vec{u}_\alpha^1$. The volume average constitutes the first-order macroscopic behavior noted as:

$$\frac{1}{|\Omega|}\int_{\Omega_1} \vec{\nabla}_y \cdot \sigma_1^1 d\Omega + \frac{1}{|\Omega|}\int_{\Omega_1} \vec{\nabla}_x \cdot \sigma_1^0 d\Omega + \frac{1}{|\Omega|}\int_{\Omega_2} \vec{\nabla}_y \cdot \sigma_2^1 d\Omega + \frac{1}{|\Omega|}\int_{\Omega_2} \vec{\nabla}_x \cdot \sigma_2^0 d\Omega = 0. \tag{3.49}$$

Applying divergence theorem, some members of Equation 3.49 can be transformed as follows:

$$\frac{1}{|\Omega|}\int_{\Omega_1} \vec{\nabla}_y \cdot \sigma_1^1 \, d\Omega = \frac{1}{|\Omega|}\int_{\partial\Omega_1} \sigma_1^1 \cdot \vec{n}_1 \, dS, \tag{3.50}$$

$$\frac{1}{|\Omega|}\int_{\Omega_2} \vec{\nabla}_y \cdot \sigma_2^1 \, d\Omega = \frac{1}{|\Omega|}\int_{\partial\Omega_2} \sigma_2^1 \cdot \vec{n}_2 \, dS, \tag{3.51}$$

where $\partial\Omega_\alpha = \Gamma \cup S_\alpha$, $(\alpha = 1,2)$, and S_α, $(\alpha = 1,2)$ is the external boundary surface over the periodic cell Ω as shown in Figure 3.2. Equation 3.50 and 3.51 can therefore be written as:

$$\frac{1}{|\Omega|}\int_{\partial\Omega_1} \sigma_1^1 \cdot \vec{n}_1 \, dS = \frac{1}{|\Omega|}\int_{S_1} \sigma_1^1 \cdot \vec{n}_1 \, dS + \frac{1}{|\Omega|}\int_{\Gamma} \sigma_1^1 \cdot \vec{n}_1 \, dS, \tag{3.52}$$

$$\frac{1}{|\Omega|}\int_{\partial\Omega_2} \sigma_1^1 \cdot \vec{n}_2 \, dS = \frac{1}{|\Omega|}\int_{S_2} \sigma_2^1 \cdot \vec{n}_2 \, dS + \frac{1}{|\Omega|}\int_{\Gamma} \sigma_2^1 \cdot \vec{n}_2 \, dS. \tag{3.53}$$

Due to the periodicity of the cell, integrating over S_α, $(\alpha = 1,2)$ is zero:

$$\frac{1}{|\Omega|}\int_{S_1} \sigma_1^1 \cdot \vec{n}_1 \, dS = 0, \tag{3.54}$$

$$\frac{1}{|\Omega|}\int_{S_2} \sigma_2^1 \cdot \vec{n}_2 \, dS = 0. \tag{3.55}$$

From Equation 3.48, we have:

$$\frac{1}{|\Omega|}\int_{\Gamma} \sigma_1^1 \cdot \vec{n}_1 \, dS + \frac{1}{|\Omega|}\int_{\Gamma} \sigma_2^1 \cdot \vec{n}_2 \, dS = 0. \tag{3.56}$$

Therefore, Equation 3.49 becomes:

$$\frac{1}{|\Omega|}\int_{\Omega_1}\vec{\nabla}_x\cdot\sigma_1^0 d\Omega+\frac{1}{|\Omega|}\int_{\Omega_2}\vec{\nabla}_x\cdot\sigma_2^0 d\Omega=\vec{\nabla}_x\cdot<\sigma_1^0>_{\Omega_1}+\vec{\nabla}_x\cdot<\sigma_2^0>_{\Omega_2}=0. \tag{3.57}$$

Let us define

$$\sigma_T^0=\begin{cases}\sigma_1^0 & within \quad \Omega_1\\ \sigma_2^0 & within \quad \Omega_2\end{cases}. \tag{3.58}$$

Equation 3.57 therefore becomes:

$$\begin{cases}\vec{\nabla}_x\cdot<\sigma_T^0>_\Omega=0 & (3.59)\\ ,<\sigma_T^0>_\Omega=<\sigma_T^0>_1+<\sigma_T^0>_2\,. & (3.60)\end{cases}$$

The Equation 3.22 can then be written as:

$$<\sigma_{T_{ij}}^0>_\Omega=<A_1:[e_y(\vec{u}_1^1)+e_x(\vec{u}_1^0)]>_{\Omega_1}+<A_2:[e_y(\vec{u}_2^1)+e_x(\vec{u}_2^0)]>_{\Omega_2.} \tag{3.61}$$

If we take into account the form of $\vec{u}_\alpha^1$ 3.40, then we have:

$$\begin{aligned}<\sigma_T^0>_\Omega &=<A_{1_{ijkh}}:[e_{y_{kh}}(\xi_1^{lm}e_{x_{lm}}(\vec{u}_1^0))+e_{x_{kh}}(\vec{u}_1^0)]>_{\Omega_1}+<A_{2_{ijkh}}:[e_{y_{kh}}(\xi_2^{lm}e_{x_{lm}}(\vec{u}_2^0))+e_{x_{kh}}(\vec{u}_2^0)]>_{\Omega_2}\\ &=<A_{1_{ijkh}}+A_{1_{ijlm}}e_{y_{lm}}(\xi_1^{kh})>_{\Omega_1}e_{x_{kh}}(\vec{u}_1^0)+<A_{2_{ijkh}}+A_{2_{ijlm}}e_{y_{lm}}(\xi_2^{kh})>_{\Omega_2}e_{x_{kh}}(\vec{u}_2^0)\\ &=C_{ijkh}e_{x_{kh}}(\vec{u}_\alpha^0),\end{aligned} \tag{3.62}$$

where C_{ijkh} is the effective elastic tensor defined by:

$$C_{ijkh}=<A_{1_{ijkh}}+A_{1_{ijlm}}e_{y_{lm}}(\xi_1^{kh})>_{\Omega_1}+<A_{2_{ijkh}}+A_{2_{ijlm}}e_{y_{lm}}(\xi_2^{kh})>_{\Omega_2}\,. \tag{3.63}$$

First-order macroscopic description

The first-order equivalent macroscopic behavior of periodic cell material is written as:

$$\begin{cases}\vec{\nabla}_x\cdot<\sigma_T^0>_\Omega=0, & (3.64)\\ <\sigma_{T_{ij}}^0>_\Omega=C_{ijkh}e_{x_{kh}}(\vec{u}_\alpha^0), & (3.65)\\ C_{ijkh}=<A_{1_{ijkh}}+A_{1_{ijlm}}e_{y_{lm}}(\xi_1^{kh})>_{\Omega_1}+<A_{2_{ijkh}}+A_{2_{ijlm}}e_{y_{lm}}(\xi_2^{kh})>_{\Omega_2}\,. & (3.66)\end{cases}$$

The macroscopic behavior is equivalent to that of a homogeneous elastic material and

the effective elastic tensor is given by Equation3.66.

3.2.1.6 Porous empty medium case

We also investigate the mechanical properties of modeled empty porous material (*Boutin et al.* [2010]). To this end, we consider the phase Ω_2 as empty in the periodic cell as shown in Figure 3.2. The microscopic description of the problem on the periodic cell Ω can be deduced as:

$$\vec{\nabla} \cdot \sigma_1 = 0 \qquad within \quad \Omega_1, \tag{3.67}$$

$$\sigma_1 = A_1 : e(\vec{u}_1) \qquad within \quad \Omega_1, \tag{3.68}$$

$$\sigma_1 \cdot \vec{n}_1 = 0 \qquad over \quad \Gamma, \tag{3.69}$$

$$\vec{u}_1 = 0 \qquad over \quad \Gamma. \tag{3.70}$$

By homogenizing this microscopic description, we obtain the macroscopic behavior, which can be written in the same form as Equations 3.65 and 3.66, where the macroscopic stress at the first order is defined by:

$$< \sigma^0_{T_{ij}} >_\Omega = < A_1 : [e_y(\vec{u}^1_1) + e_x(\vec{u}^0_1)] >_{\Omega_1}, \tag{3.71}$$

where

$$\sigma^0_T = \begin{cases} \sigma^0_1 & within \quad \Omega_1, \\ 0 & within \quad \Omega_2. \end{cases} \tag{3.72}$$

The effective elastic tensor C_{ijkh} is therefore defined as:

$$C_{ijkh} = < A_{1_{ijkh}} + A_{1_{ijlm}} e_{y_{lm}}(\xi^{kh}_1) >_{\Omega_1}, \tag{3.73}$$

where the function ξ^{kh}_1 satisfies:

$$\begin{cases} \dfrac{\partial}{\partial_{y_j}}(A_{1_{ijkh}} e_{y_{kh}}(\vec{\xi}^{lm}_1) + A_{1_{ijlm}}) = 0 & \text{within ,} & (3.74) \\ (A_{1_i jkh} e_{y_{kh}}(\vec{\xi}^{lm}_1) + A_{1_{ijlm}}) \cdot n_{1_j} = 0 & \text{over} \quad \Gamma, & (3.75) \\ \vec{\xi}^{kh}_1 = 0 & \text{over} \quad \Gamma. & (3.76) \end{cases}$$

3.2.2 Numerical solution of the homogenization equation

3.2.2.1 Finite element formulation

In order to determine the elastic properties of a periodic material, only the effective elastic tensor is necessary. From Equation 3.66, each value of the elastic tensor can be calculated as:

$$C_{ijkh} = \frac{1}{|\Omega|}\int_{\Omega_1}(A_{1_{ijkh}} + A_{1_{ijlm}}e_{y_{lm}}(\xi_1^{kh}))d\Omega + \frac{1}{|\Omega|}\int_{\Omega_2}(A_{2_{ijkh}} + A_{2_{ijlm}}e_{y_{lm}}(\xi_2^{kh}))d\Omega. \quad (3.77)$$

The first member of the integral is related to the material microstructure; it corresponds to the value of the elastic tensor weighted by the volume fraction, written as:

$$\frac{1}{|\Omega|}\int_{\Omega_\alpha} A_{\alpha_{ijkh}}d\Omega = \rho_\alpha A_{\alpha_{ijkh}}, \qquad \alpha = 1,2, \quad (3.78)$$

where ρ_α is the volume fraction of the corresponding α component.

The second member of the integral can be obtained from ξ^{kh}, which is the periodic microscopic displacement solution of the problem 3.41. For a three-dimensional medium, considering the 21 constants of the fourth-order tensor C_{ijkh}, the problem 3.41 can be transformed for six loading cases. The indices i, j, h, k, l, m take values from 1 to 3 and the loading cases are: $kh = 11$, $kh = 22$, $kh = 33$, $kh = 12$, $kh = 13$, and $kh = 23$, which correspond to three stretches or compress cases and three shear cases.

Based on the work presented by *Hassani and Hinton* [2012], Equation 3.77 can be written as:

$$C_{ijkh} = \frac{1}{|\Omega|}\int_{\Omega_1}(A_{1_{ijkh}} + a_{1_{ij}}^T B(\hat{\xi}_1^{kh}))d\Omega + \frac{1}{|\Omega|}\int_{\Omega_2}(A_{2_{ijkh}} + a_{2_{ij}}^T B(\hat{\xi}_2^{kh}))d\Omega, \quad (3.79)$$

where B is the global strain matrix, $a_{\alpha_{ij}}$, $(\alpha = 1,2)$ is the column of the elastic matrix $A_{\alpha_{ijkh}}$ corresponding to the indices ij, and $\hat{\xi}_\alpha$ is the nodal displacement solution.

We take the form presented by *Hassani and Hinton* [2012] and write Equation 3.41 as:

$$\int_{\Omega_\alpha} B^T A_{\alpha_{ijkh}} B d\Omega \hat{\xi}_\alpha^{kh} = \int_{\Omega_\alpha} B^T a_{\alpha_{kh}} d\Omega, \quad (3.80)$$

which is similar to the stiffness equation:

$$K_\alpha \hat{\xi}_\alpha^{kh} = \vec{f}_\alpha, \quad (3.81)$$

where the stiffness matrix is written as:

$$K_\alpha = \int_{\Omega_\alpha} B^T A_{\alpha_{ijkh}} B d\Omega, \tag{3.82}$$

and the force vector has the form:

$$\vec{f}_\alpha = \int_{\Omega_\alpha} B^T a_{\alpha_{kh}} d\Omega. \tag{3.83}$$

The force vector implies a unitary macroscopic deformation for the case kh. This force vector corresponds to the initial deformation. We consider the nodal force of an element e induced by the initial strain:

$$(\vec{f}_\alpha^{\varepsilon^0})^e = \int_{\Omega_\alpha^e} (B^T)^e A_{\alpha_{kh}} \varepsilon^0 d\Omega, \tag{3.84}$$

where ε^0 represents the initial strain.

If we consider one case, $kh = 11$, the force vector defined by Equation 3.83 becomes:

$$(\vec{f}_\alpha^e)_{11} = \int_{\Omega_\alpha^e} (B^T)^e a_{\alpha_{11}} d\Omega. \tag{3.85}$$

Comparing Equations 3.84 and 3.85 allows us to verify that:

$$A_\alpha \varepsilon^0 = a_{\alpha_{11}}. \tag{3.86}$$

In this case, ε^0 is defined as:

$$\varepsilon^0 = \begin{bmatrix} 1 & 0 & 0 \\ 0 & 0 & 0 \\ 0 & 0 & 0 \end{bmatrix}. \tag{3.87}$$

Furthermore, by considering the other loading cases, it is possible to find all of the elastic coefficients. Now that the force vector is defined, let us determine the solution for ξ_α^{kh}. From Equation 3.77, we notice that ξ_α^{kh} is similar to a displacement, $e_{y_{lm}}(\xi_\alpha^{kh})$ is similar to a strain, and $A_{\alpha_{ijlm}} e_{y_{lm}}(\xi_\alpha^{kh})$ is similar to a stress:

$$\sigma_{\alpha_{ij}}^{kh} = A_{\alpha_{ijlm}} e_{y_{lm}}(\xi_\alpha^{kh}). \tag{3.88}$$

In practice, discretizing the periodic domain of the cell, it is possible to run the finite element program for the each initial unit strain. The required boundary conditions and the stress calculation steps are discussed in the following section.

3.2.2.2 Integral of stress

The stress σ_{ij}^{kh} is obtained from the nodal force field, which itself is obtained by imposing a unit strain $\varepsilon_{kh}^{0} = 1$. The sign of the strain ε_{kh}^{0} does not change the solution because the mechanical model is the linear elastic model. For a "*kh*" loading, the stress calculation steps are as follows:

1. Application of a displacement field corresponding to $\varepsilon_{kh} = \pm 1$ on the coordinates of each node.
2. Calculation of the stress field associated with the displacement field without boundary conditions.
3. Calculation of the nodal force field by integrating the stress field.
4. With the periodic conditions, calculation of the displacement field by applying the force field computed previously.
5. Calculation of the stress field associated with the new displacement field.
6. Calculation of the integral of the stress field from Equation 3.88.

These steps should be repeated for each load *kh*. Steps 1, 2, and 3 are used to determine the field of the nodal forces. Step 4 is then used to determine the displacement solution with consideration of the periodic conditions; the required boundary conditions are introduced in the following section. Finally, steps 5 and 6 are used to calculate the second term of the integral Equation 3.77.

3.2.2.3 Periodic boundary conditions

To calculate the second term of the integral Equation 3.88, it is necessary to apply the particular periodic boundary conditions. These boundary conditions are described as:

$$\vec{u} = E \cdot \vec{x} + \vec{v}, \tag{3.89}$$

where $E =< \varepsilon >$ is the macroscopic strain tensor, $\vec{v}$ is an Ω-periodic variation, and $\vec{x}$ is the position of a point of Ω. The periodic boundary conditions imply that for opposite surfaces:

- the strains should be identical;
- in order to satisfy stress continuity, the stress vector $\vec{t} = \sigma \cdot \vec{n}$ takes opposite values.

As $\vec{v}$ is generally unknown, the condition Equation 3.89 cannot be applied directly. By applying the condition to the opposite surfaces " $+$ " and " $-$ ", we have:

$$\vec{u}^{+} =< E > \cdot \vec{x} + \vec{v}, \tag{3.90}$$

$$\vec{u}^{-} =< E > \cdot \vec{x} + \vec{v}. \tag{3.91}$$

Subtracting Equation 3.90 by Equation 3.91, we can eliminate the unknown $\vec{v}$ as:

$$\vec{u}^{+} - \vec{u}^{-} =< E > \cdot (\vec{x}^{+} - \vec{x}^{-}). \tag{3.92}$$

The signs " $+$ " and " $-$ " represent the opposite surface of the period. The condition Equation 3.91 expresses the periodicity of the displacement field. A schema of an example 2D cell is shown in Figure 3.3, where we indicate the periodic boundary conditions.

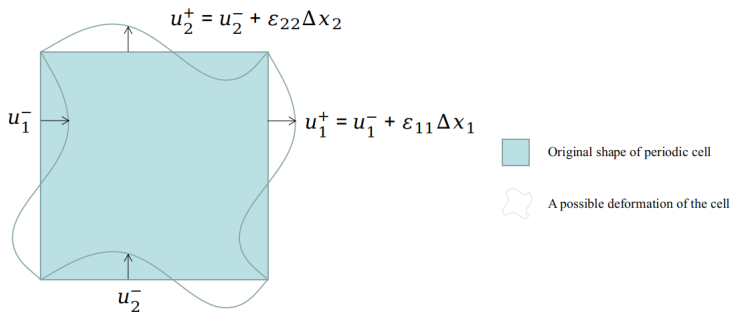

Figure 3.3: Schema of periodic boundary conditions for the displacement.

The continuity of the stress throughout the material is represented in Figure 3.4 and the periodicity of the stress implies that:

$$\sigma^{-} \cdot \vec{n}^{-} = \sigma^{+} \cdot \vec{n}^{+}. \tag{3.93}$$

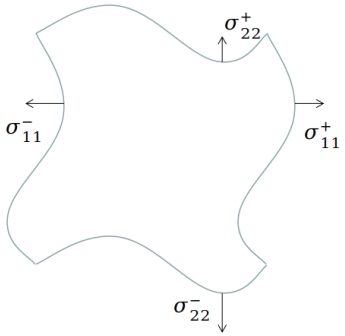

Figure 3.4: Schema of periodic boundary conditions for the stress.

In order to easily and straightforwardly impose the periodic boundary conditions, it is required that the mesh of the opposite surfaces be identical.

3.2.3 Finite element analysis method and validation

In this section, we present the finite element analysis method. We then discuss a verification step that we take to validate the method, whereby we compare an analytical solution and a numerical solution.

In our finite element study, the REV geometric design is built in SolidWorks; then FreeCAD takes the "STEP" format file exported from SolidWorks and optimizes the contact surface of two materials into one common interface using a "boolean fragments" function; subsequently, the mesh is generated by Gmsh; and finally, the finite element analysis is calculated using the numerical software Cast3M *Charras*. After calculation, the data analysis is carried out using Python programming and the resulting data are visualized in ParaView in order to verify whether or not the results satisfy periodic boundary conditions. The finite element analysis process and the output file format are shown in Figure 3.5.

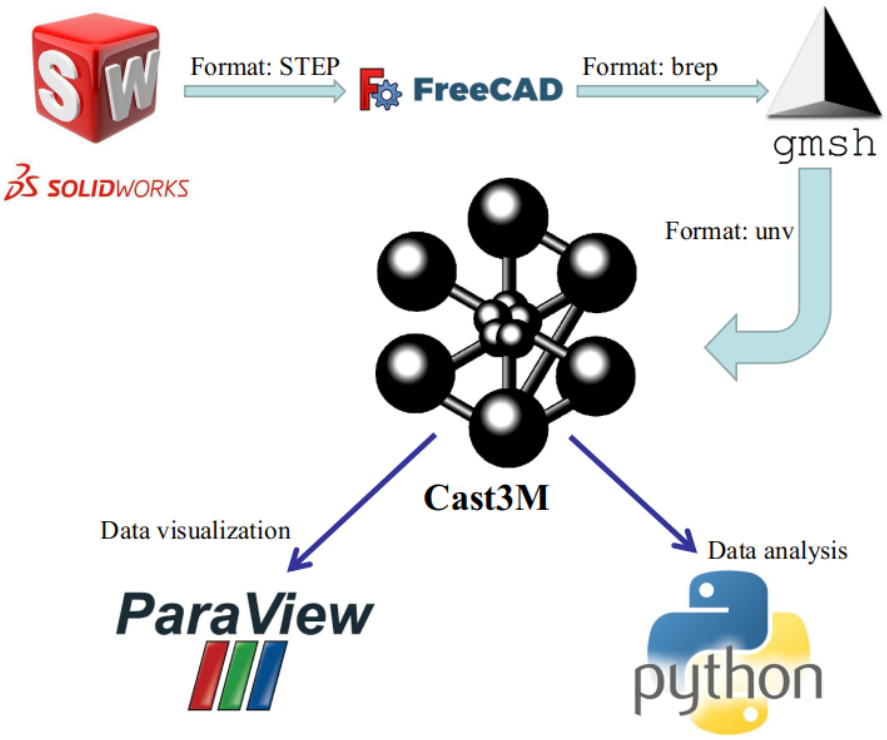

Figure 3.5: Finite element analysis process.

We consider a well-known analytical solution structure for the verification step, which consists in straight-fibre-reinforced composite. The numerical solution of this case is shown

in section 3.2.3.1, and the analytical method is presented in section 2.3.1 of Chapter 2. We reformulate the analytical equations in section 3.2.3.2 to unify the coordinate system with the numerical solution. We note that the analytical solution assumes a random and homogenized distribution of fibres in the plane perpendicular to the fibre orientation, whereas the numerical solution assumes a strong periodic arrangement of fibres in this plane. However, by experience (*Chen and Schuh* [2009]), when the volume fraction of fibres is small, there is little difference between a periodic distribution of fibres and a homogenized distribution. For our validation study example, the fibre volume fraction is set to 3.14%, the Young's moduli of fibre and matrix are set to $100MPa$ and $10KPa$, respectively, and the Poisson 's ratios of fibre and matrix are set to 0.3 and 0.4, respectively.

3.2.3.1 Numerical solution

Representative elementary volume

The material under consideration is a straight-fibre-reinforced composite as shown in Figure 3.6a, and its relative REV is shown in Figure 3.6b. The green structures represent fibres, the matrix material is set to be transparent, and the fibre orientation is set parallel to the z-axis.

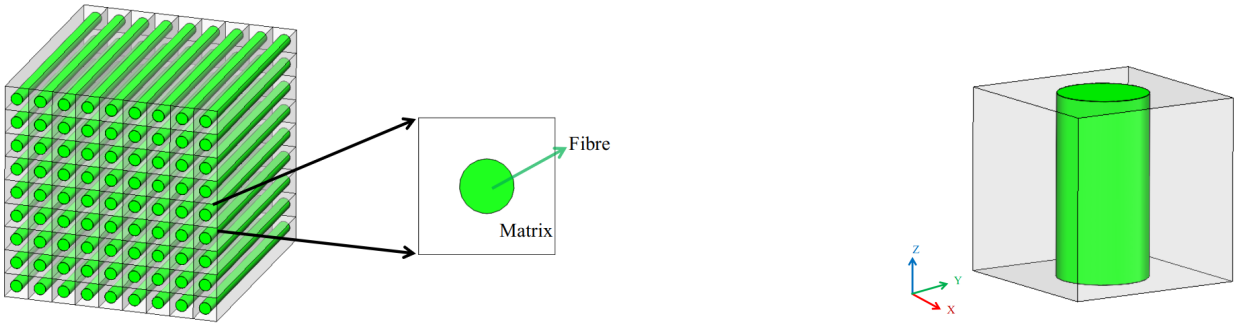

(a) (b)

Figure 3.6: (a) Periodically arranged straight-fibre-reinforced composite. (b) REV of the periodic structure under consideration.

Boundary conditions and mesh convergence study

In order to impose the periodic boundary condition as shown in equation 3.92, an example of a finite element mesh of the REV generated by the GMSH software is shown in Figure 3.7a, where each 3D element is set to the tetrahedron and the meshes on opposite boundary surfaces are identical. Figure 3.7b shows the mesh of the fibre. Here, the fibre and the matrix are bound to each other, which means the nodes on their contact surfaces belong

to two volumes at the same time. The type of element used in Cast3M is a tetrahedron element with four nodes, denoted "TET4".

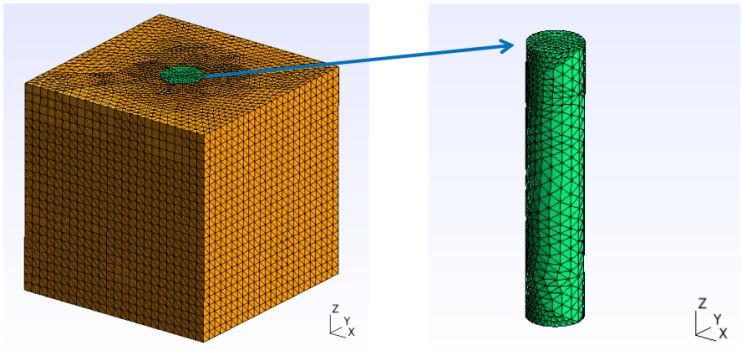

Figure 3.7: Finite element mesh of the REV under consideration here. The number of elements here is 83904. (a) Global view of the REV mesh. (b) Mesh of the fibre embedded in the REV.

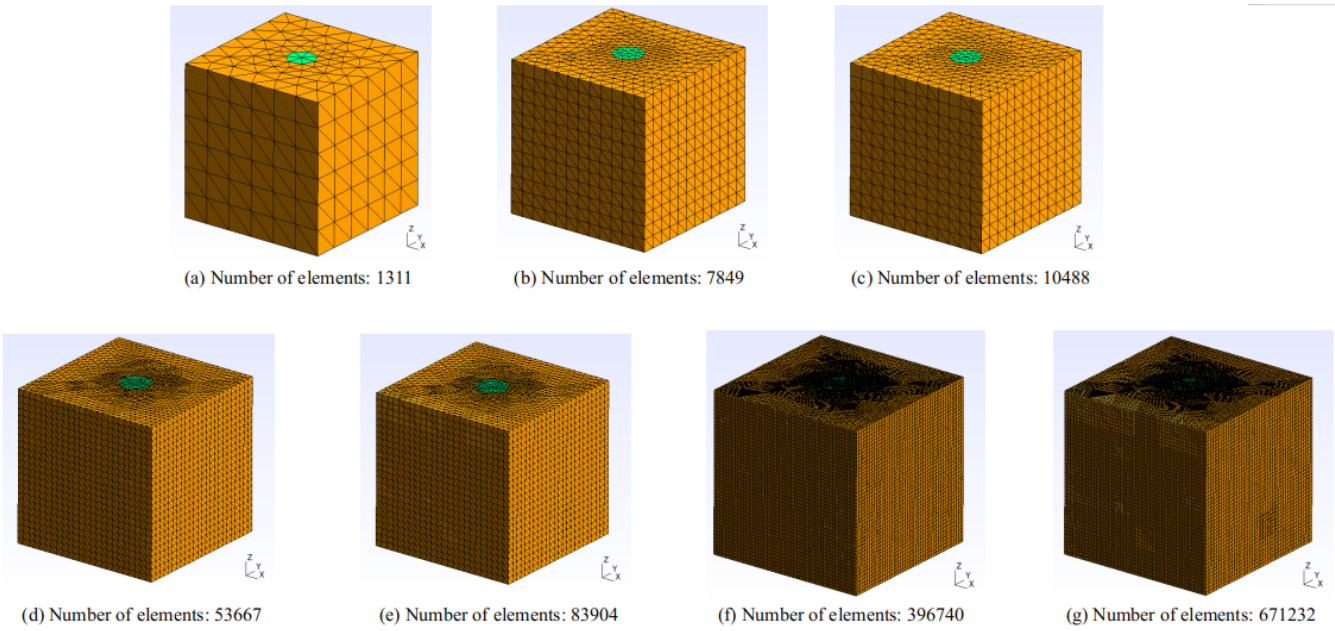

Figure 3.8: Meshes of increasing number of elements, as studied in the finite element analysis.

The number of elements in the mesh has an influence on the results of the homogenization procedure. In order to quantify this influence and to optimize the results, we carried out a mesh convergence study; the number of elements of each mesh studied is presented in Figure 3.8. This mesh convergence study is accurate to $10^{-5} MPa$, and the computed values

of each component of the effective elastic tensor for each different mesh are shown in Figure 3.9. As the material is transverse isotropic in the x-y plane, the numerical results of the effective elastic tensor C^n_{ij} can be expressed as follows.

$$\left[C^n\right] = \begin{bmatrix} {C^n}_{11} & {C^n}_{12} & {C^n}_{13} & 0 & 0 & 0 \\ {C^n}_{12} & {C^n}_{11} & {C^n}_{13} & 0 & 0 & 0 \\ {C^n}_{13} & {C^n}_{13} & {C^n}_{33} & 0 & 0 & 0 \\ 0 & 0 & 0 & {C^n}_{44} & 0 & 0 \\ 0 & 0 & 0 & 0 & {C^n}_{44} & 0 \\ 0 & 0 & 0 & 0 & 0 & {C^n}_{66} \end{bmatrix}. \tag{3.94}$$

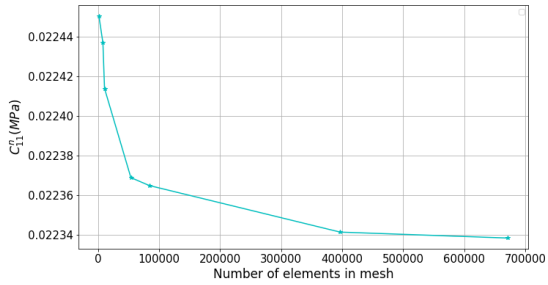

(a) C^n_{11}

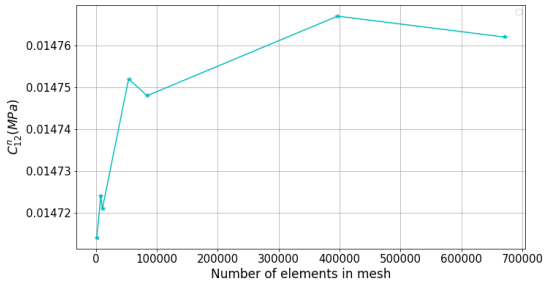

(b) C^n_{12}

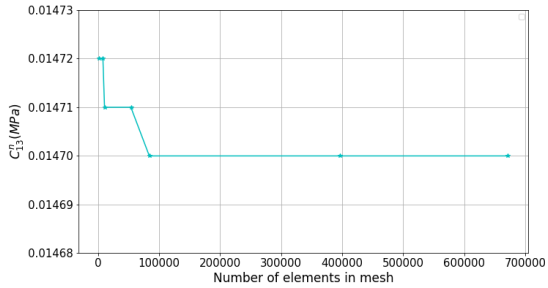

(c) C^n_{13}

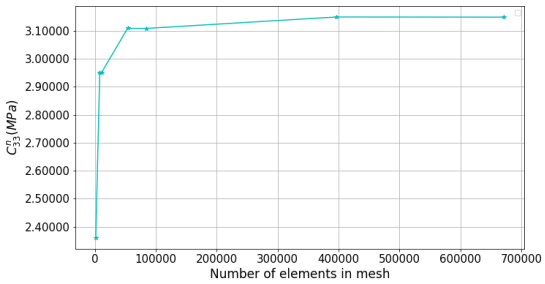

(d) C^n_{33}

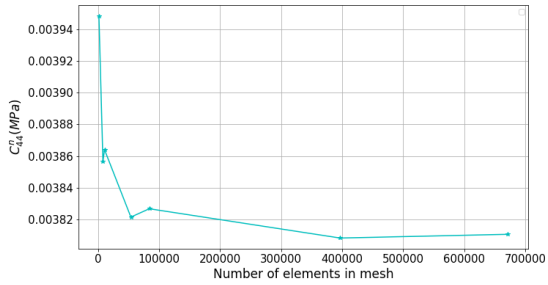

(e) C^n_{44}

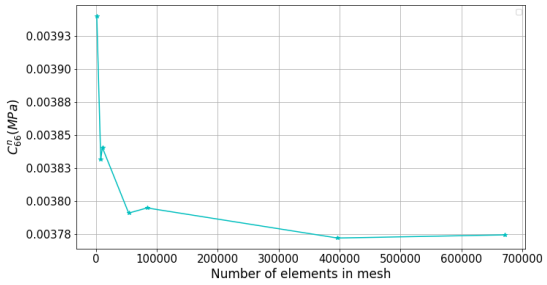

(f) C^n_{66}

Figure 3.9: Elastic tensor parameter value versus number of elements in the mesh.

As shown in Figure 3.9, as the number of elements increases, C_{11}, C_{13}, C_{44}, and C_{66} decrease, while C_{12} and C_{33} increase, and all stabilize when the number of elements in the mesh is greater than 390000. We therefore consider our calculations of the effective elastic tensor to be reliable when the number of elements in the mesh is greater than 390000.

3.2.3.2 Analytical solution

As the composite is transverse isotropic material in the y-z plane, we reformulate the analytic elastic compliance ${S^a}_{ij}$ as follows.

$$\left[S^a\right] = \begin{bmatrix} {S^a}_{11} & {S^a}_{12} & {S^a}_{13} & 0 & 0 & 0 \\ {S^a}_{12} & {S^a}_{11} & {S^a}_{13} & 0 & 0 & 0 \\ {S^a}_{13} & {S^a}_{13} & {S^a}_{33} & 0 & 0 & 0 \\ 0 & 0 & 0 & {S^a}_{44} & 0 & 0 \\ 0 & 0 & 0 & 0 & {S^a}_{44} & 0 \\ 0 & 0 & 0 & 0 & 0 & {S^a}_{66} \end{bmatrix} \tag{3.95}$$

The respective stress–strain relation is therefore

$$\begin{Bmatrix} \varepsilon_x \\ \varepsilon_y \\ \varepsilon_z \\ \gamma_{yz} \\ \gamma_{zx} \\ \gamma_{xy} \end{Bmatrix} = \left[S^a_{ij}\right] \begin{Bmatrix} \sigma_x \\ \sigma_y \\ \sigma_z \\ \tau_{yz} \\ \tau_{zx} \\ \tau_{xy} \end{Bmatrix}, \tag{3.96}$$

and the further analytical elastic tensor is calculated as

$$\left[C^a\right] = \left[S^a\right]^{-1}. \tag{3.97}$$

The nonzero elements of S^a are described as

$${S^a}_{11} = \frac{c_2}{c_3} + \frac{c_4}{4}, \tag{3.98}$$

$${S^a}_{12} = \frac{c_2}{c_3} - \frac{c_4}{4}, \tag{3.99}$$

$${S^a}_{13} = \frac{V_m \nu_m E_m (1+\nu_f)(1-2\nu_f) + E_f (1+\nu_m)[2\nu_f (1-\nu_m) + V_m (\nu_m - 2\nu_f + 2\nu_m \nu_f)]}{c_1}, \tag{3.100}$$

$$S^a{}_{33} = \frac{E_f(1+\nu_m)\left[-2+2\nu_m+V_m(1-2\nu_m)\right]-V_mE_m(1+\nu_f)(1-2\nu_f)}{c_1}, \tag{3.101}$$

$$S^a{}_{44} = \frac{2(1+\nu_m)\left[V_mE_f(1+\nu_m)+E_m(1+\nu_f)(2-V_m)\right]}{E_m\left[V_mE_m(1+\nu_f)+E_f(1+\nu_m)(2-V_m)\right]}, \tag{3.102}$$

$$S^a{}_{66} = 2(S_{11}-S_{12}), \tag{3.103}$$

where E_f and E_m represent the Young's moduli of fibre and matrix, respectively, ν_f is the Poisson's ratio of the fibre, and c_1, c_2, c_3, and c_4 are expressed as

$$\begin{aligned} c_1 =& -V_m^2E_m^2(1+\nu_f)(1-2v_f)+E_f^2(1+\nu_m)(1-V_m)\left[-2+2\nu_m+V_m(1-2\nu_m)\right] \\ &+V_mE_mE_f\left[-3+\nu_f+4\nu_m\nu_f+V_m(2-\nu_m-\nu_f-4\nu_m\nu_f)\right], \end{aligned} \tag{3.104}$$

$$\begin{aligned} c_2 =& E_mE_f(1+\nu_m)\{-2+2\nu_f+2\nu_m-2\nu_m\nu_f \\ &+V_m[3-2\nu_m-3\nu_f-2\nu_m\nu_f+V_m(-2+\nu_m+\nu_f+4\nu_m\nu_f)]\} \\ &-V_mE_f^2(1+\nu_m)^2(1-V_m)(1-2\nu_m)+V_mE_m^2(1+\nu_f)(1-2\nu_f)(-2+V_m+V_m\nu_m), \end{aligned} \tag{3.105}$$

$$\begin{aligned} c_3 =& 2E_m\{-V_m^2E_m^2(1+v_f)(1-2v_f)+E_f^2(1+v_m)(1-V_m)[-2+2\nu_m+V_m(1-2\nu_m)] \\ &+V_mE_mE_f[-3+\nu_f(1+4\nu_m)+V_m(2-\nu_m-\nu_f-4\nu_m\nu_f)]\}, \end{aligned} \tag{3.106}$$

$$c_4 = \frac{2(1+\nu_m)[V_mE_f(1+\nu_m)(3-4\nu_m)+E_m(1+\nu_f)(4-3V_m-4\nu_m+4V_m\nu_m)]}{E_m[V_mE_m(1+\nu_f)+E_f(1+\nu_m)(4-V_m-4\nu_m)].} \tag{3.107}$$

3.2.3.3 Validation results

The effective elastic tensor results calculated using the analytical method C^a and the numerical method C^n are shown in equations 3.108 and 3.109, respectively.

$$\left[C^a\right] = \begin{bmatrix} 0.02229 & 0.01475 & 0.01468 & 0 & 0 & 0 \\ 0.01475 & 0.02229 & 0.01468 & 0 & 0 & 0 \\ 0.01468 & 0.01468 & 3.16291 & 0 & 0 & 0 \\ 0 & 0 & 0 & 0.00380 & 0 & 0 \\ 0 & 0 & 0 & 0 & 0.00380 & 0 \\ 0 & 0 & 0 & 0 & 0 & 0.00377 \end{bmatrix}_{MPa}, \tag{3.108}$$

$$\left[C^n\right] = \begin{bmatrix} 0.02234 & 0.01476 & 0.01470 & 0 & 0 & 0 \\ 0.01476 & 0.02234 & 0.01470 & 0 & 0 & 0 \\ 0.01470 & 0.01470 & 3.14890 & 0 & 0 & 0 \\ 0 & 0 & 0 & 0.00381 & 0 & 0 \\ 0 & 0 & 0 & 0 & 0.00381 & 0 \\ 0 & 0 & 0 & 0 & 0 & 0.00377 \end{bmatrix}_{MPa}. \tag{3.109}$$

As shown in equations 3.108 and 3.109, all the elements of the effective elastic tensor calculated by the analytical and numerical methods are similar. To further quantify the difference between the two results, we calculated the error as follows:

$$error_{ij} = \frac{|C^a_{ij} - C^n_{ij}|}{C^a_{ij}}. \tag{3.110}$$

The difference between each of the elements of the two methods is shown in 3.111. In this simple example of our calculation, comparing the difference between each corresponding element shows that the maximum *error* does not exceed 0.5%, and we therefore consider our method to be reliable.

$$\left[error\right] = \begin{bmatrix} 0.22\% & 0.07\% & 0.14\% & 0 & 0 & 0 \\ 0.07\% & 0.22\% & 0.14\% & 0 & 0 & 0 \\ 0.14\% & 0.14\% & 0.44\% & 0 & 0 & 0 \\ 0 & 0 & 0 & 0.26\% & 0 & 0 \\ 0 & 0 & 0 & 0 & 0.26\% & 0 \\ 0 & 0 & 0 & 0 & 0 & 0\% \end{bmatrix} \tag{3.111}$$

3.3 Composite reinforced by helical fibres

In this section, we study the mechanical properties of the helical-fibre-reinforced composite model shown in Figure 3.10 using a double-scale asymptotic homogenization method.

Similar composite materials were studied by *Khani et al.* [2016], but the effective Poissonâ€™s ratio of the composite was not determined. Based on published measurements, we set the elastic modulus of the fibres to 100 *MPa* [*Dutov et al.*, 2016] and the elastic modulus of the matrix to 10 *KPa* [*Cortes and Elliott*, 2012]. The Poissonâ€™s ratio of both the fibres and the matrix is set to 0.3 [*Reese et al.*, 2010].

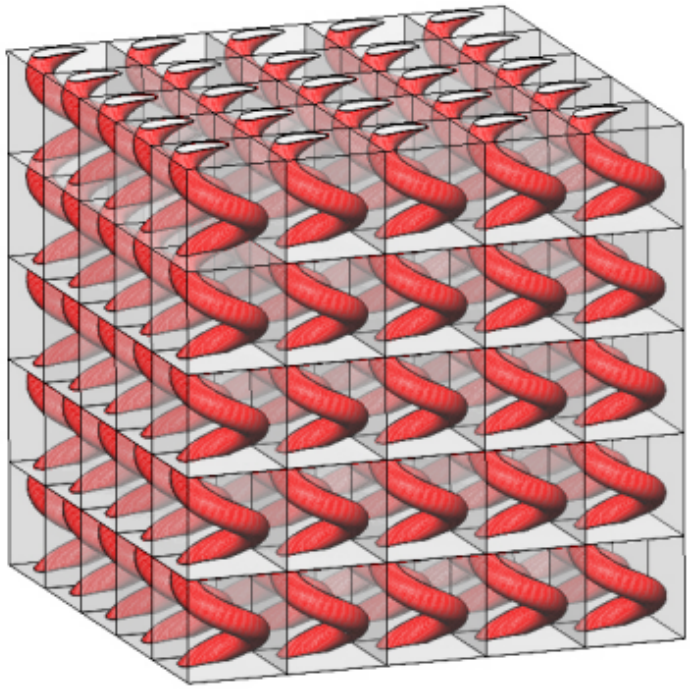

Figure 3.10: Periodically arranged helical-fibre-reinforced composite.

3.3.1 Representative elementary volume

The REV of the helical-fibre-reinforced composite is set as shown in Figure 3.11a, where the red structures represent the helical fibres and the matrix is transparent. The helical fibres are characterized by their helix pitch H_0, helix radius R_0, helix angle θ, helix period length L_0, and fibre diameter d_0 as shown in Figs. 3.11b, 3.11c, and 3.11d. In the present study, we assess the effects of changes to the fibre volume fraction ρ_f and helix angle β on the macroscopic mechanical properties of the composite model. The results are discussed in section 3.6.1.

The fibre volume fraction ρ_f is defined as

$$\rho_f = \frac{F_v}{F_v + M_v}, \tag{3.112}$$

where F_v and M_v represent the volume of the fibre and matrix, respectively,

and the helix angle β is define as

$$\beta = arctan(\frac{H_0}{2\pi R_0}). \tag{3.113}$$

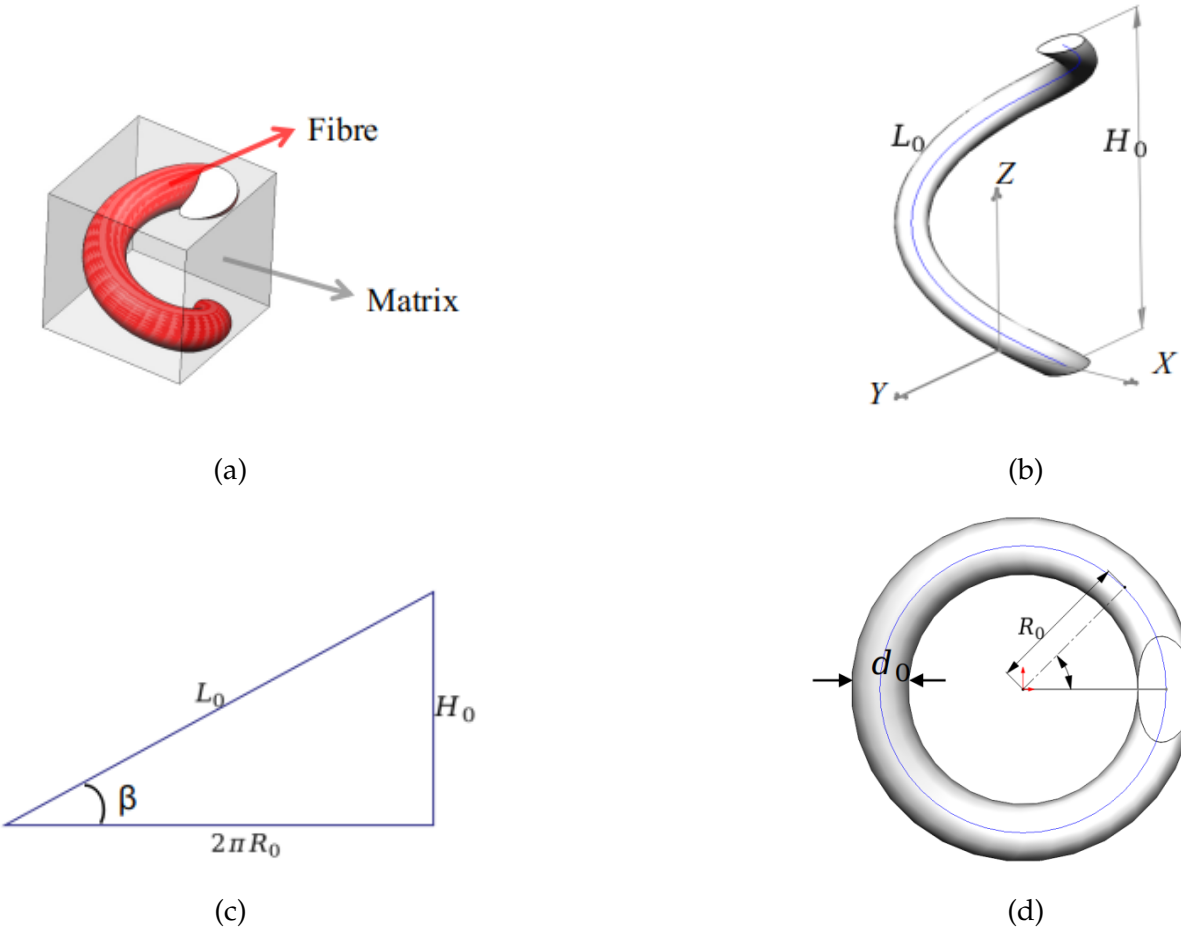

Figure 3.11: (a) REV of the helical-fibre reinforced composite. (b) Schematic diagram of a section of helical fibre showing the helix pitch H_0. (c) 2D schematic diagram of the geometric relation between the helix angle β, helix radius R_0, helix pitch H_0 and helix period length L_0. (d) Schematic diagram showing the helix radius R_0 and fibre diameter d_0.

3.3.2 Mesh convergence study

An example of a generated finite element mesh of one REV of helical-fibre-reinforced composite is shown in Figure 3.12, where the blue part represents the matrix mesh, the yellow component is the helical-fibre mesh, and each 3D element is a tetrahedron. The

meshes on the opposite boundary surfaces are identical so as to impose the periodic boundary condition. The fibre and the matrix have a common surface mesh which means the nodes on the common mesh surface belong to both the fibre and matrix volumes; the local boundary condition set by Equation 3.10 is therefore satisfied.

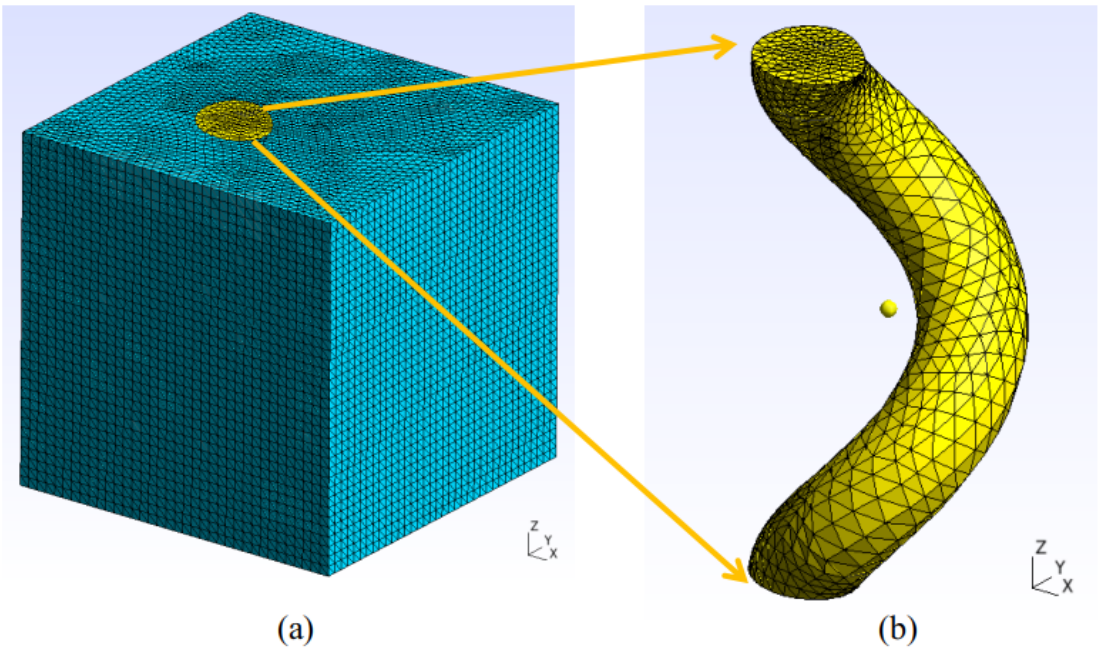

(a) (b)

Figure 3.12: An example finite element mesh of one REV of the helical-fibre-reinforced composite. Here, the number of elements is 168640. (a) Global view of the REV mesh. (b) Mesh of the helical fibre in the REV.

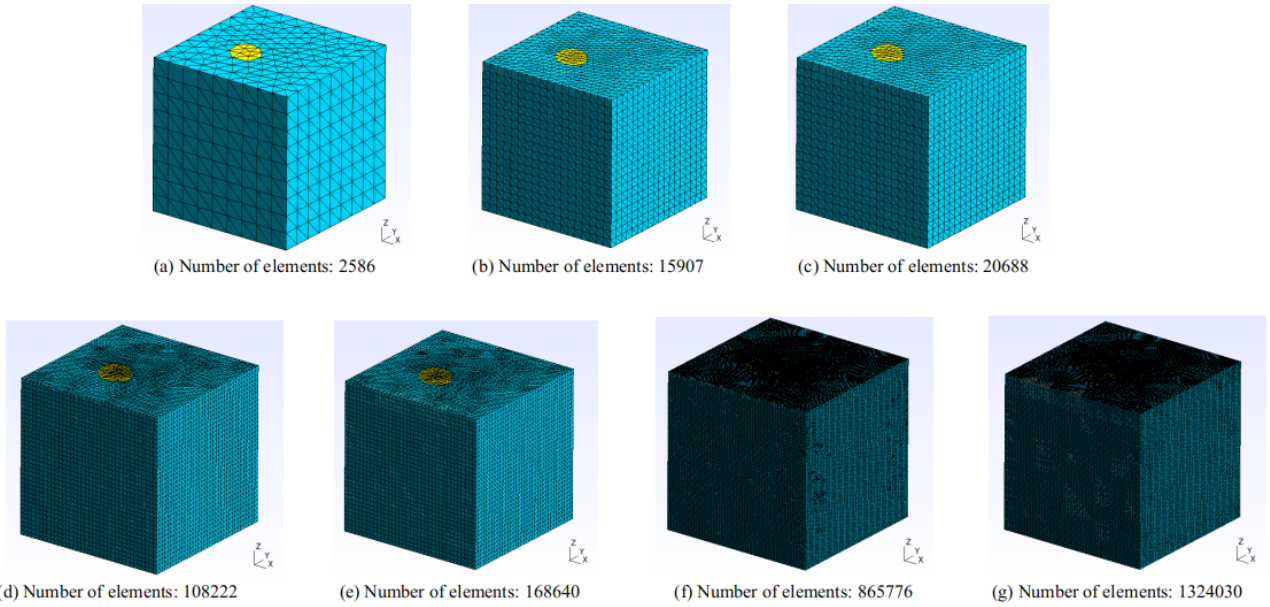

Figure 3.13: Meshes of increasing number of elements studied in finite element analysis for helical-fibres-reinforced composite.

As for the straight-fibre-reinforced composite, in order to optimize our mesh, and therefore the results that we obtain when studying its mechanical behavior in response to applied forces, we carried out a mesh-convergence study as shown in Figure 3.13, where the number of elements of each mesh is also presented. The mesh convergence study is accurate to $10^{-4}MPa$ and the computed values of each component of the effective elastic tensor for the different meshes are shown in Figure 3.14. We consider the material as an anisotropic composite and the effective elastic stiffness tensor C^H_{ij} is expressed as:

$$\left[C^H\right] = \begin{bmatrix} {C^H}_{11} & {C^H}_{12} & {C^H}_{13} & 0 & 0 & 0 \\ {C^H}_{12} & {C^H}_{22} & {C^H}_{23} & 0 & 0 & 0 \\ {C^H}_{13} & {C^H}_{23} & {C^H}_{33} & 0 & 0 & 0 \\ 0 & 0 & 0 & {C^H}_{44} & 0 & 0 \\ 0 & 0 & 0 & 0 & {C^H}_{55} & 0 \\ 0 & 0 & 0 & 0 & 0 & {C^H}_{66} \end{bmatrix}. \tag{3.114}$$

As shown in Figure 3.14, when the number of elements in the mesh is greater than 860000, each parameter of the effective elastic stiffness tensor is stable. We therefore consider our calculations of the effective elastic tensor to be reliable when the number of elements in the mesh is greater than 860000.

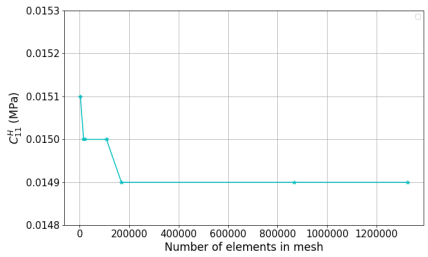

(a) C^H_{11}

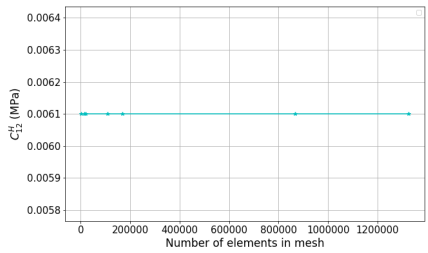

(b) C^H_{12}

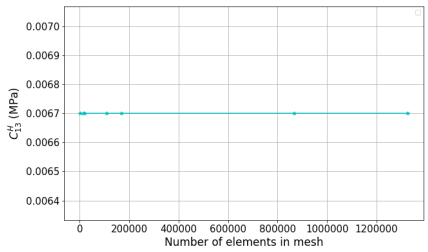

(c) C^H_{13}

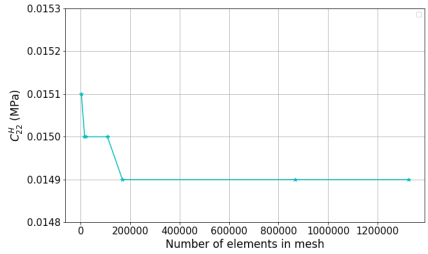

(d) C^H_{22}

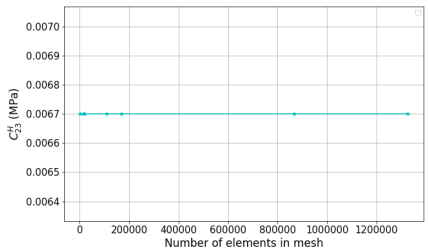

(e) C^H_{23}

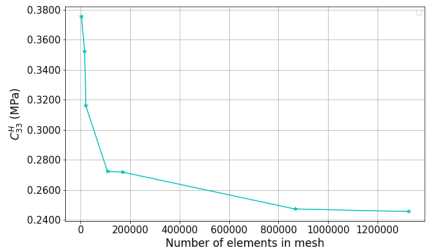

(f) C^H_{33}

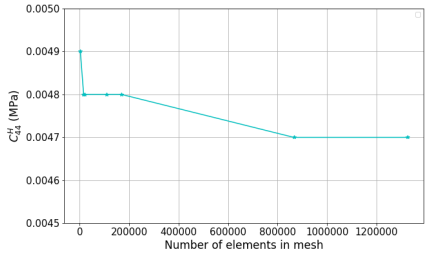

(g) C^H_{44}

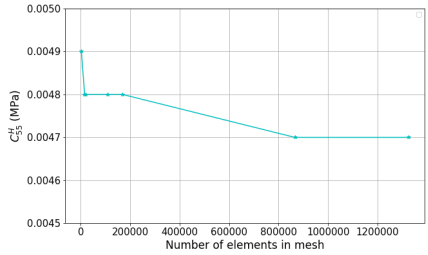

(h) C^H_{55}

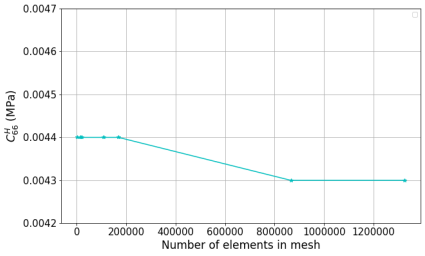

(i) C^H_{66}

Figure 3.14: Each nonzero parameter value of the elastic stiffness tensor C^H versus the number of elements in the mesh.

3.4 Helical fibres with cross-links

In this section, we study helical fibres cross-linked by straight fibres using the double-scale asymptotic homogenization method. The leading direction of the helix is set parallel to the z-axis and the cross-links are set perpendicular to the z-axis (see Fig. 3.15). The helical fibres and the cross-link fibres are set to be made from the same material, of which the elastic modulus is set to $100MPa$ and the Poisson's ratio is set to 0.3.

3.4.1 Representative elementary volume

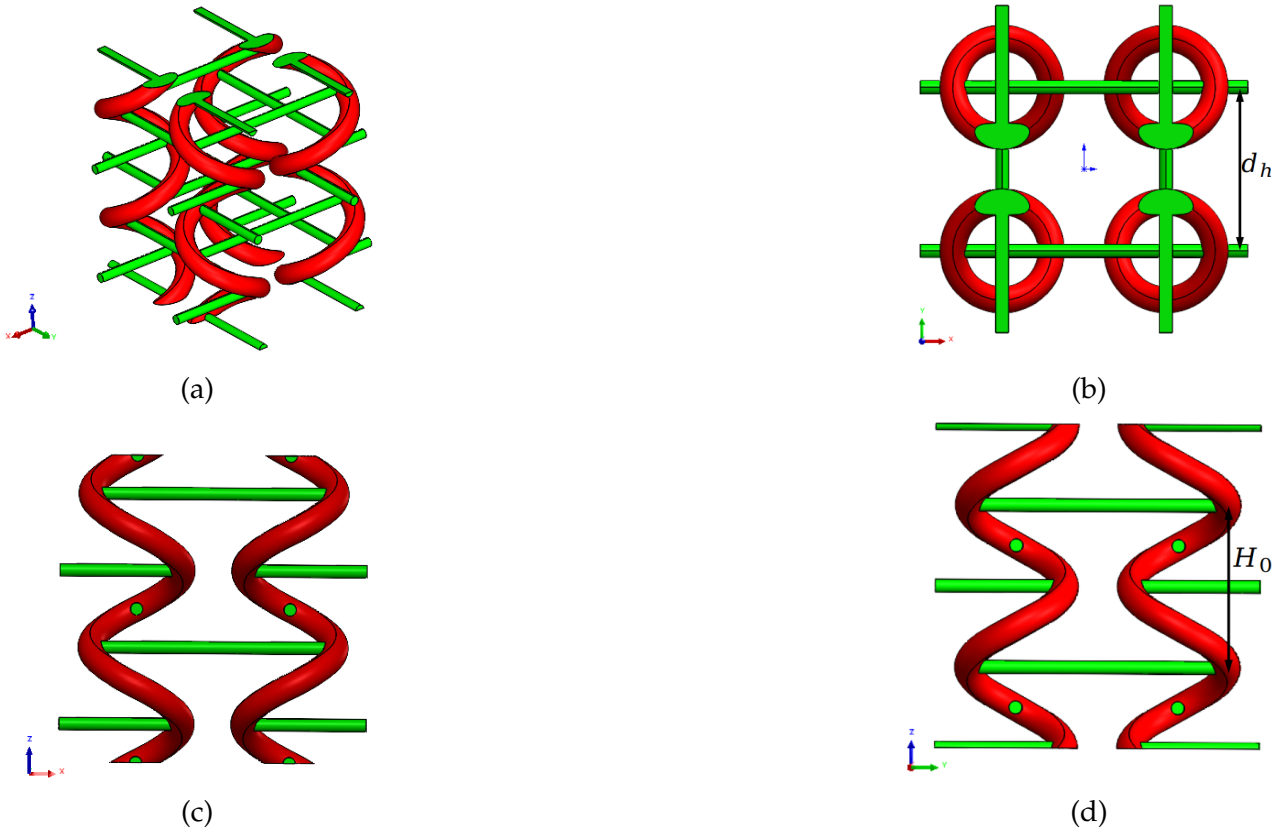

(a) (b) (c) (d)

Figure 3.15: (a) REV of helical fibres cross-linked by straight fibres. (b) View of the REV in the xy plane. (c) View of the REV in the zx plane. (d) View of the REV in the zy plane. The red structures represent the helical fibres and the cross-links are shown in green.

Figure 3.15a shows an example REV of the helical fibres cross-linked by straight fibres, and Figures 3.15b, 3.15c and 3.15d show 2D images of this REV in the xy plane, the zx plane, and the zy plane, respectively. The REV under study can be characterized by the helix shape, as presented in section 3.3.1, the diameter of the cross-link fibres, which is set to $\frac{1}{2}d_0$,

the distance between two adjacent helices d_h, which is set to the same value as helix pitch H_0, $d_h = H_0$, and the position of the cross-link fibres. The cross-linking fibres are set to connect helical fibres at either their closest points (cross-link of minimum length) or farthest points (cross-link of maximum length) as two study cases. The REV in Figure 3.15 shows an example of helical fibres connected at their farthest points. In our study, we investigate the effects of fibre volume fraction ρ_f, helix angle β, and cross-link position (closest vs farthest) on the macroscopic mechanical properties of our modeled materials. The calculation results are discussed in the section 3.6.2.

As the REV under study in this case contains just one material, the fibre volume fraction ρ_f is defined as

$$\rho_f = \frac{F_v}{V_{rev}}, \tag{3.115}$$

where V_{rev} is the volume of the periodic 3D cuboid.

3.4.2 Mesh convergence study

Figure 3.16 shows the finite element analysis mesh of one REV of cross-linked helical fibres. The surface meshes on opposite boundary surfaces are set to be identical and each 3D element of mesh is a tetrahedron.

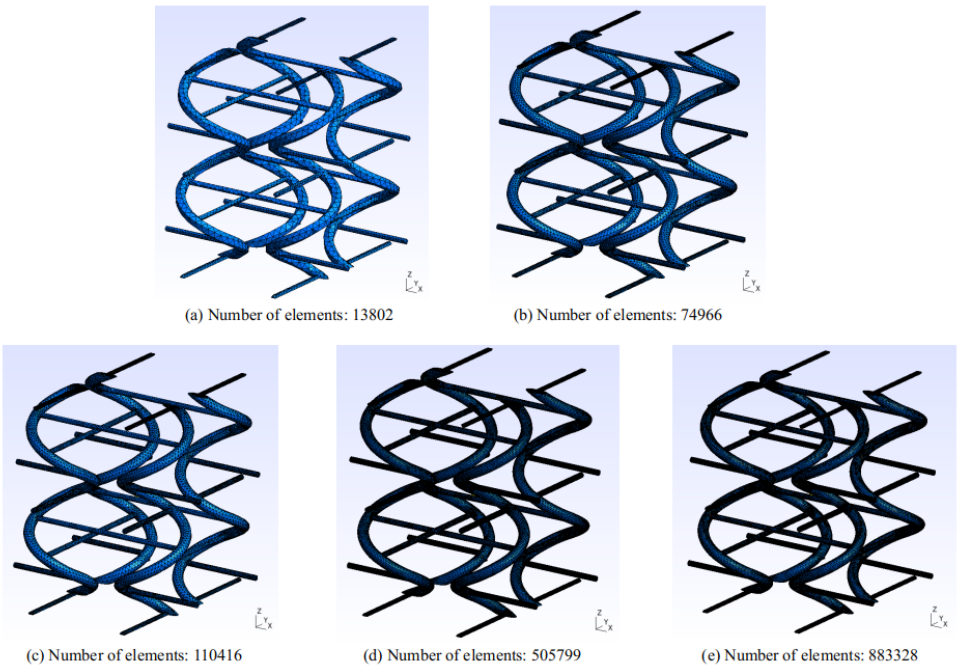

Figure 3.16: Meshes of increasing number of elements studied in a finite element analysis of cross-linked helical fibres.

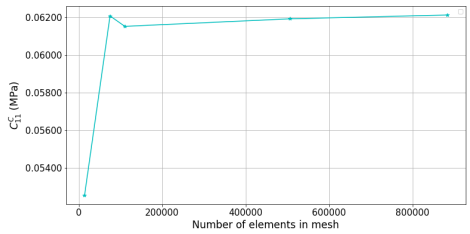

(a) C^c_{11}

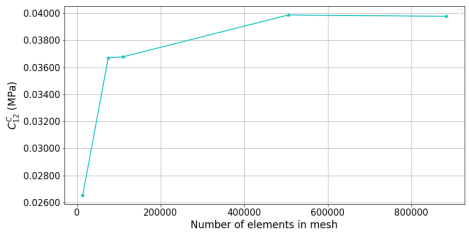

(b) C^c_{12}

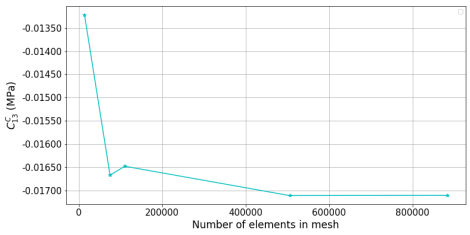

(c) C^c_{13}

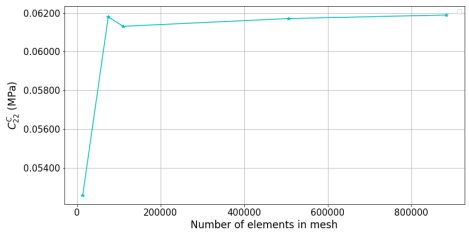

(d) C^c_{22}

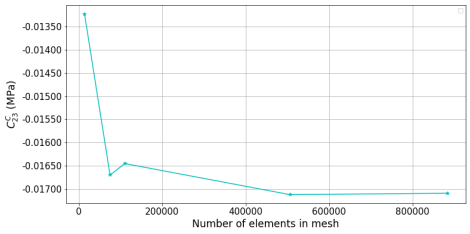

(e) C^c_{23}

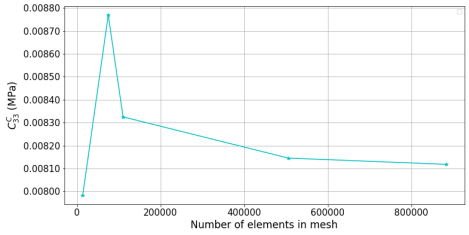

(f) C^c_{33}

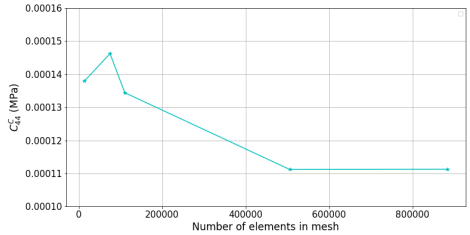

(g) C^c_{44}

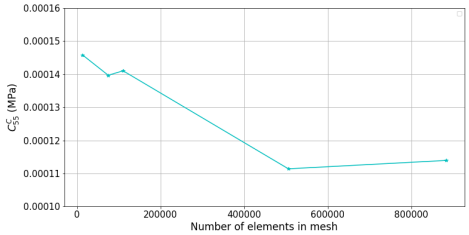

(h) C^c_{55}

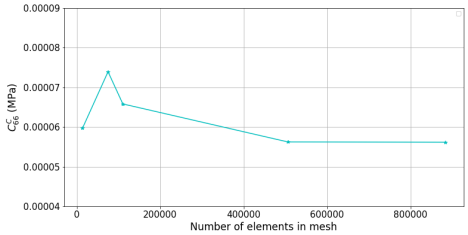

(i) C^c_{66}

Figure 3.17: Each non-zero parameter value of the elastic stiffness tensor C^c versus number of element in mesh.

As for the straight-fibre- and helical-fibre-reinforced composites, in order to optimize the results that we obtain for the helical fibres with cross-links but no matrix, we carried out a mesh convergence study as shown in Figure 3.16, where the number of elements of each mesh is also presented. This mesh convergence study is accurate to $10^{-5}MPa$ and the computed values of each component of the effective elastic tensor for different mesh sizes are shown in Figure 3.17. We consider the material as an anisotropic composite and the effective elastic stiffness tensor C^c has the same form as the tensor shown in Equation 3.114.

As shown in Figure 3.17, each parameter of the effective elastic stiffness tensor either increases or decreases as the mesh fineness increases, until the number of elements in the mesh is greater than about 500000, after which all parameters stabilize and mesh fineness no longer has an effect. We therefore consider our calculations of the effective elastic tensor of this particular mesh to be reliable when the number of elements in the mesh is greater than 500000.

3.5 Composite reinforced by cross-linked helical fibres

In this section, we use the double-scale asymptotic homogenization method to study the mechanical properties of a composite reinforced by helical fibres with cross-links. As above, the helix lead direction is set parallel to the z-axis, the cross-links are set perpendicular to the z-axis, and the helical fibres and cross-links are set to be made from the same material, as in section 3.4. The elastic modulus of the fibres is set to $100MPa$ and the elastic modulus of the matrix is set to $10KPa$. The Poissonâ€™s ratio of both the fibres and the matrix is set to 0.3.

3.5.1 Representative elementary volume

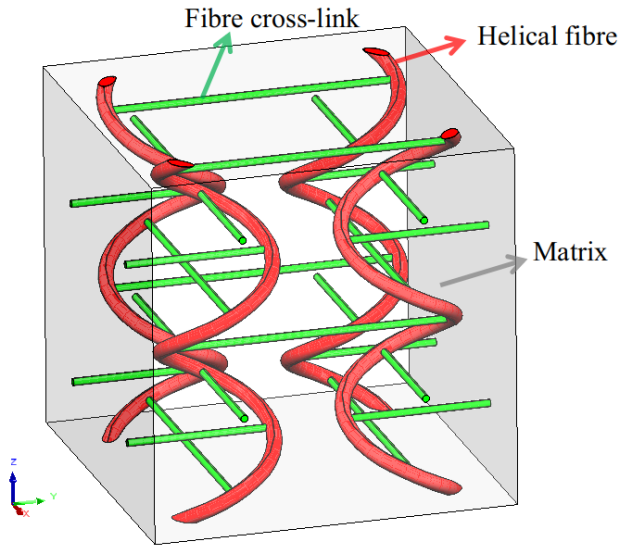

Figure 3.18: One REV of the composite of matrix reinforced by helical fibres with cross-links.

Figure 3.18 shows one REV of the composite of matrix reinforced by helical fibres with cross-links, where the red structures represent the helical fibres, the green structures are the straight cross-link fibres, and the matrix is shown in transparent gray. The fibre structure here is made up of helical fibres cross-linked by straight fibres, as described in section 3.4.1. In the present study, we study the effects of fibre volume fraction ρ_f, helix angle β, and cross-link position (closest vs farthest) on the macroscopic mechanical properties of the composite. The calculation results are discussed in the section 3.6.3.

3.5.2 Mesh convergence study

As in Section 3.3.2, we generated a REV of the finite element mesh of the composite reinforced by cross-linked helical fibres (Figure 3.19). Figure 3.19a shows a global view of the mesh of one REV and 3.19b shows just the mesh of the cross-linked helical fibres embedded within. Each 3D element of the mesh is a tetrahedron and the meshes on the opposite boundary surfaces are identical so as to impose the periodic boundary condition. The fibre and the matrix have a common surface mesh that shares the nodes of the fibre volume and those of the matrix so that the local boundary condition is satisfied.

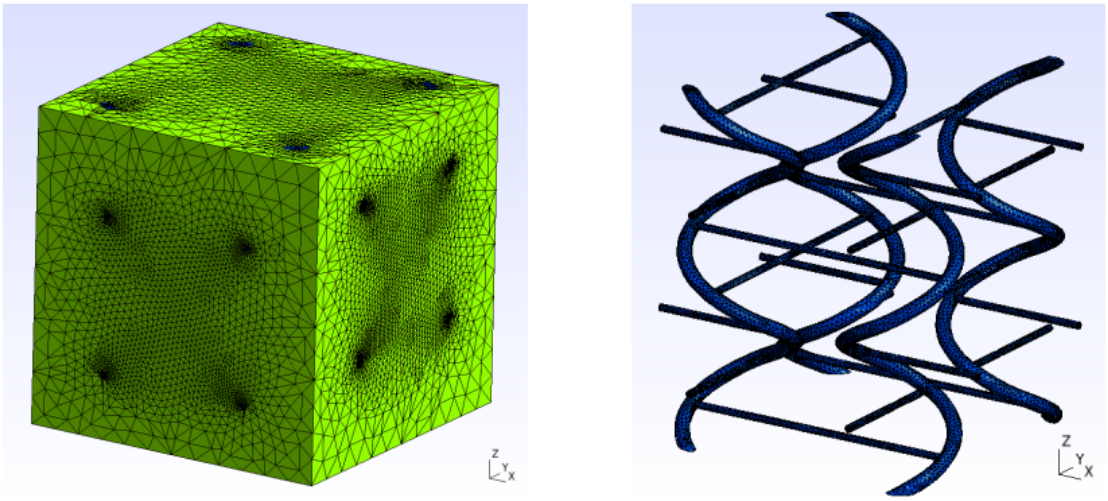

Figure 3.19: An example finite element mesh of one REV of matrix composite reinforced by cross-linked helical fibres. Here, the number of elements is 964546. (a) Global view of the REV mesh. (b) Mesh of the cross-linked helical fibres embedded in the REV.

Again, in order to optimize the results calculated using the mesh for this particular composite, we carried out a mesh convergence study, as shown in Figure 3.20, where the number of elements of each mesh is also presented. The mesh convergence study is accurate to $10^{-4}MPa$, and Figure 3.21 shows the computed values of each component of the effective elastic tensor for meshes of increasing fineness. We consider the material as an anisotropic composite and the effective elastic stiffness tensor C^{HC} has the same form as the tensor shown in equation 3.114.

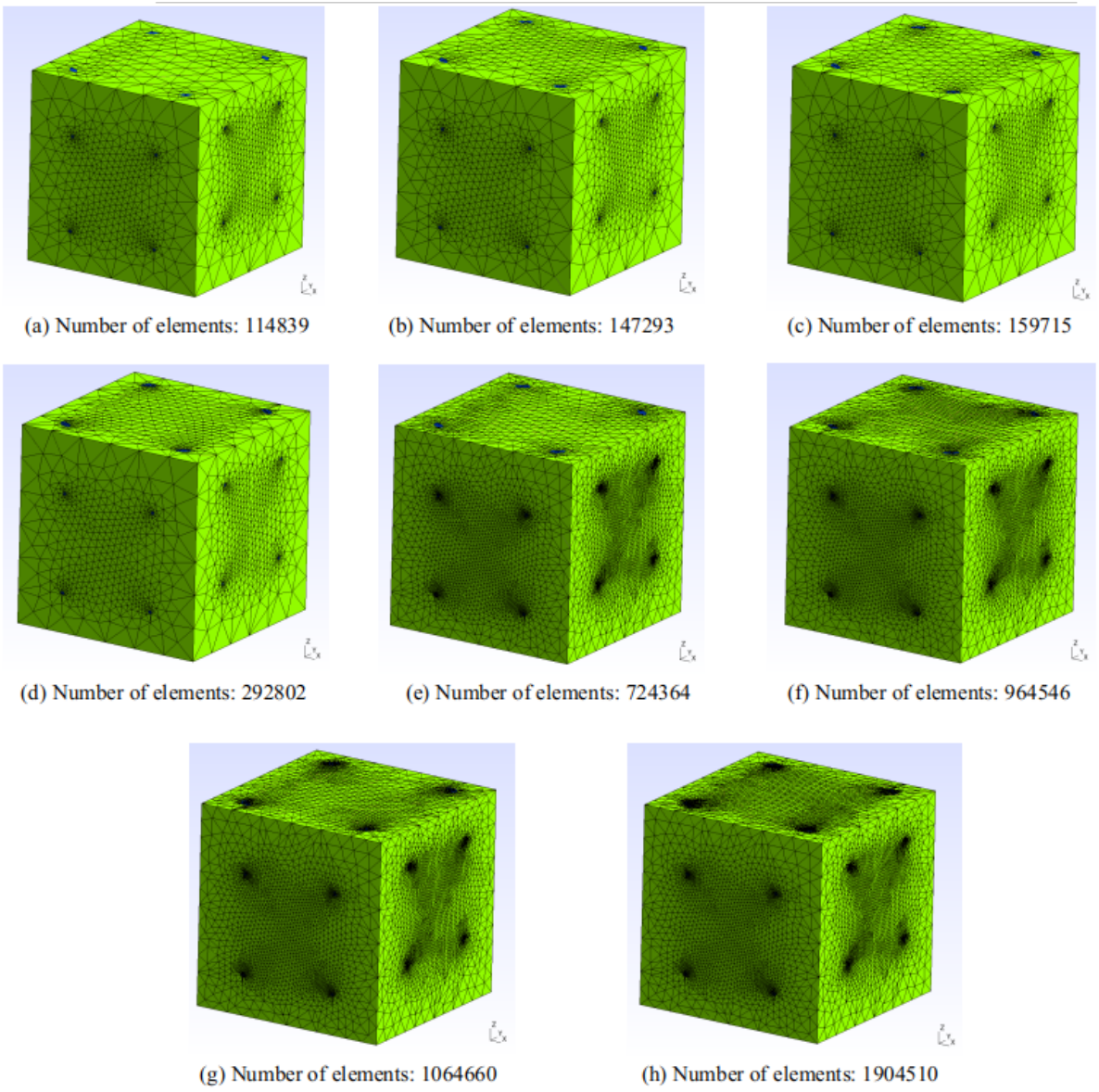

Figure 3.20: Meshes of increasing number of elements studied in a finite element analysis of one REV of composite reinforced by cross-linked helical fibres.

As shown in Figure 3.21, when the number of elements in the mesh is greater than about 10^6, each parameter of the effective elastic stiffness tensor stabilizes. Therefore, we consider that our evaluation of these parameters is reliable when the number of the elements is greater than 10^6.

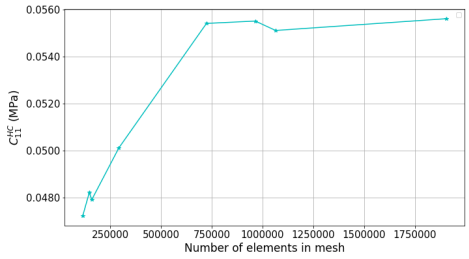

(a) C_{11}^{HC}

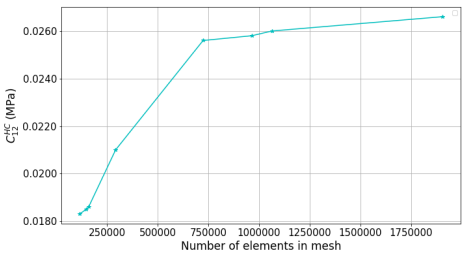

(b) C_{12}^{HC}

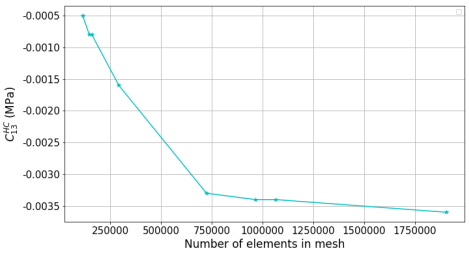

(c) C_{13}^{HC}

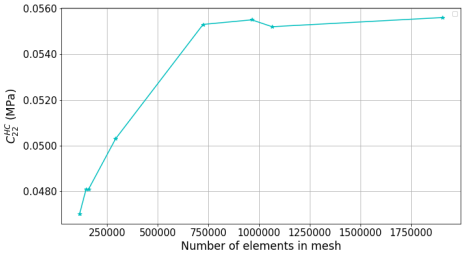

(d) C_{22}^{HC}

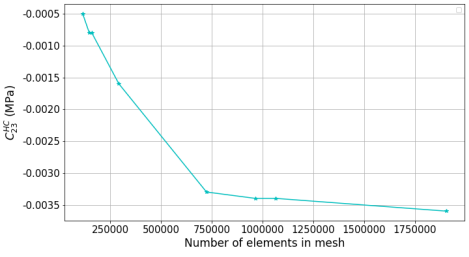

(e) C_{23}^{HC}

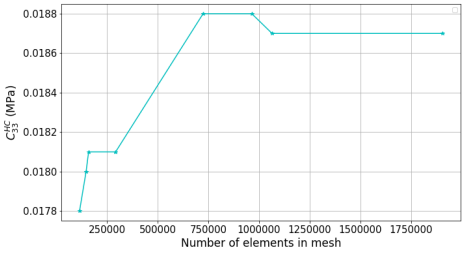

(f) C_{33}^{HC}

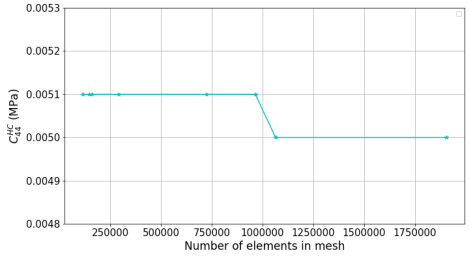

(g) C_{44}^{HC}

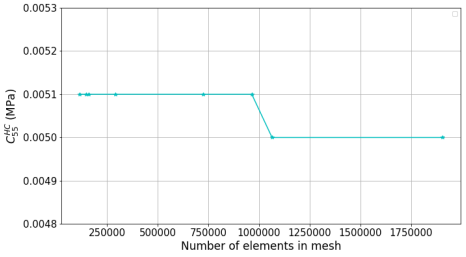

(h) C_{55}^{HC}

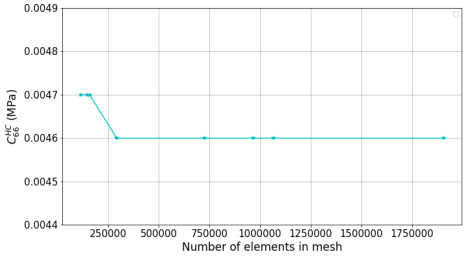

(i) C_{66}^{HC}

Figure 3.21: Each nonzero parameter value of the elastic stiffness tensor C^{HC} versus number of elements in the mesh.

3.6 Results

Here, we present the results of simulations of the effective mechanical properties of composite reinforced by helical fibres, helical fibres with cross-links and no matrix, and composite reinforced by helical fibres with cross-links in Sects. 3.6.1, 3.6.2, and 3.6.3, respectively. The effective engineering moduli are obtained from the effective elastic tensor C_{ij} (here, C_{ij} represents C_{ij}^H, C_{ij}^c, or C_{ij}^{HC} according to the application needs) as

$$\begin{cases} E_x = \dfrac{1}{S_{11}} & E_y = \dfrac{1}{S_{22}} & E_z = \dfrac{1}{S_{33}} \\ \nu_{xy} = -\dfrac{S_{21}}{S_{11}} & \nu_{xz} = -\dfrac{S_{31}}{S_{11}} & \nu_{yz} = -\dfrac{S_{32}}{S_{22}} \\ \nu_{yx} = -\dfrac{S_{12}}{S_{22}} & \nu_{zx} = -\dfrac{S_{13}}{S_{33}} & \nu_{zy} = -\dfrac{S_{23}}{S_{33}} \end{cases}, \tag{3.116}$$

where S_{ij} is the inverse effective elastic tensor C_{ij} expressed as

$$S_{ij} = C_{ij}^{-1}. \tag{3.117}$$

3.6.1 Composite reinforced by helical fibres

Figure 3.22 shows the effective elastic modulus of composite reinforced by helical fibres as a function of fibre volume fraction ρ_f and helix angle β. The red points are the results calculated using the double-scale asymptotic homogenization method, and the surface is the predicted trend surface passing through each red point. Compared with helix angle β, the fibre volume fraction ρ_f has a greater impact on the elastic moduli E_x^H and E_y^H; as the fibre volume fraction increases, E_x^H and E_y^H also increase, but as helix angle increases, E_x^H and E_y decline slightly. As ρ_f grows, E_z^H also grows, but unlike E_x^H and E_y^H, E_z grows with increasing β.

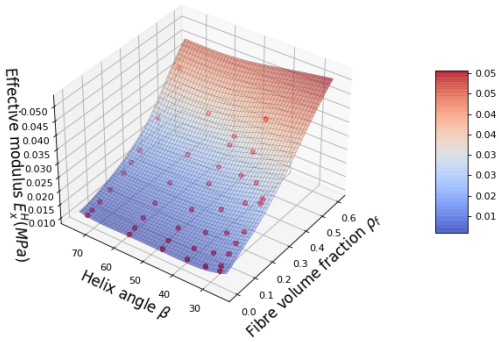

(a) E_x^H

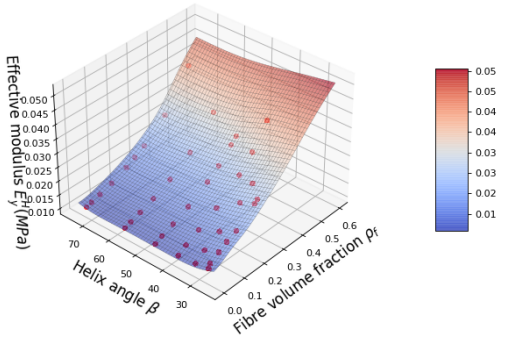

(b) E_y^H

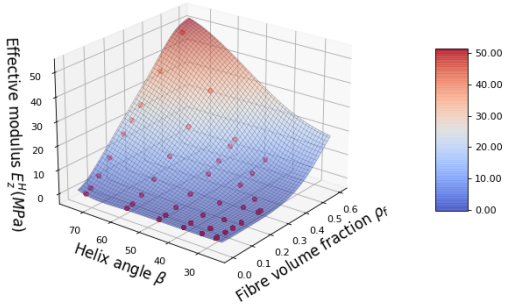

(c) E_z^H

Figure 3.22: Effective axial elastic modulus of composite reinforced by helical fibres along (a) the x-axis E_x^H, (b) y-axis E_y^H, and (c) z-axis E_z^H as a function of fibre volume fraction ρ_f and helix angle β.

Figure 3.23 shows how the effective Poisson's ratio of composite reinforced by helical fibres (no cross-links) ν_{ij}^H varies with changes to fibre volume fraction ρ_f and helix angle β. Compared with helix angle β, the fibre volume fraction ρ_f has more influence on ν_{xy}^H and ν_{yx}^H. As ρ_f increases, ν_{xy}^H and ν_{yx}^H increase until an approximate value of 0.1, after which they decrease. Both ν_{xz}^H and ν_{yz}^H reach their maximum value when ρ_f and β are small.

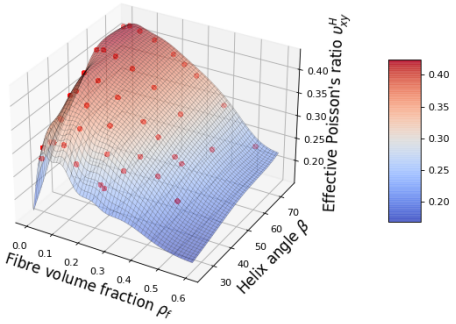

(a) ν^H_{xy}

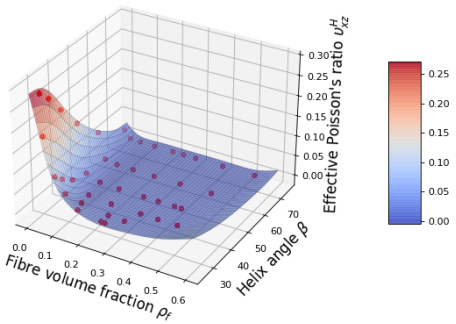

(b) ν^H_{xz}

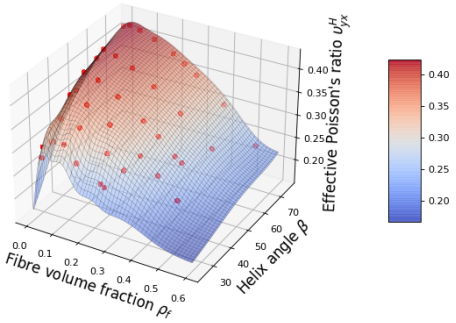

(c) ν^H_{yx}

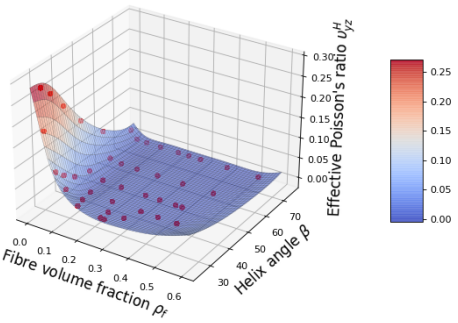

(d) ν^H_{yz}

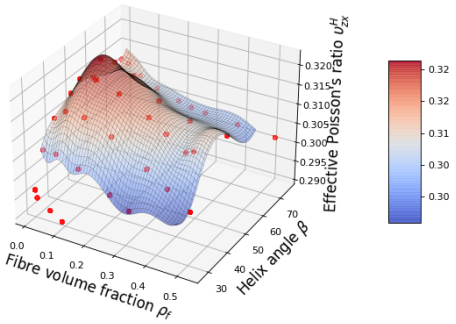

(e) ν^H_{zx}

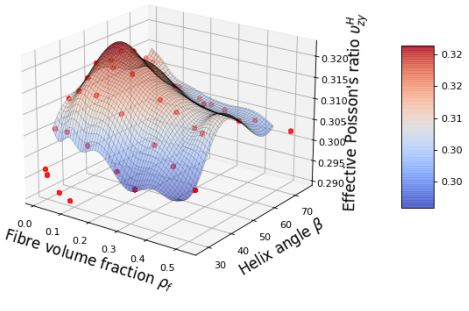

(f) ν^H_{zy}

Figure 3.23: Effective Poisson's ratios of composite reinforced by helical fibres, (a) ν^H_{xy}, (b) ν^H_{xz}, (c) ν^H_{yx}, (d) ν^H_{yz}, (e) ν^H_{zx}, and (f) ν^H_{zy} as a function of fibre volume fraction ρ_f and helix angle β.

3.6.2 Helical fibres with cross-links alone

In this section, we present the results of our calculations of the mechanical properties of helical fibres with cross-links (no matrix). In order to study the effect of cross-link position (closest vs farthest) on the mechanical properties of our model, we tested two extremes, with straight cross-links between helical fibres connecting the nearest helical fibres at the furthest possible points or at the nearest possible points; one REV of each case is shown in Figure 3.24.

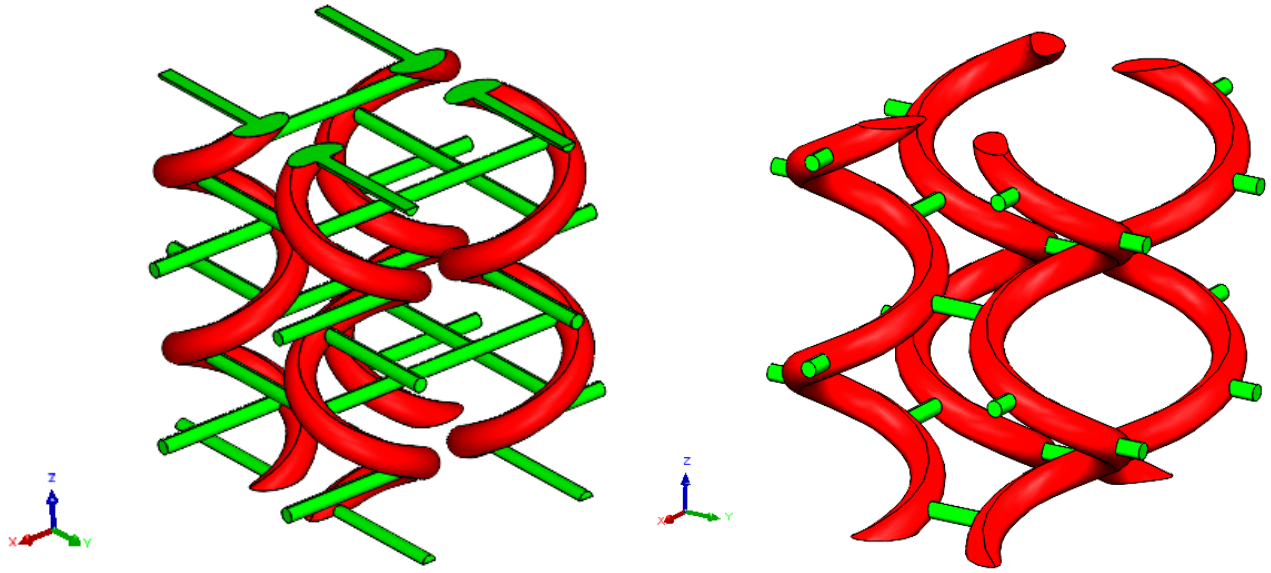

(a) (b)

Figure 3.24: REVs of the helical fibres with cross-links showing the two different cross-link positions studied. (a) Straight cross-link fibres connect adjacent helical fibres at the farthest points (longest-possible cross-links). (b) Straight cross-link fibres connect adjacent helical fibres at the nearest points (shortest-possible cross-links).

3.6.2.1 Farthest connection points case

Figure 3.25 shows how the effective elastic modulus E^c of helical fibres with the longest cross-links (furthest cross-link positions) varies with changes to fibre volume fraction ρ_f and helix angle β. As the fibre volume fraction ρ_f grows, E^c_x, E^c_y and E^c_z increase. As helix angle β rises, E^c_x, E^c_y, and E^c_z also increase slightly.

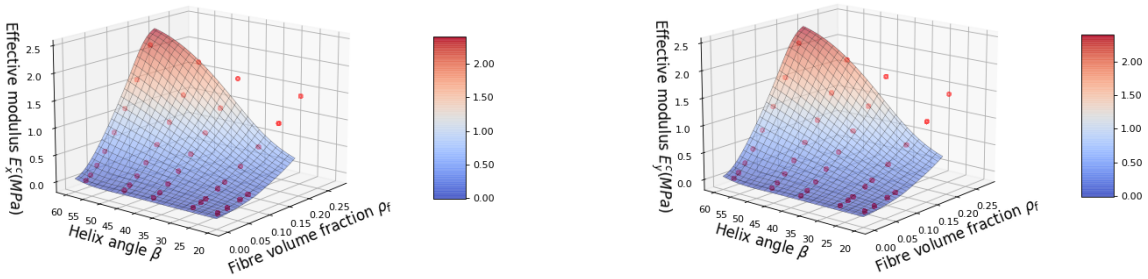

(a) E_x^c

(b) E_y^c

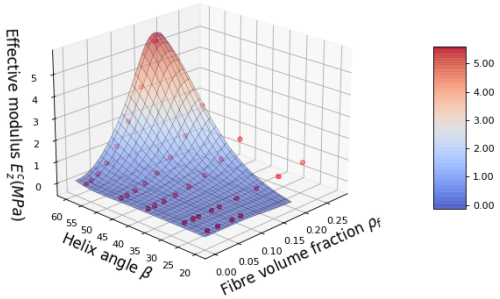

(c) E_z^c

Figure 3.25: Effective axial elastic modulus of helical fibres with the longest cross-links (connecting the nearest fibres at the farthest points) along the (a) x-axis E_x^c, (b) y-axis E_y^c, and (c) z-axis E_z^c as a function of fibre volume fraction ρ_f and helix angle β.

Figure 3.26 shows how the effective Poisson's ratio ν_{ij}^c of helical fibres with the longest cross-links, which connect the nearest fibre at the furthest point, varies with changes to fibre volume fraction ρ_f and helix angle β. As β increases, ν_{yz}^c and ν_{xz}^c increase but ν_{xy}^c, ν_{yx}^c, ν_{zx}^c, and ν_{zy}^c decrease. As ρ_f rises, ν_{xy}^c and ν_{yx}^c decrease but ν_{xz}^c and ν_{yz}^c increase. ν_{zx}^c and ν_{zy}^c both rise with increasing ρ_f when β takes large values, but as β decreases, ν_{zx}^c and ν_{zy}^c are decreasingly sensitive to changes in ρ_f. We note that the structure studied here shows some negative Poisson's ratios when the helical fibres are cross-linked at the furthest possible points; that is, ν_{xz}^c, ν_{yz}^c, ν_{zx}^c and ν_{zy}^c are observed to have a negative value. Furthermore, the values of ν_{xz}^c and ν_{yz}^c are at a minimum when ρ_f and β are small, and ν_{zx}^c and ν_{zy}^c are at their minimum when ρ_f is small and β is large.

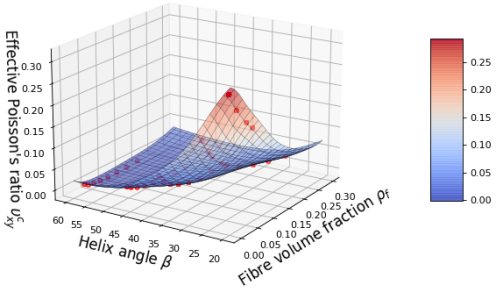

(a) ν^c_{xy}

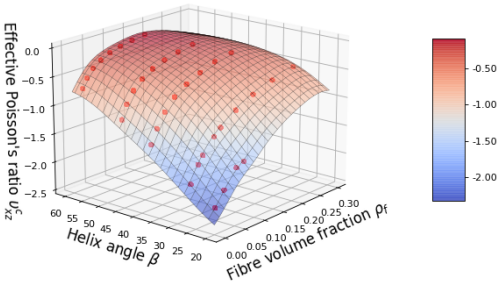

(b) ν^c_{xz}

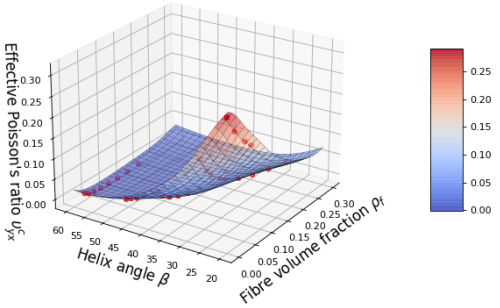

(c) ν^c_{yx}

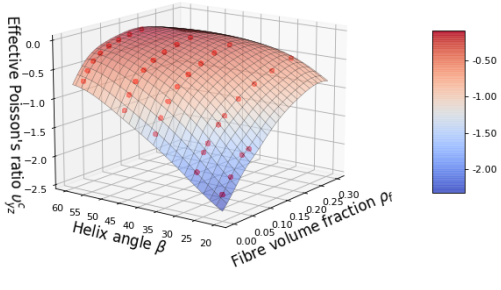

(d) ν^c_{yz}

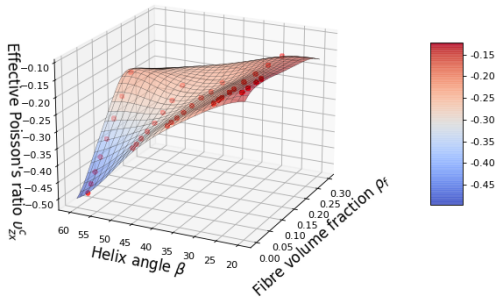

(e) ν^c_{zx}

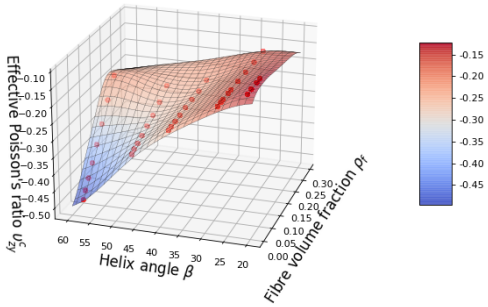

(f) ν^c_{zy}

Figure 3.26: Effective Poisson's ratios of helical fibres with the longest cross-links (connecting the nearest fibres at the furthest points): (a) ν^c_{xy}, (b) ν^c_{xz}, (c) ν^c_{yx}, (d) ν^c_{yz}, (e) ν^c_{zx}, and (f) ν^c_{zy} as a function of fibre volume fraction ρ_f and helix angle β.

3.6.2.2 Nearest connection points case

Figure 3.27 shows how the effective elastic modulus E^c of helical fibres with the shortest possible cross-links, which connect adjacent fibres at the nearest points, varies with changes to fibre volume fraction ρ_f and helix angle β. The results reveal the same tendency as seen for helical fibres cross-linked a the farthest possible points; see section 3.6.2.1. As the fibre volume fraction ρ_f grows, E_x^c, E_y^c, and E_z^c increase. As helix angle β rises, E_x^c, E_y^c, and E_z^c also increase slightly.

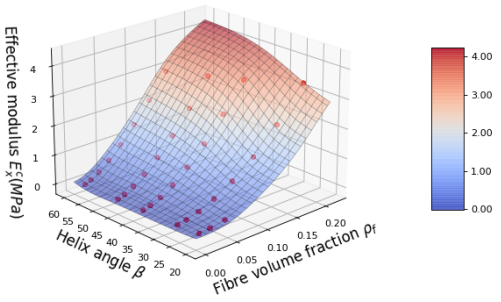

(a) E_x^c

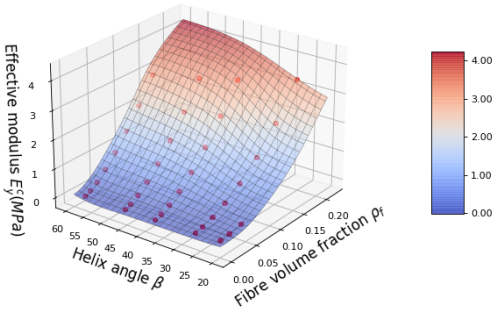

(b) E_y^c

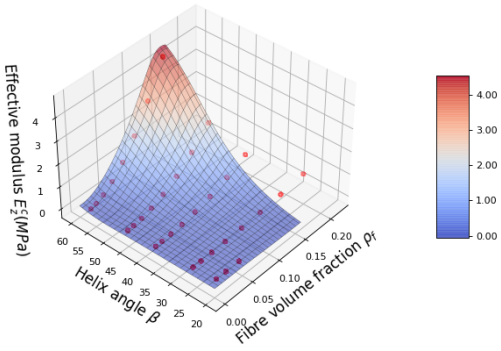

(c) E_z^c

Figure 3.27: Effective axial elastic modulus of helical fibres with the shortest possible cross-links (connecting adjacent fibres at the nearest point) along the (a) x-axis E_x^c, (b) y-axis E_y^c, and (c) z-axis E_z^c as a function of fibre volume fraction ρ_f and different helix angle β.

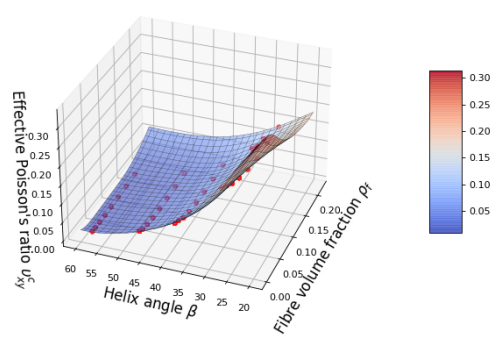

(a) ν_{xy}^c

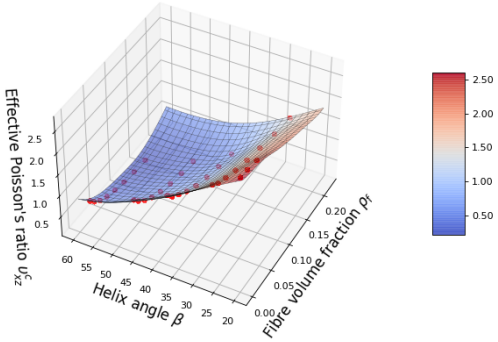

(b) ν_{xz}^c

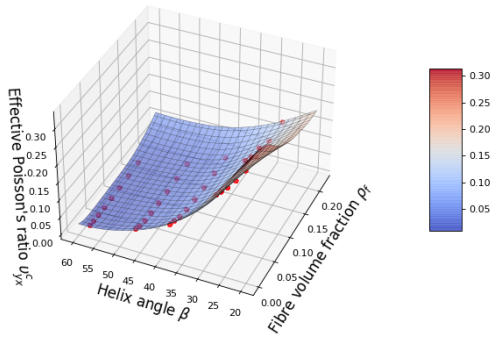

(c) ν_{yx}^c

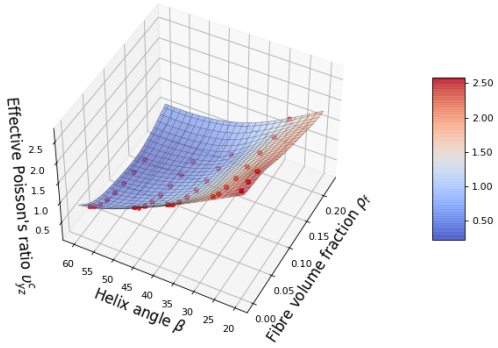

(d) ν_{yz}^c

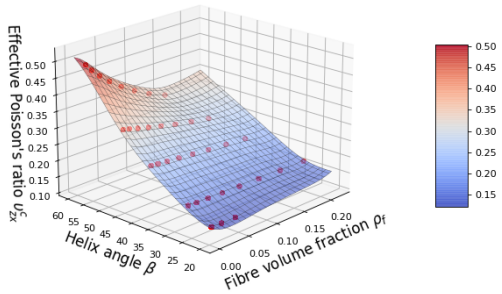

(e) ν_{zx}^c

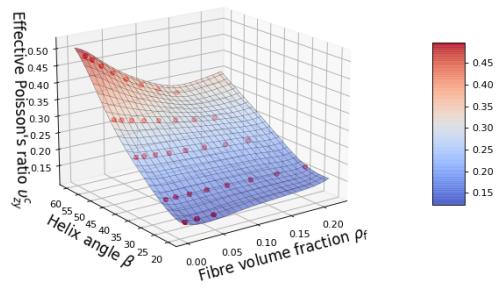

(f) ν_{zy}^c

Figure 3.28: Effective Poisson's ratios of helical fibres with the shortest possible cross-links (connecting adjacent fibres at the nearest point): (a) ν_{xy}^c, (b) ν_{xz}^c, (c) ν_{yx}^c, (d) ν_{yz}^c, (e) ν_{zx}^c, and (f) ν_{zy}^c as a function of fibre volume fraction ρ_f and helix angle β.

Figure 3.28 shows how the effective Poisson's ratios ν_{ij}^c of helical fibres with the shortest possible cross-links, which connect adjacent fibres at the nearest points, vary with changes

to fibre volume fraction ρ_f and helix angle β. As β increases, ν^c_{zx} and ν^c_{zy} also increase but ν^c_{xy}, ν^c_{yx}, ν^c_{xz}, and ν^c_{yz} decrease. As ρ_f rises, ν^c_{xy}, ν^c_{yx}, ν^c_{xz}, ν^c_{yz}, ν^c_{zx}, and ν^c_{zy} decrease slightly. As apposed to the fibres shown in Sect. 3.6.2.1, where the cross-links are as long as possible between helical fibres, the structure studied here, where the cross-links are as short as possible, shows no negative Poisson's ratios. Indeed, larger effective Poisson's ratios (> 0.5) are observed. ν^c_{xz} and ν^c_{yz} are found at their maximum values when ρ_f and β are small, and ν^c_{zx} and ν^c_{zy} are found to be at their maximum values when ρ_f is small and β is large.

3.6.3 Composite reinforced by helical fibres with cross-links

In this section, we present our calculations of the mechanical behavior of our model composite reinforced by helical fibres with cross-links. Here, we again test the same two cross-link positions as tested in Sect 3.6.2. Figure 3.29 shows REVs of the two composites studied here, with the longest- and shortest-possible cross-links between helical fibres, respectively.

(a) (b)

Figure 3.29: REVs of the matrix composites reinforced by helical fibres with cross-links, showing the two different cross-link positions studied. (a) Straight cross-link fibres connect adjacent helical fibres at the farthest points (longest-possible cross-links). (b) Straight cross-link fibres connect adjacent helical fibres at the nearest points (shortest-possible cross-links).

3.6.3.1 Farthest connection points case

Figure 3.30 shows how the effective elastic modulus E^{HC} of our composite reinforced by helical fibres with the longest possible cross-links, which connect adjacent fibres at the furthest points, varies with changes to fibre volume fraction ρ_f and helix angle β. The results show the same tendency as seen for our observations of the effective elastic modulus

of cross-linked helical fibres with no matrix presented in Sects. 3.6.2.1 and 3.6.2.2. As the fibre volume fraction ρ_f grows, E_x^{HC}, E_y^{HC}, and E_z^{HC} increase. As helix angle β rises, E_x^{HC}, E_y^{HC}, and E_z^{HC} also increase slightly.

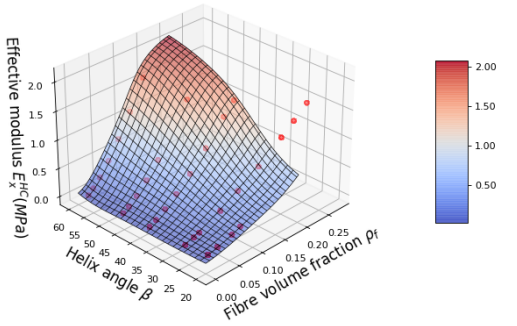

(a) E_x^{HC}

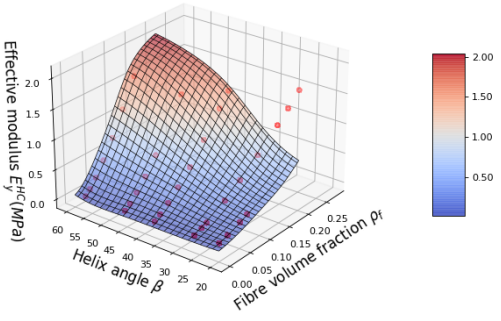

(b) E_y^{HC}

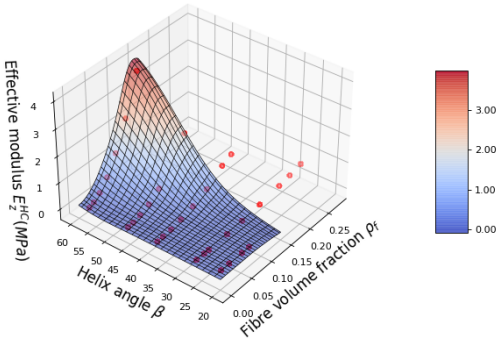

(c) E_z^{HC}

Figure 3.30: Effective axial elastic moduli of composite reinforced by helical fibres with the longest possible cross-links (connecting adjacent fibres at the furthest points) along the (a) x-axis E_x^{HC}, (b) y-axis E_y^{HC}, and (c) z-axis E_z^{HC} as a function of fibre volume fraction ρ_f and helix angle β.

Figure 3.31 shows how the effective Poisson's ratios ν_{ij}^{HC} of composite reinforced by helical fibres with the longest possible cross-links, which connect the nearest fibre at the furthest point, varies with changes to fibre volume fraction ρ_f and helix angle β. As β increases, ν_{xy}^{HC}, ν_{yx}^{HC}, ν_{zx}^{HC}, and ν_{zy}^{HC} decrease. As ρ_f increases, ν_{xy}^{HC} and ν_{yx}^{HC} decrease, ν_{zx}^{HC} and ν_{zy}^{HC} change slightly, and ν_{xz}^{HC} and ν_{yz}^{HC} decrease until a value of $_f$ of about 0.06 and then increase again. We note that the structure studied here shows some negative Poisson's ratios. Our matrix composite reinforced by helical fibres with the longest possible cross-links shows negative values for the Poisson's ratios ν_{xz}^{HC}, ν_{yz}^{HC}, ν_{zx}^{HC}, and ν_{zy}^{HC}. As opposed to the

same fibre structure but without matrix, as shown in section 3.6.2.1, the minimum values of ν_{xz}^{HC} and ν_{yz}^{HC} (-0.6) are larger than ν_{xz}^{c} and ν_{zy}^{c} (-2.5), and the minimum values do not occur at the same trend point as in the case without matrix.

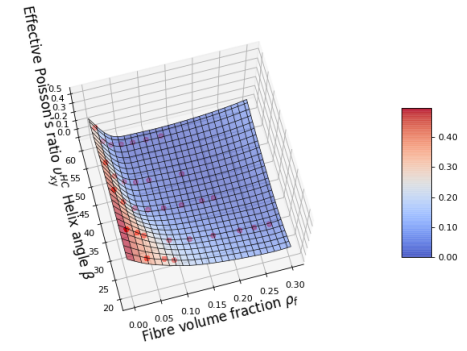

(a) ν_{xy}^{HC}

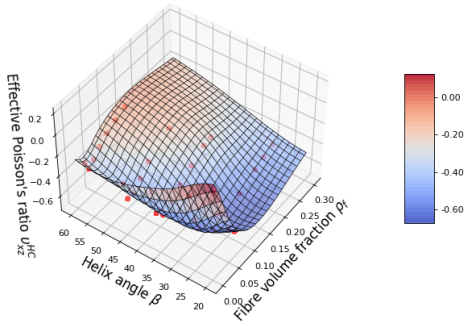

(b) ν_{xz}^{HC}

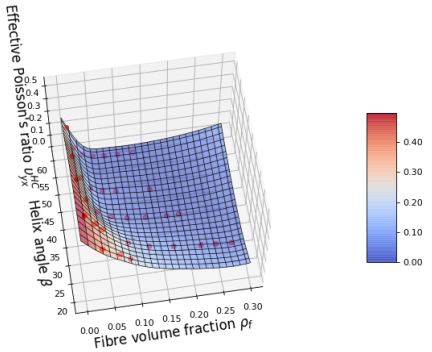

(c) ν_{yx}^{HC}

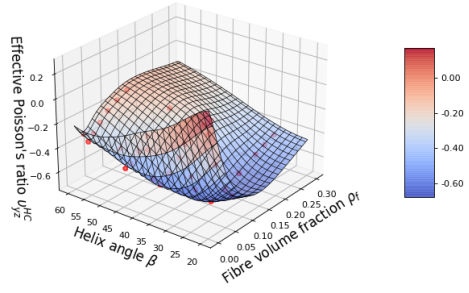

(d) ν_{yz}^{HC}

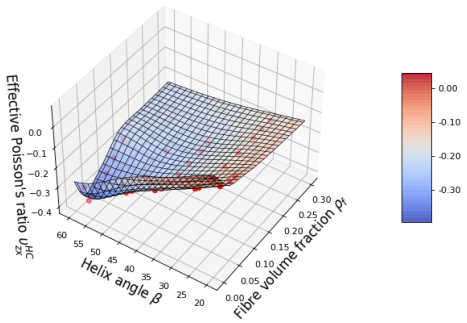

(e) ν_{zx}^{HC}

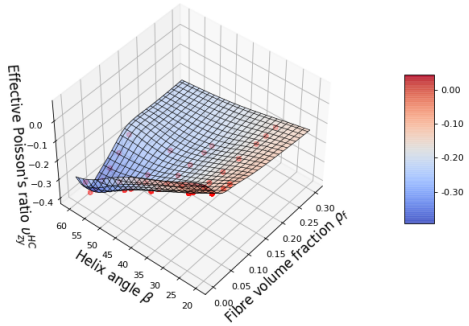

(f) ν_{zy}^{HC}

Figure 3.31: Effective Poisson's ratios of composite reinforced by helical fibres with the longest possible cross-links (connecting adjacent fibres at the furthest points): (a) ν_{xy}^{HC}, (b) ν_{xz}^{HC}, (c) ν_{yx}^{HC}, (d) ν_{yz}^{HC}, (e) ν_{zx}^{HC}, and (f) ν_{zy}^{HC} as a function of fibre volume fraction ρ_f and helix angle β.

3.6.3.2 Nearest connection points case

Figure 3.32 shows how the effective elastic modulus E^{HC} of our matrix composite reinforced by helical fibres with the shortest possible cross-links, which connect adjacent fibres at the nearest points, varies with changes to fibre volume fraction ρ_f and helix angle β. The results show the same tendencies as those seen for helical fibres with cross-links in either position and without matrix in Sections 3.6.2.1 and 3.6.2.2 and the helical fibres in matrix with longer cross-links in Section 3.6.3.1. As the fibre volume fraction ρ_f grows, E_x^{HC}, E_y^{HC}, and E_z^{HC} increase. As helix angle β rises, E_x^{HC}, E_y^{HC}, and E_z^{HC} also increase slightly.

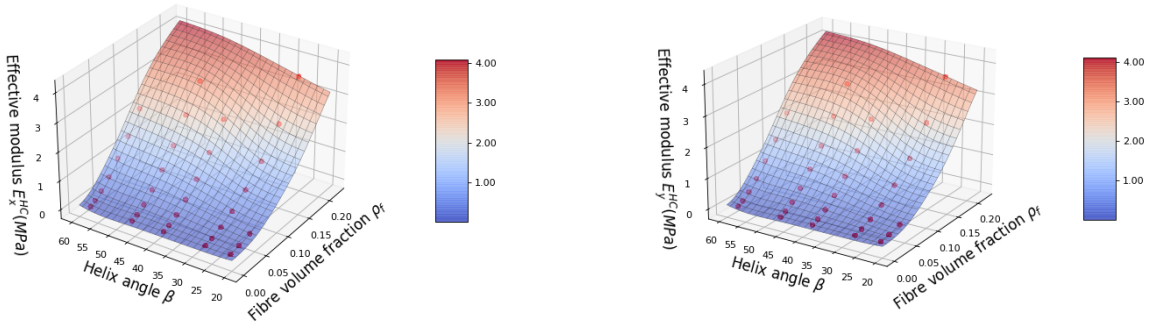

(a) E_x^{HC}

(b) E_y^{HC}

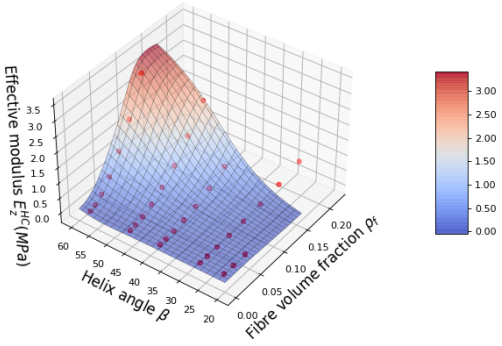

(c) E_z^{HC}

Figure 3.32: Effective axial elastic modulus of matrix composite reinforced by helical with the longest possible cross-links (connecting adjacent fibres at the nearest points) along the (a) x-axis E_x^{HC}, (b) y-axis E_y^{HC}, and (c) z-axis E_z^{HC} as a function of fibre volume fraction ρ_f and helix angle β.

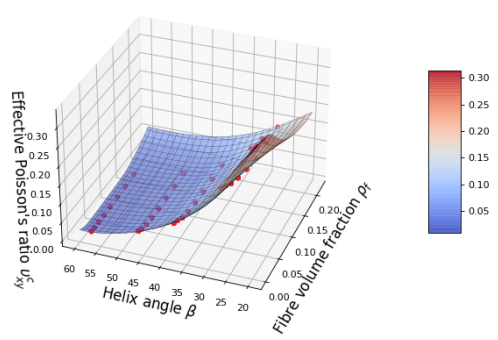

(a) ν_{xy}^{HC}

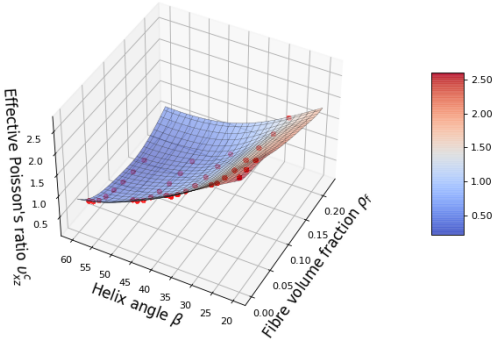

(b) ν_{xz}^{HC}

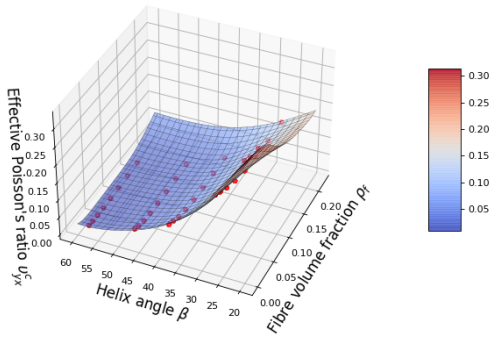

(c) ν_{yx}^{HC}

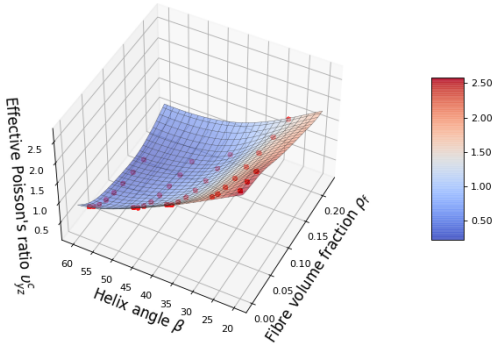

(d) ν_{yz}^{HC}

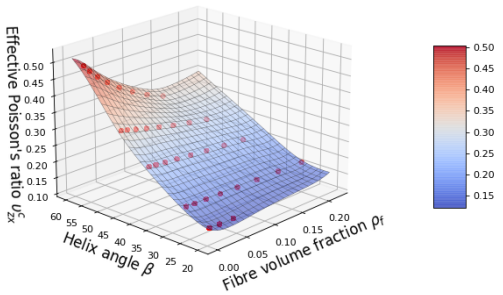

(e) ν_{zx}^{HC}

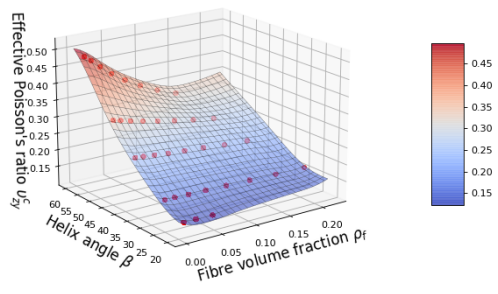

(f) ν_{zy}^{HC}

Figure 3.33: Effective Poisson's ratios of matrix composite reinforced by helical fibres with the shortest possible cross-links (connecting adjacent fibres at the nearest points): (a) ν_{xy}^{HC}, (b) ν_{xz}^{HC}, (c) ν_{yx}^{HC}, (d) ν_{yz}^{HC}, (e) ν_{zx}^{HC}, and (f) ν_{zy}^{HC} as a function of fibre volume fraction ρ_f and helix angle β.

Figure 3.33 shows how the effective Poisson's ratios ν_{ij}^{HC} of our matrix composite

reinforced by helical fibres with the shortest possible cross-links, which connect adjacent fibres at the nearest points, varies with changes to fibre volume fraction ρ_f and helix angle β. Compared with helix angle β, the fibre volume fraction ρ_f has little influence on the effective Poisson's ratios ν_{ij}^{HC}. As β increases, ν_{xy}^{HC}, ν_{yx}^{HC}, ν_{zx}^{HC}, and ν_{zy}^{HC} decrease, but ν_{zx}^{HC} and ν_{zy}^{HC} increase. Our matrix composite reinforced by helical fibres with the shortest possible cross-links shows no negative Poisson's ratios. However, it does show larger effective Poisson's ratios (> 0.5). ν_{xz}^{HC} and ν_{yz}^{HC} are found at maximum values when ρ_f and β are small, which is the same tendency observed for helical fibres with the shortest possible cross-links but without matrix, presented in section 3.6.2.2

3.7 Discussion

In this chapter, we study the mechanical properties of matrix composite reinforced by helical fibres, helical fibres with cross-links alone, and matrix composite reinforced by helical fibres with cross-links using a double-scale asymptotic homogenization method. These model structures are designed to mimic the possible structures that exist in soft tissues, which are outlined in the literature review provided in Section 3.1 of this thesis.

As shown in Figure 3.22 of section 3.6.1, helix angle β has little effect on the effective moduli E_x^H and E_y^H of a matrix composite reinforced by helical fibres without cross-links but does affect E_z^H. For this same model, as β increases, E_z^H also increases. In other words, the larger the fibre corrugation level, the smaller the effective elastic modulus in the direction of the principle fibre orientation, which is the same trend as that observed for the composite reinforced by 2D corrugated fibres presented in Chapter 2. In addition, as fibre volume fraction ρ_f increases, the effective elastic modulus increases along all three axes, that is, E_x^H, E_y^H, and E_z^H all increase, because the elastic modulus of the fibre is set to $100MPa$, which is significantly higher than the elastic modulus of the matrix $10KPa$. As shown in Figures 3.25, 3.27, 3.30, and 3.32 in sections 3.6.2.1, 3.6.2.2, 3.6.3.1 and 3.6.3.2, respectively, the effective modulus of helical fibres with cross-links shows the same tendency: as fibre volume fraction ρ_f and helix angle increase, the three effective elastic moduli along the axes x, y, and z increase regardless of the cross-link position or the presence of matrix. In addition, the matrix composite reinforced by helical fibres with no cross-links exhibits the behavior of a transverse isotropic material, with identical mechanical properties in the directions of the x and y axes but different mechanical properties in the direction of the z-axis, as shown in Figure 3.22. As we place cross-links at the same positions on adjacent helical fibres in the x-y plane, helical fibres with cross-links (with or without matrix) also show transverse isotropic mechanical behavior, as shown in Figures 3.25, 3.27, 3.30, and 3.32.

As the modeled materials studied here show identical transverse isotropic behavior

in the x-axis and y-axis, the effective Poisson's ratios are related as follows: $\nu_{xy} = \nu_{yx}$, $\nu_{xz} = \nu_{yz}$, and $\nu_{zx} = \nu_{zy}$, as shown in Figures 3.23, 3.26, 3.28, 3.31, and 3.33. As introduced in Sect. 2.6, the term ν_{ij} is the effective Poisson's ratio that characterizes the strain in the j direction produced by the load in the i direction. The Poissonâ€™s ratios of both the fibre and the matrix are set to 0.3, but the effective Poisson's ratios of the composite or helical fibres with cross-links vary with the helix angle β and the fibre volume fraction ρ_f. Negative effective Poisson's ratios are found in helical fibres with the longest possible cross-links —where adjacent helical fibres are connected at the furthest points— with or without the presence of matrix. Negative Poisson's ratios have also been reported in soft tissues such as skin [*Veronda and Westmann*, 1970], carotid arteries [*Timmins et al.*, 2010], tendons [*Gatt et al.*, 2015], and annulus fibrosus tissues [*Baldit et al.*, 2014][*Derrouiche et al.*, 2019a][*Dusfour et al.*, 2020] based on uni-axial tests. On the other hand, our modeled helical fibres with the shortest possible cross-links —where adjacent helical fibres are connected at the nearest points— show larger effective Poisson's ratios (> 0.5). Such larger Poisson's ratios are also widely reported in tendons [*Lynch et al.*, 2003] *Cheng and Screen* [2007] [*Vergari et al.*, 2011], ligament[*Hewitt et al.*, 2001], and arterial wall [*Skacel and Bursa*, 2022]. Neither negative Poisson's ratios nor larger Poisson's ratios are observed in the helical-fibre-reinforced composite without cross-links in the cases we studied. However, *Reese et al.* [2010] found larger Poisson's ratios in their uni-helical fibres reinforced composite, which might be due to one or more of the particular characteristics of their mechanical model or its helical fibre arrangement. In our study, we find the two cross-link positions we test lead to strikingly opposing Poisson's ratios, that is, larger positive and negative ratios. Cross-linking in collagen fibres is considered to be an age-related feature [*Hayashi and Hirayama*, 2017] and its effects on the stiffness of soft tissues were studied by *Holzapfel and Ogden* [2020]. However, the effects of cross-linking on the geometrical form of soft tissue has not been studied before. Interestingly, in the absence of matrix, the helical fibres with the longest possible cross-links, which connect adjacent helical fibres at furthest points, show a large negative Poisson's ratio of about -2.5, as presented in Figure 3.26. Such negative Poisson's ratios are significantly smaller in composites where the fibres are surrounded by matrix, as shown in Figure 3.31. This might suggest that the presence of matrix weakens the auxetic behavior. This may explain why negative Poisson's ratios are more rarely observed than larger positive Poisson's ratios. In order to mimic soft tissue, *Yan et al.* [2020] proposed a network material based on helical microstructure. Their material shows a good stress–strain curve match to real soft tissue, but no matrix is included in their design.

In conclusion, in the present study we focus on the helical fibre structure of soft tissue and use a modeling approach to study the effects of the presence of matrix and cross-links between helical fibres on the mechanical properties of soft fibrilar tissue. Our results

show that the position of the cross-links between helical fibres has no effect on the effective elastic modulus of a group of fibres with or without the presence of a surrounding matrix. However, cross-link position does appear to have an influence on the geometrical form of the material modeled here, and the Poisson's ratio of our model can be positive or negative depending on the position of the cross-links between helical fibres. Further, the matrix might control the auxetic behavior. We think that considering cross-links associated with specific and more realistic structural arrangements of fibres may allow greater insights to be gained from soft tissue models. In addition, the present work could become a reference for further biomimetic material design.

CHAPTER 4

Fabrication and modeling of helical-fibre-reinforced soft composite materials

4.1 Introduction

In chapters 2 and 3, we focus on the structure of 2D (sinusoid) planar and 3D (helix) fibre corrugation in soft tissue using analytical model calculations and finite element analysis, respectively. The materials under study are considered as composites reinforced by corrugated fibres, where perfect interface conditions as well as a large stiffness difference are assumed for the fibres and matrix. Such materials have received little attention so far in terms of experimental study.

In this chapter, we present our development of silicone-based helical-fibre-reinforced composite materials. Our aim here is to find a method to manufacture such model materials that satisfy the fibre and matrix boundary conditions, and to verify that our method meets the requirements for finite element analysis. In addition, the elastic modulus ratio of fibre and matrix $\frac{E_f}{E_m}$ varies from 10^3 to 10^5 in the literature. Model material with such a large modulus ratio and perfect interface conditions is not easy to fabricate. However, as demonstrated in section 2.7.1.4, changes in modulus ratio when this value is larger than 10^2 have little effect on the overall mechanical properties. We, therefore, consider the modulus ratio $\frac{E_f}{E_m}$ at this value (e.g., $\frac{E_f}{E_m} = 10^2$ in section 2.7.1.4) can be applied to study the mechanical properties of materials with higher modulus ratios $\frac{E_f}{E_m}$. In our present work, several types of silicone are tested to reach the highest possible modulus ratio.

4.2 Materials and methods

We used soft and hard silicone to fabricate matrix and fibre materials, respectively. We first manufactured the fibre and matrix test samples to characterize their mechanical parameters, and then we manufactured and modeled soft composite according to these characterizations.

4.2.1 Helical fibre-reinforced soft composite fabrication

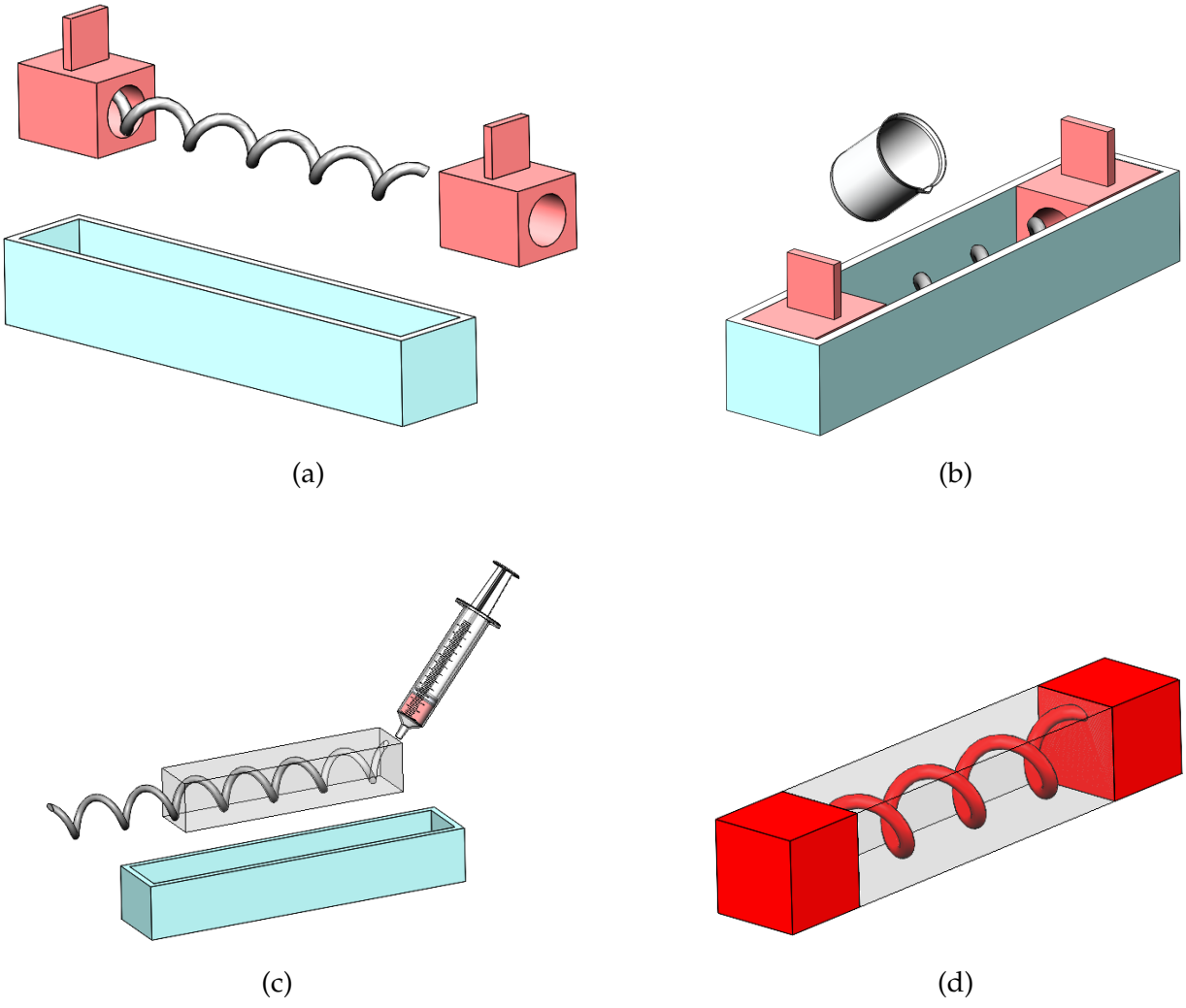

(a) (b) (c) (d)

Figure 4.1: Fabrication process of soft composites. (a) Smooth surface helix metal is placed in the plastic mold. (b) Ecoflex™ 00-10 (parts A and B mixed) is used to fill the mold and the curing process begins. (c) Helix metal is removed and Mold Max silicone (parts A and B mixed) is injected into the mold with a syringe. (d) Soft composite material sample after curing.

	Silicone product	Shore hardness	Mix ratio of part A and part B
Fibre material	Mold Max™ 29NV	29A	1 : 1
Matrix material	Ecoflex™ 00-10	10A	10 : 1

Table 4.1: Silicone material of the fibre and matrix.

The matrix material is Smooth-On Ecoflex™ 00-10 which is characterized by a Shore (durometer) hardness of 10A. The fibre materials are Mold Max™ 29NV with a Shore hardness of 29A. The silicone materials are also shown in Table 4.1. The choice of materials is based on satisfying the criteria that fibres and matrix have a large stiffness difference and that they stick to each other perfectly. For the matrix, part A and part B of the Ecoflex™ 00-10 soft silicone are mixed at a 1 : 1 ratio by weight. For the fibre, part A and part B of Mold Max™ 29NV are mixed at a 10 : 1 ratio by weight, according to the manufacturers instructions. The mixed silicone is placed in a vacuum chamber to remove the air bubbles. Before the composite fabrication, the mixed silicone materials —for both fibre and matrix— are injected into tensile specimen molds in order to manufacture tensile test specimens for characterization of material parameters for both components. The silicone is cured at room temperature ($23°C$) and then removed from the molds. The tensile test specimens of matrix and fibre are shown in Figure 4.2 (a) and 4.2 (b), respectively.

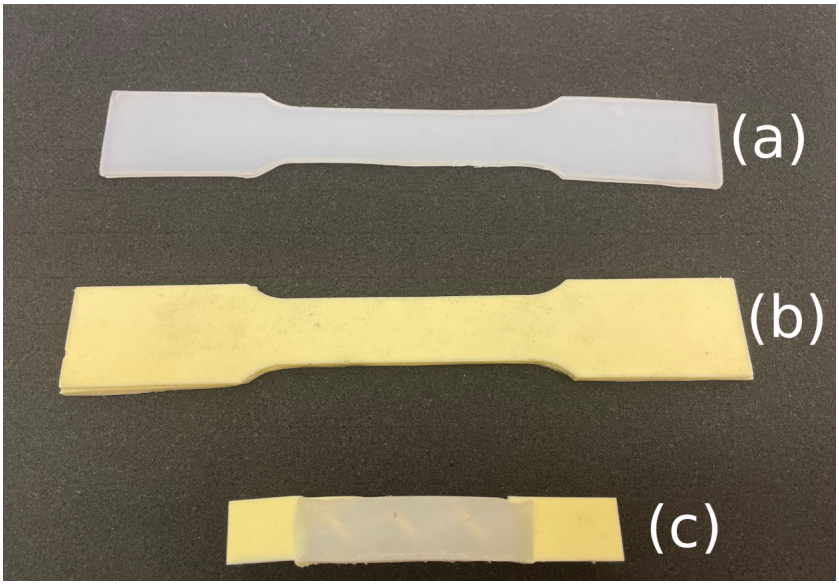

Figure 4.2: Photos of the starting materials of the helical-fibre-reinforced soft composite and the final synthesised soft-tissue composite. (a) Soft silicone matrix material, (b) hard silicone fibre material, and (c) soft tissue composites.

We note that Mold Mold Max™ series silicone can perfectly bind with Ecoflex™ series silicone during the curing process, but Ecoflex™ series silicone does not bind with Mold

Max™ series silicone. Due to the binding properties of silicone, the material of the matrix needs to be cured first: First, a metal helix with a smooth surface is used as a support and Ecoflex™ 00-10 is injected into the mold as shown in Figure 4.1a 4.1b. When the curing process is complete, the metal helix is removed and the Mold Max™ series series silicone is injected with a syringe into the cavity left behind, as shown in Figure 4.1c, to form the fibre material element of the soft-tissue composite. A schematic of the manufactured composite material is shown in Figure 4.1d and a photo of the final composite is shown in Figure 4.2c.

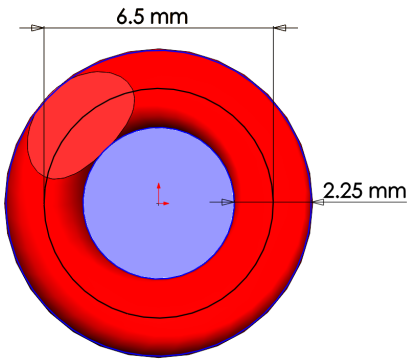

(a)

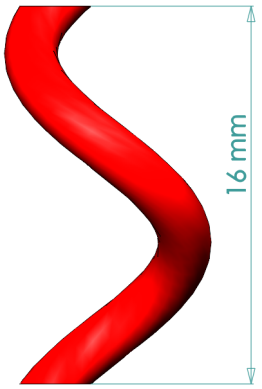

(b)

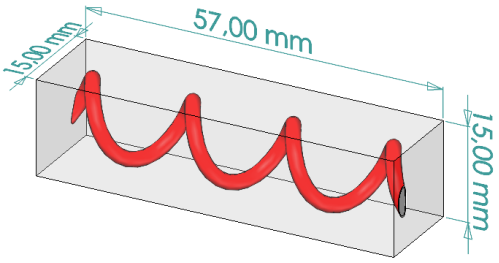

(c)

Figure 4.3: Helical-fibre-reinforced soft composite dimensions. (a) Helix diameter and fibre diameter. (b) Helical fibre pitch. (c) Soft-composite dimensions.

The section dimensions of the matrix test specimens are 20*2.9 mm^2 and the section dimensions of the fibre test specimens are 20*3.9 mm^2. The useful test part of the helical-

fibre-reinforced composite has section dimensions of 15*15 mm^2 and the length is 57 mm. The helical fibre pitch, helix diameter, and fibre diameter are respectively 16 mm, 6.5 mm, and 2.25 mm, as shown in Figure 4.3.

4.2.2 Experimental procedure

Each sample is clamped onto the Zwick/Roell tensile test machine (Type : TXT-TROLLEY-FZ.001, Xforce load cell : 200N) and is stretched at a constant velocity of 5 mm/min. Images of the samples are recorded during the tensile tests by two cameras (FUJINON/1:1.4 16mm HF16HA-1B), which are placed perpendicular to each other to record the stretch on the composite surface perpendicular to the loading direction; the strain is obtained by analysis of the images with VIC-2D® software. The tensile test equipment and image analysis interface are shown in Figures 4.4 and 4.5.

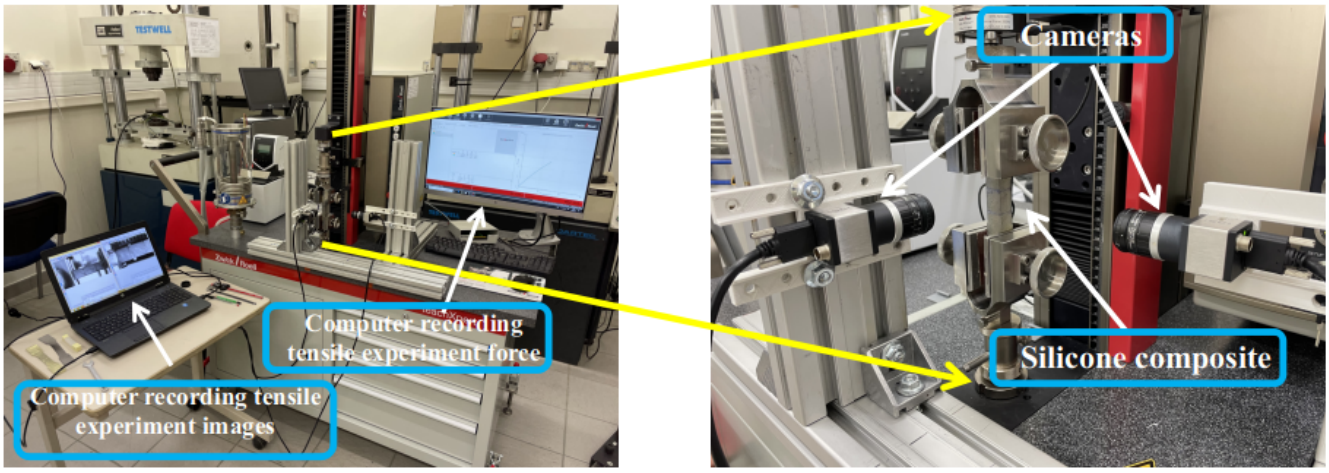

Figure 4.4: Tensile test equipment setup. The right panel shows a close-up photo of the Zwick/Roell tensile test machine and the positions of the cameras.

4.2.3 Models characterization

The fibre and matrix materials are characterized by a linear elastic model and two nonlinear hyperelastic models, one being the Yeoh model and the other the Neo-Hookean model.

The hyperelastic models are based on the definition of the strain-energy function ψ, which is dependent on the principal stretches (λ_1, λ_2, and λ_3) as:

$$\psi = \psi(B) = \psi(I_1, I_2, I_3) \tag{4.1}$$

$$B = FF^T \tag{4.2}$$

$$I_1 = Tr(B) \tag{4.3}$$

$$I_2 = \frac{1}{2}[I_1^2 - tr(B^2)] \tag{4.4}$$

$$I_3 = det(B) \tag{4.5}$$

Where F is the deformation gradient.

The constitutive equation for an incompressible, isotropic, hyperelastic material is given by *Avril and Evans* [2017] as:

$$\sigma = -p1 + 2\frac{\partial \psi}{\partial I_1}B - 2\frac{\partial \psi}{\partial I_2}B^{-1} \tag{4.6}$$

Where p is an undetermined scalar.

A particular type of strain energy functions can be written as:

$$\psi = \sum_{j=0}^{N_j}\sum_{i=0}^{N_i} C_{ij}(I_1 - 3)^i(I_2 - 3)^j \tag{4.7}$$

where when $N_i = 1$, and $N_j = 0$ is the Neo-Hookean strain energy function, and when $N_i = 3$, $N_j = 0$ is the Yeoh model strain energy function, and we take $N_i = 2$ for our Yeoh model material.

The Neo-Hookean and Yeoh models for predicting mechanical behavior under uniaxial tension can be reduced as:

$$\sigma_{Neo-Hookean} = 2C_{10}(\lambda^2 - \frac{1}{\lambda}) \tag{4.8}$$

$$\sigma_{Yeoh} = 2(C_{10} + 2C_{20}(I_1 - 3))(\lambda^2 - \frac{1}{\lambda}) \tag{4.9}$$

where λ is the stretch along the loading direction λ_1 and we assume that the stretch perpendicular to the loading direction λ_2 and λ_3 satisfies the following relationship:

$$\lambda = \lambda_1 \quad \lambda_2 = \lambda_3 = \frac{1}{\sqrt{\lambda}} \tag{4.10}$$

The hyperelastic model parameters of materials are determined by the least squares method.

4.2.4 Strain measurement

In the tensile test, since the strain at both ends is affected by the clamp, we only take the strain of the surface measured 20 mm from one end in the middle of the test sample by image analysis as shown in Figure 4.5. With two cameras, we record the strain on the side plane z-y and the side plane z-x; these axes are shown in Figure 4.5b. As the z-y and z-x planes are both parallel to the loading direction, the strain along the z-axis on the z-y plane and the strain along the z-axis on the z-x plane are identical, and this is verified by analysis of the results of the tensile test. We therefore take the strain on the z-y plane for further analysis. It is noted that the strains obtained by image-analysis software VIC-2D® are calculated with Green-Lagrangian formulations which can be expressed as (for strain along the z-axis on the z-y plane):

$$\varepsilon_{zz} = \frac{dw}{dz} + \frac{(\frac{dw}{dz})^2 + (\frac{dv}{dz})^2}{2} \tag{4.11}$$

Where ε_{zz} represents the trains along the z direction, and w, v are the displacements along the z-axis and y-axis, respectively.

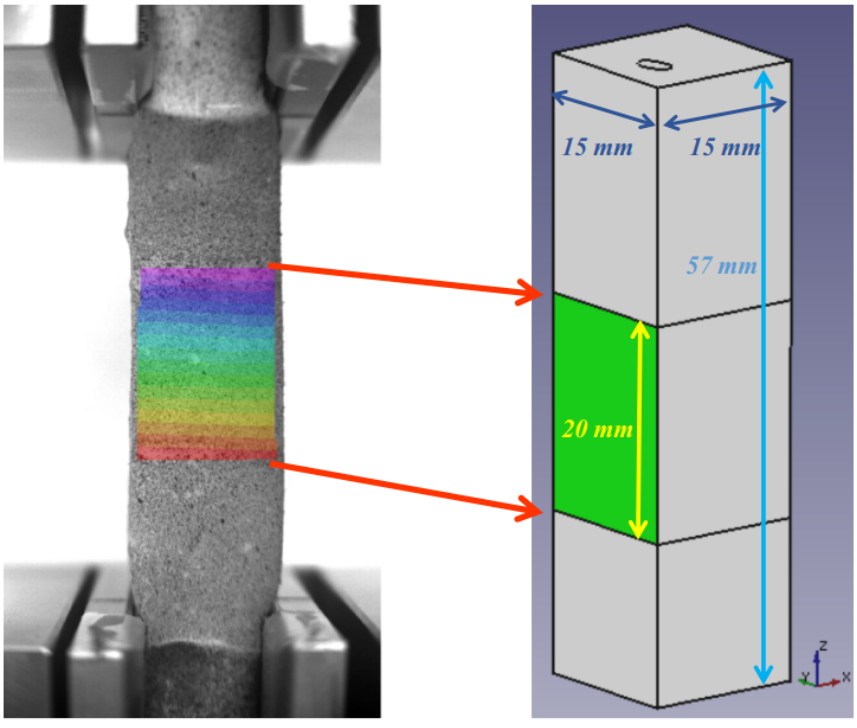

Figure 4.5: (a) Displacement field in the image-analysis interface VIC-2D®. (b) Surface imaged for the numerical analysis, from which we obtain the strain.

4.3 Finite element analysis

A finite element analysis method is used to study the manufactured composite numerically and also to verify that the composite fabrication method meets the fibre and matrix interface requirement. In our finite element study, the composite geometric design is built in FreeCAD, the mesh is generated by Gmsh, the finite element analysis is calculated by the free and open-source software LMGC90[1], and the data analysis is carried out using the Python programming language. The finite element analysis process and the output file format are shown in Figure 4.6. In our study, a linear elastic model and two nonlinear hyperelastic models are applied to study the force-strain response of the soft composite. The fibre and matrix model material parameters used in the finite analysis are determined from tensile tests on the material specimens. The strains taken in the numerical analysis are the average values of the node strains in the z-y plane on the surface of the middle section of the composite, which is where the strain measurement is taken using image analysis (see Figure 4.5). The forces used in the finite element study are the sum of the node internal forces on the end plane of the composite.

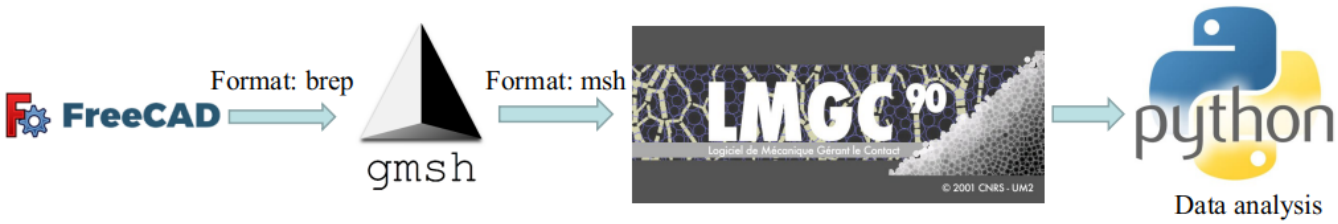

Figure 4.6: Finite element analysis process.

4.3.1 Mesh

A four-node tetrahedron finite element is used in our finite element study, in which the displacements are linearly interpolated over the element from their nodal values. The motivation for this choice is that a tetrahedron element is a close match to the curved fibre-matrix interface. The mesh elements are generated by GMSH software as shown in Figure 4.7. The yellow mesh as shown in Figure 4.7a is the middle middle section of the composite where the strain is estimated. The fibre and the matrix are bound to each other, which means the nodes on their contact surfaces belong to two volumes at the same time, and the inner fibre mesh is shown in Figure 4.7b.

[1]http://hal.archives-ouvertes.fr/hal-01717115/document

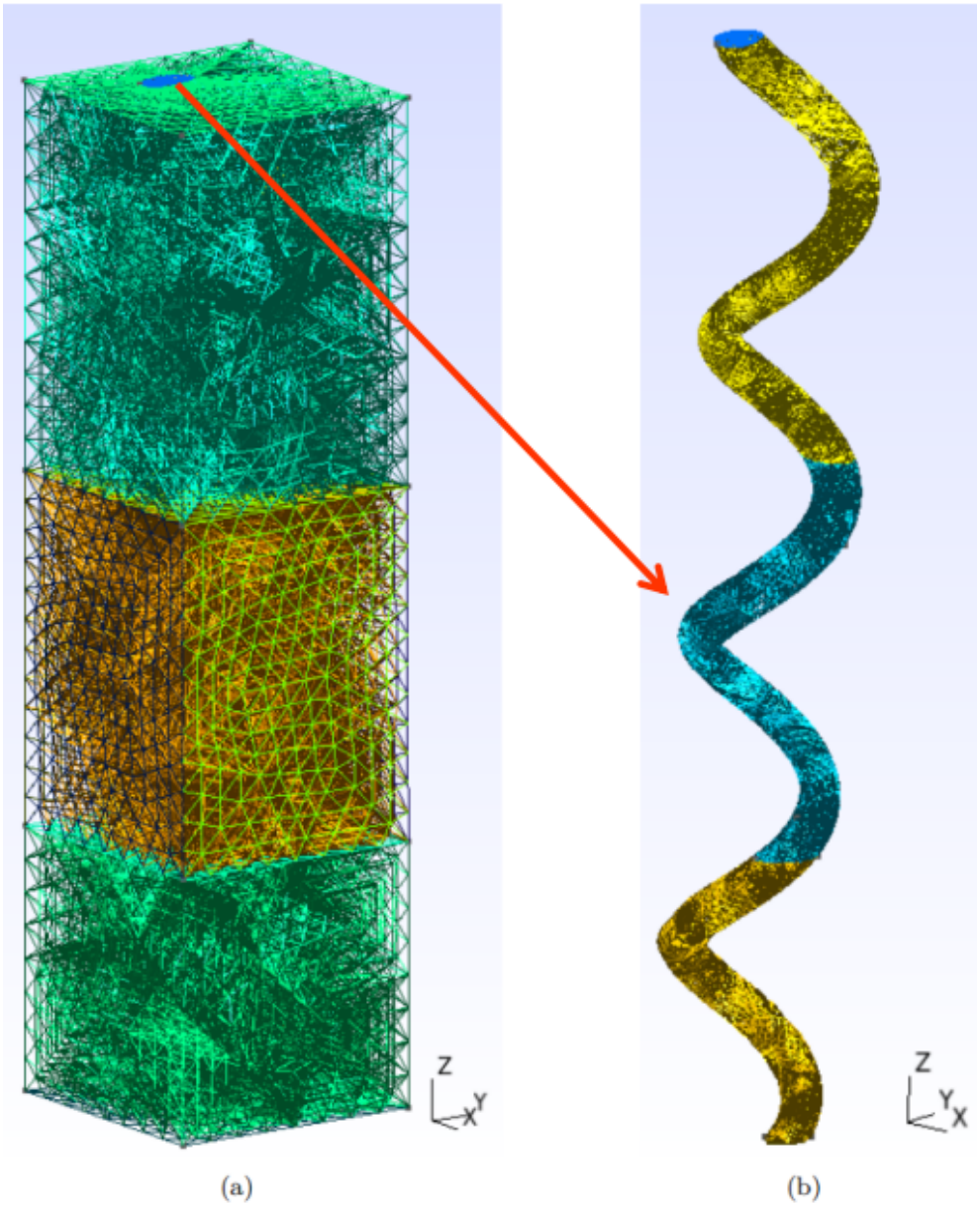

Figure 4.7: (a) Finite element mesh of the soft composites. (b) Mesh of the fibre in the composite.

4.3.2 Boundary conditions

For the boundary conditions of the finite element analysis, the bottom surface of the composite is blocked, and a displacement loading along the z-axis is applied on the top surface with a constant velocity of 0.57 mm/s until 10 % global strain.

4.4 Results

4.4.1 Mesh convergence study

In order to optimize the finite element analysis, meshes of different fineness are studied as shown in Figure 4.8. The number of nodes and tetrahedral elements of each of the meshes studied in this respect are presented in Table 4.8.

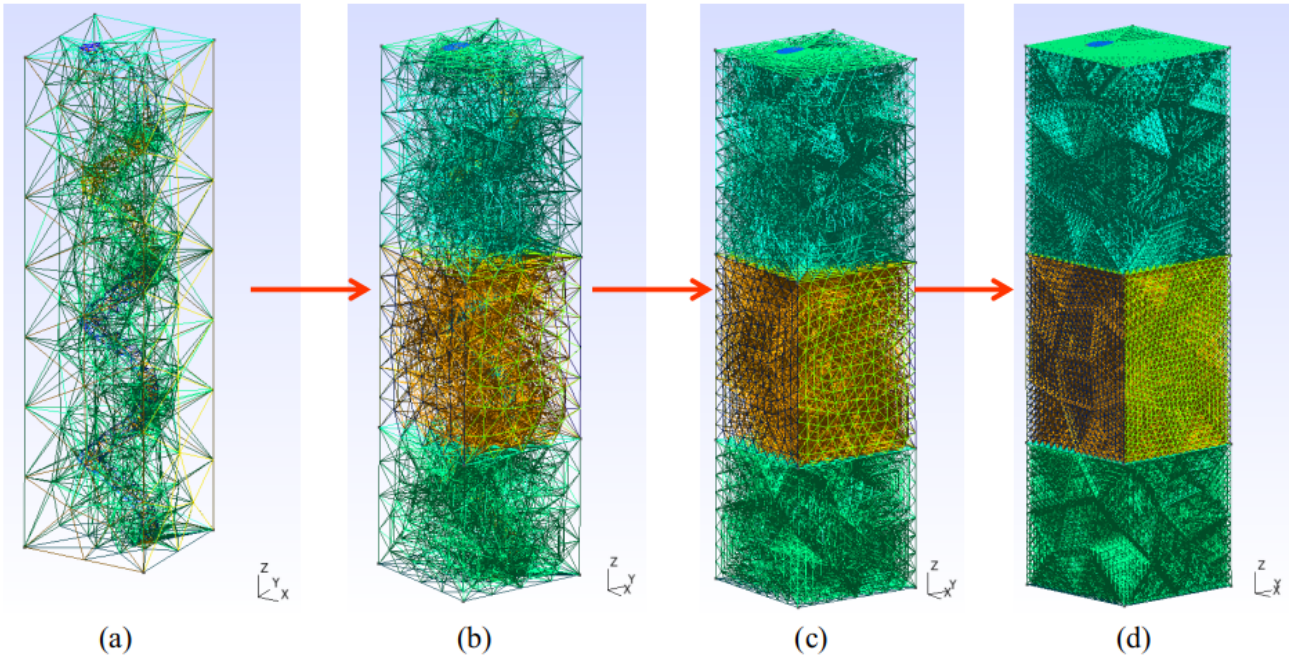

Figure 4.8: Meshes of increasing fineness used in finite element analyses.

	a	b	c	d
Number of nodes	1309	9660	74919	591661
Number of elements	6857	54856	438848	2.09423*10^6

Table 4.2: Numbers of nodes and elements producing meshes of increasing fineness from (a) to (d).

At the end of the tensile simulation tests, we calculated the strains and forces acting on the meshes of different fineness; these are shown in Figure 4.9. As the number of nodes in the mesh increases, the forces and strains calculated using the finite element method gradually stabilize. The force is stabilized at about 0.4 N as shown in Figure 4.9a, and the strain on the middle surface of the composite test specimen reaches an approximate plateau at 0.0874, as shown in Figure 4.9b. We consider the calculated results to be reliable when the number of

nodes is greater than 74919, and therefore we chose to use the mesh shown in Figure 4.8c (column (c) of Table 4.2) for all further calculations of stress and strain.

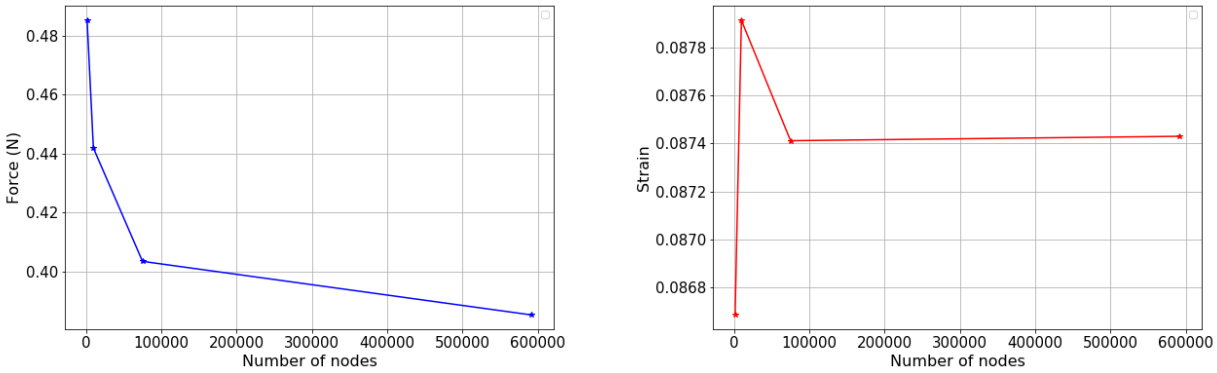

(a) (b)

Figure 4.9: (a) Force (N) versus number of nodes in the mesh. (b) Strain on the middle surface of the composite test specimen versus number of nodes in the mesh.

4.4.2 Experimental material parameter identification

The fibre and matrix materials are characterized by linear elastic, hyperelastic Yeoh, and hyperelastic Neo-Hookean models. The hyperelastic model parameters are determined by the least squares method. The experimental stress–strain curves for the matrix and fibre test samples are shown in Figure 4.10. The parameters of both the fibre and the matrix materials are determined for strains of up to 10 % of its original length. The stress taken in the process of material characterization is the first Piola–Kirchhoff stress (see details in *Hackett* [2018]). We fed the nonlinear Yeoh and Neo-hookean models with material parameters for the fibre and matrix materials calculated using the least squares method (see details in *Humphrey* [2013]). We fitted the predicted curves from these models to the experimental data we obtained for stress and strain as described above. Figure 4.10 shows that the predicted curves are a good match to the experimental data for both the fibre and matrix material. The parameters characterizing these materials are presented in Table 4.3. We tested different types of silicone for sample composite fabrication. The results shown in Table 4.3 are the characterization results of the best shaped sample among the three sample composites fabricated using Mold Max™ 29NV (fibre) and Ecoflex™ 00-10 (matrix) silicone. With these types of silicone, material modulus ratio of fibre to matrix $\frac{E_f}{E_m}$ can reach about 28.

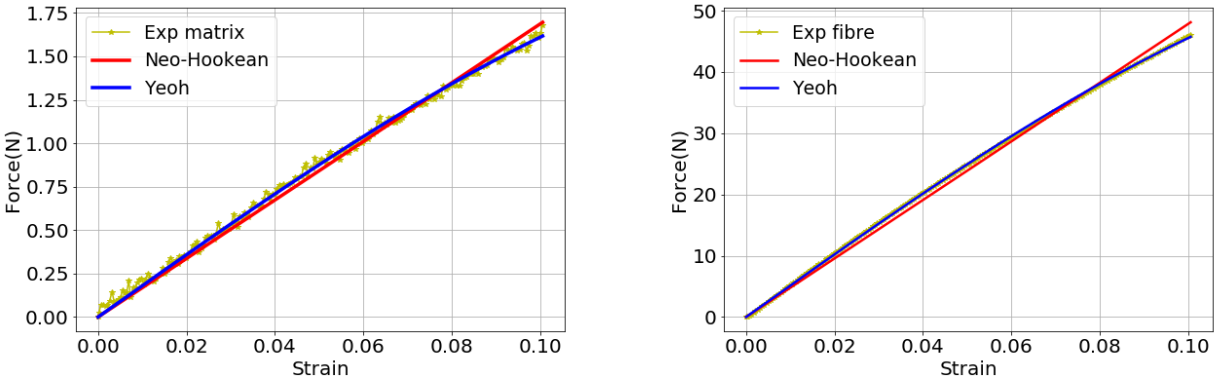

(a) (b)

Figure 4.10: Experimental stress-strain curve of the (a) matrix and (b) fibre test sample with the hyperelastic model fit curve.

Model	Parameter	Matrix Value KPa	Fibre Value KPa
Elastic model	E	16.1	456.6
Neo-Hookean model	C_{10}	2.8	79.53
Yeoh model	C_{10}	3.0	85.6
	C_{20}	-11.6	-350.16

Table 4.3: Characterised material parameters

4.4.3 Finite element analysis results

The relation between the force–strain curve calculated from the linear and nonlinear models with the material parameters as input and experimental results is shown in Figure 4.11. As mentioned above, the strain on the surface of the composite material is obtained by image analysis and calculations using Green-Lagrangian formulations, which are the same formulations used to obtain the numerical strains in our finite element analysis. The forces acting on our composite material are measured using a force sensor during the tensile test, and the force calculated from the elastic and hyperelastic models is the sum of the node internal forces on the upper surface of the composite. A 10% strain is applied to the composite as the load for the finite element study, and the strain is measured on the upper surface of the middle part of the composite. The same is true for the tensile test; strain is measured from images of the surface of the middle section of the composite material. Interestingly, the finite element analysis shows that when the composite is stretched by 10% along the z-axis, the surface of the middle part of the composite is stretched by about 9% as shown in Figure 4.11. The predicted results from our numerical simulation test calculated

by a linear elastic model, the nonlinear Neo-Hookean model, and the nonlinear Yeoh model all show a good fit to the real force-strain experimental results as shown in Figure 4.11.

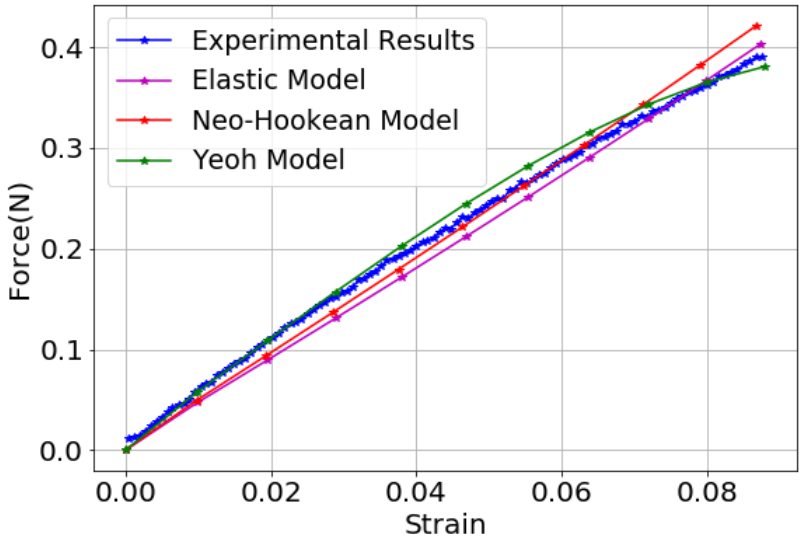

Figure 4.11: Force vs. strain as provided by the finite element analysis of our composite within the framework of the elastic and hyperelastic models and that derived from experimental results.

4.5 Discussion

In this chapter, we present our development of a soft helical-fibre-reinforced composite from silicone-based materials. We present a finite element analysis used to predict the mechanical behavior of the soft composite, which shows a good fit to experimental results from a tensile test carried out on samples of our reinforced composite. The fibre and the matrix in the composite bond well to one another, which agrees with assumptions made in the modeling.

Chanda and Callaway [2018] developed an elastomer-based soft-composite material in order to study tissue anisotropy experimentally. Their fabricated composite was made with straight fibres of different orientations and different fibre volume fractions. *Bailly et al.* [2014] studied silicone rubber membranes reinforced with straight fibre networks with a dedicated apparatus. So far, few modeling studies have focused on soft tissue. To our knowledge, here we make the first attempt to fabricate and model soft composite containing corrugated fibres.

In this work, the developed reinforced composite contains only one helical fibre, but the studies in chapters 2 and 3 focus on soft fibrous tissue, which is assumed to contain many fibres. We show that the composite fabrication method proposed here is able to provide

sample composites that can be studied experimentally. However, such samples are not easy to fabricate. We tested several types of silicone for use as the fibre material in order to reach the largest possible $\frac{E_f}{E_m}$, obtaining $\frac{E_f}{E_m} = 28$ in the present work. The modulus ratio achievable using Mold Max™ 60 series silicone and Ecoflex™ 00-10 silicone can easily reach about 100, but during the composite fabrication process, the Max™ 60 series silicone often contains residual air bubbles even though it is placed in the vacuum chamber. Moreover, it is difficult to fill a syringe with Max™ 60 series silicone and inject it due to its short curing time. Furthermore, it is not easy to leave a perfect interface when removing the metal helix from the cured matrix silicone. Therefore, further work is required to optimize the fabrication process and to produce soft composite with more fibres.

Conclusions and perspectives

The focus of this thesis is on the evolution of Poisson's ratio of fibrous soft tissues as a function of the arrangement of fibres, and, more specifically, their corrugation and spatial organization. Our aim is to gather as much information as possible from a numerical model of fibre-reinforced composite in order to better interpret the wide range of Poisson's ratios of fibrous soft tissue reported in the literature, to predict volume changes in such tissues, and to find the connection between the microstructure and the global macroscopic mechanical behavior of the soft fibrous tissue.

In the first part of this thesis, we provide a review of Poisson's ratio measurements for fibrous soft connective tissue (artery, annulus fibrosus, tendon, and ligament tissues). The reported results suggest that the artery, annulus fibrosus, and tendon tissues show orthotropic material features. Experimental observations reveal both large (larger than 0.5) positive and negative Poisson's ratios. The negative Poisson's ratio, also known as the auxetic effect, is an unusual and counterintuitive behavior, and it is suggested that the crimped microstructure might be responsible (*Lees et al.* [1991]; *Gatt et al.* [2015]). The large range of Poisson's ratios published in the literature might be due to the experimental conditions or to deviations in tissue microstructure. In the present work, we mainly focus on the influence of tissue microstructure. Therefore, we present the microstructure and components of artery, annulus fibrosus, tendon, and ligament tissues in chapter 1, in which we emphasize the corrugated collagen fibre structure in particular. Although it has been suggested that the crimped fibre structure could be responsible for the observed negative Possion's ratios, there is very little evidence in the literature for a link between the two. On the contrary, *Reese et al.* [2010] show that fibres with a helical structure may contribute to larger Poisson's ratios. Also, negative Poisson's ratios are predicted by the constitutive

model for AF tissue presented by *Derrouiche et al.* [2019b] and *Derrouiche et al.* [2020], who consider them to be driven by mechanical- and chemical-based fluid flow interactions until chemo-mechanical equilibrium. Moreover, the HGO model (*Holzapfel et al.* [2000]) and HGO-like models are capable of estimating the auxetic behavior for arterial wall as a function of fibre-matrix material stiffness and fibre dispersion. As the auxetic response is not always found in arterial tissue, several HGO-based models (*Nolan et al.* [2014]; *Latorre et al.* [2016]; *Volokh* [2017]; *Fereidoonnezhad et al.* [2020]) are proposed to avoid auxetic behaviors. Inspired by the speculations in the literature over auxetic behavior related to wavy microstructure, and given the corrugated collagen fibre structure of soft fibrous tissue, we decided to take a mechanical modeling approach to quantitatively study changes in the Poisson's ratio of fibrous soft tissue and their relation to certain characteristics of the crimped fibre microstructure. To this end, we consider the fibrous soft tissues as composite materials reinforced by crimped fibres. We therefore also present a review of the literature on composite models involving crimped structures in chapter 1.

We then propose an analytical micromechanical model with which to study the lamellar composite structure of annulus fibrosus tissue. The model is based on the crimped-fibre-reinforced composite model proposed by *Xiao et al.* [2020], although here we pay particular attention to the multiplicity of the layers and the relative orientation of the parallel fibres between successive layers. Although the lamellar composite structure has already been widely studied (*Remund et al.* [2011]; *Zhou et al.* [2020]), the novelty of our approach is to specifically consider fibre corrugation in conjunction with the relative orientation of the fibres in successive layers and their affects on the Poisson's ratios of the composite material. We consider crimped fibres of sinusoidal form in light of observations of AF tissue in the literature. The proposed micromechanical model is capable of quickly estimating the mechanical properties of layer-dispersed laminates reinforced with crimped fibre structures based solely on theoretical calculations. It can also be used to analyze the influence of changes to each parameter on the effective mechanical properties of the laminate. The following parameters are taken into account in these estimates: modulus of fibre E_f and matrix E_m, the Poisson's ratio of fibre ν_f and matrix ν_m, volume fraction of fibre V_f and matrix V_m, fibre crimp level $\frac{A}{L}$, the relative orientation angle θ_k and thickness e_k of each layer of the laminate, and the total number of layers r. In our parameter study (see Figure C.1 for a reminder of the coordinate system used in this thesis), within a single-layer composite, when the fibre crimp level $\frac{A}{L}$ is small ($\frac{A}{L} < 0.1$), it has a strong influence on the effective elastic moduli E_x and E_z, but has no effect on E_y, and each ν_{ij} is affected by $\frac{A}{L}$. The layer orientation angle θ also affects E_x and E_z as well as each ν_{ij}. The effective elastic modulus E_x has a maximum value when $\frac{A}{L}$ and θ decrease simultaneously, and E_z has a maximum

value when $\frac{A}{L}$ is small and θ is large. In addition, whenever $\theta = 45°$, ν_{xy} and ν_{zy}, ν_{xz} and ν_{zx}, ν_{yz} and ν_{yx}, and E_x and E_z are symmetrical irrespective of $\frac{A}{L}$. The fibre volume fraction V_f has little influence on ν_{ij} but affects the effective elastic moduli. Moreover, the matrix Poisson's ratio ν_m affects each effective ν_{ij} but has little impact on the effective elastic moduli. It is noted that each effective elastic modulus and ν_{ij} change significantly with changes to the elastic modulus ratio of fibre and matrix $\frac{E_f}{E_m}$, but only when $\frac{E_f}{E_m} < 10^2$. For double layer laminate on the other hand, $\frac{A}{L}$ has a measurable influence on E_y. Also, compared to a single-layer laminate, the range of ν_{ij} is significantly expanded; the minimum value is even negative and the maximum value is close to 5. The layer thickness ratio $\frac{e_2}{e_1}$ has little effect on either the effective elastic moduli or ν_{ij}. As in the single layer case, each effective elastic modulus and ν_{ij} significantly changes only when $\frac{E_f}{E_m} < 10^3$. Compared with the impact of layer orientation angle θ, the symmetry of the layer orientation either side of the x-axis has less impact on the Poisson's ratio. In a multi-layer laminate with a range of orientation angles between the successive layers, the gradient of that range is seen to influence the global effective mechanical behavior, with this latter deviating from that of a laminate with a constant orientation between successive layers. Moreover, the larger the range of θ, the larger the difference between the global effective mechanical properties of the laminate and those of the laminate with constant orientation angle.

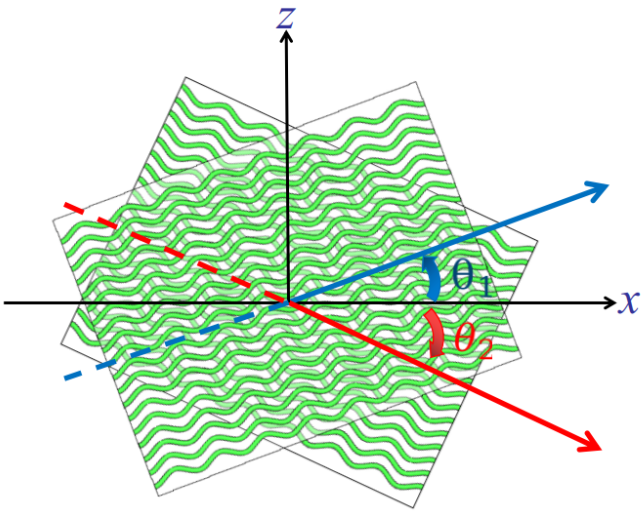

Figure C.1: Schematic of a two-layer laminate within the coordinate system used in the present thesis. The angles θ_1 and θ_1 are the orientations of the two layers relative to the x-axis.

From our parameter studies, both large positive and negative Poisson's ratios are observed. For a double layer laminate, negative Poisson's ratios are observed when the fibre crimp level $\frac{A}{L}$ is small. In these cases, the fibres are considered to be only slightly

corrugated and the negative Poisson's ratios are only seen in the plane of the laminate, that is, in the x-y and y-z planes. Such results are in line with the findings of simulation studies using a nonlinear hyperelastic anisotropic HGO model (*Holzapfel et al.* [2000]). However, as the fibre crimp level $\frac{A}{L}$ increases, the negative Poisson's ratio gradually disappears, which means the fibre crimp feature reduces the auxetic response in the composite material model studied here. In the context of the current literature (*Nolan et al.* [2014]; *Latorre et al.* [2016]; *Volokh* [2017]; *Fereidoonnezhad et al.* [2020]), the work in chapter 2 provides a new method to avoid auxetic behavior and explains why the auxetic effect is not always easy to observe.

The analytical models presented in chapter 2 are designed to broadly represent the morphology of annulus fibrosus, but the approaches and techniques employed here are also applicable to other fibre-reinforced biological tissues (such as arterial media) and bio-composites. In the interest of further applications, we reiterate here that the present work is limited to small initial strain modeled as a linear behavior, and therefore the model does not consider the effect of reorientation of crimped fibres within the matrix as load is applied (stretching). Moreover, the Eshelby equivalent inclusion method provides the best estimates for relatively low (below 60%) fibre volume fractions.

In chapter 3, we use a double-scale asymptotic homogenization method to study helical-fibre-reinforced composite, helical fibres with cross-links (without matrix), and then an amalgamation of the two, that is, helical-fibre-reinforced composite with cross-links between fibres. The crimped fibres are modeled as helical structures, which is based on observations of tendon and arterial wall in the literature. The direction of the helices is set parallel to the z-axis and the cross-links are set perpendicular to that, and are connected to the nearest helix fibre at the furthest or nearest point. In our parameter study, we examine the effects of fibre volume fraction ρ_f, helix angle β, and cross-link position on the macroscopic mechanical properties.

For helical-fibre-reinforced composite, helix angle β has little effect on effective moduli E_x^H and E_y^H, but as β increases, E_z^H increases significantly corresponding to the stiffening behavior of fibrous tissues when stretching them along the direction of the length of the fibres. Furthermore, as fibre volume fraction ρ_f increases, E_x^H, E_y^H, and E_z^H all increase, because the elastic modulus of the fibre is set to a much higher value that of the matrix. For helical fibres with cross-links, the effective moduli show the same tendency: as fibre volume fraction ρ_f and helix angle increase, the effective elastic moduli along the x, y, and z axes increase regardless of the cross-link position or whether or not a matrix is also present. Negative effective Poisson's ratios are found in both helical fibres with cross-links (without matrix) and helical-fibre-reinforced composite with cross-links when the cross-links between helical fibres join the most distant points between any two fibres (longest

possible perpendicular cross-links). Conversely, the largest effective Poisson's ratios are observed for the helical fibres with cross-links (with or without matrix) where the cross-links join the points in closest proximity between any two helices (shortest possible perpendicular cross-links). Moreover, in the absence of matrix, the helical fibres cross-linked with the longest possible cross-links show relatively large negative Poisson's ratios. The Poisson's ratios in composites where the same cross-linked fibres are surrounded by matrix, while still negative, are significantly less negative. This may signify that the presence of matrix weakens the auxetic behavior. These effects may also be what is driving the apparent difficulty in observing the negative Poisson's ratio in real tissues compared to the larger Poisson's ratio.

In summary, the study in chapter 3 focuses the helical structure of fibres in soft tissue and entails an evaluation of the effects of matrix and cross-links on the mechanical properties of soft tissue. The results suggest that the position of the cross-links between helical fibres does not affect the effective elastic modulus, but does influence the volume change of the composite model studied here. Further, the presence of matrix might control the auxetic behavior. We believe that further consideration of the cross-links of specific and more realistic structural arrangements of fibres in the development of future soft tissue models may offer greater insight into the behavior of fibre-reinforced soft tissues.

Finally, we present our development of a soft helical-fibre-reinforced composite using silicone-based materials. The composite manufacturing method satisfies our modeling assumption that the fibres and matrix bond with each other. We also present a finite element analysis that we use to predict the mechanical behavior of the soft composite, which shows a good fit with the experimental results. The work in chapter 4 represents the attempt to fabricate soft composite with corrugated fibres. Our results show that the material model of fibre-reinforced soft tissue can be studied experimentally. However, such a material model is not easy to fabricate and increasing the number of fibres within would not be straightforward.

In conclusion, first we introduce what is currently known about the Poisson's ratios of soft fibrous tissue of the human body and some animal models. We then propose an analytical model of the microstructure of the soft tissue of the AF based on observations from the literature. Finally, based on our study, we conclude that the corrugation of fibres within soft tissues influences their global Poisson's ratios. According to our model, two-dimensional corrugation of fibres reduces the auxetic behavior of a laminate structure within which they are embedded, but helical fibres with cross-links can confer a large positive or negative Poisson's ratio, depending on the positions of the cross-links, and the presence

of matrix surrounding the fibres weakens any inherent auxetic response. In the present thesis, the mechanical behavior of crimped fibre structures that may exist in soft tissue are studied by modeling. In addition, the current work focuses on the changes of Poisson's ratio, which are often ignored in modeling. The novelty of our study compared to the literature is that we consider fibre corrugation and study the effects of changes to parameters related to the nature of this corrugation on the mechanical behavior of a laminate structure designed to broadly represent annulus fibrosus tissue. Moreover, previous studies reported in the literature focused more on the effects of microstructure on stiffness, whereas in the present work, we examine the effects of cross-linking and the presence or not of matrix on changes to the geometry of soft tissues. Furthermore, the present work provides evidence of a link between corrugated fibre structure and auxetic behavior, which goes some way to addressing the speculation in the literature on this topic.

Although there is literature documenting physical measurements of the Poisson ratio of soft fibrous tissue, the reported results vary widely and are even contradictory. In order to understand these discrepancies, it is necessary to identify the factors that cause them, and further measurements of the Poisson's ratio of soft fibrous tissues are needed to confront and thus improve numerical models. Non-linear mechanical models are usually applied in soft tissue modeling, but our proposed models are limited on small initial strain which is considered as linear behavior. Therefore, further work should consider the proposed structure under large deformation. Moreover, the definition of the Poisson's ratio under large deformation also needs to be reconsidered in light of the results of *Dusfour et al.* [2020], which show that as annulus fibrosus is increasingly dilated, the deformation perpendicular to the loading direction is not linear. In other words, during the stretching process, the Poisson's ratio depends on the level of deformation. Furthermore, the matrix in our mechanical model is considered as an isotropic solid material, but the matrix found in AF tissue contains several components, such as water, cells, proteoglycans, and so on. Future modeling should therefore consider the role of matrix and the effect of fluid content on changes to the volume of soft tissue as well as the potential electro-osmotic effect of proteoglycans.

Scientific production

Conference proceedings

- Chenghe Piao, Simon Le Floc'h, Patrick Cañadas, Christiane Wagner-Kocher and Pascale Royer, Auxetic behavior in fibrous soft tissues, Journées du GDR Mecabio 2021, November 29 2021, Grenoble, France
- Chenghe Piao, Simon Le Floc'h, Patrick Cañadas, Christiane Wagner-Kocher and Pascale Royer, Crimped and Cross-Linked Collagen Fibre Structure May Lead to Auxetic Behavior in Soft Tissues, EUROMECH colloquium 627 - Current challenges in soft tissue mechanics, April 6 - 8 2022, Frankfurt, Germany
- Chenghe Piao, Simon Le Floc'h, Patrick Cañadas, Christiane Wagner-Kocher and Pascale Royer, Finite element study of Poisson's ratio for soft tissues with helical fibre structure, 47th congress of the society of biomechanics, October 26 - 28 2022, Monastir, Tunisia

Bibliography

Abdin, Y., A. Jain, I. Verpoest, and S. Lomov, Mean-field based micro-mechanical modelling of short wavy fiber reinforced composites, *Composites Part A: Applied Science and Manufacturing*, *91*, 472–483, 2016.

Ambard, D., and F. Cherblanc, Mechanical behavior of annulus fibrosus: a microstructural model of fibers reorientation, *Annals of biomedical engineering*, *37*(11), 2256–2265, 2009.

Asahara, H., M. Inui, and M. K. Lotz, Tendons and ligaments: connecting developmental biology to musculoskeletal disease pathogenesis, *Journal of Bone and Mineral Research*, *32*(9), 1773–1782, 2017.

Avril, S., and S. Evans, *Material parameter identification and inverse problems in soft tissue biomechanics*, Springer, 2017.

Bai, Q., and Y. Bai, 27 - burst strength of rtp pipeline, in *Subsea Pipeline Design, Analysis, and Installation*, edited by Q. Bai and Y. Bai, pp. 611–620, Gulf Professional Publishing, Boston, doi:https://doi.org/10.1016/B978-0-12-386888-6.00027-4, 2014.

Bailly, L., M. Toungara, L. Orgéas, E. Bertrand, V. Deplano, and C. Geindreau, In-plane mechanics of soft architectured fibre-reinforced silicone rubber membranes, *Journal of the mechanical behavior of biomedical materials*, *40*, 339–353, 2014.

Baldit, A., Micromechanics of the intervertebral disk, in *Multiscale Biomechanics*, pp. 455–467, Elsevier, 2018.

Baldit, A., D. Ambard, F. Cherblanc, and P. Royer, Experimental analysis of the

transverse mechanical behaviour of annulus fibrosus tissue, *Biomechanics and modeling in mechanobiology*, *13*(3), 643–652, 2014.

Barreto Henriksson, H., *Intervertebral disc regeneration. Studies on stem cell niches and cell transplantation*, 2010.

Bass, E., F. Ashford, M. Segal, and J. Lotz, Biaxial testing of human annulus fibrosus and its implications for a constitutive formulation, *Annals of biomedical engineering*, *32*(9), 1231–1242, 2004.

Bensoussan, A., J.-L. Lions, and G. Papanicolaou, *Asymptotic analysis for periodic structures*, vol. 374, American Mathematical Soc., 1978.

Bhattacharya, S., and D. K. Dubey, Radial variations in mechanical behaviour and fibrillar structure in annulus fibrosus has foundations at molecular length-scale: Insights from molecular dynamics simulations of type i and type ii collagen molecules, *Journal of Materials Research*, *36*(17), 3407–3425, 2021.

Billiar, K., and M. Sacks, A method to quantify the fiber kinematics of planar tissues under biaxial stretch, *Journal of biomechanics*, *30*(7), 753–756, 1997.

Bohr, D. F., A. P. Somlyo, and H. Sparks, Handbook of physiology. section 2: The cardivoascular system. volume ii: Vascular smooth muscle, edited by geiger sr, 1980.

Boresi, A. P., R. J. Schmidt, O. M. Sidebottom, et al., *Advanced mechanics of materials*, vol. 6, Wiley New York, 1985.

Boutin, C., J.-L. Auriault, and C. Geindreau, *Homogenization of coupled phenomena in heterogenous media*, vol. 149, John Wiley & Sons, 2010.

Caillerie, D., Homogenization in elasticity, in *Homogenization Techniques for Composite Media*, pp. 1–13, Springer, 1987.

Canham, P. B., H. M. Finlay, J. G. Dixon, D. R. Boughner, and A. Chen, Measurements from light and polarised light microscopy of human coronary arteries fixed at distending pressure, *Cardiovascular research*, *23*(11), 973–982, 1989.

Carew, T. E., R. N. Vaishnav, and D. J. Patel, Compressibility of the arterial wall, *Circulation research*, *23*(1), 61–68, 1968.

Carpi, F., A. Carpi, and M. Russo, Natural and artificial helical structures, *WIT Transactions on Ecology and the Environment*, *138*, 585–592, 2010.

Cassidy, J., A. Hiltner, and E. Baer, Hierarchical structure of the intervertebral disc, *Connective tissue research*, *23*(1), 75–88, 1989.

Chanda, A., and C. Callaway, Tissue anisotropy modeling using soft composite materials, *Applied Bionics and Biomechanics*, *2018*, 2018.

Charras, T., Utiliser cast3m.

Chen, Y., and C. A. Schuh, Analytical homogenization method for periodic composite materials, *Physical Review B*, *79*(9), 094,104, 2009.

Chen, Y.-c., M. Chen, E. A. Gaffney, and C. P. Brown, Effect of crosslinking in cartilage-like collagen microstructures, *Journal of the mechanical behavior of biomedical materials*, *66*, 138–143, 2017.

Cheng, V. W., and H. R. Screen, The micro-structural strain response of tendon, *Journal of Materials Science*, *42*(21), 8957–8965, 2007.

Cherblanc, F., D. Ambard, A. Baldit, and J. Lafosse, Mechanical behaviour of annulus fibrosus: the role of the fluid phase, in *3rd International Conference on Porous Media*, pp. Clé–USB, 2011.

Chernak, L. A., and D. G. Thelen, Tendon motion and strain patterns evaluated with two-dimensional ultrasound elastography, *Journal of biomechanics*, *45*(15), 2618–2623, 2012.

Chuong, C., and Y. Fung, Compressibility and constitutive equation of arterial wall in radial compression experiments, *Journal of biomechanics*, *17*(1), 35–40, 1984.

Cortes, D. H., and D. M. Elliott, Extra-fibrillar matrix mechanics of annulus fibrosus in tension and compression, *Biomechanics and modeling in mechanobiology*, *11*(6), 781–790, 2012.

Cox, R., Anisotropic properties of the canine carotid artery in vitro, *Journal of biomechanics*, *8*(5), 293–300, 1975.

Daniel, I. M., O. Ishai, I. M. Daniel, and I. Daniel, *Engineering mechanics of composite materials*, vol. 1994, Oxford university press New York, 2006.

Daroff, R. B., and M. J. Aminoff, *Encyclopedia of the neurological sciences*, Academic press, 2014.

de Campos Vidal, B., and M. L. S. Mello, Structural organization of collagen fibers in chordae tendineae as assessed by optical anisotropic properties and fast fourier transform, *Journal of structural biology*, *167*(2), 166–175, 2009.

Derrouiche, A., F. Zaïri, and F. Zaïri, A chemo-mechanical model for osmo-inelastic effects in the annulus fibrosus, *Biomechanics and modeling in mechanobiology*, *18*(6), 1773–1790, 2019a.

Derrouiche, A., A. Zaouali, F. Zaïri, J. Ismail, M. Chaabane, Z. Qu, and F. Zaïri, Osmo-inelastic response of the intervertebral disc, *Proceedings of the Institution of Mechanical Engineers, Part H: Journal of Engineering in Medicine*, *233*(3), 332–341, 2019b.

Derrouiche, A., A. Karoui, F. Zaïri, J. Ismail, Z. Qu, M. Chaabane, and F. Zaïri, The two poisson's ratios in annulus fibrosus: relation with the osmo-inelastic features, *Mechanics of Soft Materials*, *2*(1), 1–12, 2020.

Di Puccio, F., S. Celi, and P. Forte, Review of experimental investigations on compressibility of arteries and introduction of a new apparatus, *Experimental mechanics*, *52*(7), 895–902, 2012.

Diamant, J., A. Keller, E. Baer, M. Litt, and R. Arridge, Collagen; ultrastructure and its relation to mechanical properties as a function of ageing, *Proceedings of the Royal Society of London. Series B. Biological Sciences*, *180*(1060), 293–315, 1972.

Dingemans, K. P., P. Teeling, J. H. Lagendijk, and A. E. Becker, Extracellular matrix of the human aortic media: an ultrastructural histochemical and immunohistochemical study of the adult aortic media, *The Anatomical Record: An Official Publication of the American Association of Anatomists*, *258*(1), 1–14, 2000.

Drago, A., and M.-J. Pindera, Micro-macromechanical analysis of heterogeneous materials: Macroscopically homogeneous vs periodic microstructures, *Composites science and technology*, *67*(6), 1243–1263, 2007.

Ducheyne, P., *Comprehensive biomaterials*, vol. 1, Elsevier, 2015.

Dusfour, G., S. LeFloc'h, P. Cañadas, and D. Ambard, Heterogeneous mechanical hyperelastic behavior in the porcine annulus fibrosus explained by fiber orientation: An experimental and numerical approach, *Journal of the mechanical behavior of biomedical materials*, *104*, 103,672, 2020.

Dutov, P., O. Antipova, S. Varma, J. P. Orgel, and J. D. Schieber, Measurement of elastic modulus of collagen type i single fiber, *PloS one*, *11*(1), e0145,711, 2016.

Eberlein, R., G. A. Holzapfel, and C. A. Schulze-Bauer, An anisotropic model for annulus tissue and enhanced finite element analyses of intact lumbar disc bodies, *Computer methods in biomechanics and biomedical engineering*, *4*(3), 209–229, 2001.

Elliott, D. M., and L. A. Setton, Anisotropic and inhomogeneous tensile behavior of the human anulus fibrosus: experimental measurement and material model predictions, *Journal of biomechanical engineering*, *123*(3), 256–263, 2001.

Evans, J., and J. Barbenel, Structural and mechanical properties of tendon related to function, *Equine veterinary journal*, *7*(1), 1–8, 1975.

Farand, P., A. Garon, and G. E. Plante, Structure of large arteries: orientation of elastin in rabbit aortic internal elastic lamina and in the elastic lamellae of aortic media, *Microvascular research*, *73*(2), 95–99, 2007.

Fereidoonnezhad, B., C. O'connor, and J. McGarry, A new anisotropic soft tissue model for elimination of unphysical auxetic behaviour, *Journal of Biomechanics*, *111*, 110,006, 2020.

Finlay, H. M., L. McCullough, and P. B. Canham, Three-dimensional collagen organization of human brain arteries at different transmural pressures, *Journal of vascular research*, *32*(5), 301–312, 1995.

Freed, A. D., and T. C. Doehring, Elastic model for crimped collagen fibrils, 2005.

Garnich, M. R., and G. Karami, Finite element micromechanics for stiffness and strength of wavy fiber composites, *Journal of Composite Materials*, *38*(4), 273–292, 2004.

Gasser, T. C., R. W. Ogden, and G. A. Holzapfel, Hyperelastic modelling of arterial layers with distributed collagen fibre orientations, *Journal of the royal society interface*, *3*(6), 15–35, 2006.

Gatt, R., et al., Negative poisson's ratios in tendons: an unexpected mechanical response, *Acta biomaterialia*, *24*, 201–208, 2015.

Gattu, M., H. Khatam, A. S. Drago, and M.-J. Pindera, Parametric finite-volume micromechanics of uniaxial continuously-reinforced periodic materials with elastic phases, *Journal of engineering materials and technology*, *130*(3), 2008.

Giudici, A., I. B. Wilkinson, and A. W. Khir, Review of the techniques used for investigating the role elastin and collagen play in arterial wall mechanics, *IEEE Reviews in Biomedical Engineering*, *14*, 256–269, 2020.

Guerin, H. A. L., and D. M. Elliott, Degeneration affects the fiber reorientation of human annulus fibrosus under tensile load, *Journal of biomechanics*, *39*(8), 1410–1418, 2006.

Hackett, R. M., Stress measures, in *Hyperelasticity primer*, pp. 29–48, Springer, 2018.

Harvey, A. K., M. S. Thompson, and S. Brady, Helical crimp model predicts material properties from tendon microsctructure, in *Medical Image Understanding and Analysis*, pp. 1–5, Citeseer, 2010.

Hasegawa, H., H. Kanai, N. Chubachi, and Y. Koiwa, Non-invasive evaluation of poisson's ratio of arterial wall using ultrasound, *Electronics letters*, *33*(4), 340–342, 1997.

Hashin, Z., Analysis of composite materials—a survey, 1983.

Hassani, B., and E. Hinton, *Homogenization and structural topology optimization: theory, practice and software*, Springer Science & Business Media, 2012.

Hayashi, K., and E. Hirayama, Age-related changes of wall composition and collagen cross-linking in the rat carotid artery–in relation with arterial mechanics, *Journal of the mechanical behavior of biomedical materials*, *65*, 881–889, 2017.

Herakovich, C. T., Composite laminates with negative through-the-thickness poisson's ratios, *Journal of Composite Materials*, *18*(5), 447–455, 1984.

Hewitt, J., F. Guilak, R. Glisson, and T. P. Vail, Regional material properties of the human hip joint capsule ligaments, *Journal of Orthopaedic Research*, *19*(3), 359–364, 2001.

Hill, M. R., X. Duan, G. A. Gibson, S. Watkins, and A. M. Robertson, A theoretical and non-destructive experimental approach for direct inclusion of measured collagen orientation and recruitment into mechanical models of the artery wall, *Journal of biomechanics*, *45*(5), 762–771, 2012.

Hill, R., A self-consistent mechanics of composite materials, *Journal of the Mechanics and Physics of Solids*, *13*(4), 213–222, 1965.

Holzapfel, G. A., and R. W. Ogden, An arterial constitutive model accounting for collagen content and cross-linking, *Journal of the Mechanics and Physics of Solids*, *136*, 103,682, 2020.

Holzapfel, G. A., T. C. Gasser, and R. W. Ogden, A new constitutive framework for arterial wall mechanics and a comparative study of material models, *Journal of elasticity and the physical science of solids*, *61*(1), 1–48, 2000.

Holzapfel, G. A., C. A. Schulze-Bauer, G. Feigl, and P. Regitnig, Single lamellar mechanics of the human lumbar anulus fibrosus, *Biomechanics and modeling in mechanobiology*, *3*(3), 125–140, 2005.

Hsiao, H. M., and I. Daniel, Effect of fiber waviness on stiffness and strength reduction of unidirectional composites under compressive loading, *Composites science and technology*, *56*(5), 581–593, 1996.

Humphrey, J. D., *Cardiovascular solid mechanics: cells, tissues, and organs*, Springer Science & Business Media, 2013.

Im, G.-I., and T.-K. Kim, Stem cells for the regeneration of tendon and ligament: a perspective, *International Journal of Stem Cells*, *13*(3), 335–341, 2020.

Iwanuma, S., R. Akagi, T. Kurihara, S. Ikegawa, H. Kanehisa, T. Fukunaga, and Y. Kawakami, Longitudinal and transverse deformation of human achilles tendon induced by isometric plantar flexion at different intensities, *Journal of Applied Physiology*, *110*(6), 1615–1621, 2011.

Jiang, Y., et al., 3d-printed auxetic-structured intervertebral disc implant for potential treatment of lumbar herniated disc, *Bioactive materials*, *20*, 528–538, 2023.

Jin, Y., C. Xie, Q. Gao, X. Zhou, G. Li, J. Du, and Y. He, Fabrication of multi-scale and tunable auxetic scaffolds for tissue engineering, *Materials & Design*, *197*, 109,277, 2021.

Jozsa, L., P. Kannus, J. Balint, and A. Reffy, Three-dimensional infrastructure of human tendons, *Cells Tissues Organs*, *142*(4), 306–312, 1991.

Ju, J., and K. Yanase, Micromechanics and effective elastic moduli of particle-reinforced composites with near-field particle interactions, *Acta Mechanica*, *215*(1), 135–153, 2010.

Kandil, K., F. Zaïri, A. Derrouiche, T. Messager, and F. Zaïri, Interlamellar-induced time-dependent response of intervertebral disc annulus: A microstructure-based chemo-viscoelastic model, *Acta biomaterialia*, *100*, 75–91, 2019.

Kannus, P., Structure of the tendon connective tissue, *Scandinavian journal of medicine & science in sports*, *10*(6), 312–320, 2000.

Karami, G., and M. Garnich, Effective moduli and failure considerations for composites with periodic fiber waviness, *Composite Structures*, *67*(4), 461–475, 2005a.

Karami, G., and M. Garnich, Micromechanical study of thermoelastic behavior of composites with periodic fiber waviness, *Composites Part B: Engineering*, *36*(3), 241–248, 2005b.

Karami, G., N. Grundman, N. Abolfathi, A. Naik, and M. Ziejewski, A micromechanical hyperelastic modeling of brain white matter under large deformation, *Journal of the mechanical behavior of biomedical materials*, *2*(3), 243–254, 2009.

Karimi, A., T. Sera, S. Kudo, and M. Navidbakhsh, Experimental verification of the healthy and atherosclerotic coronary arteries incompressibility via digital image correlation, *Artery Research*, *16*, 1–7, 2016.

Kashtalyan, M., Application of the boundary shape perturbation method to stress analysis of laminated composites with ply waviness, *Composites Part A: Applied Science and Manufacturing*, *36*(2), 137–143, 2005.

Kastelic, J., A. Galeski, and E. Baer, The multicomposite structure of tendon, *Connective tissue research*, *6*(1), 11–23, 1978.

Khani, N., M. Yildiz, and B. Koc, Elastic properties of coiled carbon nanotube reinforced nanocomposite: A finite element study, *Materials & Design*, *109*, 123–132, 2016.

Khatam, H., and M.-J. Pindera, Thermo-elastic moduli of periodic multilayers with wavy architectures, *Composites Part B: Engineering*, *40*(1), 50–64, 2009.

Kim, Y., K. H. Son, and J. W. Lee, Auxetic structures for tissue engineering scaffolds and biomedical devices, *Materials*, *14*(22), 6821, 2021.

Kuksenko, D., H. J. Böhm, and B. Drach, Effect of micromechanical parameters of composites with wavy fibers on their effective response under large deformations, *Advances in Engineering Software*, *121*, 206–222, 2018.

Kwon, P., and C. Dharan, Effective moduli of high volume fraction particulate composites, *Acta metallurgica et materialia*, *43*(3), 1141–1147, 1995.

Latorre, M., X. Romero, and F. J. Montans, The relevance of transverse deformation effects in modeling soft biological tissues, *International Journal of Solids and Structures*, *99*, 57–70, 2016.

Lees, C., J. F. Vincent, and J. E. Hillerton, Poisson's ratio in skin, *Bio-medical materials and engineering*, *1*(1), 19–23, 1991.

Lewis, N. T., M. A. Hussain, and J. J. Mao, Investigation of nano-mechanical properties of annulus fibrosus using atomic force microscopy, *Micron*, *39*(7), 1008–1019, 2008.

Liao, J., *Mechanical and structural properties of mitral valve chordae tendineae*, Cleveland state university, 2003.

Liao, J., and I. Vesely, A structural basis for the size-related mechanical properties of mitral valve chordae tendineae, *Journal of biomechanics*, *36*(8), 1125–1133, 2003.

Lillie, M., R. Shadwick, and J. Gosline, Mechanical anisotropy of inflated elastic tissue from the pig aorta, *Journal of biomechanics*, *43*(11), 2070–2078, 2010.

Liu, Y., W. Zhang, C. Wang, and G. Kassab, A linearized and incompressible constitutive model for arteries, *Journal of theoretical biology*, *286*, 85–91, 2011.

Lynch, H., W. Johannessen, M. Bey, D. Elliott, et al., Poisson's ratio and modulus for tendon transverse and longitudinal fiber orientations, in *Transations of annual meeting-orthopaedic research society*, pp. 243–243, 2002.

Lynch, H. A., W. Johannessen, J. P. Wu, A. Jawa, and D. M. Elliott, Effect of fiber orientation and strain rate on the nonlinear uniaxial tensile material properties of tendon, *J. Biomech. Eng.*, *125*(5), 726–731, 2003.

Maganaris, C. N., Y. Kawakami, and T. Fukunaga, Changes in aponeurotic dimensions upon muscle shortening: in vivo observations in man, *The Journal of Anatomy*, *199*(4), 449–456, 2001.

Marchand, F., and A. M. Ahmed, Investigation of the laminate structure of lumbar disc anulus fibrosus., *Spine*, *15*(5), 402–410, 1990.

Marcolongo, M., S. Sarkar, and N. Ganesh, 7.11 trends in materials for spine surgery, 2017.

Mardling, P., A. Alderson, N. Jordan-Mahy, and C. L. Le Maitre, The use of auxetic materials in tissue engineering, *Biomaterials science*, *8*(8), 2074–2083, 2020.

Marino, M., and G. Vairo, Multiscale elastic models of collagen bio-structures: from cross-linked molecules to soft tissues, in *Multiscale computer modeling in biomechanics and biomedical engineering*, pp. 73–102, Springer, 2013.

Mori, T., and K. Tanaka, Average stress in matrix and average elastic energy of materials with misfitting inclusions, *Acta metallurgica*, *21*(5), 571–574, 1973.

Morin, C., W. Krasny, and S. Avril, Multiscale mechanical behavior of large arteries, *arXiv preprint arXiv:1912.06052*, 2019.

Moulton, D. E., T. Lessinnes, and A. Goriely, Morphoelastic rods iii: Differential growth and curvature generation in elastic filaments, *Journal of the Mechanics and Physics of Solids*, p. 104022, 2020.

Mura, T., *Micromechanics of defects in solids*, Springer Science & Business Media, 2013.

Nahon, D., J. Lee, and G. Wilson, A two-dimensional incremental study of the static mechanical properties of vascular grafts, *Clinical Materials*, *1*(3), 177–197, 1986.

Niestrawska, J. A., C. Viertler, P. Regitnig, T. U. Cohnert, G. Sommer, and G. A. Holzapfel, Microstructure and mechanics of healthy and aneurysmatic abdominal aortas: experimental analysis and modelling, *Journal of The Royal Society Interface*, *13*(124), 20160,620, 2016.

Niestrawska, J. A., A. Pukaluk, A. R. Babu, and G. A. Holzapfel, Differences in collagen fiber diameter and waviness between healthy and aneurysmal abdominal aortas, *Microscopy and Microanalysis*, pp. 1–15, 2022.

Nolan, D. R., A. L. Gower, M. Destrade, R. W. Ogden, and J. McGarry, A robust anisotropic hyperelastic formulation for the modelling of soft tissue, *Journal of the mechanical behavior of biomedical materials*, *39*, 48–60, 2014.

Obst, S. J., R. Newsham-West, and R. S. Barrett, In vivo measurement of human achilles tendon morphology using freehand 3-d ultrasound, *Ultrasound in medicine & biology*, *40*(1), 62–70, 2014.

O'Connell, M. K., et al., The three-dimensional micro-and nanostructure of the aortic medial lamellar unit measured using 3d confocal and electron microscopy imaging, *Matrix Biology*, *27*(3), 171–181, 2008.

O'Connell, G. D., H. L. Guerin, and D. M. Elliott, Theoretical and uniaxial experimental evaluation of human annulus fibrosus degeneration, 2009.

O'Connell, G. D., S. Sen, and D. M. Elliott, Human annulus fibrosus material properties from biaxial testing and constitutive modeling are altered with degeneration, *Biomechanics and modeling in mechanobiology*, *11*(3), 493–503, 2012.

Parnell, W. J., The eshelby, hill, moment and concentration tensors for ellipsoidal inhomogeneities in the newtonian potential problem and linear elastostatics, *Journal of Elasticity*, *125*(2), 231–294, 2016.

Patel, D. J., J. S. Janicki, and T. E. Carew, Static anisotropic elastic properties of the aorta in living dogs, *Circulation Research*, *25*(6), 765–779, 1969.

Patten, K., and T. Wess, Suprafibrillar structures of collagen, evidence for local organization and auxetic behaviour in architectures, *Journal of Biophysical Chemistry*, *2013*, 2013.

Peng, X., Z. Guo, and B. Moran, An anisotropic hyperelastic constitutive model with fiber-matrix shear interaction for the human annulus fibrosus, 2006.

Pezowicz, C., Analysis of selected mechanical properties of intervertebral disc annulus fierosus in macro and microscopic scale, *Journal of theoretical and applied mechanics*, *48*(4), 917–932, 2010.

Pezowicz, C. A., P. A. Robertson, and N. D. Broom, Intralamellar relationships within the collagenous architecture of the annulus fibrosus imaged in its fully hydrated state, *Journal of anatomy*, *207*(4), 299–312, 2005.

Piao, C., S. Lefloch, P. Cañadas, C. Wagner-Kocher, and P. Royer, Auxetic behavior in fibrous soft tissues, in *Journées du GDR Mecabio 2021*, 2021.

Reese, S. P., and J. A. Weiss, Tendon fascicles exhibit a linear correlation between poisson's ratio and force during uniaxial stress relaxation, *Journal of biomechanical engineering*, *135*(3), 2013.

Reese, S. P., S. A. Maas, and J. A. Weiss, Micromechanical models of helical superstructures in ligament and tendon fibers predict large poisson's ratios, *Journal of biomechanics*, *43*(7), 1394–1400, 2010.

Remund, T. S., T. J. Layh, T. M. Rosenboom, L. A. Koepsell, Y. Deng, and Z. Hu, A novel finite element model for annulus fibrosus tissue engineering using homogenization techniques, *American transactions on engineering & applied sciences*, *1*, 1–23, 2011.

Rezakhaniha, R., A. Agianniotis, J. T. C. Schrauwen, A. Griffa, D. Sage, C. v. Bouten, F. Van De Vosse, M. Unser, and N. Stergiopulos, Experimental investigation of collagen waviness and orientation in the arterial adventitia using confocal laser scanning microscopy, *Biomechanics and modeling in mechanobiology*, *11*(3), 461–473, 2012.

Roy, S., C. Boss, R. Rezakhaniha, and N. Stergiopulos, Experimental characterization of the distribution of collagen fiber recruitment, *Journal of biorheology*, *24*(2), 84–93, 2010.

Saadat, F., V. Birman, S. Thomopoulos, and G. M. Genin, Effective elastic properties of a composite containing multiple types of anisotropic ellipsoidal inclusions, with application to the attachment of tendon to bone, *Journal of the Mechanics and Physics of Solids*, *82*, 367–377, 2015.

Sánchez-Palencia, E., Non-homogeneous media and vibration theory, *Lecture notes in physics*, *127*, 1980.

Santamaría, V. A. A., M. F. García, J. Molimard, and S. Avril, Characterization of chemoelastic effects in arteries using digital volume correlation and optical coherence tomography, *Acta Biomaterialia*, *102*, 127–137, 2020.

Schlecht, S. H., Understanding entheses: bridging the gap between clinical and anthropological perspectives, *The Anatomical Record: Advances in Integrative Anatomy and Evolutionary Biology*, *295*(8), 1239–1251, 2012.

Schrauwen, J., A. Vilanova, R. Rezakhaniha, N. Stergiopulos, F. Van De Vosse, and P. Bovendeerd, A method for the quantification of the pressure dependent 3d collagen configuration in the arterial adventitia, *Journal of structural biology*, *180*(2), 335–342, 2012.

Sharabi, M., Structural mechanisms in soft fibrous tissues: A review, *Front. Mater. 8: 793647. doi: 10.3389/fmats*, 2022.

Sharabi, M., K. Wade, and R. Haj-Ali, The mechanical role of collagen fibers in the intervertebral disc, *Biomechanics of the Spine*, pp. 105–123, 2018.

Shekhonin, B. V., S. P. Domogatsky, V. R. Muzykantov, G. L. Idelson, and V. S. Rukosuev, Distribution of type i, iii, iv and v collagen in normal and atherosclerotic human arterial wall: immunomorphological characteristics, *Collagen and related research*, *5*(4), 355–368, 1985.

Sinha, P., Composite materials and structures, *Composite Centre of Excellence, AR&DB, Department of Aerospace Engineering IIT Kharagpur*, 2006.

Skacel, P., and J. Bursa, Poisson s ratio of arterial wall–inconsistency of constitutive models with experimental data, *Journal of the mechanical behavior of biomedical materials*, *54*, 316–327, 2016.

Skacel, P., and J. Bursa, Poisson's ratio and compressibility of arterial wall–improved experimental data reject auxetic behaviour, *Journal of the Mechanical Behavior of Biomedical Materials*, *131*, 105,229, 2022.

Skaggs, D., M. Weidenbaum, J. C. Iatridis, A. Ratcliffe, and V. C. Mow, Regional variation in tensile properties and biochemical composition of the human lumbar anulus fibrosus., *Spine*, *19*(12), 1310–1319, 1994.

Snir, Y., and R. D. Kamien, Entropically driven helix formation, *Science*, *307*(5712), 1067–1067, 2005.

Staubesand, J., Anatomie der blutgefäße. i. funktionelle morphologie der arterien, venen und arterio-venösen anastomosen, *Angiology*, pp. 23–82, 1959.

Sun, C. T., and S. Li, Three-dimensional effective elastic constants for thick laminates, *Journal of composite materials*, *22*(7), 629–639, 1988.

Thorpe, C. T., C. Klemt, G. P. Riley, H. L. Birch, P. D. Clegg, and H. R. Screen, Helical sub-structures in energy-storing tendons provide a possible mechanism for efficient energy storage and return, *Acta biomaterialia*, *9*(8), 7948–7956, 2013.

Thorpe, C. T., G. P. Riley, H. L. Birch, P. D. Clegg, and H. R. Screen, Effect of fatigue loading on structure and functional behaviour of fascicles from energy-storing tendons, *Acta biomaterialia*, *10*(7), 3217–3224, 2014.

Timmins, L. H., Q. Wu, A. T. Yeh, J. E. Moore Jr, and S. E. Greenwald, Structural inhomogeneity and fiber orientation in the inner arterial media, *American Journal of Physiology-Heart and Circulatory Physiology*, *298*(5), H1537–H1545, 2010.

Ushiki, T., Collagen fibers, reticular fibers and elastic fibers. a comprehensive understanding from a morphological viewpoint, *Archives of histology and cytology*, *65*(2), 109–126, 2002.

Vasquez-villegas, Exploration des propriétés des microstructures tpms pour mimer le comportement mécanique du disque intervertébral cervical humain dans l'objectif de réaliser une prothèse par fabrication additive, 2022.

Vella Wood, M., A. Casha, A. Gatt, C. Formosa, N. Chockalingam, J. N. Grima, and R. Gatt, 3d printed clamps to study the mechanical properties of tendons at low strains, *physica status solidi (b)*, *256*(1), 1800,159, 2019.

Vergari, C., P. Pourcelot, L. Holden, B. Ravary-Plumioën, G. Gerard, P. Laugier, D. Mitton, and N. Crevier-Denoix, True stress and poisson's ratio of tendons during loading, *Journal of biomechanics*, *44*(4), 719–724, 2011.

Vergari, C., D. Chan, A. Clarke, J. C. Mansfield, J. R. Meakin, and P. C. Winlove, Bovine and degenerated human annulus fibrosus: a microstructural and micromechanical comparison, *Biomechanics and modeling in mechanobiology*, *16*(4), 1475–1484, 2017.

Veronda, D., and R. Westmann, Mechanical characterization of skin—finite deformations, *Journal of biomechanics*, *3*(1), 111–124, 1970.

Verzár, F., Aging of the collagen fiber, *International review of connective tissue research*, *2*, 243–300, 1964.

Volokh, K., Compressibility of arterial wall in ring-cutting experiments, *Molecular & Cellular Biomechanics*, *3*(1), 35, 2006.

Volokh, K. Y., On arterial fiber dispersion and auxetic effect, *Journal of biomechanics*, *61*, 123–130, 2017.

von der Mark, K., Localization of collagen types in tissues, *International review of connective tissue research*, *9*, 265–324, 1981.

Wagner, D. R., and J. C. Lotz, Theoretical model and experimental results for the nonlinear elastic behavior of human annulus fibrosus, *Journal of orthopaedic research*, *22*(4), 901–909, 2004.

Weizsäcker, H. W., H. Lambert, and K. Pascale, Analysis of the passive mechanical properties of rat carotid arteries, *Journal of biomechanics*, *16*(9), 703–715, 1983.

Wiebe, C., and G. W. Brodland, Tensile properties of embryonic epithelia measured using a novel instrument, *Journal of biomechanics*, *38*(10), 2087–2094, 2005.

Williams, J., and J. Lewis, Properties and an anisotropic model of cancellous bone from the proximal tibial epiphysis, 1982.

Wu, H.-C., and R.-F. Yao, Mechanical behavior of the human annulus fibrosus, *Journal of biomechanics*, *9*(1), 1–7, 1976.

Xiao, S., Y. Shao, B. Li, and X.-Q. Feng, A micromechanical model of tendon and ligament with crimped fibers, *Journal of the mechanical behavior of biomedical materials*, *112*, 104,086, 2020.

Yahia, L.-H., and G. Drouin, Microscopical investigation of canine anterior cruciate ligament and patellar tendon: collagen fascicle morphology and architecture, *Journal of orthopaedic research*, *7*(2), 243–251, 1989.

Yan, D., J. Chang, H. Zhang, J. Liu, H. Song, Z. Xue, F. Zhang, and Y. Zhang, Soft three-dimensional network materials with rational bio-mimetic designs, *Nature communications*, *11*(1), 1–11, 2020.

Yin, L., and D. M. Elliott, A biphasic and transversely isotropic mechanical model for tendon:: application to mouse tail fascicles in uniaxial tension, *Journal of biomechanics*, *37*(6), 907–916, 2004.

Yosibash, Z., I. Manor, I. Gilad, and U. Willentz, Experimental evidence of the compressibility of arteries, *Journal of the mechanical behavior of biomedical materials*, *39*, 339–354, 2014.

Zhang, D., C. D. Eggleton, and D. D. Arola, Evaluating the mechanical behavior of arterial tissue using digital image correlation, *Experimental mechanics*, *42*(4), 409–416, 2002.

Zhang, D., U. Chippada, and K. Jordan, Effect of the structural water on the mechanical properties of collagen-like microfibrils: a molecular dynamics study, *Annals of biomedical engineering*, *35*(7), 1216–1230, 2007.

Zhou, M., S. E. Bezci, and G. D. O'Connell, Multiscale composite model of fiber-reinforced tissues with direct representation of sub-tissue properties, *Biomechanics and modeling in mechanobiology*, *19*(2), 745–759, 2020.

Zorzetto, L., and D. Ruffoni, Wood-inspired 3d-printed helical composites with tunable and enhanced mechanical performance, *Advanced Functional Materials*, *29*(1), 1805,888, 2019.